UNIVERSITY OF EXETER

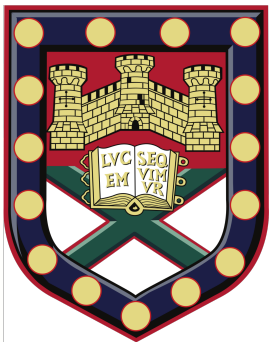

DOCTORAL THESIS

Nonlinear optical effects in two dimensional and thin film materials

---

Author:

Craig John TOLLERTON

Supervisors:

Professor Euan HENDRY

Professor William L. BARNES

Submitted by Craig John Tollerton to the University of Exeter as a thesis for the degree of Doctor of Philosophy in Physics/Engineering, September 2019

Declaration of Authorship

I, Craig John TOLLERTON, declare that this thesis titled, "Nonlinear optical effects in two dimensional and thin film materials" and the work presented in it are my own. I confirm that:

- This work was done wholly or mainly while in candidature for a research degree at this University.
- Where any part of this thesis has previously been submitted for a degree or any other qualification at this University or any other institution, this has been clearly stated.
- Where I have consulted the published work of others, this is always clearly attributed.
- Where I have quoted from the work of others, the source is always given. With the exception of such quotations, this thesis is entirely my own work.
- I have acknowledged all main sources of help.
- Where the thesis is based on work done by myself jointly with others, I have made clear exactly what was done by others and what I have contributed myself.

Signed:

CJTollerton

Date:

20^{th} September 2019

Nonlinear optical effects in two dimensional and thin film materials

Craig John TOLLERTON

Abstract

This thesis comprises work on three different projects in nonlinear optics. Those are the second order conductivity of graphene, plasmon enhanced four-wave mixing in graphene and intensity dependent differential reflection of ITO.

The second order conductivity of graphene has been a contentious area for some time as, in a centro-symmetric material like graphene, one would expect no response within the dipole approximation. As experiments have shown strong second order signals for graphene, the field has sought explanations outwith the dipole approximation to explain the results. However, there has not been a consensus that agrees with experiments. Here we derive the second order conductivity of graphene through perturbation theory and, agreeing that this result cannot account for observed responses, seek alternate explanations for second order signals observed in experiment. This work concludes with the presentation of a photothermal model, based on the Seebeck effect, that predicts response two order of magnitude higher than the results of perturbation theory. This work provides a very promising first step to advancing the understanding the discrepancy between theory and experiment for second order nonlinear effects in graphene.

Graphene is predicted to have large third order nonlinear effects due to its linear band structure in the vicinity of the Dirac points. This work presents a detailed study into the possibility of plasmon enhanced resonant cascaded four-wave mixing. An experimental setup is designed such that a four-wave mixing signal is generated from a graphene sheet and the DFG mode of the same incident beams can couple to the surface plasmon polariton in graphene through a difference frequency generation interaction. This work shows that the signal from a cascaded effect is not strong enough to contribute significantly to the wavemixing signal observed. This implies

that the enhancement of electric field at the plasmon resonance is not sufficient to overcome the inherent weakness of multiple second order processes in graphene.

Indium tin oxide (ITO) has recently been identified as a high promising nonlinear material, in particular for use optical switching devices, where the reflectance of one beam is changed through intensity of itself or another pump beam. This work presents a new geometry that predicts and measures a change in reflectivity at a glass-ITO-air interface larger than previously measured and for significantly smaller intensities. Further to this finding, models are presented that reveal constraints to the use of ITO as a nonlinear material. In particular, both the switching and pumping of the ITO must occur on femtosecond timescales, at higher picosecond timescales the strong electron-phonon coupling and high specific heat capacity of the lattice prevent such effects being observed. This work provides an excellent platform for moving towards an optical switch with ITO as the nonlinear active component.

Acknowledgements

I've always said that if you can't name at least three people who were instrumental to your success, you didn't pay enough attention to what other people have done for you. As it turns out, for a PhD, this number is raised to an unfathomable amount of people. Here I would like to acknowledge but a few of those who have particularly stuck in my mind for their support during this work and without whom I would not have been able to complete this project.

Firstly I would like to thank the support staff of the university, though I stress that the term support staff really does not do justice to the workload placed on them. From the workshop I would like to thank Nick Cole and Peter Savage, who beyond being talented technicians who hold my project together with more than the glue and blue tac I would apply myself, are fantastic to stop by and say "hello" to on a rough day, greeting me with nothing but friendly faces. From the IT department, the workload of Chris Forrest is immense, and I feel that if he was allowed to have a proper understanding of normal work hours the system would fall apart. Many a time have I asked for help, on things I should probably be able to do myself, after works hours and the problem been fixed before the next day without comment.

Thanks to the academics beyond my project, who stepped in and shared their skills and expertise without hesitation. David Phillips for his assistance with Fourier imaging, Philip Thomas for his help with ellipsometry measurements, Simon Horsley for his assistance with some of the more challenging mathematics I came across, Fred Withers for preparing the graphene flakes used in this work and Kishan Menghrajani for his assistance with all things fabrication, in particular a vast number of experimental samples that didn't amount to much but he was always willing to make at the drop of a hat.

To my collaborators at ICFO, Darrick Chang and David Li, whose tireless work through a lengthy review process helped us get our knowledge out there into the literature. And in particular to David Li, who offered some supportive words to a PhD student going through his first review process when things looked gloomy.

At the start of my PhD, I was warmly invited into an incredible research group. In particular the assistance of Tom Constant and Sam Hornett was instrumental in

getting me off the ground in the first months, and they never stopped being on call with assistance on equipment to results analysis. I'm sure we will all fondly remember "Lads on Conference", as Sam and I fell down a mountain (they may have given us skis but we certainly weren't skiing) while Tom gave encouragement from the sidelines. In the more recent years, Justus Bohn has been a fantastic project partner since beginning his project here.

To the friends who made the workload manageable, Alastair Litterick who stepped in without even being asked to correct my 11-year old schoolboy grammar, something that seems to have barely improved from when we first met. And my deskmate Harry Penketh, whose consistent good chat has lightened many a day stuck chained to the desk.

To the supervisors who helped guide my project through some rocky waters, Bill Barnes for stepping in as a supervisor part way into the project to provide an invaluable contribution, and Euan Hendry, whose thirst for science keeps us all going and can spark excitement in any project.

To my partner Lucy Abbs, who like so many has had to put up with being a PhD widow for so long. Whose faith in me never faltered, whose encouragement never diminished and whose support never waned. I could not have done this without you and I am so glad you were with me for it.

Lastly I would like to thank my family, my brother Ryan and my sister Laura, whose unconditional support has always held us together in tougher times. I think we all go further because of the consistent support we know comes from each other. My stepfather Danny Kimble who would do anything to see me and my siblings succeed, I have seen no finer example of how to carry yourself as a man.

Thanks to all those and more, who give of themselves to help others succeed.

For Lesley Tollerton, my mother.

Because no person has, or could have, contributed more to my success.

I hope I make you as proud of me as I am of you.

Contents

List of Figures

List of Tables

List of Symbols

ϵ	permittivity
ω	angular frequency
ω_F	Fermi angular frequency
ω_{nm}	effective frequency difference between states n and m
σ	conductivity
δ	nearest neighbour vectors in graphene
$\chi^{(n)}$	n-th order susceptibility
Φ	fluence
ψ	wavefunction
ρ	density matrix
θ, ϕ	angle
γ	scattering rate
ρ_r	complex reflectance ratio
Δ	complex reflectance phase
Ψ	complex reflectance amplitude (Chapter 3); phase offset (Chapter 5)
μ	permeability
μ_a	mobility associated with a-type scattering
$\vec{\tau}$	nearest neighbour vectors
ζ	area of graphene sheet
Θ	Heaviside step function
Γ	photon flux
α	fine structure constant (Chapter 3); diffusivity (Chapter 5
$\vec{J}$	current density
$\vec{E}$	electric field
$\vec{k}$	wavevector

$\vec{D}$	displacement vector
$\vec{P}$	polarisation
$\vec{H}$	magnetic field strength
$\vec{\hat{\sigma}}$	Pauli spin matrix vector
$\vec{A}$	vector potential
$\vec{\mu}$	transition dipole moment vector
$\vec{B}$	magnetic field
$\hat{H}$	Hamiltonian operator
$\hat{\vec{P}}$	Momentum operator
n	refractive index
m	mass
e	charge of an electron
p	dipole polarisation
t	time
c	speed of light in a vacuum
R	Reflectivity
f	focal length
a	graphene lattice vectors
v_f	Fermi velocity
$\hbar$	Planck's constant reduced by 2π
T	transmission
q	in-plane wavevector
k_F	Fermi wavevector
E_F	Fermi energy
$r_{TE,TM}$	reflection coefficient
V	voltage
R_s	sheet resistance
$\mathcal{E}_{nm}$	energy level difference
N	number of electrons
$s_{n,m}$	band index
g	degeneracy factor

$a^\dagger, b^\dagger$	creation and annihilation operators
$\mathcal{T}, \mathcal{T}'$	graphene hopping parameters
R	graphene sublattice sites
I	intensity
S	Seebeck coefficient
P	Power per unit area
C_e	specific heat capacity of electrons
C_p	specific heat capacity of phonons
g_{ep}	electron-phonon coupling parameter
k_b	Boltzmann's constant
L_f	electron mean free path

Chapter 1

Introduction

1.1 Thesis Overview

The field of two dimensional materials has stimulated a great deal of research in a number of areas of physics. In particular, the first isolation of graphene with its remarkable optical and electronic properties, has lead to many potential future applications being theorised. Whilst there are limitations to graphene, it is fair to say that graphene instigated a field of research around it. The field is very broad in applications and properties, this work will focus on the combination of nonlinear optical properties and plasmonics in two dimensional and thin film materials. Except for comparisons, this thesis focuses on the materials of graphene and indium tin oxide.

The first area of investigation is the second order response of graphene relevant to optical DFG experiments. There have been to date many theories attempting to quantify the second order response of graphene, with most using a perturbative approach. However the theories published before this work indicate that the growing consensus of this approach estimates a value that cannot explain the experimental signals which have been observed to date. Therefore the work presented in this thesis begins by investigating this discrepancy and identifying other possible explanations beyond the established perturbative approach.

In the relevant experiments to date, extremely high field intensities have been used to observe such typically weak non-linear effects. It is fully expected, and has been demonstrated, that such pulses induce many photothermal effects in a material such as graphene. Whilst many aspects of these effects have been quantified and published, there has been little research on the effect on the nonlinearity of graphene.

This work presents the first quantified photothermal model of second order conductivity in graphene. Starting from an intensity pattern imprinted on a graphene sheet from incident laser beams at oblique angles, the photothermal currents generated from this intensity pattern are considered, along with the constructive interference in the case of a plasmon resonance. The model produces an expected field that is two orders of magnitude larger than that predicted by perturbation theory. Whilst this is still smaller than the experimental observations there are, as discussed in Chapter 5, many difficult to quantify parameters that have not been accurately measured in relevant experiments. This model provides a crucial first step to advancing understanding of the non-linear response of graphene.

Since the second order response of graphene has been experimentally established as unexpectedly strong, it is natural to characterise the third order response as the next step. Third order responses are expected to be stronger than second order effects in graphene because it is an allowed interaction in centrosymmetric materials. However, if there is a significant second order contribution it is possible that cascaded effects could provide a substantial contribution to the signals observed in certain circumstances. A cascaded third order effect is one in which there are two separate instances of second order interactions which lead to a third order signal with an intermediate step. Whilst this effect is necessarily present, such effects are usually extremely small due to the inherent weakness of each second order interaction. However there has been some consideration given to the possibility that such an effect could be enhanced if the intermediate step coupled to a resonant state.

Chapter 6 presents the results of an experimental investigation into this possibility. The most distinguishing feature of this process would be a resonance in the FWM signal when coupling to an enhanced intermediate state as opposed to a 'virtual' state. For this experiment we use the plasmon resonance in graphene as the real state that can be coupled to and all other non-phasematched oscillations of electrons are 'virtual' states. Whilst a sweep across angles or wavelengths would achieve this (as has been done in previous coupling experiments), this experiment provides a more convenient scheme to investigate this by imaging the Fourier plane of a third order signal. Further to this, Chapter 6 concludes by estimating the non-linear susceptibility of graphene, adding to the body of work already published on the size of

different third or non-linear effects in graphene.

Chapter 7 details and investigation into the differential reflectivity of ITO. Using a prism and a total internal reflection setup (see Section 4.3.1), this chapter both models and measures the changes in reflection due to and intense femtosecond pump beam. The chapter also investigates the origins of the temperature dependent differential reflection through a two temperature model, allowing for discussion on the magnitude of the response on different timescales.

1.2 Thesis Structure

In order to follow the works presented in this thesis it is important to have some grounding in plasmonics, nonlinear optics and 2D materials. Chapter 2 covers the theoretical concepts and history of non-linear optics, plasmonics and Fourier optics, this will enable the reader to follow the work and results presented later in this thesis.

In addition to the concepts above, Chapter 3 discusses the 2D materials used within this work. As 2D materials in general can vary greatly from sample to sample, this chapter includes both the general theory of the 2D materials involved (graphene and indium tin oxide), as well as data taken specific to the samples used in the later chapters. As the properties of individual samples were not the point of investigation, these are not considered results of this work.

Chapter 4 provides the details for how the experiments were carried out. This includes details of homogenising the beam and the spatial patterning required for the experiments, as well as alignment procedures. Additionally, Chapter 4 discusses established theoretical methods for modelling data and interpreting results such as the transfer matrix method and Fourier plane imaging decomposition.

Chapter 5 begins the original work conducted during this PhD. This chapter focuses on the theoretical derivation of second order conductivity in graphene. There has been much controversy surrounding the second order response of graphene, in particular, theoretical calculations have not always been consistent, and few have provided reasonable agreement with the experimental observations. This chapter focuses on the work trying to understand this discrepancy. The second order response

of graphene relevant to a DFG process is derived through perturbation theory and, having identified and corrected errors in previous works, provides a comparison between the published theories and experimental works. Concluding that the results of perturbation theory do not explain relevant experimental observations, Chapter 5 presents alternative explanations, modelling both an enhanced substrate response and possible photothermal effects. This work identifies the Seebeck effect as a strong possibility and the photothermal model established estimates a response that is significantly higher than that from perturbation theory.

Chapter 6 presents a study of plasmon enhanced resonant FWM in graphene. Here we discuss and investigate the possibility of a resonance in the third order response of graphene when the intermediate difference frequency state is phase-matched to the graphene plasmon, implying a cascaded process. This work also provides an estimate for the third order susceptibility of graphene in both exfoliated and chemical vapor deposition graphene.

Chapter 7 presents a study into the differential reflectivity of indium tin oxide (ITO). ITO is an epsilon near zero (ENZ) material and, near the ENZ region, shows large changes in the reflection of an incident pulse when changing the incident power. This is a crucial step into creating an all-optical switch for communications. Experimentally, this work focuses on the study of differential reflection near both the ENZ point and the critical angle of a glass-ITO-air interface. As the results show that the differential reflectivity is strongly dependent on pulse length, a theoretical two temperature model is presented to account for this observation. This model is extended to predict changes in plasma frequency and scattering rate.

This thesis concludes with Chapter 8, a summary of the work presented here as well as ideas for future work. In particular, the directions one could take to extend the promising work into the differential reflectivity of ITO, that has a multitude of plausible extensions.

Chapter 2

Background

2.1 nonlinear optics

nonlinear optics is a very wide field, at its broadest, encompassing any effect where the magnitude of the response is not linearly proportional to the electric field. Most nonlinear effects of interest are super-linear, that is to say, proportional to a power of electric field greater than one. This thesis concerns work regarding a variety of super-linear effects in thin film media.

2.1.1 History of nonlinear optics

Usually, nonlinear optical effects are usually relatively weak compared to linear ones of similar physical origin. Additionally, nonlinear effects tend to weaken with increasing order. For example, the third harmonic of a field is generally stronger than the fifth. With a higher dependence on the electric field, it is crucial that the electric fields involved in such experiments are suitably high. For this reason there is very little experimental work on nonlinear optics prior to the development of the laser by Maiman [1] and Collins [2] simultaneously in 1960.

The field of nonlinear optics is generally considered to begin with the first observation of second harmonic generation in crystalline quartz by Franken [3]. This work was enabled by the development of pulsed ruby lasers in the preceeding years [1, 2], allowing for large electric fields. Franken [3] used a source of $694.3nm$, observing the harmonic of $347.2nm$, achieving electric fields as high as $10^5 V/cm$. This was achieved with a modest $3J$ in a one milisecond pulse. From this point the areas

of nonlinear optics and lasers have advanced together; the more powerful the laser, the weaker and more exotic the effects that can be observed with that source.

In the beginning, nonlinear optics primarily revolved around harmonic generation, as this effect is relatively straight forward in nonlinear optics. Soon after [3], there were observations of weak third harmonics [4], with stronger signals being observed as the experiments were refined throughout the 1960s [5, 6, 7, 8, 9, 10]. Alongside this series of experiments exploring this new field, the development of a theoretical framework that could predict the responses was crucial, and Armstrong [11] and Bloembergen [12] were the first to explore this. The application of time dependent perturbation theory yielded theoretical results for the nonlinear coefficients, particularly in the work of Sitz and Yaris [13] and Ward and New [10]. Time dependent perturbation theory is still the base for many derivations of nonlinear responses today [14, 15, 16] although there are now many different approaches. However, as outlined in Chapter 5, there are experimental results that these theories do not cover, giving cause to look into other origins for wave mixing signals in certain circumstances [17, 18].

As mentioned above, the area of nonlinear optics has always been closely aligned with the development of lasers. After the first experiments in nonlinear optics, subsequent experiments soon required improvements in laser technology. A large step forward for both fields was the development of the first optical parametric oscillator laser (OPO) in 1965 by Giordmaine [19], and similar work by Akhmanov in a soviet report of the time [20]. An optical parametric oscillator is one that allows conversion of an incident pump photon of frequency ω_p into two photons of lower frequency designated signal (ω_s) and idler (ω_i), subject to conservation of energy ($\omega_p = \omega_s + \omega_i$). Optical parametric oscillators are one example of a highly used nonlinear process that has been well characterised and is crucial in modern physics. Indeed the experiments detailed in this work utilise an OPO to provide a laser source that can output a range of wavelengths. As the area expanded through the 1980s and 1990s, many optical effects were observed and put to use. Fainman comprehensively reviewed the field as it stood in 1993 [21].

With lasers, spectroscopy and sensing being so crucial to a wide range of physics,

nonlinear optics has become commonplace in today's research. A particular highlight is the exploitation of optical rectification to produce terahertz radiation. Optical rectification is a process wherein a static polarisation can be produced from a time dependent oscillating source. If the source is pulsed, then the static polarisation will now develop a temporal oscillation on the scale of the laser pulse length, thus femtosecond pulses produce terahertz radiation in such a system [22]. The process of optical rectification is discussed more in Section 2.1.3 .

nonlinear optics are used in a wide variety of applications today including sensors, data storage and information transfer [23]. With its ubiquitous use and great potential, the field of nonlinear optics remains a high priority for investigation. One such application, which also exploits thin film materials, is that of high harmonic generation. High harmonics are a promising area [24, 25, 26, 27] as they can give insight into ultrafast electron dynamics and investigate attosecond timescales [28]. High harmonics is not a precise term, but generally range from 5th upwards. Harmonics as high as the 25th order have been observed in bulk zinc oxide (ZnO) crystals [29], and up the the 13th order in atomically thin molybdenum disulphide (MoS_2) [28]. Exploiting the high harmonics of materials, particularly atomically thin ones, is highly desirable but must be preceded by a clear understanding of the underlying physics of lower order harmonic generation within such materials. For example, graphene has shown to be a material of great promise, but the theory behind the nonlinear response still remains unclear at the second [17] and third [18] order.

2.1.2 Basic mathematical treatment of nonlinear optics

For this work it is convenient to start from Ohm's Law defined in the following way

$$\vec{J} = \sigma \vec{E}. \tag{2.1}$$

This equation actually represents a small aspect of the interaction involved when an electromagnetic (EM) field is incident on a material with a conductivity σ. In equation 2.1, only the linear conductivity has been included, giving a current response

proportional to the incident intensity. If one were to include higher order interactions the full equation would be described by the following:

$$\vec{J} = \sigma\vec{E} + \sigma^{(2)}\vec{E}^2 + \sigma^{(3)}\vec{E}^3 + ... \tag{2.2}$$

or more generally,

$$\vec{J} = \sum_n \sigma^{(n)}\vec{E}^n. \tag{2.3}$$

Here the n^{th} order conductivities, $\sigma^{(n)}$, represent tensors, each having different dimensions and different elements related to the particular material. Equation 2.2 only includes one incident field, therefore the resultant fields will represent harmonics of the incident field (or special cases such as optical rectification or the Kerr nonlinearity discussed in Section 2.1.3). One can readily extend this interaction to multiple fields, for two fields one observes

$$\vec{J} = \sum_{n=1}^{\infty} \sigma^{(n)}(\omega_c;\omega_a,\omega_b) \sum_{i=1}^{\infty} E_a^i E_b^{n-i}.$$

Here $\sigma^{(n)}(\omega_c;\omega_a,\omega_b)$ here indicates that the nonlinearity will not be the same for all processes of the same order n, and is dependent on both the input frequencies (ω_a,ω_b) and the resulting frequency of the process (ω_c). This formulation will be used extensively in Chapter 5, where the mathematics of second order nonlinearity in graphene is laid out. Whilst the maths can be trivially extended to more than two fields, it becomes increasingly cumbersome without providing further insight and is not relevant to this work.

2.1.3 Difference frequency generation

Difference frequency generation (DFG) was a natural extension to the harmonics and sum frequencies observed in the infancy of nonlinear optics. Mathematically, one can consider the complex conjugate of one of the fields to represent a difference frequency interaction. In this case Equation 2.1.2 becomes,

$$\vec{J} = \sigma^{(2)}(\omega_a - \omega_b;\omega_a,\omega_b)E_a E_b^*. \tag{2.4}$$

Equation 2.4 has been simplified as there are many more increasingly small contributions to the second order response through high order 'folded' interactions. A 'folded' interaction is one in which a number of interaction fields cancel out their frequency dependence, an example of which is optical rectification. In optical rectification, a second order interaction gives rise to a static polarisation, which is equivalent to a DFG interaction with a single input field. In this case, the field and its complex conjugate mix, cancelling the time dependence and leading to a static polarisation from a time dependent source. In a third order interaction, if two of the fields were to cancel in such a way, the resultant oscillation frequency would be the same as the remaining input field. Thus, one would observe a polarisation at the fundamental frequency based on a third order interaction. This effect appears as an intensity dependent correction to the linear refractive index and is known as the Kerr effect. Such folded interactions are generally very weak and provide little contribution to the overall signal as is expected to be the case here.

Originally, DFG was proposed as a method to optically generate millimetre waves [30] and there was soon experimental verification of the process generating microwave [31] and mid-infrared radiation [32]. These works highlight the exciting potential of DFG that makes it so appealing, that is, the ability to optically generate radiation of much longer wavelengths.

DFG has generally focused on the frequency of the field produced from the interaction. Recently, however, groups have started exploiting the properties of the wavevector associated with DFG (or other nonlinear wave-mixing process) [33, 34, 35]. The wavevector of a difference frequency interaction follows the same conservation principles as the frequency, that is, one would take the sum in a sum frequency interaction and the difference in a difference frequency one. However, unlike the frequency, the wavevector of a field can be positive or negative. In such a case one can observe

$$\vec{k}_1 - \vec{k}_2 = |\vec{k}_1| + |\vec{k}_2|,$$

assuming the wavevectors are solely in the same axis. This interaction would result in a field with frequency $\omega_1 - \omega_2$ and wavevector $|\vec{k}_1| + |\vec{k}_2|$, allowing for the generation of low frequency fields with extraordinarily high wavevectors. These low

frequency, high momentum fields are crucial in plasmon excitation, particularly in two dimensional (2D) systems where prism coupling is not possible [35] (see Section 2.3.4).

DFG is now commonplace within modern optics for generating infrared radiation [36, 37, 38], and is also standard in OPO lasers. Even more applications have been proposed such as producing a room temperature terahertz laser source [39], a spectral region long devoid of efficient devices. With the current use, as well as proposed extensions, difference frequency generation remains a highly relevant field of study across a wide number of materials.

2.1.4 Four-wave mixing

Four-wave mixing (FWM) is a nonlinear process in which three input fields combine to create a fourth, generally as a $\chi^{(3)}$ process. The theory of FWM was extensively studied in the late 1970s, in particular for imaging applications such as spatial convolution and correlation [40], beam time reversal and phase conjugation [41, 42, 43, 44] as well as extending the range of parametric oscillation [45]. The experimental viability of image reconstruction was demonstrated repeatedly [46, 47, 48], with Liao the first to show backward wave generation in ruby [49]. Other materials such as lithium niobate also showed promise soon after [50]. FWM also exhibited further applications in spectroscopy, particularly high-frequency spectroscopy [51, 52], an area that already exploited nonlinear principles [53].

FWM, much like DFG, has found much purpose within laser systems and amplifiers [54, 55], but still has potential to be explored including, crucially, plasmon excitation [56, 33, 34, 35], as will be discussed in Section 2.3.4.

2.1.5 Visual representations of nonlinear wave-mixing processes

nonlinear optical processes are often represented on energy level diagrams as a simple visual aid to understanding. Figure 2.1 shows two simple second order processes on an energy level diagram. Panel **a** represents a second harmonic generation process, whereas Panel **b** represents a difference frequency process. Panel **b** provides useful insight into the difference frequency process as it is observed that one photon

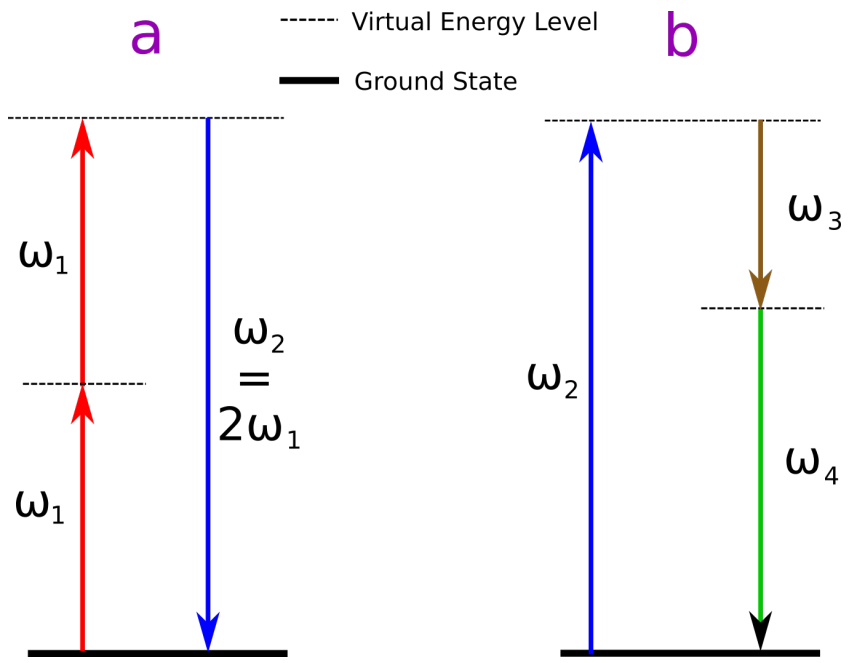

FIGURE 2.1: Visual representations of two nonlinear processes. Panel **a** is a second harmonic generation process. In this interaction two photons of frequency ω_1 combine to form a photon of frequency $\omega_2 = 2\omega_1$. Panel **b** represents a difference frequency process. In this diagram a photon of frequency ω_2 breaks down into two photons of frequency ω_3 and ω_4 subject to conservation of energy $\omega_4 = \omega_2 - \omega_3$.

splits into two of lower frequency. From this we can explain the physical effect of the low frequency beam having increased fluence in DFG experiments [35]. Whilst any combination of ω_3 and ω_4 that satisfies conservation of energy is technically valid, the presence of one frequency stimulates a singular pairing over all others. Thus, the presence of ω_3 stimulates the specific down-conversion of ω_3 and ω_4.

Additionally, these diagrams can be altered in subtle ways to illustrate differences in the way the process is observed. Figure 2.2 shows two different four-wave mixing processes that result in the same frequency ω_4, as a combination of three incident frequencies. Here, the differences in the diagrams are used to highlight a relevant intermediate energy level. Depending on the convention, Panel **a** might represent a FWM process based on a single $\chi^{(3)}$, whereas Panel **b** shows a two stage process based on two separate $\chi^{(2)}$. This two step process is termed cascaded [57, 58, 59].

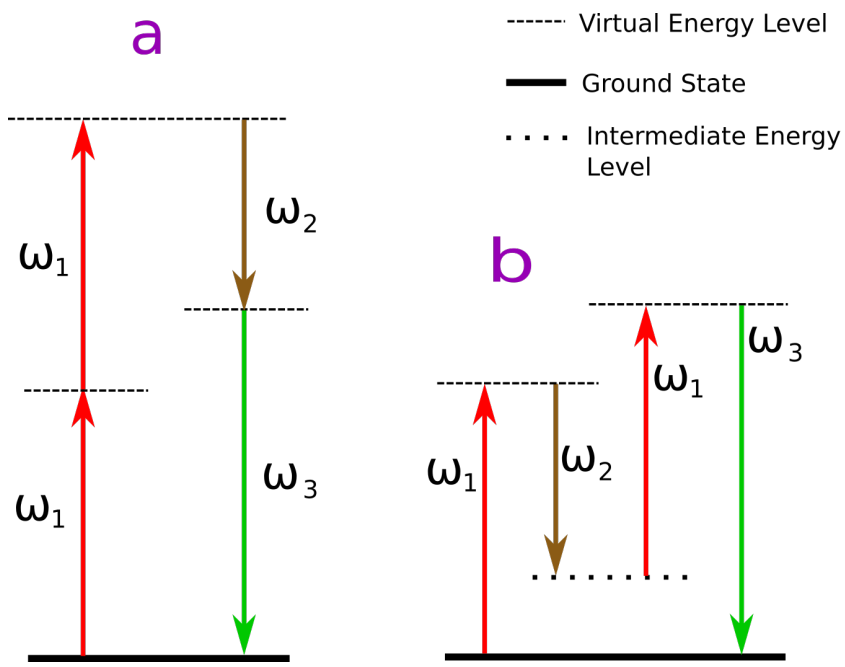

FIGURE 2.2: Figure showing two possible FWM configurations. Panel **a** represents a conventional third order FWM interaction with a resultant frequency of $2\omega_1 - \omega_2$. Panel **b** represents an interaction with the same resultant frequency but involving an intermediate energy level at $\omega_1 - \omega_2$. If the system resonates at the intermediate energy level one would expect an enhancement in the overall process.

2.1.6 Intensity dependent reflectivity

Intensity dependent reflectivity is a crucial step in creating an all-optical switching device. An all-optical switch allows one optical signal to control the intensity or direction of either itself or another signal. Optical switching potentially has a huge advantage over electronic switching due to low losses [60] and operating at shorter timescales often limited only by material combination time [61].

Many nonlinear process can give rise to optical switching effects, for example stimulated Brillouin zone scattering (BZS) can be used to increase an optical signal's intensity. However, the back-scattering of BZS is accompanied by a frequency shift and limited by phonon lifetimes [62]. Whilst BZS is an example of optical switching, increasing the fluence, as is common for BZS, is not always the goal. For many applications the desire is to recreate a binary signal with a high low state, as is observed in voltage for electronic signals. A switch that could reduce a signal to such an extent that one could register 'on' and 'off' states would replicate this behaviour. For example if one could decrease the reflection by 99%, one could sufficiently measure

this as an 'off' signal, enabling binary coding. As much of today's communications moves towards fibre optic communication, efficient optical switching is highly desirable for ease of integration as well as the aforementioned advantages of lower loss and faster switching times [63].

When refractive indices are intensity dependent, one will observe a change in the reflectivity of a sample, as such the Kerr nonlinearity is an effective method of optical switching. This method was first demonstrated in an optical fibre by Park in 1988 [64], but now has many developed systems [65] including response times as low as $210fs$ [66]. The origin of the Kerr effect is a third order ($\chi^{(3)}$) interaction, however, similar changes to refractive indices can also arise from changes to the plasma frequency [67].

A large proportion of optical switching devices rely on resonators [61, 68] and cavities [69, 70, 71], however a single material exhibiting such properties would be highly desirable. One of the most exciting recent works was conducted by Alam in 2016 [67]. Alam showed that indium tin oxide (ITO), a highly promising nonlinear thin film material, exhibited extraordinary changes in reflectivity around its epsilon near zero (ENZ) point. ENZ materials are ones which have a region of their dispersion where the real part of the permittivity is extremely close to zero. In these regions one observes large changes in refractive index for a small change in the permittivity through the relation,

$$\Delta n = \frac{\Delta \epsilon}{\sqrt{\epsilon}},$$

assuming a relative permeability of 1. In the work of Alam [67], the observed change in the refractive index was attributed to a red shift in the plasma frequency. This work has great potential for extension at different wavelengths and high wavevector excitation as discussed in Chapter 7.

2.2 Drude model

The Drude model was first proposed by Paul Drude in 1900 [72, 73]. Drude was attempting to explain the behaviour of electrons within a metal under an electric field. Drude applied a relatively simple model of negatively charged electrons moving and interacting only with larger positive ion cores, ignoring electron-electron interactions.

2.2.1 Derivation

The derivation for the most simplified one dimensional Drude model begins with the equation of motion for an electron in an electric field,

$$m\frac{d^2x}{dt^2} = -eE.$$

Here E is the magnitude of the electric field in the x direction. One assumes that both the electric field and position x have time dependence of $e^{-i\omega t}$, therefore

$$\begin{aligned} -m\omega^2 x &= -eE \\ \Rightarrow x &= \frac{eE}{m\omega^2}. \end{aligned}$$

When an electron is displaced from equilibrium, one observes a dipole. The polarisation of an individual dipole is $-ex$, and for a collective system of n such dipoles

$$p = -nex. \tag{2.5}$$

One can replace Equation 2.5 into the definition of polarisation

$$\begin{aligned} \epsilon_r(\omega) &= \frac{D(\omega)}{\epsilon_0 E(\omega)} \\ &= 1 + \frac{P(\omega)}{\epsilon_0 E(\omega)} \\ &= 1 - \frac{ne^2 x}{\epsilon_0 m\omega^2}. \end{aligned} \tag{2.6}$$

From this it is conventional to define a plasma frequency (ω_p) such that

$$\epsilon_r = 1 - \frac{\omega_p^2}{\omega^2}$$
$$\Rightarrow \omega_p^2 = \frac{ne^2}{\epsilon_0 m}.$$

One can make this model more realistic by including a Drude damping term γ, generally associated with scattering in the sample. This is included through

$$\epsilon_r = 1 - \frac{\omega_p^2}{\omega^2 - i\omega\gamma}$$

This simple model have shown to be incredibly robust over the years. However there have been significant extensions to the theory presented by Drude. In 1905 Lorentz [74] extended the model to include multiple resonances (such as phonons) which affect the permittivity. Today, Drude's model, and its extensions, form the basis for understanding the permittivities of metallic materials [75].

2.3 Plasmonics

Today, the terms plasmon and their related quasiparticles (such as surface plasmons and surface plasmon polaritons) are often treated as interchangeable, even though they describe distinct phenomena. Plasmons are quantized oscillations of electrons within a material under a collective response, and can therefore be considered as a quasi-particle within the medium. Bulk plasmons are oscillations within a 3D material and exhibit longitudinal wave dynamics (the oscillation is in the direction of propagation). As such they cannot be excited by light, which is a transverse wave. Therefore, bulk plasmons are generally excited by the losses of fast electrons travelling through a medium [76, 77, 78].

Surface plasmons are collective oscillations occurring at interfaces and thus do not experience the third dimension as a bulk plasmon would. Surface plasmon polaritons (SPPs) are coupled modes of a surface plasmon resonance with a photonic mode. This coupling is allowed because a photon incident at an angle to a surface can generate a longitudinal wave component parallel to the surface, providing it exhibits transverse magnetic (TM, also known as *p*-type) polarisation. This longitudinal component can match the frequency and wavevector of the surface plasmon resonance. For this reason transverse electric (TE, also known as *s*-type) light cannot excite a surface plasmon resonance and form a surface plasmon polariton at an interface, like the mode shown in Figure 2.5. This constraint was noted by Hagglund [79] and Ritchie [80] both experimentally and theoretically.

2.3.1 History of plasmonics

The effects of plasmons were observed long before they were explained or predicted. The first published work exhibiting a plasmon is Wood [81] who reported on an “incomprehensible" uneven distribution of light in a diffraction grating spectrum. Wood observed that multiple diffraction gratings could exhibit extraordinarily sharp bright and dark lines within the line spectrum produced from sodium lamp illumination. These lines also moved with respect to one another when the illumination angle was changed. Wood would never manage an explanation of the physics behind his observation, indeed the two aspects would be explained many

years apart. In 1907 Lord Rayleigh explained the presence of the dark lines observed as the boundary when a diffracted order is predicted to propagate parallel to the surface [82], this is now interpreted as a bound plasmonic mode. However, Rayleigh's theory predicts no bright response anywhere in the spectrum corresponding to the lines observed by Wood.

In 1936 Strong [83] would provide important confirmation of Lord Rayleigh's predictions with regards to the dark lines within the grating spectra. Additionally, Strong noted that the position of the bright lines within spectra was dependent on the metal that coated the grating, empirically determining a relation for the position of the bright lines. It would take Fano in 1941 [84], to first provide a method of treatment for lossy waves on a metal that would explain the effect of the bright lines within the spectrum. In this work Fano considered a waveguide mode supported by a thin film, taking the thickness of this film to zero. Fano predicted the 'existence of polarised quasi-stationary waves which represent an energy current rolling along the surface', an effect we now term a surface plasmon.

In 1952, Pines and Bohm outlined the theoretical origin of plasmons [85], established by analysing the behaviour of electrons in a dense electron gas. The resulting behaviour, derived from the Hamiltonian, leads to an overall density fluctuation that can be split into two components. The first is the random thermal behaviour of the electrons, showing no collective effect. The second is a collective oscillation of the whole system termed a 'plasma' oscillation. This term eventually lead to the name plasmon and gave rise to a rich field of physics trying to exploit these oscillations. These collective oscillations were derived for a three dimensional (3D) gas and are more specifically nowadays defined as bulk plasmons to distinguish them from the many hybrid plasmonic modes observed today. The most explored of these modes is the surface plasmon polariton (SPP) which is a plasmonic oscillation both confined to the surface and coupled to a light-like electromagnetic field, creating a hybrid state.

The work of Pines and Bohm advanced the theory that the energy losses of electrons passing through a thin film are attributed to a 'plasma' oscillation, however it was not the only explanation circulating at the time. Many people working in the

area attributed the losses to interband transitions within the thin film. The experiments at the time contributed to both explanations with Watanabe [86] verifying Bohms and Pines theory for Be, Al, Mg and Ge but Leder [87] showing correlation between x-ray absorption and characteristic loss lines. Ritchie sought to clarify this area in his work in 1957 [76], which is now considered the defining work of surface plasmonics [88]. Ritchie analysed the angle-energy distribution of fast electrons losing energy to conduction electrons in a thin film, agreeing with Pines and Bohm regarding the presence of a collective oscillation within a metal film.

Prism coupling is now one of the most common ways to excite surface plasmons. As with diffraction grating coupling, the combination of experiment and theoretical interpretation would be missed by Turbadar. Turbadar showed in 1959 that a prism with an aluminium interface would exhibit perfect absorption at a certain angle [89] an effect that is now known to be caused by plasmon excitation. He later showed the same effect with silver, copper and gold interfaces [90]. Due to the missed link, credit for plasmon excitation using a prism is generally given to Otto [91], and later Kretschmann for refining the method [92] (see Figure 2.7).

Once one could control the excitation of plasmons, researchers sought opportunities to exploit their properties. Owing to their high electric fields, plasmons found a huge number of applications in sensing, first proposed in the 1970s for characterising thin films [93] and observing interactions on metal surfaces [94]. Later it was used for biosensing and gas detection by Liedberg and Nylander [95, 96]. Surface plasmon resonance sensors (SPRs) are now commonplace for experimental and commercial applications [97].

More recently, the use of plasmons in circuitry and enhancing electronic components such as modulators and sensors has been proposed [98, 99]. In particular the development of two dimensional (2D) materials such as graphene [100] and thin film conductive oxides [101] has reignited the field. Surface plasmons in such thin film materials exhibit exaggerated properties, such as higher confinement and larger field densities [100]. This comparison can be seen in Figure 2.3, which compares the wavevectors of a gold and graphene plasmon.

As can be seen from Figure 2.3, the graphene plasmon dispersion lies significantly beyond the light line, and much further than the gold plasmon dispersion.

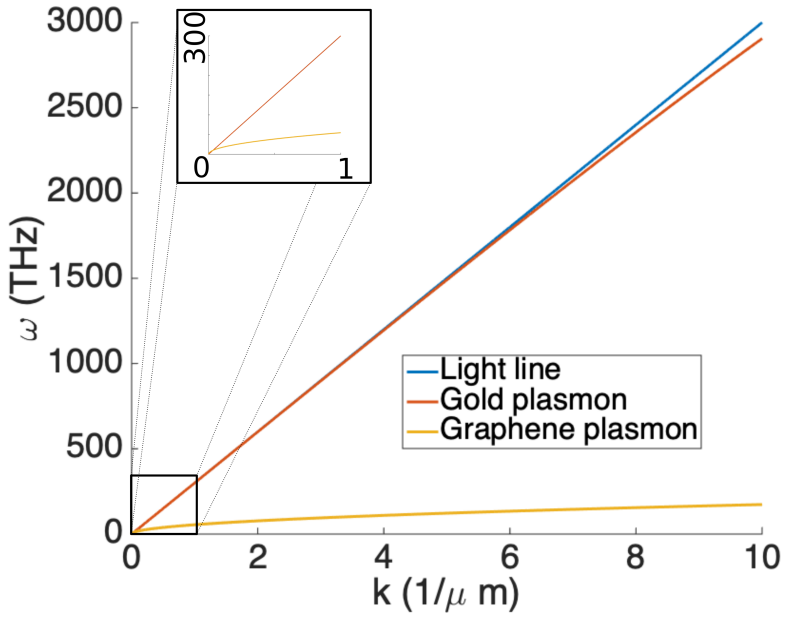

FIGURE 2.3: Figure showing the comparison of the plasmon dispersions of gold (Equation 2.10 modelled with $\epsilon_\infty = 6.1$, $\omega_p = 13.7PHz$ and $\gamma = 41THz$[102]) and graphene (Equation 3.1 modelled with $E_f = 0.45eV$ and $\gamma = 4THz$ [103]). Inset: a zoom in of the low frequency region of the plasmon dispersion. Here the gold plasmon is indistinguishable from the light line and illustrates the extremely high confinement of the graphene plasmon.

As such the excitation of plasmons in graphene would require new thinking about how to match the wavevector required. Whilst the high wavevector is highly valued for the confinement of the EM field, it also makes coupling to the plasmon far more difficult than conventional plasmonic metals such as gold or silver. Therefore, the field sought out new excitation methods to be able to control and exploit these plasmonic effects and their extreme properties.

2.3.2 Plasmon dispersion

One can derive the necessary conditions and dispersion relation for a surface plasmon from Maxwell's equations. Figure 2.4 shows a dielectric - metal interface with $z > 0$ being the dielectric and $z < 0$ being the metal. For both the metal and the dielectric one approximates plane wave solutions to both the $\vec{E}$ and $\vec{H}$ fields. As defined in Figure 2.4, this derivation will consider TM light as only this can excite surface plasmon polaritons. Therefore, the $\vec{H}$ field is in the $\hat{y}$ direction and the $\vec{E}$

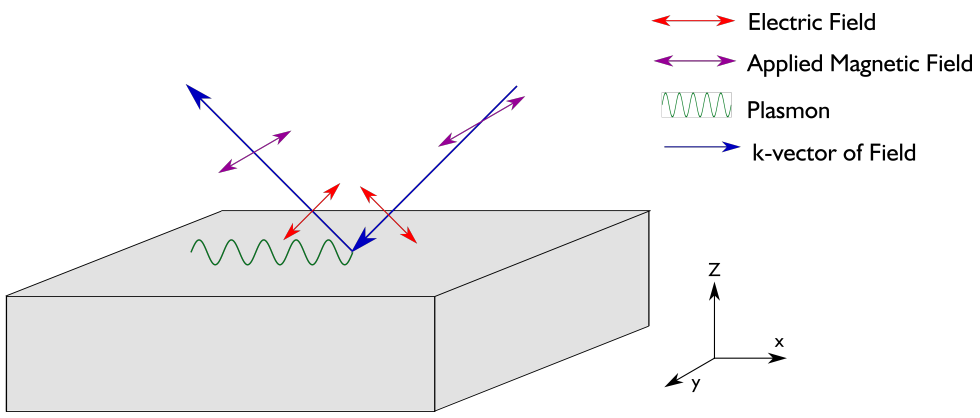

FIGURE 2.4: Wave and sample orientation considered for the plasmon derivation of a metal-dielectric interface

field is in the $\hat{x} - \hat{z}$ plane. The fields in the metal and dielectric can be defined as,

$$\begin{aligned}
\vec{H}_d &= (0, H_{yd}, 0)e^{i[k_{xd}x + k_{zd}z - \omega t]} \\
\vec{E}_d &= (E_{xd}, 0, E_{zd})e^{i[k_{xd}x + k_{zd}z - \omega t]} \\
\vec{H}_m &= (0, H_{ym}, 0)e^{i[k_{xm}x - k_{zm}z - \omega t]} \\
\vec{E}_m &= (E_{xm}, 0, E_{zm})e^{i[k_{xm}x - k_{zm}z - \omega t]}.
\end{aligned}$$

Here the subscripts m and d represent the metal and dielectric respectively. At the interface ($z = 0$) there must be continuity in the fields and so one observes,

$$\begin{aligned}
E_{xm}(z=0) = E_{xd}(z=0), \quad H_{ym}(z=0) = H_{ym}(z=0) \\
\Rightarrow k_{xm} = k_{xd}.
\end{aligned}$$

Utilising Maxwell's equations one can find a relation between the $\vec{H}$ field components and $\vec{E}$

$$\begin{aligned}
\nabla \mathrm{x} \vec{H} &= \frac{\epsilon}{c}\frac{\partial}{\partial t}\vec{E} \\
\begin{pmatrix} -\partial_z H_y \\ 0 \\ \partial_x H_y \end{pmatrix} &= -\epsilon\frac{\omega}{c}\begin{pmatrix} E_x \\ 0 \\ E_z \end{pmatrix}.
\end{aligned}$$

In the metal one finds the follwoing solutions for the fields,

$$k_{zm}H_{ym} = -\epsilon_m \frac{\omega}{c} E_{xm}$$
$$k_{xm}H_{ym} = -\epsilon_m \frac{\omega}{c} E_{zm}.$$

The analogous relations for the dielectric are,

$$k_{zd}H_{yd} = \epsilon_d \frac{\omega}{c} E_{xd}$$
$$k_{xd}H_{yd} = -\epsilon_d \frac{\omega}{c} E_{xd}.$$

To relate the two equations, one can take the quotient

$$\frac{k_{zm}H_{ym}}{k_{zd}H_{yd}} = -\frac{\epsilon_m}{\epsilon_d}\frac{E_{xm}}{E_{xd}}.$$

However due to boundaries one can state $E_{xm} = E_{xd}$ and $H_{ym} = H_{yd}$. Therefore,

$$\frac{k_{zm}}{k_{zd}} = -\frac{\epsilon_m}{\epsilon_d}$$
$$\frac{k_{zd}}{\epsilon_d} + \frac{k_{zm}}{\epsilon_m} = 0, \tag{2.7}$$

now one can relate these quantities to the freespace values.

$$
\begin{aligned}
k^2 = k_x^2 + k_y^2 + k_z^2 &= \epsilon \frac{\omega^2}{c^2} \\
k_{xm}^2 + k_{zd}^2 &= \epsilon_d \frac{\omega^2}{c^2} \\
k_{xm}^2 + k_{xd}^2 &= \epsilon_m \frac{\omega^2}{c^2} \\
k_{zd}^2 - k_{zm}^2 &= \frac{\omega^2}{c^2}(\epsilon_d - \epsilon_m) \\
k_{zd}^2 - k_{zd}^2 \left(\frac{\epsilon_m}{\epsilon_d}\right)^2 &= \frac{\omega^2}{c^2}(\epsilon_d - \epsilon_m) \\
k_{zd}^2 \left(1 - \frac{\epsilon_m^2}{\epsilon_d^2}\right) &= \frac{\omega^2}{c^2}(\epsilon_d - \epsilon_m) \\
k_{zd}^2 &= \frac{\omega^2}{c^2}\epsilon_d^2 \left[\frac{\epsilon_d - \epsilon_m}{\epsilon_d^2 - \epsilon_m^2}\right] \\
k_{zd}^2 &= \frac{\omega^2}{c^2}\epsilon_d^2 \left[\frac{\epsilon_d - \epsilon_m}{(\epsilon_d - \epsilon_m)(\epsilon_d + \epsilon_m)}\right],
\end{aligned}
$$

and finally one arrives at the simplified expression for k_{zd},

$$k_{zd}^2 = \frac{\omega^2}{c^2}\frac{\epsilon_d^2}{\epsilon_m + \epsilon_d}. \tag{2.8}$$

This yields the penetration depth into the dielectric medium, from this one can easily obtain the equivalent for the metal using Equation 2.7.

$$k_{zm}^2 = \frac{\omega^2}{c^2}\frac{\epsilon_m^2}{\epsilon_m + \epsilon_d} \tag{2.9}$$

Thus, one can obtain an expression for $k_x = k_{xm} = k_{xd}$ by using the the vector addition of momentum components.

$$
\begin{aligned}
k^2 &= k_x^2 + k_y^2 + k_z^2 = \epsilon \frac{\omega^2}{c^2} \\
k_x^2 &= \epsilon \frac{\omega^2}{c^2} - k_z^2 \\
k_x^2 &= \epsilon_m \frac{\omega^2}{c^2} - k_{zm}^2 \\
k_x^2 &= \frac{\omega^2}{c^2} \left(\epsilon_m - \frac{\epsilon_m^2}{\epsilon_m + \epsilon_d} \right) \\
k_x^2 &= \frac{\omega^2}{c^2} \left(\frac{\epsilon_m(\epsilon_m + \epsilon_d) - \epsilon_m^2}{\epsilon_m + \epsilon_d} \right) \\
k_x^2 &= \frac{\omega^2}{c^2} \left(\frac{\epsilon_m \epsilon_d}{\epsilon_m + \epsilon_d} \right)
\end{aligned} \tag{2.10}
$$

In the above k_x represents the in plane wavevector of the plasmon, $epsilon_{m,d}$ are the permittivities of the metal and dielectric medium respectively. If one assumes the dielectric medium to be air for simplicity, Equation 2.10 becomes

$$
k_x^2 = \frac{\omega^2}{c^2} \left(\frac{\epsilon_m}{\epsilon_m + 1} \right). \tag{2.11}
$$

As stated, plasmons are bound surface waves at the interface of two media, in this consideration a metal and air. In order for a wave to be bound to the surface, its wavevector must exceed its freespace wavevector. Thus in the above equation one can use $\frac{\omega^2}{c^2} = k_{freespace}$ leaving the condition for a plasmon supporting metal as

$$
\left| \frac{\epsilon_m}{\epsilon_m + 1} \right| > 1 \Rightarrow \epsilon_m \leq -1. \tag{2.12}
$$

2.3.3 Properties of surface plasmon polaritons

Equation 2.12 states that the in-plane wavevector of the plasmon k_x, is higher than the maximal freespace propagation wavelength of light of the same frequency $k_x > \frac{\omega^2}{c^2}$ for a bound plasmon. This condition means that the field associated with a plasmon is confined to smaller spatial dimensions than the free space equivalent. With high confinement, and shorter wavelengths, such fields can be exploited at smaller scales as the wavelength is typical of the length scale a field can be manipulated on [104, 105]. Much of the promise of plasmons surrounds using this high confinement to enable smaller circuitry than currently available. However this benefit has always

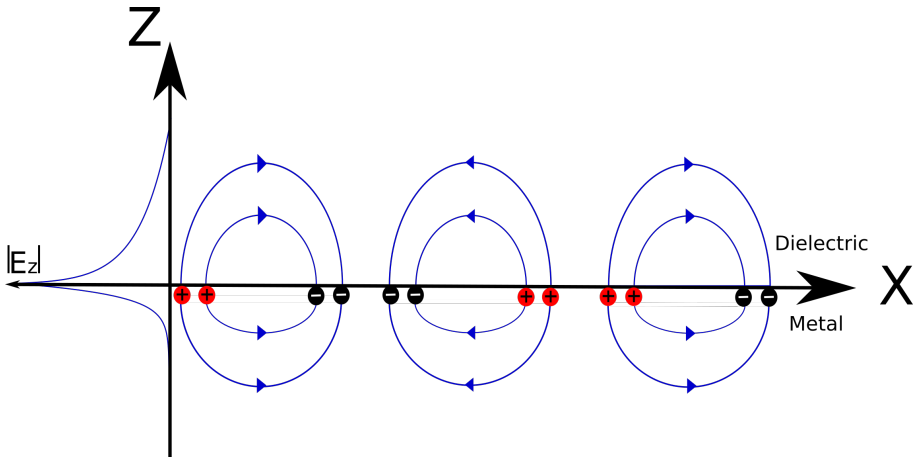

FIGURE 2.5: Representation of the fields associated with a surface plasmon polariton. Charge is grouped at the surface causing field lines in both media. The penetration of each field line is dependent on the permittivity of the medium, and associated with the decay length represented on the z-axis.

contended with the low propagation lengths due to high losses of plasmons. Great efforts have been made to overcome these problems including the use of liquid crystals [106]. To date, many components of plasmonic circuits have been manufactured [107] and even an all-plasmonic optical modulator capable of encoding at $70GHz$ in a $10\mu m$ waveguide [108].

A further significant property, that has inspired plasmonic sensing, is the high electric field density associated with plasmons. Due to the high electric field, plasmons are very sensitive to the surface they are bound to, and also surfaces sufficiently close to experience the evanescently decaying field. The use of plasmons in sensors has been proposed and investigated since the late 70s [93, 94] and has steadily become a staple of sensing measurements [97, 109]. As plasmons have realised their promise, the search for better plasmonic materials has followed, both in terms of losses and confinement. In particular this search has lead to the characterisation of 2D materials for plasmonic applications as they became available. While Chapter 3 details the history and properties of graphene from its isolation in 2004 [110], this isolation has provided great promise for the plasmonic and the nonlinear optics community including combining both in a proposed terahertz laser [111].

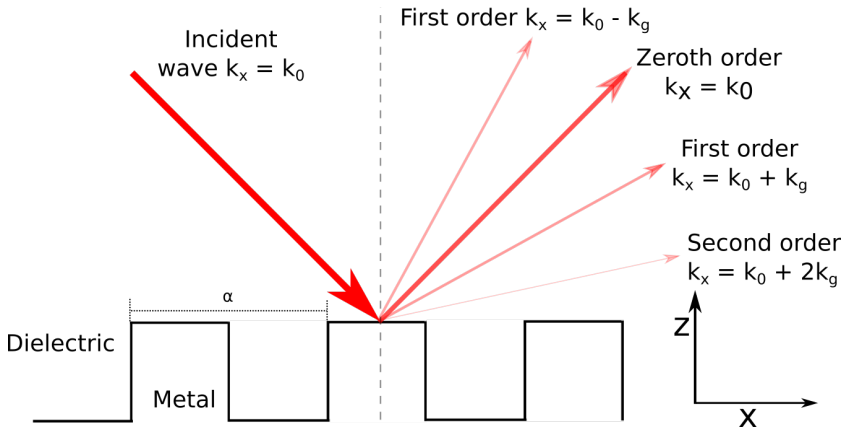

FIGURE 2.6: Figure showing the diffraction orders from a standard grating. k_0 represents the incident in-plane wavevector, k_x is the resultant in-plane wavevector and k_g is the grating wavevector related to the period α through $k_g = \frac{2\pi}{\alpha}$.

2.3.4 Coupling to surface plasmon polaritons

Plasmon generation was incidental in the experiment of Wood [81]. However, with the field rapidly expanding, it was important to develop a consistent and controlled excitation method. Wood excited the SPP through the use of a diffraction grating, which has become a standard excitation method [112, 113, 80]. A diffraction grating alters the wavevector of incident light with integer multiples of the grating wavevector k_g, such that the resultant wavevector (k) can be defined by $k = k_0 + nk_g$, where k_0 is the incident wavevector.

Diffraction grating coupling is a very powerful method for excitation. However, it does require a patterned surface which is not always available. Turbadar would instigate the method of prism coupling [89], although not fully understanding the physics involved with his observations. As such, credit for prism coupling is generally given to Otto [91], and to Kretschmann who refined the method [92].

Figure 2.7 shows the configurations for both the Otto [91] and Kretschmann [92] methods of excitation. Both methods rely on the same principle of frustrated total internal reflection. Total internal reflection (TIR) occurs when light propagating from a high refractive index medium (in this case the prism) is forbidden from propagating into the low refractive index medium (air). This phenomena occurs when the predicted in-plane wavevector of light coming from the prism is greater than the maximal wavevector allowed in the air. When this occurs the field cannot propagate

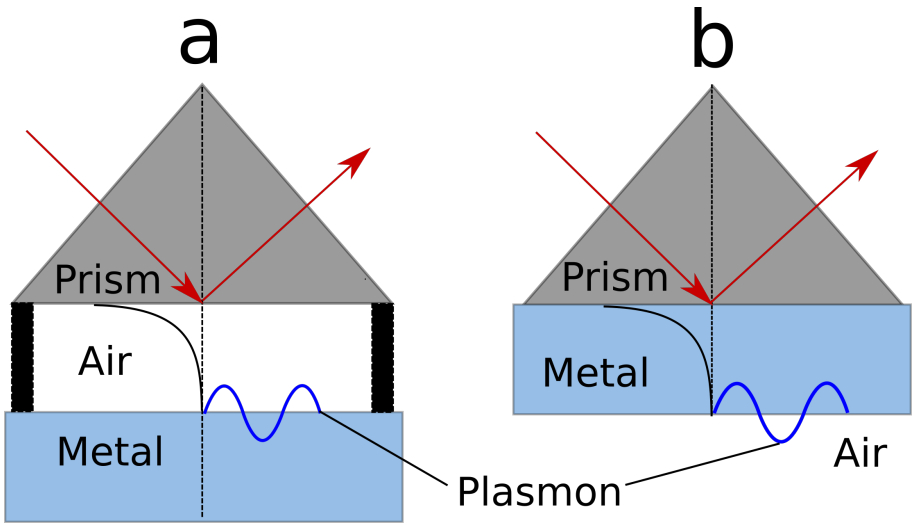

FIGURE 2.7: Figure depicting two prism coupling setups. Panel **a** shows a system in which the evanescent field tunnels through the air layer to the metal air interface. This method was first used by Otto in 1968 [91]. Panel **b** shows a configuration where the metal is placed directly on the prism surface. In this orientation the evanescent field tunnels through the metal to the air-metal interface on the far side. This variation was first performed by Kretschmann later in 1968 [92].

in air, thus all the intensity is reflected. However, it can be shown that continuity of field requires an evanescent wave along the interface that does not carry energy. Despite not usually transferring energy, this wave can couple to an allowed plasmon mode, if there is an interface that supports one nearby. As the field does not propagate, the interface supporting the plasmon must be close, relative to the decay length of the evanescent field. When coupling, the evanescent field will transfer energy to the supported plasmon mode and one can measure a decrease in the reflected beam corresponding to this energy transfer; this is frustrated total internal reflection.

In 2004, the isolation of graphene by Novoselov and Geim [110] sparked a revolution in the physics world, promising applications ranging across all of science, including in nonlinear optics and plasmonics. Graphene, along with many other 2D materials, supports plasmons with extremely high wavevectors (see Figure 2.3). These wavevectors are too high to achieve with the previously common method of prism excitation, so the field searched for new ways to excite surface plasmons.

In 2012, two groups would simultaneously use the method of AFM tip scattering to excite graphene plasmons [114, 115]. This method is based on the scattered waves that one would expect when illuminating the metal point used in an AFM with a

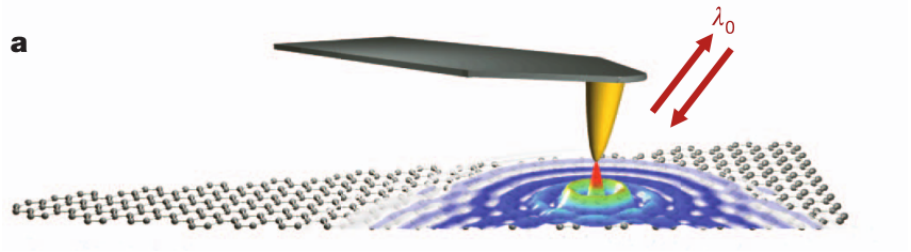

FIGURE 2.8: Visualisation of the AFM tip scattering process used to excite graphene plasmons. Image obtain from [115].

high intensity light field, shown in Figure 2.8. This incident wave would be scattered from the tip, generating waves with a wide range of wavevectors including evanescent waves with extremely high momenta. Some of these evanescent waves possess sufficient momentum to couple to the SPP. The frequency of this field is unchanged from the incident light and so when coupling to the plasmon one would have full knowledge of the frequency but have limited information on the coupling wavevector. Whilst highly effective, this method has limited control over the directionality of the excited plasmons, making it difficult to exploit in systems such as circuits without further wave-guiding.

Prior to this development, Renger developed an elegant method for coupling to the surface plasmon of a metal using FWM in 2009 [33]. However, this technique of nonlinear wave-mixing would not be used to excite a graphene plasmon until Constant in 2015 [35]. Renger showed that by carefully selecting the incident frequencies and wavevectors of light one could couple directly to a specific point of the plasmon dispersion as shown in Figure 2.9. Renger used this method to couple to a gold surface and was also able to show that not only could FWM excite a plasmon but in coupling to a plasmonic mode the FWM process was enhanced [34, 116]. This enhancement can be seen in Figure 2.10.

In 2015 Constant showed that nonlinear wave-mixing could be used to excite surface plasmons in graphene [35]. Constant, unlike the FWM approach of Renger, used DFG to excite plasmons on graphene with two optical beams of close frequencies [35]. This result caused some controversy as the inherent weakness of a second order process in a centrosymmetric material implied a much smaller susceptibility ($\chi^{(2)}$) than that observed ($\sigma^{(2)} \approx 7.5 \times 10^{-14} AmV^{-2}$ [35]). This discrepancy is discussed in detail in Chapter 5.

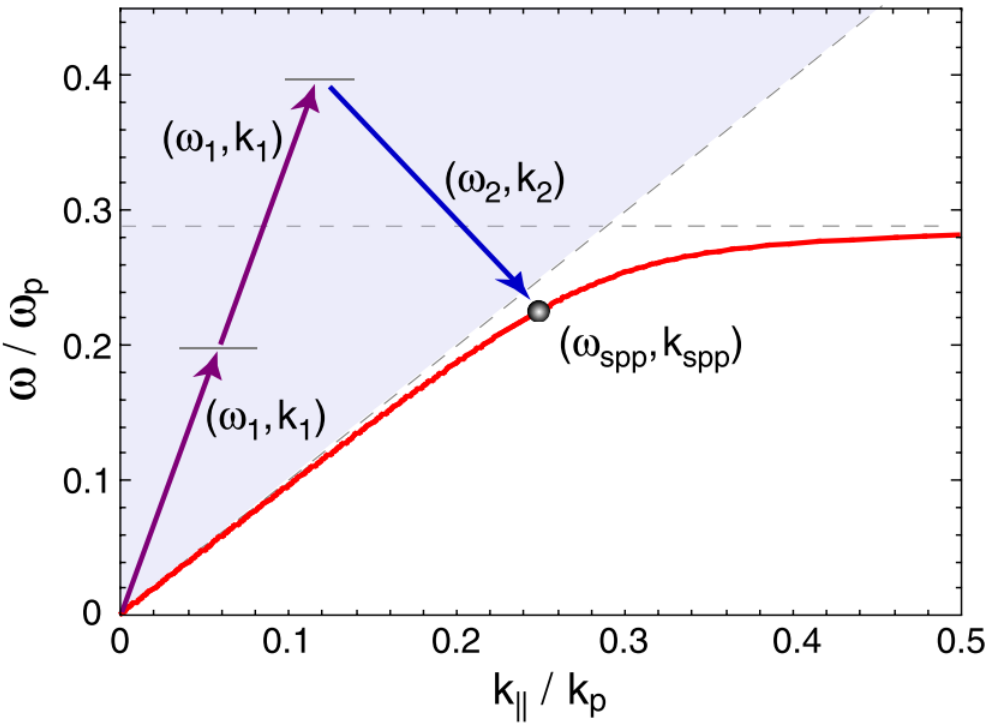

FIGURE 2.9: Dispersion diagram for the FWM experiment of Renger. The red line represents the gold plasmon dispersion, while the purple and blue arrows represent the two incident beams. The y-axis is normalised to the plasma frequency of gold $\omega_p = \frac{9eV}{\hbar}$, the x-axis represent the in-plane wavevector $k_{||}$ normalised to the plasma wavevector $k_p = \frac{\omega_p}{c}$. Image obtained from [33].

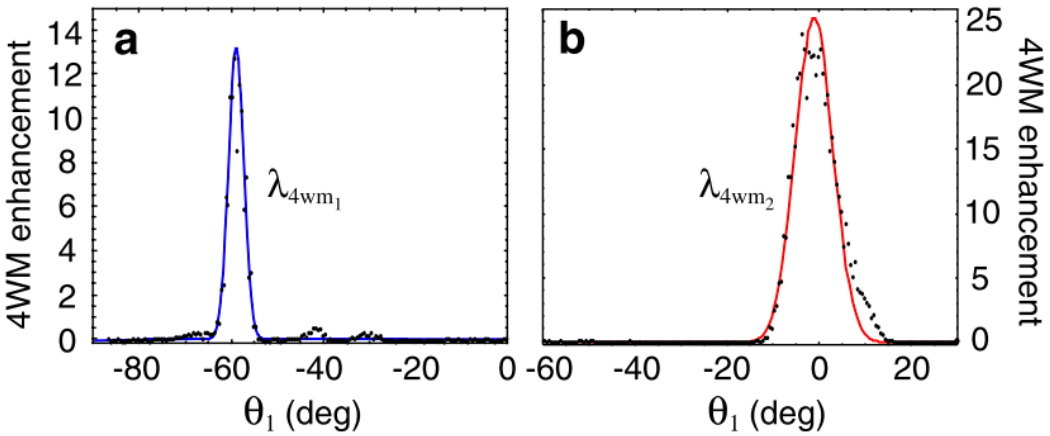

FIGURE 2.10: Enhancement in FWM intensity observed by Renger. Black dots are measured data points and the blue/red lines are Gaussian fits. The y-axis is normalised to the measured FWM from gold at normal incidence. Image obtained from [34].

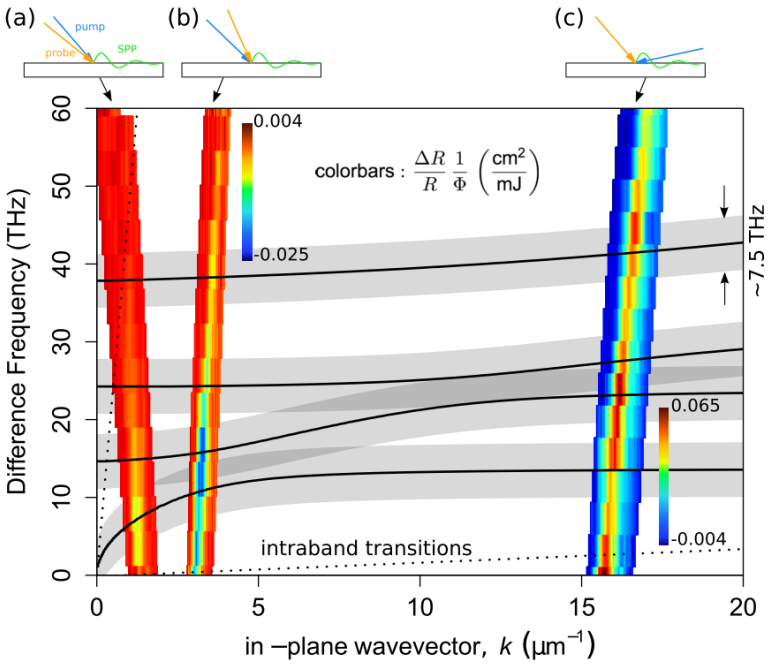

FIGURE 2.11: Figure showing the results of the DFG plasmon excitation of Constant [35]. Each geometry (a), (b) and (c) represents a different slice of the dispersion as marked. The black lines represent the hybrid mode of the graphene SPP and the substrate phonons, the width of the grey shading is the convolution of the bandwidth of three femtosecond pulses. The coloured bars represent the differential reflection of the probe beam ($\frac{\Delta R}{R}$) normalised to the pump fluence (Φ).

2.4 Fourier optics

The elements of Fourier optics have some base in works as early as 1946 [117], however its history is relatively concise. The text considered to have defined the field is still the most prevalent today, that is, the 1968 volume “Introduction to Fourier Optics" by Joseph Goodman [118]. Fourier optics is based on applying the principles of Fourier transforms to analyse the propagation of classical waves of light. It is particularly useful for any optical experiment looking to exploit angular emission, transmission or reflection in a sample. Fourier optics allows one to perform a range of these measurements simultaneously, by separating the angles of an incident light beam.

Whilst Fourier optics can be applied to signals for information regarding frequency/time dynamics and converting signals between those two domains, this work focuses on using the spatial and momentum-space relationship. The key principle of Fourier optics is that a lens applies a Fourier transform to the beam incident on it relative to the focal point of that lens. Therefore, if one applies a Fourier transform to a distribution of light, the resulting distribution will be equivalent to the distribution of light at a focal length away from a lens.

Figure 2.12 shows this principle in a ray optics diagram. The Fourier plane represents momentum space, thus all rays emitted at the same angle from the image plane focus to the same spot on the Fourier plane. Therefore, were one to look at the planes in 2D, one could state the axes as $[x, y]$ in the image plane and $[k_x, k_y]$ in the Fourier plane as detailed in Figure 2.12.

Fourier optics is particularly useful in a microscope setup, in that the Fourier plane can be considered as the back aperture of the objective, and the image plane the sample. This means any pattern imprinted onto the back aperture represents the illumination of the sample in momentum space. Conversely, any light collected through the objective on the back aperture represents the angular emission from the sample. Thus one can use this principle to define angular excitation and/or analyse angular results of a system, which will prove crucial in the experiments laid out in Chapter 4.

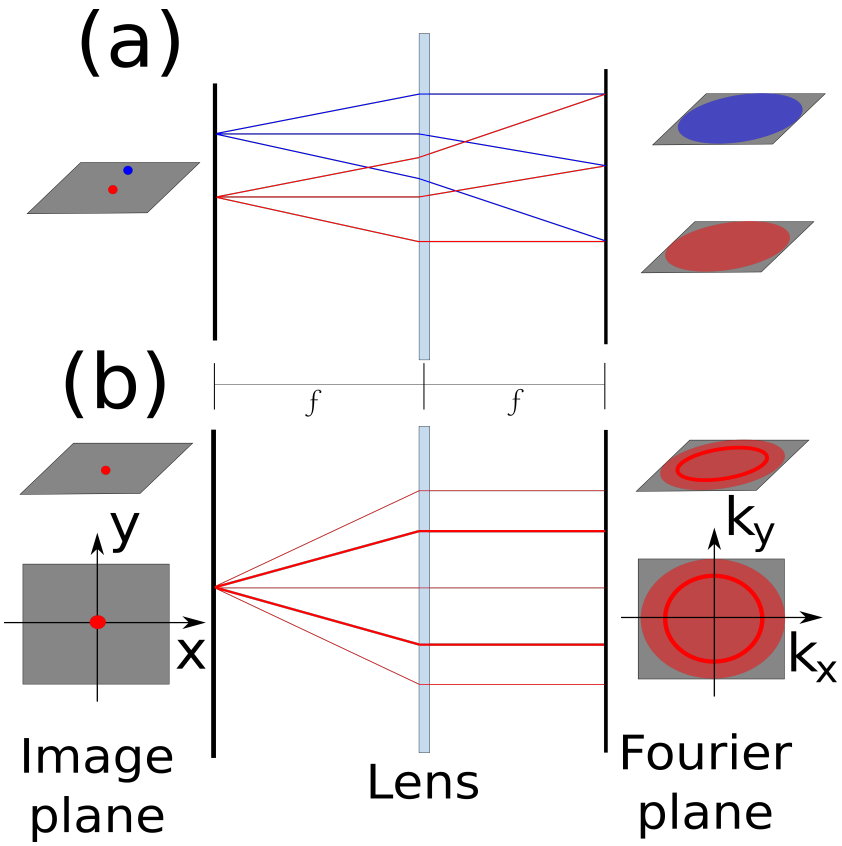

FIGURE 2.12: Representation of the Fourier transform applied through a lens. Panel **a** represents the two point sources located at different points in the image plane. Both point sources here are considered to emit uniformly in all directions. As shown in the Fourier plane, both point sources have identical spatial profiles in the Fourier plane, uniform distribution across all possible wavevectors. Panel **b** represents a single point source with an enhancement at a specified magnitude of wavevector, although independent of direction of that wavevector. In this case one observes a uniform distribution in the background with an enhanced ring at the specific wavevector. IP represents the image plane of a source, and FP represents the Fourier plane after an applied optical transformation with a lens of focal length f.

Chapter 3

Materials

3.1 Graphene

Graphene is a remarkable material that has sparked a revolution across many areas in engineering, physics and chemistry. Graphene is a one atom thick sheet of carbon atoms that exhibits characteristics of a two dimensional (2D) material [110], and do not experience the third dimension. Graphene was theoretically explored by Wallace in 1947 [119], however, conclusive isolation and identification would come decades later in 2004 [110]. One of the main reasons for the gap between these two events is that 2D crystals were thought to be unstable at finite temperatures [120, 121]. Prior to graphene's isolation, quasi-2D crystals had been formed through molecular beam epitaxy, a process which significantly alters growth and electronic properties [122]. In contrast, the 2004 isolation of graphene by Novoselov and Geim [110] used mechanical exfoliation, producing samples of single and few layer graphene flakes held on the substrate only by the van der Waal's force, and could even be made free-standing by etching away the substrate afterwards[123, 124].

While mechanical exfoliation proved to be a very effective method of isolating monolayer graphene, it is usually time consuming and samples can vary greatly in size, shape and quality. Therefore, new techniques were sought to isolate graphene, at the forefront of these was the technique of chemical vapor deposition (CVD). Chemical vapor deposition is a process whereby a substrate is exposed to precursor substances that react and/or decompose on the substrate to form the desired thin film. In graphene, methane is one of the most a highly used gases to achieve this [125], along with ethane and propane [126], however the relative expense of these

gases has also lead to significant work with cheaper substances such as petroleum asphalt [127]. The methane, or other hydrocarbon gas, is used as a source of carbon atoms, and a second hydrogen gas source is used to erode the carbon atoms away, allowing for deposition [128] onto a substrate. Generally, CVD graphene is grown onto a metal substrate with low carbon solubility such as copper to enable high quality layers, and then transferred to other substrates if necessary, as noted in [129].

CVD was developed around 2008/2009, with many research groups working on perfecting the technique [130, 131, 132, 133, 134]. Typically, CVD graphene is of a lower quality than that of exfoliated flakes with regards to its mobility and defects within the lattice structure [135, 136, 137, 138], however as groups refine the method, the quality of CVD graphene has fast approached that of exfoliated [139]. Today, CVD graphene is reported to have been grown defect-free with the use of a ultrathin titanium catalyst layer [140].

When graphene was first isolated, a great number of potential applications were proposed across photovoltaic devices, field effect transistors, sensors, memory devices and far infra-red filters [141, 142]. However, many of these applications have yet to come to fruition, thus improving the quality of manufactured graphene is vital to fully exploit the properties of graphene that created such interest when it was first isolated.

3.1.1 Crystal structure

Graphene exhibits a honeycomb lattice structure, such as that depicted in Figure 3.1, with lattice vectors given by

$$\mathbf{a}_1 = \frac{a}{2}(3, \sqrt{3}), \qquad \mathbf{a}_2 = \frac{a}{2}(3, -\sqrt{3}),$$
$$\delta_1 = \frac{a}{2}\left(1, \sqrt{3}\right), \qquad \delta_2 = \frac{a}{2}\left(1, -\sqrt{3}\right), \qquad \delta_3 = -a\,(1, 0)\,.$$

This lattice structure is treated as two interlaced triangular sublattices. Electrons within this lattice structure behave like massless Dirac fermions [144], as relativistic particles of zero rest mass with an effective speed of light given by $c^* \approx 10^6 ms^{-1}$. This behaviour leads to very peculiar consequences such as the conductivity of

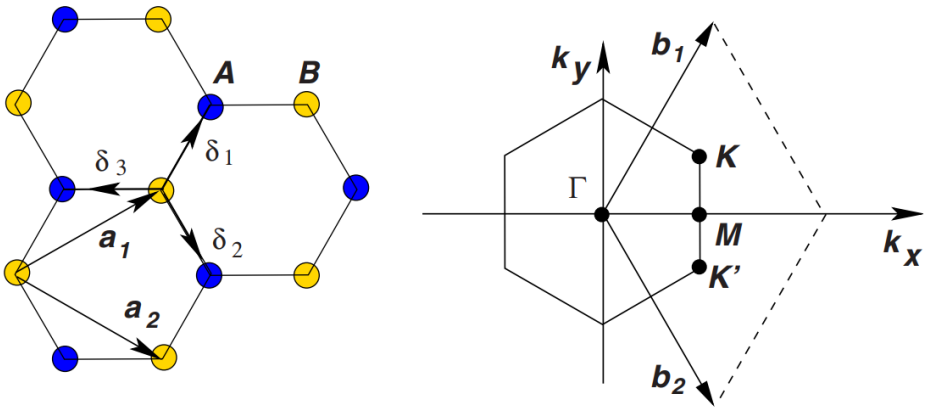

FIGURE 3.1: Honeycomb lattice structure of graphene (left) and the accompanying Brillouin zone. The lattice consists of two interwoven triangular sublattices (marked with blue and yellow atom sites). $\mathbf{a}_1$, and $\mathbf{a}_2$ represent the lattice vectors of the triangular lattice, δ_1, δ_2 and δ_3 are the vectors to the 3 nearest neighbours. On the right, $\mathbf{b}_1$ and $\mathbf{b}_2$ represent the reciprocal lattice vectors. **K** and **K'** represent to two distinct Dirac points in reciprocal space. Figure obtained from [143]

graphene never dropping below the minimum quantum unit of conductance, even as the carrier concentration tends to zero [144]. Additionally, as can be seen in Figure 3.2, the massless nature of the electrons near the Dirac points creates a linear dispersion of the electronic band structure.

Honeycomb lattices also give rise to a property of electrons known as pseudospin. As there are two wavefunctions, one associated with each sublattice, the overall electron wavefunction forms a spinor, which in momentum space takes of the form

$$\psi_{\pm,\mathbf{K}}(\mathbf{k}) = \frac{1}{\sqrt{2}} \begin{bmatrix} e^{i\theta_k/2} \\ \pm e^{-i\theta_k/2} \end{bmatrix},$$

where **K** indicates the associated Dirac point and θ_k is the angle the momentum vector of the electron makes with the x-axis. This spinor wavefunction gives rise to a helicity associated with the electron and therefore a pseudo-spin quantity. The pseudo-spin of electrons in graphene can lead to some remarkable and exotic effects. In particular, the concept of chiral tunneling and the Klein paradox has created great interest. As pseudo-spin must be conserved, certain systems will exhibit unimpeded quantum tunneling through extremely wide and/or high potentials [146].

The properties of graphene have lead to its use in applications across transistors

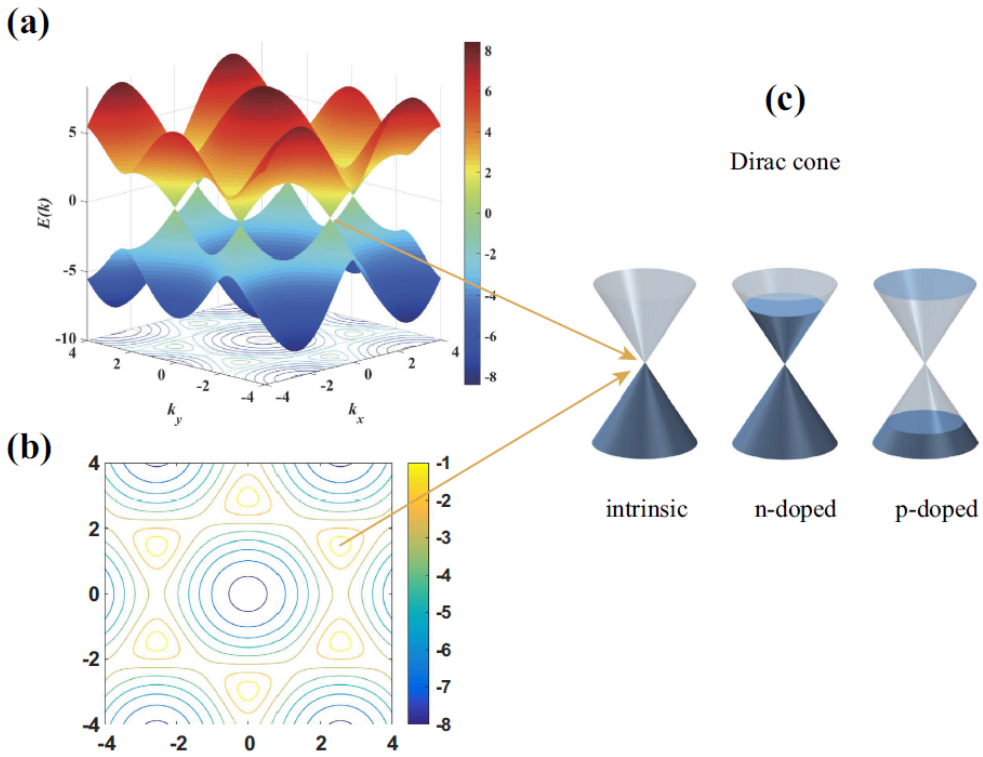

FIGURE 3.2: Figure showing the electronic dispersion of graphene's honeycomb lattice. Panels **a** and **b** show the 3D dispersion and contour plot respectively. Panel **c** highlights the linear band structure in the vicinity of the Dirac points, forming a Dirac cone in the low energy approximation. As displayed the Fermi energy of graphene lies at $E = 0$, but can be shifted either way with p or n-type doping. Figure obtained from Wang [145].

[147]; photonics and optoelectronics [148]; energy production and storage [149]; as well as biosensing applications [150]. With such a wide range of promise, and huge untapped potential, graphene physics remains a vibrant and rich area of study. Of particular note is the universal linear absorption of graphene. This result is remarkable for two reasons; firstly the optical absorption of a one atom layer is high enough to be visible to the naked eye with a 2.7% absorption; and secondly that the absorption depends only on the fine structure constant and not frequency. This optical absorption has also been shown to combine linearly with stacks up to nine layers [151].

Additionally, the linear band structure of graphene is theorised to give rise to large nonlinear effects, in particular at microwave and terahertz frequencies [152], leading to much work in the area of graphene nonlinear optics [153, 18, 154, 155, 156, 157, 145, 15, 14]. The nonlinear response of graphene is the primary focus of graphene work within this thesis.

3.1.2 Surface plasmon polaritons in graphene

This derivation is combined from the work of Bludov [103] and Jablan [158]. As previously discussed in Section 2.3.2 of Chapter 2, surface plasmon polaritons (SPPs) can only be excited by TM light so one assumes the fields take the form

$$\vec{E} = (E_{m,x}, 0, E_{m,z})\, e^{iqx} e^{-\kappa_m |z|}$$
$$\vec{B} = (0, B_{m,y}, 0)\, e^{iqx} e^{-\kappa_m |z|}.$$

where $m = 1, 2$ refers to the two media at the interface. One seeks to obtain a dispersion relation of the form $\omega = \omega(q)$ where q is the wavevector along the graphene sheet. In this case one can write Maxwell's equations as,

$$c(-1)^m \kappa_m E_{m,x} - iqE_{m,z} = i\omega B_{m,y}$$
$$(-1)^{m+1} \kappa_m B_{m,y} = -i\omega c^{-2} \epsilon_m E_{m,x}$$
$$qB_{m,y} = -\omega c^{-2} \epsilon_m E_{m,z},$$

where κ_m are the wavenumbers associated with the fields. These equations can be solved in terms of the amplitude of the magnetic field and allow for the determination of κ_m

$$
\begin{aligned}
E_{m,x} &= i\frac{\kappa_m c^{=2}}{\omega\epsilon_m}B_{m,y}(-1)^{m+1} \\
E_{m,z} &= -\frac{qc^2}{\omega\epsilon_m}B_{m,y} \\
\kappa_m^2 &= q^2 - \omega^2\epsilon_m/c^2,
\end{aligned}
$$

with $B_{m,y}$ a constant. The SPP spectrum follows from the boundary conditions,

$$
\begin{aligned}
E_{1,x} = E_{2,x} \Leftrightarrow B_{1,y} &= -\frac{\kappa_2\epsilon_1}{\kappa_1\epsilon_2}B_{2,y} \\
B_{1,y} &= B_{2_y} - \sigma_{xx}E_{1,x},
\end{aligned}
$$

where σ_{xx} is the element of the conductivity tensor generating a current in the x direction from a field also in the x direction. From these, one can obtain the dispersion relation

$$
\begin{aligned}
1 + \frac{\kappa_1\epsilon_2}{\epsilon_1\kappa_2} + i\sigma_{xx}\frac{\kappa_1}{\varepsilon_0\omega\epsilon_1} &= 0 \\
\frac{\epsilon_1}{\kappa_1} + \frac{\epsilon_2}{\kappa_2} + i\frac{\sigma_{xx}}{\varepsilon_0\omega} &= 0.
\end{aligned} \tag{3.1}
$$

If one considers the electrostatic limit such that $q \gg \frac{\omega^2}{c^2}$ then Equation 3.1 simplifies to;

$$
\kappa_1 \approx \kappa_2 \approx q_{plas} = \epsilon_0\frac{\epsilon_1+\epsilon_2}{2}\frac{2i\omega}{\sigma(q,\omega)}.
$$

If one employs a semi-classical model for the conductivity of the graphene sheet, the conductivity takes the form [159]

$$
\sigma(\omega) = \frac{e^2E_f}{\pi\hbar^2}\frac{i}{\omega+i\gamma},
$$

where E_f is the Fermi energy of the graphene and γ is the scattering of the electrons. One can thus express the dispersion of graphene as

$$q_{plas}(\omega) = \frac{\pi\hbar^2\epsilon_0(\epsilon_1+\epsilon_2)}{e^2E_f}(\omega^2 + i\omega\gamma). \tag{3.2}$$

3.1.3 Graphene plasmonics

Since the isolation of graphene, there has been great interest in exploiting its plasmonic applications [160, 161]. Graphene SPPs are far more confined, with higher field densities than plasmonic metals such as gold (see Figure 2.3 in Chapter 2). Therefore, applications of plasmonics such as sensing which exploited the high field density and confinement would be vastly improved by using a graphene based plasmonic component. Such strong confinement can lead to remarkable effects, such as the use of a single molecule defect as a peta-Hertz atomic antenna [162]. Crasse [163] also found that defects, such as wrinkles, in epitaxial graphene created strong THz plasmonic peaks, allowing for coupling to THz radiation without sample patterning.

The field of graphene plasmonics is still young and current practical applications are few. However, plasmonics with conventional metals created great excitement due to properties such as the high confinement allowing for decreasing the size of optical components. These properties are even more pronounced in graphene plasmonics, therefore the future of plasmonics lies within structures that exploit these extreme properties to a much higher degree, as is the case in 2D materials. For more on the uses and applications of plasmonics see Chapter 2.

3.2 Graphene samples utilised

This work has used three graphene samples throughout this investigation. One of those samples is commercially purchased CVD graphene. The remaining two samples are mechanically exfoliated graphene flakes on an hexagonal boron nitride (HbN) substrate.

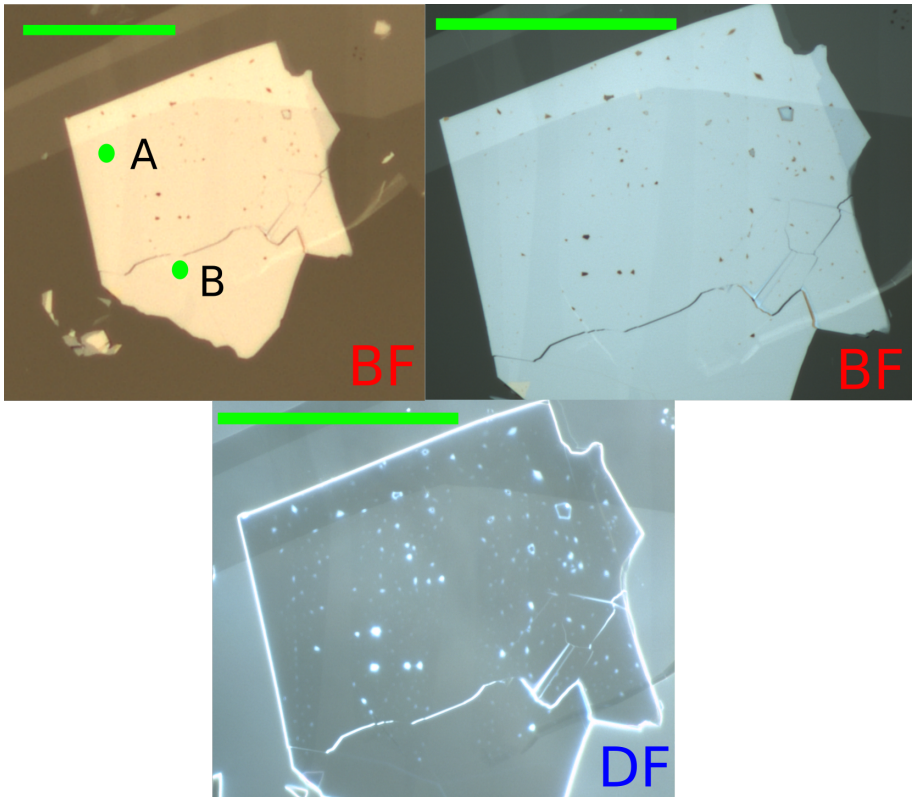

FIGURE 3.3: Optical microscopy images of **GF1**. Images are marked as bright field (BF) and dark field (DF). The scale bar is $50\mu m$.

3.2.1 Graphene Flakes

This work has utilised two different samples of mechanically exfoliated graphene. The flakes are situated on an HbN spacer layer and a SiO_2 substrate. Figures 3.3 and 3.4 show the optical microscopy images of the two flake samples, **GF1** and **GF2** respectively. The positions marked on the images correspond to the Raman spectra taken and shown in Figure 3.5.

From the Raman data, positions **B** and **C** are the best fit monolayer graphene with peak ratios of ≈ 2 and 4 respectively. The presence of a seemingly abnormally high D peak is actually the response of the HbN E2g peak which occurs at $1366cm^{-1}$ [165]. Whilst during experiments, FWM was observed at many points on the sample, unless explicitly stated others measurements on **GF1** take place at point **B**, and measurements on **GF2** take place at point **C**.

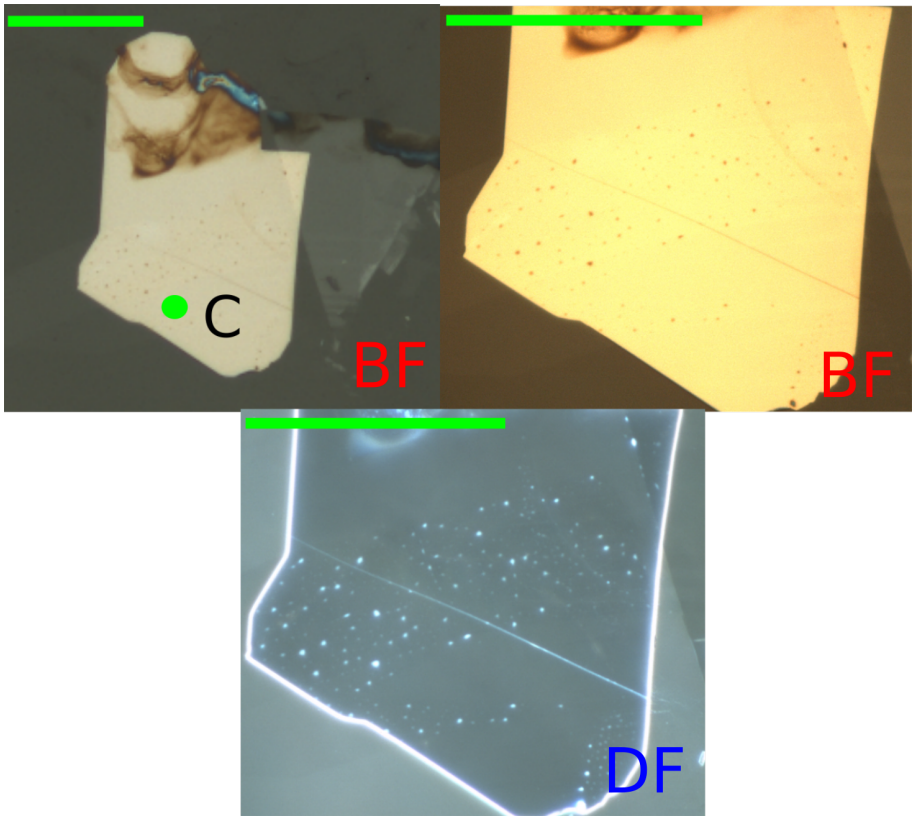

FIGURE 3.4: Optical microscopy images of **GF2**. Images are marked as bright field (BF) and dark field (DF). The scale bar is $50\mu m$

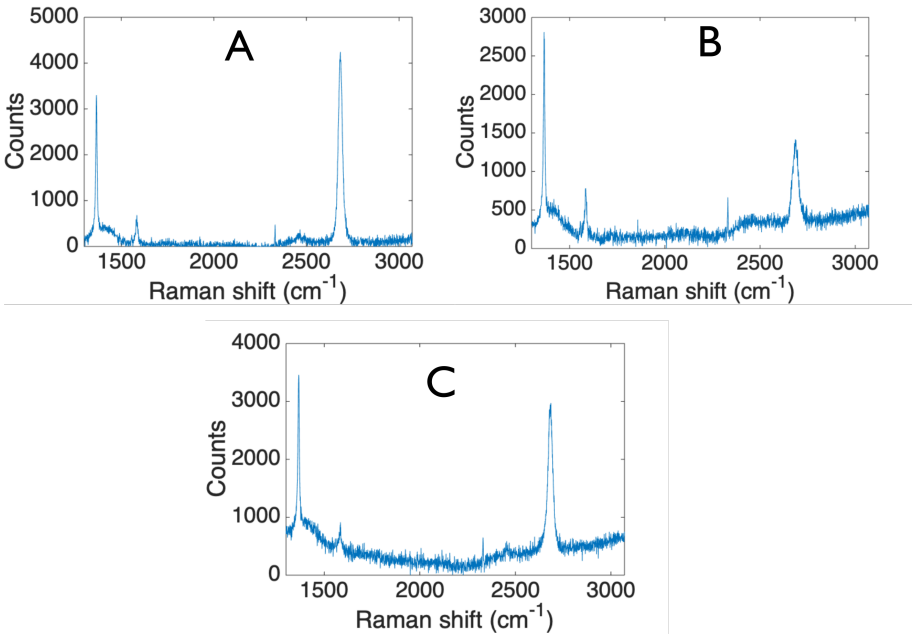

FIGURE 3.5: The Raman scans taken at positions A, B and C. In general, one expects monolayer graphene to exhibit a ratio of around 2 between the intensity of the 2D peak at $2700cm^{-1}$ and the intensity of the G peak at $1577cm^{-1}$. However, it has been noted that monolayer graphene can exhibit ratios around 4 aswell [164]. The Raman spectroscopy was performed with a Renishaw RM1000 Raman microscope at a wavelength of $532nm$, with a $50x$ objective.

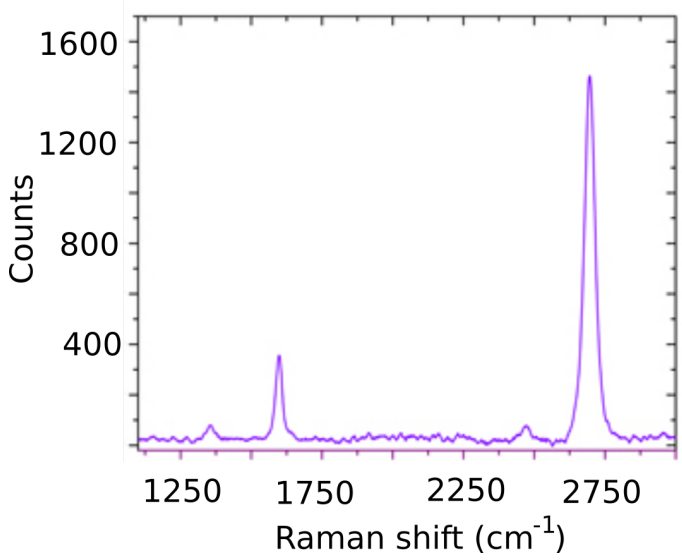

FIGURE 3.6: Characteristic Raman spectrum of the CVD graphene provided by *Graphene Supermarket*. Image is adapted from quoted specifications.

3.2.2 CVD graphene

The CVD graphene used is commercially available from *Graphene Supermarket*[1], and is monolayer graphene (90% coverage) on a SiO_2 substrate. Its Raman profile is given in Figure 3.6.

[1]http://graphene-supermarket.com

3.3 Indium Tin Oxide

3.3.1 Epsilon near zero materials

Epsilon near zero (ENZ) materials are materials that exhibit a vanishingly small permittivity at a specific wavelength. This can be achieved in materials with a Drude dispersion curve or in synthetic structures where the effective permittivity is related to that of the component materials as well as the structural form [166]. ENZ materials were first used in antennas [167] and this continues to be a wide area of investigation [168, 169] as well as beam shaping through tailoring the radiation phase pattern [166].

However, ENZ materials have also proven to be extremely efficient in enabling non-linear optical phenomena [170, 171], especially conductive metal oxides such as indium tin oxide (ITO) [67, 172] and cadmium oxide [173]. This is due to the nonlinear relationship between a change in permittivty and the change in refractive index, an effect that is most extreme and the ENZ point. In a material with a relative permeability $\mu = 1$, the refractive index (n) can be related to the permittivity (ϵ) through

$$n = \sqrt{\epsilon}.$$

From this one observes that changes in the refractive index are inversely proportional to square root of the permittivity,

$$\Delta n = \frac{\Delta \epsilon}{\sqrt{\epsilon}}.$$

In the case that $\epsilon \to 0$ one observes extremely large changes in n for relatively small changes to ϵ. This property can lead to some remarkable effects [174] including subwavelength tunneling [175].

3.3.2 Electronic and Optical Properties

Indium tin oxide is a conductive metal oxide compound that can, depending on the oxygen content, be described as a ceramic or an alloy. Typically, ITO is valued for its optical transparency and conductivity allowing it to be used for a wide range of

applications, particularly modern displays [176]. However, more recently there has been a focus on using ITO for its ENZ and nonlinear optical properties. ITO can produce changes in the refractive index from optical excitation up to 0.7 [67]. This was achieved through manipulation of the ENZ resonance with an optical pump, paving the way for potential optical switches.

3.4 ITO sample characterisation

3.4.1 ITO1

ITO1 is a custom made ITO sample obtained from *UQG Ltd*[2]. It comrpises a thin layer of ITO with a low sheet resistance on a glass cover slip. The permittivity of an ITO sample, along with its thickness, is usually obtained through ellipsometry. Ellipsometry measures the complex reflectance ratio ρ_r,

$$\rho_r = \frac{r_{TM}}{r_{TE}} = \tan\Psi e^{i\Delta},$$

where r_{TE} (r_{TM}) is the reflection coefficient for TE (TM) light, $\tan\Psi$ represents the amplitude change and Δ is the phase change upon reflection. From this, it is possible for establish the complex permittivty and refractive index of the sample [177].

For this work, it is convenient to model the ellipsometry data only in the region of 1200-1700nm, this is sufficient to include the ENZ region but allows the permittivity parameters to be well defined by Drude model. In general, the ellipsometer will fit a Drude Tauc-Lorentz model to the permittivity including potential poles above and below the the region of interest denoted by 'IR-pole' and 'UV-pole'. In practise, for the sample under investigation the material properties in the region can be adequately described without these poles, as seen in Figure 3.7. This ellipsometry measurement gives a thickness estimate of $251nm$ along with Drude parameters $\omega_p = 2.66 \times 10^{15} s^{-1}$ and $\gamma = 2.56 \times 10^{14} s^{-1}$. This places the ENZ point at around $1340nm$.

Commercially sold ITO is generally quoted in terms of thickness and sheets resistance. The sheet resistance can be established through a 4-point probe technique.

[2] https://www.uqgoptics.com

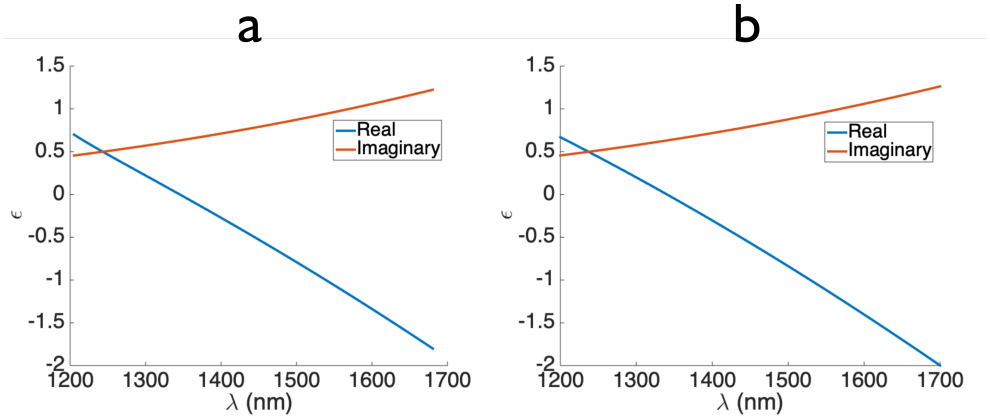

FIGURE 3.7: Ellipsometry data from the ITO sample. Panel **a** is the Ellipsometer estimated Drude-Tauc-Lorentz model. Panel **b** is the same model reduced from a Drude Tauc-Lorentz model by removal of the IR and UV poles.

TABLE 3.1: Table showing the measured sheet resistance of **ITO1** through the 4-point probe technique.

$V_3(mV)$	$V_1(mV)$	$R_s(\Omega/sq)$
5.1	1.8	7.5
4.6	1.5	7.0
4.7	1.5	7.3

The 4-point probe technique measures the potential difference across 4 different positions to achieve a more accurate measurement of the resistance. The voltage is measured and recorded at currents of $3mA(V_3)$ and $1mA(V_1)$, then one can establish the sheet resistance (R_s) through

$$R_s = 4.5324\frac{V_3 - V_1}{3mA - 1mA}.$$

Table 3.1 shows a series of measurements taken on three of the samples (the samples were provided as a batch of 10), which had a specified sheet resistance of $8 - 12\Omega/sq$. As can be seen there is a small variation across the samples but slightly lower than the quoted resistance specification implying improved sample quality.

Through the ellipsometer and 4-point probe measurements, **ITO1** is well characterised within the region of interest (1200-1700nm).

3.4.2 Sandia samples (ITO2 and ITO3)

In addition to sample **ITO1**, which aimed to resemble the samples used in [67], samples of lower thicknesses were sought to investigate their behaviour around the ENZ

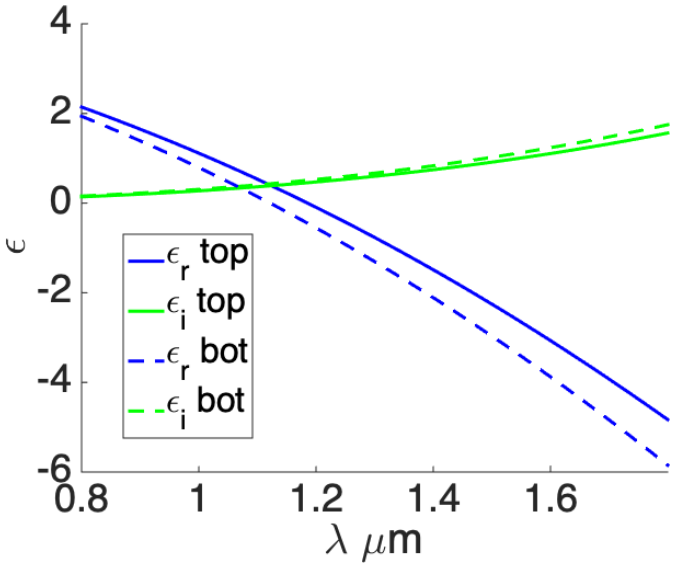

FIGURE 3.8: Permittivity as a function of wavelength for **ITO2**. The ENZ point is located at 1185nm for the top side and 1120nm for the bottom side

region. T.S. Luk of Sandia National Laboratories produced and characterised the following samples.

ITO2 is an ITO sample with a measure thickness of 55.1nm. Its permittivty is given in Figure 3.8, corresponding an ENZ point of $1120 - 1185nm$. This data shows a slight variation across the sample as there is a different index measured at the top surface of the layer (furthest from substrate) and at the bottom surface, this is common in the ITO deposition process of extremely thin films. This effect is prominent to varying degrees in a variety of $\approx 50nm$ samples and even more pronounced in $\approx 30nm$ samples, unused in this work. **ITO3** is an ITO sample with a measure thickness of 109.1nm. Its permittivty is given in Figure 3.9, this data shows an ENZ point of 1265nm. This sample does not show a graded index across the sample thickness, likely due to the thicker layer deposited.

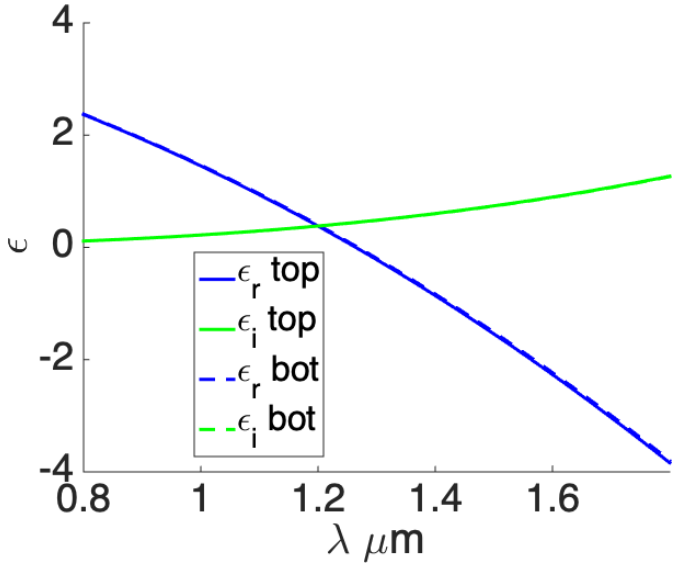

FIGURE 3.9: Permittivity as a function of wavelength for **ITO3**. The ENZ point is located at 1265nm.

Chapter 4

Experimental Methods

4.1 Four-wave mixing

4.1.1 Equipment list

The experimental setup designed for this work is detailed in Figure 4.1. This setup requires a number of specific components to be able to investigate the desired effect. The laser source used is an amplified picosecond OPO system, it has a pulse rate of $1MHz$, a pulse length $8ps$ and a time averaged output of $10-50mW$ depending on the wavelength selected. The signal ranges from $635-920nm$, the idler ranges from $1240-2200nm$, although these outputs are not independent. There is an additional pump output at $532nm$ with a time averaged power $\approx 1W$.

In order to access the graphene plasmon, one requires a very small difference frequency, and thus a small difference in the wavelengths used. Therefore, it is not possible to directly use any of the three outputs in combination to provide a difference frequency in the $\approx 15THz$ regime. This is instead achieved through the use of a conversion crystal.

In order to achieve two separate pulses that are similar in wavelength, one can perform second harmonic generation on the idler beam which, when the input wavelengths are correctly chosen, can match, or be very close to the signal wavelength. As the powers are relatively low in the idler beam ($\approx 10mW$), this experiment requires a high efficiency conversion crystal. This experiment uses a Covesion® poled conversion crystal (reference code MSHG1550-0.5) designed for second harmonic generation at $1550nm$. The range of second harmonic generation can be extended to wavelengths up to $1750nm$ through use of a heating 'oven', which can be adjusted to

optimise efficiency at the required wavelength. Using this setup, the experimental was able to observe a conversion efficiency of $\approx 35\%$, allowing for significant power generation in the second harmonic beam.

The spectrometer used to identify time overlap is an Ocean Optics Ltd. Red Tide® USB spectrometer with a wavelength range of $200 - 1100nm$. As the time averaged powers of the sources, and also the sum frequency generation of a BBO crystal, are high, one does not need to enhance the signal to be detectable in this spectrometer.

The microscope used to investigate the signal is an inverted IXplore Standard microscope from Olympus®, which has multiple advantages for the setup considered here. The system has accessible input and output pathways, which means one can provide an input signal and also manipulate the output signal prior to detection. Additionally, the input pathway has an user replaceable optic that directs input light to the back aperture of the objective. When the optic is correctly selected, this allows for the input beams to be reflected at close to 100%, and filtered out when reflected from the sample prior to the imaging. Whereas, the FWM signal generated from the experiment will be transmitted with high efficiency to the imaging equipment. Additionally, the microscope system has an overhead white light source, which is crucial in aligning the Fourier plane (discussed further in Section 4.1.5). This experiment used a 0.7 numerical aperture $60x$ objective, which yields a spot size of approximately $1.3\mu m$. It is vital that one achieves a small spot size to work with high quality exfoliated graphene. As noted in Chapter 3, CVD graphene tends to be of lower quality than exfoliated graphene, but more homogeneous over long length scales. Therefore, in order to accurately irradiate single layer graphene, one needs a small spot size with respect to the size of the patches in the exfoliated graphene.

The camera used to image the signal is a Quantem® 512sc camera with a cooled EMCCD array. The CCD array measures $512x512$ pixels enabling sufficient resolution in the Fourier plane. The camera has single photon efficiency in the optical range allowing for the detection of small signals, such as is expected from a FWM process. High exposure images can be obtained to improve signal to noise using the Micro-Manager[1] open source software, which can also control the gain to provide

[1] https://micro-manager.org/

real time observation of the FWM signal.

4.1.2 Experimental setup

Figure 4.1 shows the experimental setup used to investigate the four-wave mixing (FWM) signal in graphene. The lilac highlighted area represents the beam quality and transformation optics placed within the beams. Both beams require a cylindrical telescope in order to correct axial divergence originating within the laser, for both beams this divergence was parallel to the optical surface of the table. The idler beam undergoes a frequency doubling within a Covesion® poled conversion crystal. In order to achieve the high conversion efficiencies required, the idler beam is focused with a $5cm$ lens into the centre of the crystal. The conversion efficiency was found to be optimal at around 90^oC for $1656nm$, which is the primary idler output of investigation. However, this optimal temperature is dependent on surrounding conditions within the laboratory such as temperature and humidity. The strong focusing, combined with the original poor beam quality (see Section 4.1.3) means the output beam exhibits high inhomogeneity. Therefore this output must be spatially filtered to enable its use in Fourier plane imaging, this achieved through a $5cm - 5cm$ telescope.

In order to adjust temporal overlap a delay line is placed within the idler beam path, allowing for a path change of up $\pm 20cm$. The beams are spatially overlapped through the use of a $805nm$ short pass dichroic filter (D1), allowing transmission of the signal beam and reflection the idler.

Immediately after the dichroic, a flipper mirror (F1) can redirect the spatially overlapped beams to the temporal overlap setup (highlighted peach). Here the spatially overlapped beams are focused via a $5cm - 5cm$ telescope through a beta barium borate (BBO) crystal. The BBO crsytal outputs second harmonic generation (SHG) of each of the beams individually, which can be observed with a spectrometer. When the beams are both spatially and temporally overlapped one observes the sum frequency generation (SFG) signal of the signal and idler beams, which can be frequency resolved by the spectrometer.

When F1 is not extended, the beam undergoes 4F imaging through lenses L1 and L2. This imaging system recreates the spatial profile of the signal beam observed

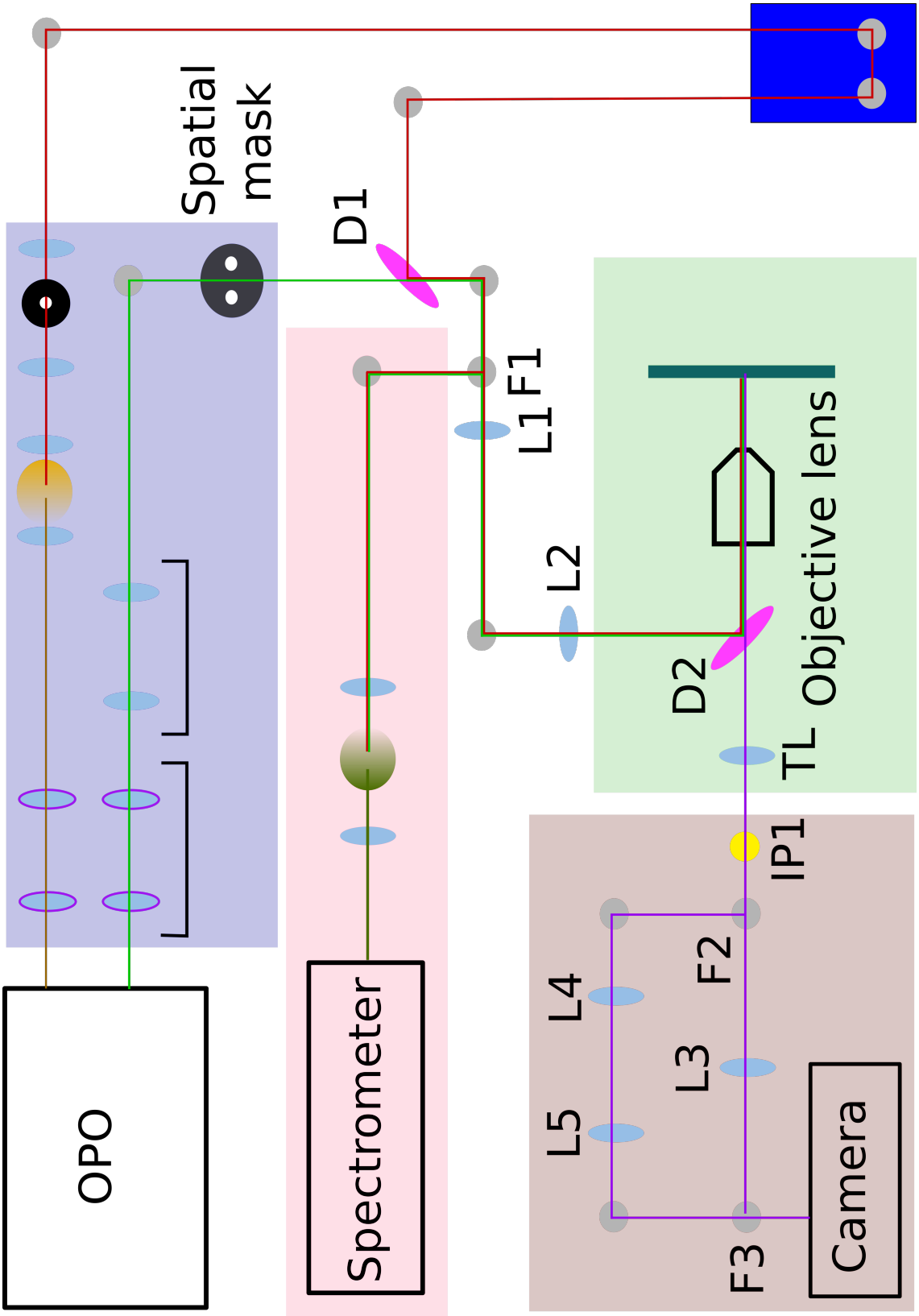

FIGURE 4.1: Experimental setup used to investigate four-wave mixing in graphene. A component key is included in Figure 4.2, and the setup is fully explained in Section 4.1.2.

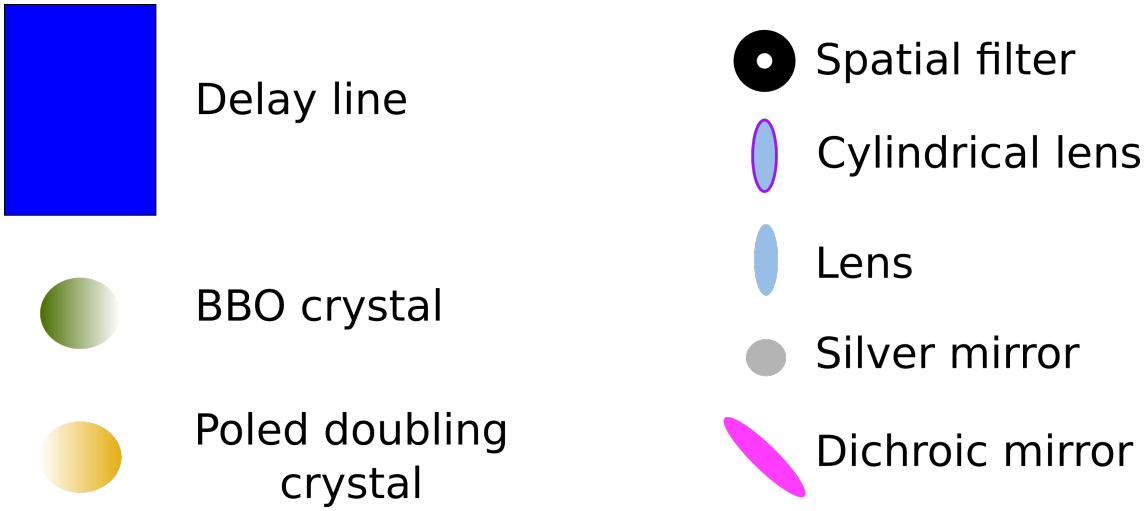

FIGURE 4.2: Key showing the symbols use in Figure 4.1.

at the spatial mask onto the back aperture of the objective lens. For the idler beam, an arbitrary point after the delay stage is recreated on the back aperture, a highly beneficial effect as it effectively removes $2m$ of path length from the beam, which degrades significantly over long propagation lengths. The principle of 4F imaging is represented in Figure 4.5.

The microscope imaging system (highlighted green) is an Olympus® inverted micrsope using a lens with a numerical aperture of 0.7 and working distance of approximately $0.2mm$. This lens produces a spot size of $\approx 1.3\mu m$. The microscope contains a $775nm$ short pass dichroic beamsplitter (D2) which reflects the signal and the idler, transmitting only the FWM signal generated through $\omega_{FWM} = 2\omega_s - \omega_i$. Therefore, both the signal and idler are incident on the sample and the FWM is filtered through to the plane re-imaging area (highlighted brown). The microscope itself contains a tube lens (TL), this lens reforms the image plane of the camera at a position approximately marked by IP1. Tube lens positions are generally not specified within a microscope setup and therefore a precise position for the IP is determined through other means (see Section 4.1.5).

In the re-imaging area there are two beam paths differentiated by flipper mirrors F2 and F3. Both of these beams paths operate the equivalent of a 4F imaging system. If F2 is extended and F3 dropped, the beam will re-image through lenses L4 and L5, this path maps the position IP1 onto the camera. If F2 is dropped and F3 extended, the path maps the back aperture through the TL and L3 onto the camera. It is crucial

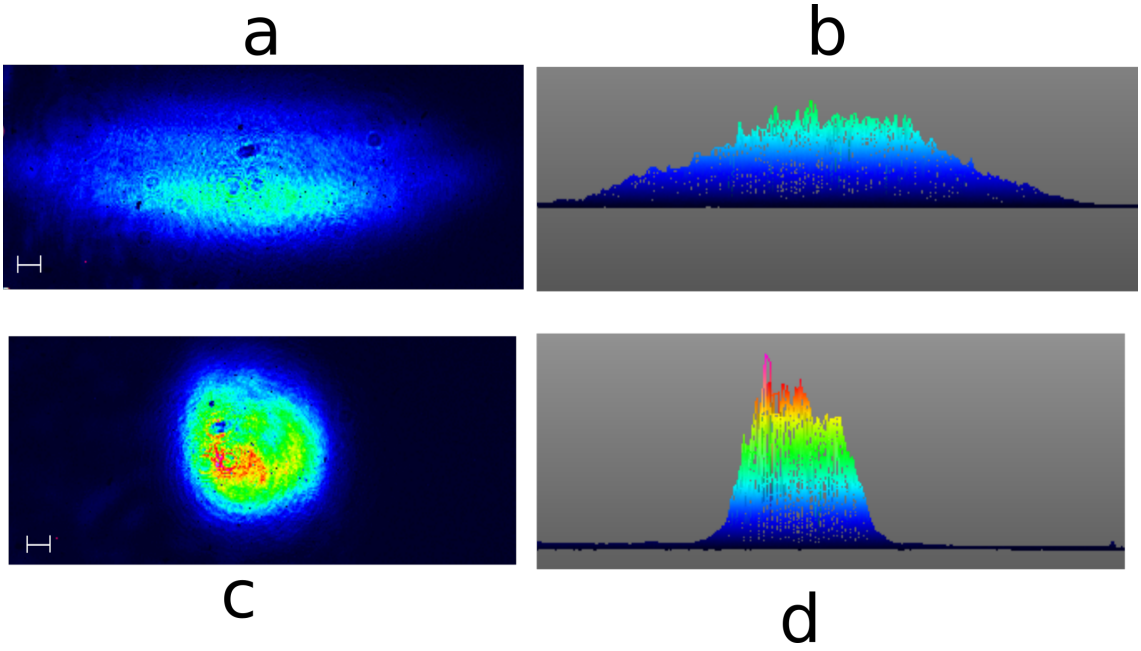

FIGURE 4.3: Figure showing the effect of the corrective optics on the signal beam. Panel **a** and **b** represent the profile without correction. Panel **a** represents the spatial distribution of the beam, while **b** shows the intensity cross-section on a linear scale of arbitrary units. Panel **c** and **d** are the equivalent data to **a** and **b** after correction. Scale bars are 1mm.

for aligning to have access to both the image plane and the Fourier plane with ease.

4.1.3 Beam quality

As shown in Figure 4.1, both laser outputs suffer from poor spatial profiles. As such, both require a significant number of optics to improve their quality prior to experimentation, these optics are situated in the lilac shaded area of Figure 4.1.

Firstly, both beams have a significant axial divergence parallel to the plane of the table. This axial divergence is shown in Panels **a** and **b** of Figure 4.3 for the signal beam, along with the beam imaged at the same area with the corrective lenses. In order to correct for this divergence one requires a single axis telescope, created through cylindrical lens. A telescope is a combination of lens that focus and re-image that focus, collimating the beam. In general, this is done through the use of two lens, in the same positions as shown in Figure 4.5. Importantly, unlike in a standard telescope, the lenses are not at their focal lengths from the focus, it is this deviation that can correct the divergence. The correcting telescopes are placed as early as possible within the beam path because a telescope can correct either the divergence of the beam or

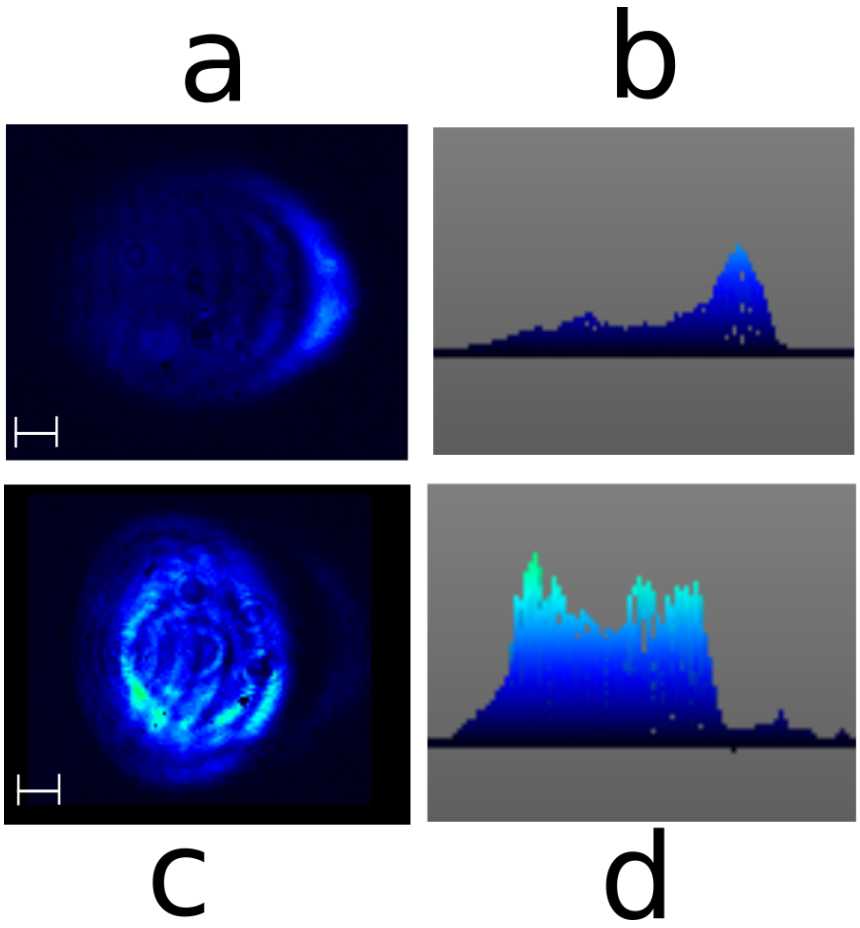

FIGURE 4.4: Figure showing the idler beam before and after spatial filtering. Panels **a** and **b** represent the beam after frequency doubling but without spatial filtering. Panels **c** and **d** represent the same beam filter through a 140μm diameter pinhole. The right hand panels represent intensities in arbitrary units. Scale bars are 1mm.

and spatial distortion already introduced but not both. Correcting the divergence early removes the need for a second telescope to correct spatial distortion. The signal beam undergoes a simple expansion telescope to increase its size to complete its spatial correction optics.

The idler beam path has two telescopes, one that focuses the beam inside the doubling crystal, and then a further telescope to apply a spatial filter. As the doubling crystal applies a non-linear process any spatial distortions are amplified in the output of the crystal. As such the beam exiting the crystal has a more inhomogenous profile than either of the original beams, and this is not limited to axial divergence. An example of the profile after the doubling crystal is shown in Panel **a** of Figure 4.4, along with the corrected beam when filtered through a 140μm pinhole in Panel **c**. Whilst the curved vertical lines appear strong in the coloured 2D projection, the

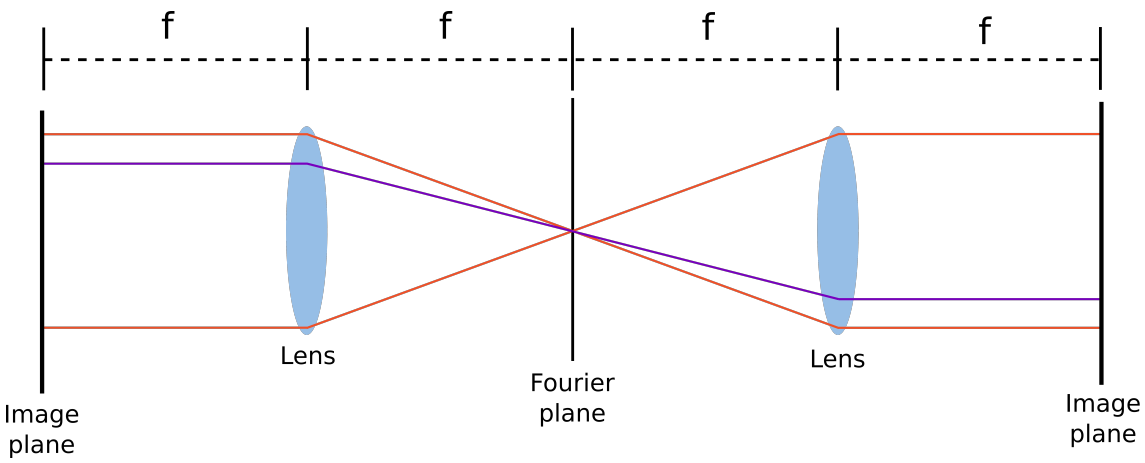

FIGURE 4.5: Representation of a 4F imaging process. The image plane on the left hand side is recreated at the right hand image plane, however, as observed in the purple beam, the image is reversed in the vertical direction. The same is true for the horizontal direction.

3D profile shows the actual intensity variation to be relatively low. A smaller spatial filter was found to reduced intensity too much to allow for accurate experimentation.

4.1.4 Beam patterning

Figure 4.1 shows the entire experimental setup used for this study. In order to define wavevectors incident on the graphene sheet, one must pattern the beam on the back aperture of the microscope. Imaging the Fourier plane of a signal in a microscope setting is equivalent to imaging the back aperture of the objective lens. The most simple practice for this would be to place a mask directly onto the back aperture of the objective, or near as possible to reduce diffraction effects. However, the use of two beams, with a desire to pattern only one, prevents this option. One beam, in this case the high frequency beam, must be patterned, whilst the other completely fills the back aperture of the microscope, illuminating the sample with the maximal range of wavevector. Due to this constraint one must place any patterning optics sufficiently far from the back aperture that they occur before the beams overlap at point D1 in Figure 4.1.

Here, one uses 4F imaging, as shown in Figure 4.5, in order to recreate the spatial profile present at the mask on the back aperture of the microscope. The beam profile will continue to evolve with distance travelled from the back aperture of the

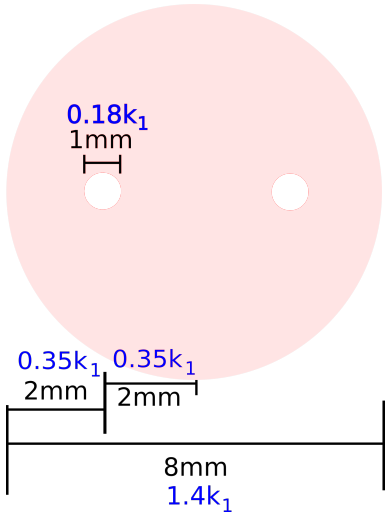

FIGURE 4.6: The spatial mask used to pattern the signal beam at the back aperture of the microscope. Black text indicates real space dimensions, the blue highlighted text is the represented dimension in Fourier space on the back aperture, relative to the freespace wavevector of the signal beam k_1.

microscope, including through the objective itself. In order to minimise this effect we choose relatively long focal length lenses ($500mm$) with respect to the working distance of the aperture ($0.2mm$) so that this effect is negligible. The 4F imaging also has a beneficial effect on the doubled idler beam. In this setup, the 4F imaging reforms a point in the idler beam path prior to the dichroic D1, effectively removing the path length between this point and the back aperture. As the beam quality is noted to reduce drastically with propagation distance this cuts out two metres of path length for this beam, improving the profile at the back aperture.

The mask used in the experiment is shown in Figure 4.6. This mask profile was chosen for a number of reasons related to the experiment and practical manufacturing. The circular holes are sufficiently small ($1mm$) to consider a defined wavevector on the back aperture of the microscope, while still maintaining a high enough beam intensity to generate significant FWM signal. The diameter of $1mm$ on the mask corresponds to a diameter of $0.18k_1$, where k_1 is the free space wavevector of the ω_1 beam, in Fourier space on the back aperture. It is important here that the profile be symmetrical across the mask such that the summation of the wavevectors from both apertures cancels out. This consideration is to make the resultant FWM signal lie within the light cone and with a wavevector generated only from the coupled ω_2 photon (this concept is described in full in Chapter 6).

4.1.5 Aligning the Fourier plane

Aligning the Fourier plane of an experiment can cause great difficulty, particularly when there are unknown optics involved. As discussed in Section 4.1.2, the position of the tube lens within the microscope is unknown. Whilst it is possible to estimate this length, it would involve a multi-step estimation introducing large numbers of minor errors. Therefore, it is simpler to align the Fourier plane by implementing a setup that provides a distinct and known image in the Fourier plane.

In the experimental setup designed for this work, the tube lens is used in two separate imaging systems, one that re-images the back aperture of the objective lens onto the camera and one that forms the image plane. In this imaging system, one must align the image plane, the Fourier plane and the sample plane within the experiment, such that all are consistent.

In practice, it is most convenient to first align the sample and the image plane. The system used for this experiment is an inverted microscope with an overhead white light source (WLS). In such a configuration the simplest way to align the sample and image planes is to image a sample that has a small transmissive area near a highly reflective area. One can then, by choosing appropriate intensities, simultaneously image a beam coming through the objective that is reflected at the same time as the transmission region with the WLS. When the sample plan is at the focus of the objective, one observes the sharpest features in the transmissive section. However, as the image plane position is not known, one cannot align to this alone. It is also true that, when the sample plane is at the focus of the objective, one observes the sharpest focus of a collimated laser beam incident on the back aperture. Therefore, only when the image plane and sample planes are both in the correct position will one observe the sharpest features and the smallest spot. The variation is achieved through the adjustment of both the sample stage, as provided by the microscopy system, and lens L4.

Once the sample and image planes are aligned, one can align the Fourier plane with a diffraction grating placed at the sample plane. This produces an expected pattern at the back aperture and thus on the camera when the imaging is aligned. One can thus adjust the position of lens L3, to adjust the relative position between the

Fourier plane and the camera array. An additional check can be carried out using an objective with a phase contrast ring on the back aperture. Which will be observable in the Fourier plane, when the Fourier plane is properly aligned this feature will be well defined.

4.2 Indium Tin Oxide

4.3 Transfer matrix method

The transfer matrix method is a procedure used for analysing the transmission and reflection coefficients from an arbitrarily large stack of metal or dielectric media [178]. In this thesis, it is used to analyse the angularly dependent reflection of indium tin oxide (ITO) for a variety of permittivities.

This derivation is taken wholly from “Principles of Optics" [178]. The derivation assumes transverse electric (TE) polarisation but can be extended to transverse magnetic (TM) as discussed later.

One assumes a stack of media in the z direction with TE polarisation, therefore, $E_y = E_z = 0$. If one assumes a time dependence to the electric and magnetic fields of $e^{-i\omega t}$, Maxwell's equations can be represented by the following six scalar equations:

$$\begin{aligned}
\frac{\partial H_z}{\partial y} - \frac{\partial H_y}{\partial z} + \frac{i\epsilon\omega}{c} E_x &= 0, \\
\frac{\partial H_x}{\partial z} - \frac{\partial H_z}{\partial x} &= 0, \\
\frac{\partial H_y}{\partial x} - \frac{\partial H_x}{\partial y} &= 0, \\
\frac{i\omega\mu}{c} H_z &= 0, \\
\frac{\partial E_x}{\partial z} - \frac{i\omega\mu}{c} H_y &= 0, \\
\frac{\partial E_x}{\partial y} + \frac{i\omega\mu}{c} H_z &= 0.
\end{aligned}$$

These equations show that H_y, H_z and E_x are functions only of y and z. eliminating H_y and H_z, one observes

$$\frac{\partial^2 E_x}{\partial y^2} + \frac{\partial^2 E_x}{\partial z^2} + n^2 k_0^2 E_x = \frac{d(\log \mu)}{dz}\frac{\partial E_x}{\partial z}, \tag{4.1}$$

where $n^2 = \epsilon\mu$ and $k_0 = \frac{\omega}{c} = \frac{2\pi}{\lambda_0}$. The simplest solution is one of the form

$$E_x(y,z) = Y(y)U(z).$$

With this substitution Equation 4.1 becomes,

$$\frac{1}{Y}\frac{d^2Y}{dy^2} = -\frac{1}{U}\frac{d^2U}{dz^2} - n^2k_0^2U + \frac{d(\log \mu}{)}dz\frac{1}{U}\frac{dU}{dz}.$$

As the left hand side is only a function y and the right hand side is only a function of z one can equate both sides to a single constant (here designated $-(k_0\alpha)^2$). Therefore the two equations can be decoupled such that,

$$\begin{aligned} \frac{1}{Y}\frac{d^2Y}{dy^2} &= -(k_0\alpha)^2, \\ Y &= const.e^{ik_0\alpha y} \\ \Rightarrow E_x &= U(z)e^{ik_0\alpha y} \end{aligned} \tag{4.2}$$

and

$$\frac{d^2U}{dz^2} - \frac{d(\log \mu)}{dz}\frac{dU}{dz} + n^2k_0^2U = -(K_0\alpha)^2U.$$

Recalling Maxwell's equations, one observes

$$\begin{aligned} H_y &= V(z)e^{i(k_0\alpha y - \omega t)}, \\ H_z &= W(z)e^{i(k_0\alpha y - \omega t)}, \end{aligned}$$

and also the relations for U, V and W as

$$V' = ik_0(\alpha W + \epsilon U),$$
$$U' = ik_0\mu V,$$
$$\alpha U + \mu W = 0,$$

with the prime denoting a differentiation with respect to z. Eliminating W from these equations yields a pair of simultaneous first-order differential equations for U and V:

$$U' = ik_0\mu V, \tag{4.3}$$
$$V' = ik_0\left(\epsilon - \frac{\alpha^2}{\mu}\right)U. \tag{4.4}$$

Elimination between these equations finally gives the following second order linear differential equations for U and V:

$$\frac{d^2U}{dz^2} - \frac{d(\log\,\mu}{dz}\frac{dU}{dz} + k_0^2(n^2 - \alpha^2)U = 0, \tag{4.5}$$
$$\frac{d^2V}{dz^2} - \frac{d\left[\log\,\left(\epsilon - \frac{\alpha^2}{\mu}\right)\right]}{dz}\frac{dV}{dz} + k_0^2(n^2 - \alpha^2)V = 0. \tag{4.6}$$

The symmetry of Maxwell's equations allows any result calculated for a TE mode to be converted to a TM mode through the substitution of E with H and simultaneously ϵ with μ, therefore the corresponding TM equations are

$$\frac{d^2U}{dz^2} - \frac{d(\log\,\epsilon)}{dz}\frac{dU}{dz} + k_0^2(n^2 - \alpha^2)U = 0, \tag{4.7}$$
$$\frac{d^2V}{dz^2} - \frac{d\left[\log\,\left(\mu - \frac{\alpha^2}{\epsilon}\right)\right]}{dz}\frac{dV}{dz} + k_0^2(n^2 - \alpha^2)V = 0. \tag{4.8}$$

U, V and W are in general complex functions of z. The surfaces of constant amplitude of E_x are given by $|U(z)| = const$, and the surfaces of constant phase follow

$$\phi(z) + k_0\alpha y = const,$$

where $\phi(z)$ is the phase of U. Since $U(z)$ and $V(z)$ each satisfy a second-order linear

differential equation, it follows that Y and V can be expressed as a linear combination of two particular, the particular solutions must be coupled by the first order differential equations 4.3 and 4.4.

$$\begin{aligned} U_m' &= ik_0\mu V_m, \\ V_m' &= ik_0\left(\epsilon - \frac{\alpha^2}{\mu}\right)U_m, \end{aligned}$$

where m can be either 1 or 2. It follows that

$$\begin{aligned} V_1U_2' - U_1'V_2 &= 0 \\ U_1V_2' - V_1'U_2 &= 0, \\ \Rightarrow \frac{d}{dz}(U_1V_2 - U_2V_1) &= 0. \end{aligned}$$

This relation can be expressed as the determinant of a 2x2 matrix,

$$D = \begin{vmatrix} U_1 & V_1 \\ U_2 & V_2 \end{vmatrix}.$$

One can chose a range of solutions to satisfy this condition. Here, it is convenient to choose solutions in the following manner

$$\begin{aligned} U_1 &= f(z), \qquad U_2 = F(z), \\ V_1 &= g(z), \qquad V_2 = G(z), \end{aligned}$$

such that

$$f(0) = G(0) = 0, \tag{4.9}$$

$$F(0) - g(0) = 1. \tag{4.10}$$

One can now write the equations as

$$\begin{aligned} U &= FU_0 + fV_0, \\ V &= GU_0 + gV_0, \end{aligned}$$

where $U_0 = U(0)$ and $V_0 = V(0)$. Although it is more convenient to express such simultaneous equations in matrix form,

$$\begin{bmatrix} U(z) \\ V(z) \end{bmatrix} = \begin{bmatrix} F(z) & f(z) \\ G(z) & g(z) \end{bmatrix} \begin{bmatrix} U_0 \\ V_0 \end{bmatrix}. \tag{4.11}$$

Thus one can define a matrix **M** that describes the propagation of a field through a medium. For the purpose of this derivation **M** is defined such that

$$\begin{bmatrix} U_0 \\ V_0 \end{bmatrix} = \begin{bmatrix} F(z) & f(z) \\ G(z) & g(z) \end{bmatrix} \begin{bmatrix} U(z) \\ V(z) \end{bmatrix},$$

allowing for the definition

$$\mathbf{M} = \begin{bmatrix} g(z) & -f(z) \\ -G(z) & F(z) \end{bmatrix}. \tag{4.12}$$

If one now considers a homogenous film, where ϵ, μ and $n = \sqrt{\epsilon\mu}$ are constants, and θ defines the angle which the normal to the wave makes with the z-axis, one observes the following previously derived relations,

$$\begin{aligned} n \sin\theta &= \alpha \\ \frac{d^2U}{dz^2} + (k_0^2 n^2 \cos^2\theta)U &= 0 \\ \frac{d^2V}{dz^2} + (k_0^2 n^2 \cos^2\theta)V &= 0. \end{aligned}$$

The solutions to these equations, when considered with the conditions imposed by Equations 4.3 and 4.4, are given by

$$\begin{aligned} U(z) &= A\ \cos(k_0 n z\ \cos\theta) + B\ \sin(k_0 n z\ \cos\theta) \\ V(z) &= \frac{1}{i}\sqrt{\frac{\epsilon}{\mu}}\ \cos\theta(B\ \cos(k_0 n z\ \cos\theta) - A\ \sin(k_0 n z\ \cos\theta)). \end{aligned}$$

Hence the particular solution which satisfies the boundary conditions of Equations 4.9 and 4.10 are

$$\begin{aligned} U_1 = f(z) &= \frac{i}{\cos\theta}\sqrt{\frac{\mu}{\epsilon}}\,\sin(k_0 nz\,\cos\theta), \\ V_1 = g(z) &= \cos(k_0 nz\,\cos\theta), \\ U_2 = F(z) &= \cos(k_0 nz\,\cos\theta), \\ V_2 = G(z) &= i\sqrt{\frac{\epsilon}{\mu}}\cos\theta\,\sin(k_0 nz\,\cos\theta). \end{aligned}$$

One can now define the full characteristic matrix **M**, however, it is first convenient to define the quantity $p = \sqrt{\frac{\epsilon}{\mu}}\cos\theta$, therfore

$$\mathbf{M}(z) = \begin{bmatrix} \cos(k_0 nz\,\cos\theta & -\frac{i}{p}\sin(k_0 nz\,\cos\theta) \\ -ip\sin(k_0 nz\,\cos\theta) & \cos(k_0 nz\,\cos\theta). \end{bmatrix} \tag{4.13}$$

One obtains similar matrices for the TM mode, if one exchanges ϵ and μ as discussed previously.

4.3.1 Experimental setup

This experimental setup was designed and built by Justus Bohn.

Freespace excitation has been shown to exhibit extremely large charges in the reflectivity of ITO [67]. However, modelling presented in Chapter 7 shows regions of high interest beyond the critical angle of glass. In order to investigate these regions, one requires a setup that can excite beyond the light line. Plasmonics has used prism coupling for many decades to enable high wavevector excitation, a geometry that is useful here.

In the setup shown in Figure 4.7, two independent outputs are produced through Topas® wavelength control systems. These systems are able to generate outputs with a range of $1150 - 1550nm$, before a filter adjustment is required. The pump output path (marked green in Figure 4.7) includes a motorized delay stage in order to sweep time overlap between the two outputs. After this a variable ND filter allows control of the pumping intensity, which is then directed onto the glass-ITO interface through the prism. Importantly the pump beam is significantly larger than

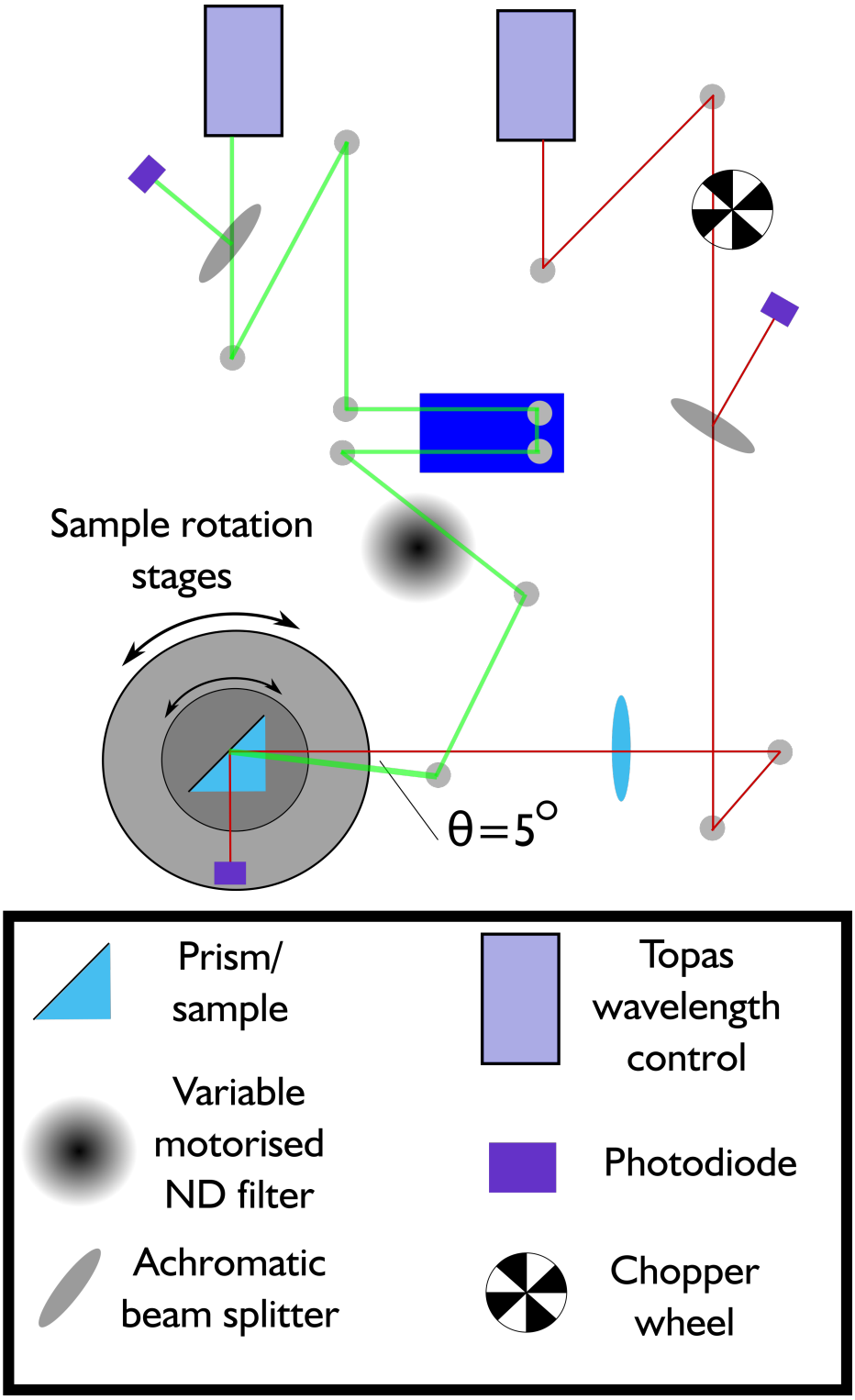

FIGURE 4.7: Figure showing the experimental setup used to investigate the differential reflectivity of ITO in the prism geometry.

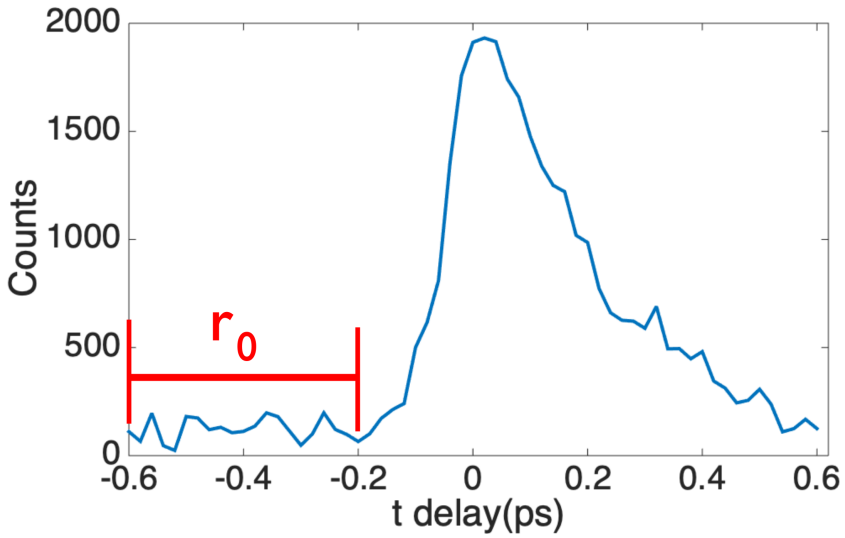

FIGURE 4.8: An example of a delay line scan corresponding to each data point in 2D plots presented in Chapter 7. The red region labeled r_0 is the range taken to be the non-photoexcited region of the sample response. This data set corresponds to **ITO2** with $\theta_{probe} = 49^o$, $\lambda_{probe} = 1201nm$ and $\lambda_{pump} = 1211nm$. This is a region of strong nonlinearity, for details see Figure 7.10 of Chapter 7.

the probe beam (the probe beam is focused onto the sample with a $20cm$ lens), simplifying the spatial overlap of the two beams. The probe beam is chopped and then directed onto the glass-ITO interface through the prism. For convenience, the probe beam is directed such that it is normal to the surface of the prism at 45^o, so there is no refraction during alignment. Rotation of the upper sample stage allows for a change in the incident angle of the probe and pump beam, while the lower sample stage allows rotation of the detector to ensure coupling of the probe beam into the photodiode. For each investigated data set (corresponding to a specific λ_{probe}, λ_{pump} and θ_{probe}) a delay line scan is performed across time overlap. The length of this delay scan is chosen as $\pm 0.6ps$ either side of time overlap, this investigates the entire nonlinear regime of interest. A sample scan is shown in Figure 4.8, the prior the point marked at $-0.2ps$ is used to calculate r_0, the non photoexcited response of the sample.

4.4 Fourier Analysis

4.4.1 Polarisation in the Fourier plane

When EM radiation is focused through a lens onto a sample, the polarisation of the light at the sample plane is altered. This is due to a change in the wavevector of light (dependent on the position in the Fourier plane) forcing a change in the electric or magnetic field to preserve orthogonality, this concept is shown in Figure 4.9.

In this thesis, all experimental works are dependent on the type of polarisation incident on the sample, either transverse electric (TE) or transverse magnetic (TM). In the FWM experiment, only TM light can excite a SPP, which is the desired effect under investigation (this consideration is discussed in Section 2.3.2 of Chapter 2). In the case of ITO the transfer matrices established have different forms for TE and TM light. Therefore for any Fourier plane analysis, one must split the incident light into the TE and TM components.

If one considers the polarisation of the electric field to be vertical in the Fourier plane, one can deconstruct the field into its TE and TM components as shown in Figure 4.9. The interaction of the electric field components with the sample can then be analysed separately, allowing for the differing boundary conditions. The resultant field can then be calculated by superposition of the component fields. In the case of FWM (Chapter 6) this is relevant as only TE light can interact with the difference frequency plasmon. For ITO the transfer matrices used to calculated the reflectivity of the sample differ for TE and TM polarisation.

Using the geometry shown in Figure 4.9, one can calculate the fraction of TE (or TM) light for any arbitrary point in the Fourier plane,

$$\vec{E}_{TE} = E\cos\theta\,\hat{r},$$
$$\vec{E}_{TM} = E\sin\theta\,\hat{\theta},$$

where $\hat{r}$ is the unit vector from point to the centre of the Fourier plane, and $\hat{\theta}$ is the unit vector perpendicular to this. One can then apply the boundary conditions relevant to the system separately for TE and TM illumination, and combine them to form the intensity profile predicted.

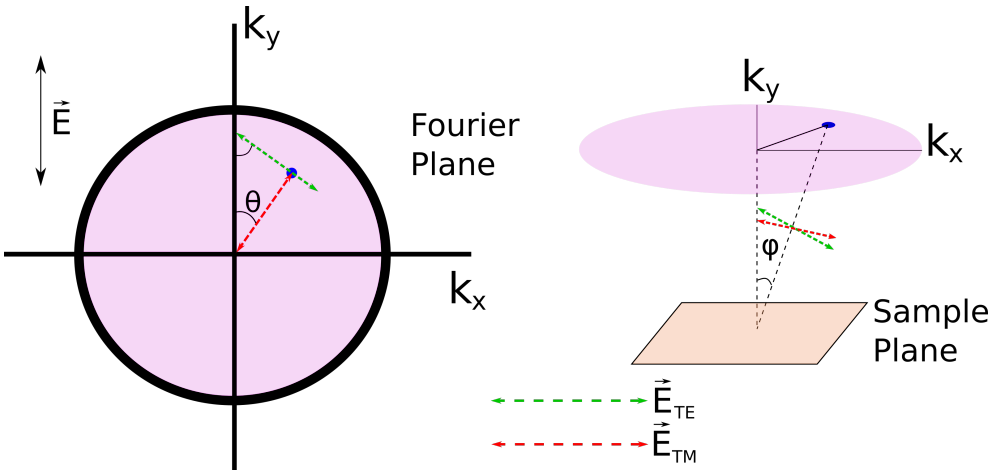

FIGURE 4.9: Image showing the geometry used to decompose a Fourier plane into its component signals. Each arbitrary point (marked blue) has a component of its field projected onto and axis directly to the centre of the Fourier plane, this is the TE component (marked red). The perpendicular component represents the TM component of the electric field (marked green). The angle of incidence is marked ϕ, this is calculated through the working distance of the objective lens and the magnitude of the wavevector in the Fourier plane.

Chapter 5

Second order response of graphene

5.1 Impact

The work presented in this chapter details a theoretical investigation into the second order nonlinear response of graphene. Firstly, errors in previous literature are identified and, where possible, corrected[14, 15, 179]. The results of theoretical treatments are then compared to relevant experimental works [180, 181] showing a large discrepancy. Finally, other possible origins of nonlinear signals are investigated, including the substrate response and photothermal effects. Photothermal effects show a stronger predicted response than perturbative approaches by around two orders of magnitude. Whilst this response is still weaker than experimental observations, there are, as discussed, several parameters than are not accurately measured on ultrafast timescales and could account for the discrepancy. This work forms the basis of the manuscript "Origins of All-Optical Generation of Plasmons in Graphene" [17].

5.2 Motivation

The second order nonlinear response of graphene has undergone limited research due to its centrosymmetry. In a centrosymmetric system such as graphene, second order responses are forbidden. It has been known, however, that such symmetry arguments can be broken in materials via the use of oblique beams and an interface [155]. This discussion will focus on the experimental work on Constant [35], which was the most notable experimental measurement of difference frequency generation (DFG) in graphene. Since this work there has been confirmation of the magnitude of this effect in the work of B. Yao [181] .

Constant used two optical femtosecond pulses to illuminate a graphene sheet and varied the angles of incidence and one of the wavelengths. This technique enabled phasematching to the graphene plasmon, showing an enhancement in the differential reflection of the probe beam when coupling to the plasmon. As noted previously, the second order response of graphene is expected to be weak due to centrosymmetry, but Constant's work suggested a second order conductivity of $\sigma^{(2)} \approx 10^{-14} - 10^{-13}\mathrm{AmV}^{-2}$, which was considered high by comparison to bulk nonlinear crystals[1]. At the time of this thesis' theoretical work, there were several theoretical papers discussing the second order response of graphene and showing the size of this effect, the most relevant of which was by Yao [14]. Yao predicted a hugely enhanced difference frequency nonlinearity in graphene when phasematching to the plasmon, describing an experimental setup very similar to that used in the experiment of Constant. Indeed, when applying the parameters of Constant, the response predicted is even higher than that observed in experiment, but only by an order of magnitude (see Figure 5.3). This was deemed to be reasonable agreement, though slightly high, and gave a theoretical formalism for the observation, using the conventional method of perturbation theory to derive the response.

Whilst the work of Yao provided reasonable agreement with the experimental results of Constant, the paper was not well understood across the field. The paper produced a remarkably non-physical result with a divergence in the non-linear response as the wavevector tended to zero. That is to say that Yao predicted an infinite nonlinear response at normal incidence. Not only is this non-physical, it is also counterintuitive. The second order response of graphene is only allowed through the broken symmetry of oblique beams and yet when this symmetry is restored at normal incidence Yao's theory predicts a higher response. It is here this work begins, reproducing the derivation of Yao, highlighting the key points that lead to this non-physical result.

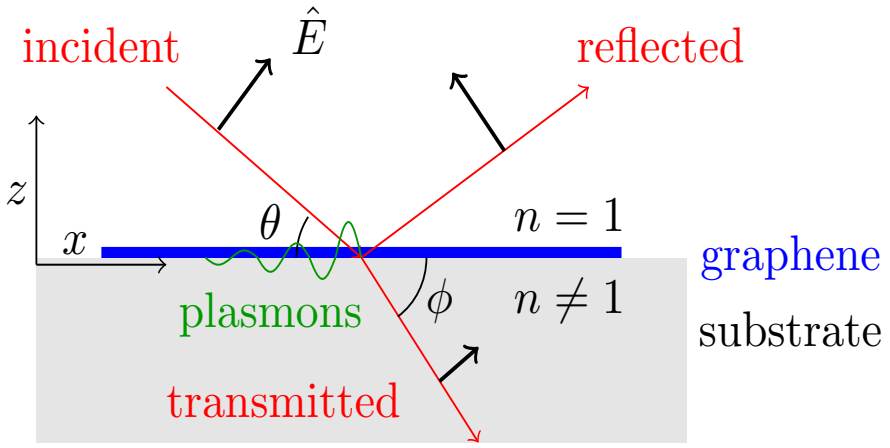

FIGURE 5.1: Illustration of electromagnetic fields ($\vec{E}$) (applicable to pump, probe, and DFG) propagating in the x-z plane. All the fields are p-polarized and the directions of propagation and polarizations are indicated by the red and black arrows respectively. The angles of incidence and transmission are defined in the Figure as θ and ϕ.

5.3 Derivation of non-linear susceptibility

5.4 Perturbation theory

The most conventional way to derive the non-linear response of graphene is to use perturbation theory applied to the electron energy states within a sample. One begins here with the time dependent Schrödinger equation expressed in the following form

$$\frac{\partial \rho}{\partial t} = -\frac{i}{\hbar}(\epsilon_n - \epsilon_m)\rho_{nm} - \frac{i}{\hbar}[\hat{H}_{int}, \hat{\rho}]_{nm} - \gamma_{nm}(\rho_{nm} - \rho_{nm}^{(eq)}), \tag{5.1}$$

where ρ is the density matrix of the electrons in graphene and $\epsilon_{n,m}$ is the energy level of the state n and m respectively. The first term on the right hand side represents $\hat{H}_0$, the non-interacting Hamiltonian of graphene and $\hat{H}_{int}$ is the interaction Hamiltonian with γ_{nm} being the scattering rate between states n and m. One notes that the equilibrium state of the graphene sheet is the Fermi distribution, therefore both the equilibrium density matrix $\rho_{nm}^{(eq)}$ and the zeroth order $\rho_{nm}^{(0)}$ are comprised of the Fermi distribution along the leading diagonal and reduce to the form $\delta_{n,m} f_n$ where f is the Fermi distribution. One can now form the iterative solution to Equation 5.1

$$\rho_{nm}^{(N)} = \int^{t} -\frac{i}{\hbar}[\hat{H}_{int}, \hat{\rho}^{(N-1)}]_{nm} e^{(i\omega_{nm}+\gamma)(t'-t)} dt'. \tag{5.2}$$

[1] if compared as a bulk susceptibility $\chi^{(2)}_{bulk}$ 3×10^{-7} which is three orders of magnitude larger than gallium arsenide (GaAs)[35]

The iterative nature of this solution means that the interactions of the two different light pulses are considered to happen separately. That is, field A interacts first and then field B interacts with the electrons which have a perturbed density of states from interaction A, and vice versa.

5.4.1 The interaction Hamiltonian of an electric field

In Equation 5.1, $\hat{H}_{int}$ is a generalised interaction Hamiltonian, here the specific case of an incident electric field causes this interaction, defined in the following way:

$$\begin{aligned} \hat{H}_{int} &= \frac{iev_f}{\omega} \overrightarrow{\hat{\sigma}} . \overrightarrow{E}, \\ \overrightarrow{\hat{\sigma}} &= \hat{\sigma}_x \hat{x} + \hat{\sigma}_y \hat{y}, \\ \hat{\sigma}_x &= \begin{bmatrix} 0 & 1 \\ 1 & 0 \end{bmatrix}, \\ \hat{\sigma}_y &= \begin{bmatrix} 0 & -i \\ i & 0 \end{bmatrix}. \end{aligned} \tag{5.3}$$

Here e is the elementary charge, v_f is the Fermi velocity, ω is the frequency of the incoming EM field $\vec{E}$ and $\hat{\vec{\sigma}}$ is the 2D Pauli spin matrix vector as defined above. It is also convenient here to replace the commutator with its summation form

$$[\hat{A}, \hat{B}]_{nm} = [\hat{A}\hat{B}]_{nm} - [\hat{B}\hat{A}]_{nm} = \sum_l (A_{nl}B_{lm} - B_{nl}A_{lm}),$$

and substitute this into Equation 5.2

$$\rho^{(N)}_{nm} = \int^t -\frac{i}{\hbar} \sum_l (H_{nl}\rho^{(N-1)}_{lm} - \rho^{(N-1)}_{nl} H_{lm}) e^{(i\omega_{nm}+\gamma)(t'-t)} dt'. \tag{5.4}$$

5.4.2 Linear response

Equation 5.4 is now an analytically soluble form, albeit iterative. Therefore the first order perturbed density matrix $\rho^{(1)}$ is sought. However to reduce this summation one observes the form of $\rho^0_{nl} = \delta_{nl} f_n$. This now restricts the values of l in the first order. In addition one can separate the time dependence of the Hamiltonian such that

$H_{nl} \rightarrow H'_{nl}e^{i\omega t}$. It is crucial to note here that ω is the frequency of the incident light and not the associated energy frequency difference ($\omega_{nl} = \frac{E_n - E_l}{\hbar}$). The initial and final states (n and m respectively) are separated by the wavevector of the incident light and not the energy of the transition.

$$\begin{aligned}
\rho^{(1)}_{nm} &= \int^t -\frac{i}{\hbar}H'_{nm}e^{-i\omega t'}f_m - f_n H'_{nm}e^{-i\omega t'}e^{(i\omega_{nm}+\gamma)(t'-t)}dt', \\
\rho^{(1)}_{nm} &= \int^t -\frac{i}{\hbar}H'_{nm}(f_m - f_n)e^{-i\omega t'}e^{(i\omega_{nm}+\gamma)(t'-t)}dt', \\
\rho^{(1)}_{nm} &= -\frac{i}{\hbar}(f_m - f_n)H'_{nm}e^{(i\omega_{nm}+\gamma)t}\int^t e^{-i\omega t'}e^{(i\omega_{nm}+\gamma)t'}dt', \\
\rho^{(1)}_{nm} &= -\frac{i}{\hbar}(f_m - f_n)H'_{nm}e^{-(i\omega_{nm}+\gamma)t}\frac{e^{-i\omega t}e^{(i\omega_{nm}+\gamma)t}}{i\omega_{nm} - i\omega + \gamma}, \\
\rho^{(1)}_{nm} &= -\frac{i}{\hbar}\frac{(f_m - f_n)H'_{nm}}{(i\omega_{nm} - i\omega + \gamma)}e^{-i\omega t}, \\
\rho^{(1)}_{nm} &= -\frac{(f_m - f_n)H'_{nm}}{\hbar(\omega_{nm} - \omega - i\gamma)}e^{-i\omega t}, \\
\rho^{(1)}_{nm} &= -\frac{(f_m - f_n)}{\hbar\omega}\frac{iev_f\hat{\vec{\sigma}}.\vec{E}}{(\omega_{nm} - \omega - i\gamma).}
\end{aligned} \tag{5.5}$$

This solution to the linear density matrix can now be used to give the linear susceptibility of graphene as outlined in Yao[14]. One notes here that the manuscript [14] appears to have an unacknowledged error in the un-numbered equation between (9) and (10) in the supplementary material of [14], and the correct integral would be

$$\frac{2\pi(\omega + i\gamma)}{(v_f q)^2}\left[1 - \frac{\omega + i\gamma}{\omega + i\gamma + v_f q}\left(1 + \sqrt{\frac{2v_f q}{v_f q - \omega - i\gamma}}\right)\right]$$

However this is not of particular relevance to the discussion of second order nonlinearity pursued here and it is only noted for completeness. For now, one can use the solution of the linear density matrix (as that is all that is required) to proceed with the nonlinear response.

5.5 Non-linear conductivity

Having solved for the linear density matrix upon interaction with a single electric field, this perturbed system must now interact with a second field. To avoid confusion the two fields are labelled with subscripts 1 and 2:

$$\rho^{(2)}_{nm} = -\frac{i}{\hbar}\int^t [H,\rho^{(1)}]_{nm} e^{(i\omega_{nm}+\gamma)(t'-t)}dt'$$
$$\rho^{(2)}_{nm} = -\frac{i}{\hbar}\int^t \sum_l \left(H_{nl}\rho^{(1)}_{lm} - \rho^{(1)}_{nl}H_{lm}\right) e^{(i\omega_{nm}+\gamma)(t'-t)}dt'.$$

Here one can replace Equation 5.5 to substitute for $\rho^{(1)}$:

$$\rho^{(2)}_{nm} = -\frac{i}{\hbar}\int^t \sum_l \left(H_{nl}\left(-\frac{(f_m-f_l)H_{lm}}{\hbar(\omega_{lm}-\omega-i\gamma)}\right) - \left(-\frac{(f_l-f_n)H_{nl}}{\hbar(\omega_{nl}-\omega_1-i\gamma)}\right)H_{lm}\right) e^{(i\omega_{nm}+\gamma)(t'-t)}dt'$$
$$\rho^{(2)}_{nm} = \frac{i}{\hbar^2}\int^t \sum_l \left(H_{nl}H_{lm}\left(\frac{(f_m-f_l)}{\omega_{lm}-\omega-i\gamma} - \frac{(f_l-f_n)}{\omega_{nl}-\omega-i\gamma}\right)\right) e^{(i\omega_{nm}+\gamma)(t'-t)}dt'.$$

One can now put in the time dependence of Hamiltonians as follows $H_{nl} = H'_{nl}e^{-i\omega_1 t}$ and $H_{lm} = H'_{lm}e^{-i\omega_2 t}$, allowing us to remove the summation from the integral.

$$\rho^{(2)}_{nm} = \frac{i}{\hbar^2}\int^t \sum_l \left(H'_{nl}H'_{lm}\left(\frac{(f_m-f_l)}{\omega_{lm}-\omega_2-i\gamma} - \frac{(f_l-f_n)}{\omega_{nl}-\omega_1-i\gamma}\right)\right) e^{-i\omega_1 t'}e^{-i\omega_2 t'}e^{(i\omega_{nm}+\gamma)(t'-t)}dt',$$
$$\rho^{(2)}_{nm} = \frac{i}{\hbar^2}\sum_l \left(H'_{nl}H'_{lm}\left(\frac{(f_m-f_l)}{\omega_{lm}-\omega_2-i\gamma} - \frac{(f_l-f_n)}{\omega_{nl}-\omega_1-i\gamma}\right)\right)\int^t e^{-i\omega_1 t'}e^{-i\omega_2 t'}e^{(i\omega_{nm}+\gamma)(t'-t)}dt',,$$
$$\rho^{(2)}_{nm} = \frac{i}{\hbar^2}\sum_l \left(H'_{nl}H'_{lm}\left(\frac{(f_m-f_l)}{\omega_{lm}-\omega_2-i\gamma} - \frac{(f_l-f_n)}{\omega_{nl}-\omega_1-i\gamma}\right)\right)\int^t e^{i(\omega_{nm}-\omega_1-\omega_2-i\gamma)t'}e^{(i\omega_{nm}+\gamma)t}dt',$$
$$\rho^{(2)}_{nm} = \frac{i}{\hbar^2}\sum_l \left(H'_{nl}H'_{lm}\left(\frac{(f_m-f_l)}{\omega_{lm}-\omega_2-i\gamma} - \frac{(f_l-f_n)}{\omega_{nl}-\omega_1-i\gamma}\right)\right)\left(\frac{e^{i(\omega_{nm}-\omega_1-\omega_2-i\gamma)t}e^{(i\omega_{nm}+\gamma)t}}{\omega_{nm}-\omega_1-\omega_2-i\gamma)}\right),$$
$$\rho^{(2)}_{nm} = -\frac{1}{\hbar^2}\sum_l \left(H'_{nl}H'_{lm}\left(\frac{(f_m-f_l)}{\omega_{lm}-\omega_2-i\gamma} - \frac{(f_l-f_n)}{\omega_{nl}-\omega_1-i\gamma}\right)\right)\left(\frac{e^{-i(\omega_1+\omega_2)t}}{\omega_{nm}-\omega_1-\omega_2-i\gamma)}\right). \tag{5.6}$$

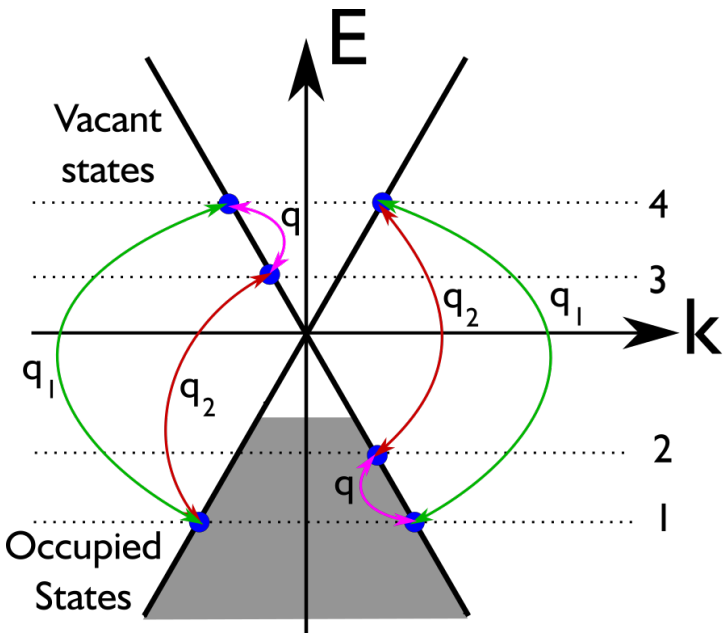

FIGURE 5.2: Band diagram showing the two triplet states relevant to the DFG calculation. The red (green) arrow represents an excitation from the low (high) frequency field and the pink arrow represents the difference frequency oscillation at the plasmon wavevector q. Importantly, the energy difference between the levels is defined through the momentum q and not the frequency of the incident light.

5.5.1 DFG susceptibility

Equation 5.6 is a generalised form of the density matrix in a second order perturbation. The solution accounts for SHG ($\omega_1 = \omega_2$), optical rectification ($\omega_1 = -\omega_2$) as well as sum frequency and difference frequency generation. However, this work considers only the DFG possibilities where $\omega_1 \neq \omega_2$ and consider the frequencies to be of opposite sign. In order to isolate the terms of interest one can use the rotating wave approximation (RWA), selecting the terms that oscillate with the frequency of interest, in this case the DFG frequency. With two incident fields of frequency ω_a and ω_b, one defines $\omega_1 = \omega_a$, $\omega_2 = -\omega_b$ and $\omega_3 = \omega_a - \omega_b$.

With two incoming fields the relevant states are defined by Figure 5.2 similar to Figure 2 of Yao [14].

$$\rho^{(2)}_{nm} = -\frac{1}{\hbar^2}\sum_l \left(H'_{nl}H'^{*}_{lm}\left(\frac{(f_m - f_l)}{\omega_{lm} - \omega_{ml} - i\gamma} - \frac{(f_l - f_n)}{\omega_{nl} - \omega_{ln} - i\gamma}\right)\right)\left(\frac{e^{-i(\omega_{nl}-\omega_{lm})t}}{\omega_{nm} - (\omega_{lm} - \omega_{nl}) - i\gamma}\right)$$

Now, one isolates the terms corresponding to the desired oscillation which will be $\rho_{43}^{(2)}$ and $\rho_{12}^{(2)}$, which both show the difference frequency oscillation:

$$\rho_{43}^{(2)} = -\frac{1}{\hbar^2} H'_{41} H'^{*}_{13} \left(\frac{(f_3 - f_1)}{\omega_2 - \omega_{13} - i\gamma} - \frac{(f_1 - f_4)}{\omega_1 - \omega_{41} - i\gamma} \right) \frac{e^{-i\omega_3 t}}{\omega_{43} - \omega_3 - i\gamma} \tag{5.7}$$

$$\rho_{12}^{(2)} = -\frac{1}{\hbar^2} H'_{14} H'^{*}_{42} \left(\frac{(f_2 - f_4)}{\omega_2 - \omega_{42} - i\gamma} - \frac{(f_4 - f_1)}{\omega_1 - \omega_{41} - i\gamma} \right) \frac{e^{-i\omega_3 t}}{\omega_{12} - \omega_3 - i\gamma} \tag{5.8}$$

Also it is important to note the resonance that exists in these terms ($\omega_3 = \omega_{43} = \omega_{12}$) will be later smeared through integration. In order to obtain the polarisation of the graphene sheet, one requires the expectation value of the dipole moment, achieving this through the general property

$$\langle \hat{O} \rangle = Tr(\rho . \hat{O}),$$

which states that the expectation value of any operator $\hat{O}$ is given by the trace of that operator on the density matrix. More specifically in the case of polarisation

$$\vec{P} = N . \mathrm{Tr}(\rho . \hat{\mu}),$$

where N is the number of electrons. For now, the transition dipole moment between two states n, m is defined as μ_{nm}. The transition dipole moment will be discussed in greater depth in the Section 5.5.3.

$$< \hat{P}^{(2)}(\omega_3) >= \sum_{1,3,4} \mu_{34} \rho_{43}^{(2)} + \sum_{1,2,4} \mu_{21} \rho_{12}^{(2)}$$

Substituting values from Equations 5.7 and 5.8, and removing the stated time dependence of interest ($e^{-i\omega_3 t}$) to find the amplitude of the oscillation

$$\begin{aligned} < \hat{P}^{(2)}(\omega_3) >= & \sum_{1,3,4} -\frac{\mu_{34}}{\hbar^2} H'_{41} H'^{*}_{13} \left(\frac{(f_3 - f_1)}{\omega_2 - \omega_{13} - i\gamma} - \frac{(f_1 - f_4)}{\omega_1 - \omega_{41} - i\gamma} \right) \frac{1}{\omega_{43} - \omega_3 - i\gamma} \\ & + \sum_{1,2,4} -\frac{\mu_{21}}{\hbar^2} H'_{14} H'^{*}_{42} \left(\frac{(f_2 - f_4)}{\omega_2 - \omega_{42} - i\gamma} - \frac{(f_4 - f_1)}{\omega_1 - \omega_{41} - i\gamma} \right) \frac{1}{\omega_{12} - \omega_3 - i\gamma}, \end{aligned}$$

where $\sum_{1,3,4}$ represents that the sum is over a linked triplet of states, that is to say the states do not have a specific vector or energy but do have specific differences in

wavevectors corresponding to the wavevector of the incident light. Then using the definition of $\hat{H}_{int}$ from Equation 5.3 and replacing the summation over linked states with an integral over all space one arrives at

$$\begin{aligned} < \hat{P}^{(2)}(\omega_3) >= & \frac{-e^2}{\hbar^2\omega_1\omega_2}\int\int\frac{d^2\vec{k}_1}{(2\pi)^2} \\ & \times\left[\frac{\mu_{34}v_{41}v_{13}}{\omega_{43}-\omega_3-i\gamma}\left(\frac{(f_1-f_3)}{\omega_2-\omega_{13}-i\gamma}+\frac{(f_1-f_4)}{\omega_1-\omega_{41}-i\gamma}\right)\right. \\ & \left.+\frac{\mu_{21}v_{14}v_{42}}{\omega_{12}-\omega_3-i\gamma}\left(\frac{(f_2-f_4)}{\omega_2-\omega_{42}-i\gamma}-\frac{(f_4-f_1)}{\omega_1-\omega_{41}-i\gamma}\right)\right] \end{aligned} \tag{5.9}$$

5.5.2 Approximation of the integral

The integral in Equation 5.9 should in principle be solved numerically, however as with Yao [14], one looks for an estimate under the relevant experimental conditions of Constant [35], starting by considering only the kernel (Γ) (the coefficients will be reintroduced later):

$$\begin{aligned} \Gamma = & \int\int\frac{d^2\vec{k}_1}{(2\pi)^2}\left(\left(\frac{f_1-f_4}{\omega_{41}-\omega_2-i\gamma}+\frac{f_1-f_3}{-\omega_{31}+\omega_1-i\gamma}\right)\frac{\mu_{34}v_{31}v_{12}}{\omega_{43}-\omega_3-i\gamma}\right) \\ & -\int\int\frac{d^2\vec{k}_1}{(2\pi)^2}\left(\left(\frac{f_1-f_4}{\omega_{41}-\omega_b-i\gamma}+\frac{f_2-f_4}{-\omega_{42}+\omega_a-i\gamma}\right)\frac{\mu_{21}v_{14}v_{42}}{\omega_{12}-\omega_3-i\gamma}\right) \end{aligned}$$

As per Figure 5.2, states 1 and 2 are occupied and states 3 and 4 are unoccupied. The limit $k_bT \to 0$ is applied therefore the Fermi distribution is represent by a step function,

$$\begin{aligned} \Gamma = & \int\int\frac{d^2\vec{k}_1}{(2\pi)^2}\left(\left(\frac{1}{\omega_{41}-\omega_2-i\gamma}+\frac{1}{-\omega_{31}+\omega_1-i\gamma}\right)\frac{\mu_{34}v_{41}v_{13}}{\omega_{43}-\omega_3-i\gamma}\right) \\ & -\int\int\frac{d^2\vec{k}_1}{(2\pi)^2}\left(\left(\frac{1}{\omega_{41}-\omega_2-i\gamma}+\frac{1}{-\omega_{42}+\omega_1-i\gamma}\right)\frac{\mu_{21}v_{14}v_{42}}{\omega_{12}-\omega_3-i\gamma}\right) \end{aligned}$$

One now considers individual components and how they can be approximated. First the energy level difference ω_{nm},

$$\begin{aligned}
\omega_{nm} &= \frac{\epsilon_n - \epsilon_m}{\hbar}, \\
\omega_{nm} &= v_f(|\vec{k}_n| - |\vec{k}_m|), \\
\omega_{nm} &= v_f(|\vec{k}_1 + q_n| - |\vec{k}_1 + q_m|), \\
\omega_{nm} &= v_f((k_1^2 + 2q_n k_1 \cos\phi_n + q_n^2)^{\frac{1}{2}} - (k_1^2 + 2q_m k_1 \cos\phi_m + q_m^2)^{\frac{1}{2}}).
\end{aligned}$$

As $q < k_1$ one can entirely disregard the $q_{n,m}^2$ terms and apply a Taylor expansion to the remaining square root bracket,

$$\begin{aligned}
\omega_{nm} &= v_f(s_n(k_1^2 + 2q_n k_1 \cos\phi_n)^{\frac{1}{2}} - s_m(k_1^2 + 2q_m k_1 \cos\phi_m +)^{\frac{1}{2}}) \\
\omega_{nm} &= v_f k_1 \left(s_n(1 + 2\frac{q_n}{k_1} \cos\phi_n)^{\frac{1}{2}} - s_m(1 + 2\frac{q_m}{k_1} \cos\phi_m)^{\frac{1}{2}} \right) \\
\omega_{nm} &= v_f k_1 \left(s_n(1 + \frac{q_n}{k_1} \cos\phi_n) - s_m(1 + \frac{q_m}{k_1} \cos\phi_m) \right)
\end{aligned}$$

As k_1 is much larger than q then $\phi_{n,m} \to \phi_1$.

$$\omega_{nm} = v_f k_1 \cos\phi_1 \left(s_n(1 + \frac{q_n}{k_1}) - s_m(1 + \frac{q_m}{k_1}) \right)$$

There are two clear cases; that of an interband transition and intraband transition.

$$\begin{aligned}
\text{Intraband} \quad (s_n = s_m) &: \omega_{nm} = v_f(q_n - q_m)\cos\phi_1 \\
\text{Interband} \quad (s_n = -s_m) &: \omega_{nm} = \pm 2 v_f k_1
\end{aligned}$$

Only interband terms have significant contributions to denominators and intraband are eliminated through $v_f q << \omega$.

$$\Gamma = \int\int \frac{d^2\vec{k}_1}{(2\pi)^2}\left(\left(\frac{1}{2v_f k_1 - \omega_2 - i\gamma} + \frac{1}{-2v_f k_1 + \omega_1 - i\gamma}\right)\frac{\mu_{34}v_{41}v_{13}}{-\omega_3 - i\gamma}\right)$$
$$- \int\int \frac{d^2\vec{k}_1}{(2\pi)^2}\left(\left(\frac{1}{2v_f k_1 - \omega_2 - i\gamma} + \frac{1}{-2v_f k_1 + \omega_1 - i\gamma}\right)\frac{\mu_{21}v_{14}v_{42}}{-\omega_3 - i\gamma}\right)$$

In these expressions, the negative signs have been removed from the denominator involving μ as has the coefficient of $\frac{1}{(2\pi)^2}$; these will be reflected in the coefficients in front of the integral. Also taking the approximation $\omega_1 \sim \omega_2$, the integral becomes

$$\frac{\Gamma}{(2\pi)^2} = \int\int d^2\vec{k}_1\left(\left(\frac{1}{2v_f k_1 - \omega_1 - i\gamma} + \frac{1}{-2v_f k_1 + \omega_1 - i\gamma}\right)\frac{\mu_{34}v_{41}v_{13}}{\omega_3 + i\gamma}\right)$$
$$- \int\int d^2\vec{k}_1\left(\left(\frac{1}{2v_f k_1 - \omega_1 - i\gamma} + \frac{1}{-2v_f k_1 + \omega_1 - i\gamma}\right)\frac{\mu_{21}v_{14}v_{42}}{\omega_3 + i\gamma}\right),$$

setting $\omega_1 - 2v_f k_1 = z$

$$\frac{\Gamma}{(2\pi)^2} = \int\int d^2\vec{k}_1\left(\left(\frac{1}{z - i\gamma} + \frac{1}{-z - i\gamma}\right)\frac{\mu_{34}v_{41}v_{13}}{\omega_3 + i\gamma}\right) - \int\int d^2\vec{k}_1\left(\left(\frac{1}{z - i\gamma} + \frac{1}{-z - i\gamma}\right)\frac{\mu_{21}v_{14}v_{42}}{\omega_3 + i\gamma}\right),$$
$$\frac{\Gamma}{(2\pi)^2} = \int\int d^2\vec{k}_1\left(\left(\frac{1}{z - i\gamma} + \frac{1}{-z - i\gamma}\right)\left(\frac{\mu_{34}v_{41}v_{13}}{\omega_3 + i\gamma} - \frac{\mu_{21}v_{14}v_{42}}{\omega_3 + i\gamma}\right)\right).$$

Now, one can evaluate the velocity operators. Remembering the integration over all space in the Bra-Ket is taken into account purely through the phasematching

conditions applied.

$$
\begin{aligned}
v_{nm} &= \langle n| \, v_f \sigma \, |m\rangle \\
v_{nm} &= \frac{v_f}{2}(\psi_n^\dagger \sigma_x \psi_m) \\
v_{nm} &= \frac{v_f}{2}\begin{bmatrix} s_n & e^{-i\phi_1} \end{bmatrix}\begin{bmatrix} 0 & 1 \\ 1 & 0 \end{bmatrix}\begin{bmatrix} s_m \\ e^{i\phi_1} \end{bmatrix} \\
v_{nm} &= \frac{v_f}{2}(s_n e^{i\phi_1} + s_m e^{-i\phi_1})
\end{aligned}
$$

As all v operations of interest are interband the band indices ($s_{n,m}$) are inverted giving us

$$
\begin{aligned}
v_{nm}^{inter} &= \pm\frac{v_f}{2}(e^{i\phi_1} - e^{-i\phi_1}) \\
v_{nm} &= \pm v_f(i\sin\phi_1) \\
v_{41} &= +iv_f \sin\phi_1 \\
v_{13} = v_{24} &= -iv_f \sin\phi_1
\end{aligned}
$$

$$
\frac{\Gamma}{(2\pi)^2} = \int\int d^2\vec{k}_1 \left(\left(\frac{1}{z - i\gamma} + \frac{1}{-z - i\gamma} \right) \frac{-(iv_f \sin\phi_1)^2}{\omega + i\gamma} (\mu_{32} - \mu_{21}) \right)
$$

For the μ terms one again assumes, like the velocity operators, that the integral over all space has been performed to account for phase matching conditions.

$$
\begin{aligned}
\mu_{21} &= \frac{i\hbar e}{\epsilon_1 - \epsilon_2} \langle 2| \, v_f \sigma \, |1\rangle \\
\mu_{21} &= \frac{i\hbar e}{\hbar\omega_{12}} \langle 2| \, v_f \sigma \, |1\rangle \\
\mu_{21} &= \frac{ie}{v_f q \cos\phi_1} \langle 2| \, v_f \sigma \, |1\rangle \\
\mu_{21} &= \frac{ie}{v_f q \cos\phi_1} v_{21} \\
v_{21} &= \frac{v_f}{2}(-e^{i\phi_1} - e^{-i\phi_1}) \\
v_{21} &= -v_f \cos\phi_1 \\
\mu_{21} &= -\frac{ie}{q}
\end{aligned}
$$

Following the same derivation one achieves $\mu_{34} = \frac{ie}{q}$.

$$\frac{\Gamma}{(2\pi)^2} = \int\int d^2\vec{k}_1 \left(\left(\frac{1}{z - i\gamma} + \frac{1}{-z - i\gamma} \right) \frac{-(iv_f \sin\phi_1)^2}{\omega + i\gamma} (\frac{2ie}{q}) \right) \tag{5.10}$$

$$\tag{5.11}$$

Again, the constants not involved in the integration are removed for simplicity and also $\frac{1}{z-i\gamma} + \frac{1}{-z-i\gamma} = \frac{2i\gamma}{z^2+\gamma^2}$ is substituted.

$$\frac{\Gamma}{(2\pi)^2} \frac{q(\omega + i\gamma)}{2ie} = \int\int d^2\vec{k}_1 \left(\frac{2i\gamma}{z^2 + \gamma^2} \sin^2\phi_1 \right)$$
$$\frac{\Gamma}{(2\pi)^2} \frac{q(\omega + i\gamma)}{2ie} = \int \sin^2\phi_1 d\phi_1 \int \frac{2i\gamma}{z^2 + \gamma^2} k_1 dk_1$$

Next, the term in k_1 is investigated, as the sin term will be a constant.

$$\Xi = \int \frac{2i\gamma}{z^2 + \gamma^2} k_1 dk_1$$
$$\left(k_1 = \frac{z + \omega_1}{2v_f}; \qquad dk_1 = \frac{dz}{2v_f} \right)$$
$$\Xi = \frac{2i\gamma}{(2v_f)^2} \int \frac{z + \omega_1}{z^2 + \gamma^2} dz$$
$$\Xi = \frac{2i\gamma}{(2v_f)^2} \int \left(\frac{z}{z^2 + \gamma^2} + \frac{\omega_1}{z^2 + \gamma^2} \right) dz$$

Looking at this term, one notes that in the denominator of the original expression is the term $z - i\gamma$, this will resonant and provide the greatest contribution when $z \sim 0$. Since the integral is known to resonate around $z = 0$, one can ignore the first term in

the integrand, and the integral approximates to

$$\begin{aligned}
\Xi &\approx \frac{2i\gamma}{(2v_f)^2}\int \frac{\omega_1}{z^2+\gamma^2}dz \\
\Xi &\approx \frac{2i\gamma}{(2v_f)^2}\left(\frac{\omega_1}{\gamma}\left[\arctan\left(\frac{z}{\gamma}\right)\right]_{k_1=k_f}^{k_1=\infty}\right) \\
\Xi &= \frac{2i\gamma}{4v_f^2}\frac{\omega_1}{\gamma}\left(\arctan(-\infty)-\arctan\left(\frac{\omega_1-2v_fk_f}{\gamma}\right)\right) \\
\Xi &= -\frac{2i\gamma}{4v_f^2}\frac{\omega_1}{\gamma}\left(\frac{\pi}{2}+\arctan\left(\frac{\omega_1-2v_fk_f}{\gamma}\right)\right).
\end{aligned}$$

Next, the removed coefficients are restored, the approximation $\omega + i\gamma \sim \omega$ is substituted and g, a degeneracy factor incorporating both spin and valley degeneracy is introduced (generally taken to be 4 as each aspect is two fold degenerate).

$$\chi^{(2)}_{xxx} \sim \left(\frac{ge^2}{\hbar^2\omega_a\omega_a}\right)\frac{1}{(2\pi)^2}\frac{(iv_f)^2}{\omega}\frac{2ie}{q}\pi\frac{-2i\gamma}{4v_f^2}\frac{\omega_a}{\gamma}\left(\frac{\pi}{2}+\arctan\left(\frac{\omega_a-2v_fk_f}{\gamma}\right)\right),$$

here $\chi^{(2)}_{xxx}$ represents the tensor nature of susceptibility in general, but that only the component of field generated along the $\hat{x}$- axis from electric fields oscillating parallel to this is relevant here. This work seeks to obtain a magnitude of $\chi^{(2)}_{xxx}$ so the phase is also removed.

$$|\chi^{(2)}_{xxx}| \sim \frac{ge^3}{4\pi\hbar^2\omega_1\omega_3 q}\left(\frac{\pi}{2}+\arctan\left(\frac{\omega_1-2v_fk_f}{\gamma}\right)\right) \tag{5.12}$$

This result is a factor of 2 different from the result quoted in Equation(5) of Yao [14]. However there are no clear steps to follow in that manuscript and one seeks an order of magnitude estimate. There are two points to note here. The first is that this result does not actually contain the resonance when phasematched to the plasmon - that resonance is in the field generated at the phasematched conditions from the nonlinear susceptibility. The second, as has been discussed, is that this result has a dependence inversely proportional to q the in-plane wavevector component, creating a divergence in the response at normal incidence. This will be discussed in detail in Section 5.5.3.

5.5.3 The transition dipole moment

The transition dipole moment is, this work concludes, the heart of the problem with this derivation. It is this which yields the divergence at small q and whilst the origin of this problem is still unclear, the result is clearly non-physical. The transition dipole moment is expressed by Equation(4) of Yao [14] and in SI units is as follows,

$$\vec{\mu}_{sk,s'k'} = e.\langle s,\vec{k}|\,\vec{r}\,|s',\vec{k}'\rangle = \frac{i\hbar e}{\epsilon_{s',k'}-\epsilon_{s,k}}\langle s,\vec{k}|\,v_f\vec{\sigma}\,|s',k'\rangle\,. \tag{5.13}$$

This replacement is not directly explained by Yao [14] but the derivation of this is as follows.

$$\begin{aligned}
G &= \langle s,\vec{k}|\,[\hat{H},\vec{r}]\,|s',\vec{k}'\rangle \\
G &= \langle s,\vec{k}|\,\hat{H}\vec{r}\,|s',\vec{k}'\rangle - \langle s,\vec{k}|\,\vec{r}\hat{H}\,|s',\vec{k}'\rangle \\
G &= \langle s,\vec{k}|\,\epsilon\vec{r}\,|s',\vec{k}'\rangle - \langle s,\vec{k}|\,\vec{r}\epsilon'\,|s',\vec{k}'\rangle \\
G &= (\epsilon-\epsilon')\,\langle s,\vec{k}|\,\vec{r}\,|s',\vec{k}'\rangle\,, \qquad (5.14)\\
& \qquad (5.15)
\end{aligned}$$

and the solution to the same operation through the 2D Pauli spin matrix vector ($\vec{\sigma} = \sigma_x\hat{x}+\sigma_y\hat{y}$) is

$$\begin{aligned}
G &= \langle s,\vec{k}|\,[\hat{H},\vec{r}]\,|s',\vec{k}'\rangle \\
G &= \langle s,\vec{k}|\,[v_f\vec{\sigma}.\vec{p},\vec{r}]\,|s',\vec{k}'\rangle \\
G &= \sum_i v_f\,\langle s,\vec{k}|\,[\sigma_i p_i, r_i]\,|s',\vec{k}'\rangle \\
G &= \sum_i v_f\,\langle s,\vec{k}|\,\sigma_i[p_i, r_i]\,|s',\vec{k}'\rangle \\
G &= \sum_i v_f\,\langle s,\vec{k}|\,(-\sigma_i i\hbar)\,|s',\vec{k}'\rangle \\
G &= \langle s,\vec{k}|\,(-i\hbar v_f\vec{\sigma})\,|s',\vec{k}'\rangle\,. \qquad (5.16)\\
& \qquad (5.17)
\end{aligned}$$

If one combines Equations 5.14 and 5.16

$$-i\hbar \langle s,\vec{k}|\, v_f\vec{\sigma}\, |s',\vec{k}'\rangle = (\epsilon-\epsilon')\, \langle s,\vec{k}|\, \vec{r}\, |s',\vec{k}'\rangle \tag{5.18}$$

$$\langle s,\vec{k}|\, \vec{r}\, |s',\vec{k}'\rangle = \frac{i\hbar}{\epsilon'-\epsilon}\, \langle s,\vec{k}|\, v_f\vec{\sigma}\, |s',\vec{k}'\rangle \tag{5.19}$$

For the purpose of this work, this replacement leads to the divergence, as the final term is inversely proportional to the energy difference of the two states involved in the transition. It is important to also consider the boundary conditions assumed by Yao. The relevant condition stated is that the frequency of DFG oscillation is much less than the associated frequency of the Fermi velocity momentum product ($\omega \gg v_f q$), implying that this result is valid only for small wavevectors and consequently small energy differences which is where the divergence occurs.

To avoid this divergence, one must focus the derivation on the conductivity of the graphene sheet as opposed to susceptibility, eliminating the transition dipole moment from the calculation. This revised derivation is explained in Section 5.5.4

5.5.4 Conductivity

This derivation was instigated through discussions with collaborators Dr. David Zhaozhe Li and Prof. Darrick Chang. The final derivation was completed by D.Z. Li who also wrote most of the mathematical derivation for the related paper[17].

The interaction of a vector potential $\vec{A}$ with an electron in a crystal potential $V(\vec{r})$, with Hamiltonian $\hat{H} = \hat{\vec{p}}^2/2m + V(\vec{r})$, can be incorporated into $\hat{H}$ via the substitution $\hat{\vec{p}} \to \hat{\vec{p}} + e\vec{A}$, where $\hat{\vec{p}}$ is the canonical momentum and e is the elemental charge. For graphene the Hamiltonian is typically taken to be of a tight-binding model, and the Peierls substitution [182] formally enables one to incorporate $\vec{A}$ into such a model without the need to actually solve for the eigenstates of $\hat{H}$ with the replacement $\hat{\vec{p}} \to \hat{\vec{p}} + e\vec{A}$. The tight-binding Hamiltonian of graphene with $\vec{A}$ thus reads:

$$\hat{H} = \mathcal{T} \sum_{i=1,\ldots,N} \left(\hat{a}^\dagger_{\vec{R}_i} \hat{a}_{\vec{R}_i} + \hat{b}^\dagger_{\vec{R}_i+\vec{\tau}_1} \hat{b}_{\vec{R}_i+\vec{\tau}_1} \right) - \mathcal{T}' \sum_{\substack{i=1,\ldots,N \\ l=1,2,3}} \left(e^{\mathrm{i}\frac{e}{\hbar}\vec{A}\cdot\vec{\tau}_l}\, \hat{a}^\dagger_{\vec{R}_i} \hat{b}_{\vec{R}_i+\vec{\tau}_l} + e^{-\mathrm{i}\frac{e}{\hbar}\vec{A}\cdot\vec{\tau}_l}\, \hat{b}^\dagger_{\vec{R}_i+\vec{\tau}_l} \hat{a}_{\vec{R}_i} \right). \tag{5.20}$$

Here $\mathcal{T}$ and $\mathcal{T}'$ are the diagonal and nearest-neighbour off-diagonal matrix elements of the Hamiltonian respectively in the basis of atomic orbitals in absence of $\vec{A}$; $(\hat{a}_{\vec{R}_i}, \hat{a}^\dagger_{\vec{R}_i})$ and $(\hat{b}_{\vec{R}_i+\vec{\tau}_l}, \hat{b}^\dagger_{\vec{R}_i+\vec{\tau}_l})$ are annihilation and creation operators for the two sublattices in graphene, with $\vec{R}_i$, $i = 1, ..., N$ denoting the sublattice sites, and τ_l, $l = 1, 2, 3$ denoting the vectors from a lattice site to its three nearest neighbours (see Figure 3.1 of Chapter 3 for clarification). The current density operator can then be obtained by $\hat{\vec{j}}\left(\vec{R}_i\right) = \partial\hat{H}/\partial\vec{A}$ [183].

In weak electromagnetic (EM) fields, both $\hat{H}$ and $\hat{\vec{j}}$ can be expanded in terms of $\vec{A}$. $\hat{H}$ can be broken into a non-interacting part $\hat{H}_0$ and an interacting part $\hat{H}_I$, with $\hat{H}_I = \hat{H}_I^{(1)} + \hat{H}_I^{(2)} + \cdots$ and the superscripts indicating the order of $\vec{A}$:

$$\hat{H}_0 = \mathcal{T} \sum_{i=1,...,N} \left(\hat{a}^\dagger_{\vec{R}_i}\hat{a}_{\vec{R}_i} + \hat{b}^\dagger_{\vec{R}_i+\vec{\tau}_1}\hat{b}_{\vec{R}_i+\vec{\tau}_1}\right) - \mathcal{T}' \sum_{\substack{i=1,...,N \\ l=1,2,3}} \left(\hat{a}^\dagger_{\vec{R}_i}\hat{b}_{\vec{R}_i+\vec{\tau}_l} + \hat{b}^\dagger_{\vec{R}_i+\vec{\tau}_1}\hat{a}_{\vec{R}_i}\right), \tag{5.21}$$

$$\hat{H}_I^{(1)} = -\mathrm{i}\frac{e\mathcal{T}'}{\hbar} \sum_{\substack{i=1,...,N \\ l=1,2,3}} \vec{A}\left(\vec{R}_i, t\right)\cdot\vec{\tau}_l \left(\hat{a}^\dagger_{\vec{R}_i}\hat{b}_{\vec{R}_i+\vec{\tau}_l} - \hat{b}^\dagger_{\vec{R}_i+\vec{\tau}_l}\hat{a}_{\vec{R}_i}\right), \tag{5.22}$$

$$\hat{H}_I^{(2)} = \frac{e^2\mathcal{T}'}{2\hbar^2} \sum_{\substack{i=1,...,N \\ l=1,2,3}} \left[\vec{A}\left(\vec{R}_i, t\right)\cdot\vec{\tau}_l\right]^2 \left(\hat{a}^\dagger_{\vec{R}_i}\hat{b}_{\vec{R}_i+\vec{\tau}_l} + \hat{b}^\dagger_{\vec{R}_i+\vec{\tau}_l}\hat{a}_{\vec{R}_i}\right). \tag{5.23}$$

and similarly $\hat{\vec{j}} = \hat{\vec{j}}_0 + \hat{\vec{j}}^{(1)} + \hat{\vec{j}}^{(2)} + \cdots$:

$$\hat{\vec{j}}_0\left(\vec{R}_i\right) = \mathrm{i}\frac{e\mathcal{T}'}{\hbar} \sum_{l=1,2,3} \vec{\tau}_l \left(\hat{a}^\dagger_{\vec{R}_i}\hat{b}_{\vec{R}_i+\vec{\tau}_l} - \hat{b}^\dagger_{\vec{R}_i+\vec{\tau}_l}\hat{a}_{\vec{R}_i}\right), \tag{5.24}$$

$$\hat{\vec{j}}^{(1)}\left(\vec{R}_i\right) = -\frac{e^2\mathcal{T}'}{\hbar^2} \sum_{l=1,2,3} \left[\vec{A}\left(\vec{R}_i, t\right)\cdot\vec{\tau}_l\right] \vec{\tau}_l \left(\hat{a}^\dagger_{\vec{R}_i}\hat{b}_{\vec{R}_i+\vec{\tau}_l} + \hat{b}^\dagger_{\vec{R}_i+\vec{\tau}_l}\hat{a}_{\vec{R}_i}\right), \tag{5.25}$$

$$\hat{\vec{j}}^{(2)}\left(\vec{R}_i\right) = -\mathrm{i}\frac{e^3\mathcal{T}'}{2\hbar^3} \sum_{l=1,2,3} \left[\vec{A}\left(\vec{R}_i, t\right)\cdot\vec{\tau}_l\right]^2 \vec{\tau}_l \left(\hat{a}^\dagger_{\vec{R}_i}\hat{b}_{\vec{R}_i+\vec{\tau}_l} - \hat{b}^\dagger_{\vec{R}_i+\vec{\tau}_l}\hat{a}_{\vec{R}_i}\right). \tag{5.26}$$

Crucially, the Peierls substitution yields terms in Equations 5.23, 5.25 and 5.26, which cannot be obtained by replacing $\hat{\vec{p}}$ with $\hat{\vec{p}} + e\vec{A}$ in the Dirac Hamiltonian, as done in previous works [15, 184, 185] (see Section 5.5.5). At the Dirac points, one can perform a Fourier expansion on the operators $(\hat{a}_{\vec{R}_i}, \hat{a}^\dagger_{\vec{R}_i})$ and $(\hat{b}_{\vec{R}_i+\vec{\tau}_l}, \hat{b}^\dagger_{\vec{R}_i+\vec{\tau}_l})$ in the tight-binding Hamiltonian in terms of the operators in the reciprocal lattice space:

$$\hat{a}_{\vec{R}_i} = \frac{1}{\sqrt{N}} \sum_{\vec{k}\in\Omega_B} \hat{a}_{\vec{k}}\, e^{\mathrm{i}\vec{k}\cdot\vec{R}_i}, \quad \text{and} \quad \hat{b}_{\vec{R}_i+\vec{\tau}_l} = \frac{1}{\sqrt{N}} \sum_{\vec{k}\in\Omega_B} \hat{b}_{\vec{k}}\, e^{\mathrm{i}\vec{k}\cdot\left(\vec{R}_i+\vec{\tau}_l\right)}, \tag{5.27}$$

in which Ω_B denotes the first Brillouin zone, $\vec{k}$ is the electron momentum and N is the number of sites in one sublattice. One can then substitute these expansions into the expressions of the Hamiltonian Equations. 5.21-5.23 and current density operators Equations 5.24-5.26. As usual, near the two Dirac points $\vec{K}$ and $-\vec{K}$ [186], the operators can be expanded in orders of $\vec{k}$ referenced from $\vec{K}$ or $-\vec{K}$: $\vec{k} \mp \vec{K} \rightarrow \vec{k}$. One can then derive equivalent spinor forms for Equations 5.21-5.26 in the first quantisation picture. If only the terms to lowest order of $\vec{k}$ are kept, then

$$\hat{H}_0 \rightarrow v_F \hat{\vec{\sigma}} \cdot \hat{\vec{p}} \quad \text{at } \vec{K}, \quad \text{and} \quad -v_F \hat{\vec{\sigma}}^* \cdot \hat{\vec{p}} \quad \text{at } -\vec{K}, \tag{5.28}$$

in which the Fermi velocity $v_F = \sqrt{3}a\mathcal{T}'/2\hbar$, with a being the lattice constant of the underlying sublattices, and $\hat{\vec{\sigma}} \equiv \hat{\sigma}_x \hat{x} + \hat{\sigma}_y \hat{y}$ with $\hat{\sigma}_{x,y}$ representing the Pauli spin matrices. Meanwhile, for $\hat{H}_I$:

$$\hat{H}_I^{(1)} \rightarrow \pm e v_F A(\vec{r}, t) \hat{\sigma}_x, \tag{5.29}$$

with "+" at $\vec{K}$ and "−" at $-\vec{K}$, and for simplicity one assumes $\vec{A}$ is along the x-axis. The second order component is meanwhile given by

$$\hat{H}_I^{(2)} \rightarrow -\frac{e^2 a^2 \mathcal{T}'}{8\hbar^2} \frac{A_1 A_2^*}{4} e^{\mathrm{i}(qx-\omega t)} \hat{\sigma}_x, \tag{5.30}$$

at both $\vec{K}$ and $-\vec{K}$, where $\vec{A}$ has been taken to be in the form

$$\vec{A}\,(\vec{r}, t) = (1/2) \sum_{m=1,2} \left[A_m \hat{x}\, e^{\mathrm{i}(q_m x - \omega_m t)} + \text{c.c.} \right], \tag{5.31}$$

where q_m is the in-plane component of the momentum and only kept the terms that give rise to a perturbation at $\omega = \omega_1 - \omega_2$ and $q = q_1 - q_2$ (DFG). For $\hat{H}_0$ one finds that the single-particle eigenenergies $\mathcal{E}_s = s v_F \hbar k$ and eigenstates are

$$\psi_{\vec{k}s} = \frac{1}{\sqrt{2\xi}} e^{\mathrm{i}\vec{k}\cdot\vec{r}} \chi_s, \quad \text{with} \quad \chi_s = \begin{pmatrix} 1 \\ s e^{\mathrm{i}\theta_{\vec{k}}} \end{pmatrix} \text{ at } \vec{K}, \quad \text{and} \quad \chi_s = \begin{pmatrix} -s e^{\mathrm{i}\theta_{\vec{k}}} \\ 1 \end{pmatrix} \text{ at } -\vec{K}. \tag{5.32}$$

Here $s = \pm 1$ is the band index, ξ is the area of the graphene sheet, and $\theta_{\vec{k}}$ is the polar angle of $\vec{k}$. Similarly, the spinor forms of the current densities can be found as

$$\hat{\vec{j}}_0(\vec{r}) \to -ev_F\hat{\vec{\sigma}} \quad \text{at } \vec{K}, \quad \text{and} \quad ev_F\hat{\vec{\sigma}}^* \quad \text{at } -\vec{K}, \tag{5.33}$$

$$\hat{j}_x^{(1)} \to \frac{e^2a^2\mathcal{T}'}{4\hbar^2}A(\vec{r},t)\hat{\sigma}_x \text{and} \quad \hat{j}_x^{(2)} \to \pm\frac{e^3a^2v_F}{32\hbar}A_1A_2^*e^{\mathrm{i}(qx-\omega t)}\hat{\sigma}_x \quad \text{“+” at } \vec{K} \text{ and “}-\text{” at } -\vec{K}. \tag{5.34}$$

The expectation value of the current density in the presence of the fields can be calculated as $\langle\hat{\vec{j}}\rangle = \mathrm{Tr}\left(\hat{\rho}\,\hat{\vec{j}}\right)$, where $\hat{\rho}$ is the (self-consistent) single-particle density matrix. The matrix elements can be calculated by using the time evolution equation $\mathrm{d}\hat{\rho}/\mathrm{d}t = (\mathrm{i}/\hbar)\left[\hat{\rho}, \hat{H}_0 + \hat{H}_I\right]$ and solving the density matrix $\hat{\rho} = \sum_n \hat{\rho}^{(n)}$ perturbatively in powers of $\hat{H}_I$.

5.5.5 Linear conductivity

In previous works calculating graphene conductivities using the vector potential [15, 184, 185], the authors typically replace $\hat{\vec{p}}$ by $\hat{\vec{p}} + e\vec{A}$ in the Dirac Hamiltonian. However, the linear current thus calculated has a term that diverges when the integration limit of the electronic momenta is taken to be infinity. This issue was fixed in [184] by adding an artificial quadratic term to the Dirac Hamiltonian. In this section it is shown that when both Equations 5.24 and 5.25 are included in the calculation this problematic term is cancelled and one automatically obtains the correct form for the linear conductivity, thus no artificial term needs to be introduced to regularize the calculation.

To begin with one considers the current response to an in-plane electric field described by a vector potential $\vec{A}(\vec{r},t) = (1/2)A\,\hat{x}\,e^{\mathrm{i}(\vec{q}\cdot\vec{r}-\omega t)} + \text{c.c.}$, where $\vec{q} = q\hat{x}$. The current generated at $\vec{q}$ and ω is calculated through the expectation value of $\hat{j}_x(\vec{q}) = 2/\xi\, e^{-\mathrm{i}qx}\,\hat{j}_x(\vec{r})$, applied to the density matrix

$$\langle\hat{j}_x(\vec{q})\rangle = \mathrm{Tr}\left(\hat{\rho}\,\hat{j}_x(\vec{q})\right) \approx \sum_{n,m}\rho_{nm}^{(1)}j_x^{(0)}(\vec{q})_{mn} + \rho_{nm}^{(0)}j_x^{(1)}(\vec{q})_{mn}, \tag{5.35}$$

where the superscripts (0), (1), ... denote the order of $\vec{A}$ included in the terms. According to Equation 5.2, the first-order density matrix is given by

$$\rho_{nm}^{(1)}(t) = \frac{eAv_F}{2\hbar}\frac{f_m - f_n}{\omega - \omega_{nm} + i\gamma}\langle n|\,\hat{\sigma}_x e^{iqx}\,|m\rangle\, e^{-i\omega t}. \tag{5.36}$$

The matrix elements of the current density operators can be obtained by using Equations 5.32-5.34. Now, one can substitute these results into Equation 5.35. Then the summation of states is replaced by an integral over Bloch momenta $\vec{k}$, introducing an upper bound on the range of integration $k < k_c$ (which approximately captures the edge of the Brillouin zone). The first term of Equation 5.35 becomes

$$\sum_{n,m}\rho_{nm}^{(1)}\, j_x^{(0)}\,(\vec{q})_{mn} = \frac{e^2 Av_F}{8\pi\hbar}e^{-i\omega t}\left\{2\,(k_c - k_F) + \frac{\omega}{2v_F}\left[\ln\frac{\omega + 2\omega_F}{|\omega - 2\omega_F|} + i\pi\,\Theta\,(\omega - 2\omega_F)\right]\right\}, \tag{5.37}$$

where k_F is the Fermi wavevector. If k_c is extended to infinity like in a free-electron gas, Equation 5.37 will yield a divergent linear current, as discussed by Wang [184]. The second term gives zero. Next This strong dependence on k_c is shown to be cancelled by the lowest order non-zero contribution to the second term. The linear current density operator Equation 5.25 is expanded to first order of $\vec{k}$, and obtain an additional term to $\hat{j}_x^{(1)}$ in Equation(5.34) which is labelled as $\hat{j}_x^{(1)'}$:

$$\hat{j}_x^{(1)'} = \frac{e^2a^2}{4\hbar^2}v_F A(\vec{r},t)\left(\pm\hat{\sigma}_x\hat{p}_x + \frac{1}{3}\hat{\sigma}_y\hat{p}_y\right), \tag{5.38}$$

where "+" or "−" sign corresponds to the Dirac point $\vec{K}$ or $-\vec{K}$. Now the second term in Equation 5.35 becomes:

$$\sum_{n,m}\rho_{nm}^{(0)}\, j_x^{(1)'}\,(\vec{q})_{mn} = -\frac{e^2Av_F}{8\pi\hbar}e^{-i\omega t}\frac{a^2\left(k_c^3 - k_F^3\right)}{9}. \tag{5.39}$$

One notes $k_F \ll k_c$ and $a^2k_F^3 \ll k_F$, thus Equation 5.39 cancels with the k_c term in Equation 5.37 at $k_c = 3\sqrt{2}/a \approx \left|\vec{K}\right|$, the edge of the Brillouin zone[187]. An exact calculation beyond the Dirac cone approximation would also result in the same qualitative cancellation and a small correction depending on the details of the entire band structure.

Eliminating A by $\vec{E} = -\partial\vec{A}/\partial t$ in the expression of $\langle \hat{j}_x(\vec{q}) \rangle$, using the definition $\vec{j} = \sigma^{(1)}\vec{E}$ where $\sigma^{(n)}$ denotes the nth order conductivity, and multiplying by the valley and spin degeneracy factor of 4, one finally reaches

$$\sigma^{(1)}(\omega) = \frac{e^2}{\hbar}\left[\frac{1}{4}\Theta(\omega - 2\omega_F) + \frac{\mathrm{i}}{\pi}\left(\frac{\omega_F}{\omega} + \frac{1}{4}\ln\frac{|\omega - 2\omega_F|}{\omega + 2\omega_F}\right)\right], \tag{5.40}$$

which is in agreement with the result derived by various other theoretical approaches, *e.g.* using a scalar potential [188]. One sees that both $\hat{\tilde{j}}_0$ and $\hat{\tilde{j}}^{(1)}$ (Equations 5.24 and 5.25) play an important role in obtaining the correct linear conductivity; they are actually analogous to the paramagnetic and diamagnetic parts of current respectively in the case of free electrons coupled to a vector potential. However the replacement $\hat{\vec{p}} \to \hat{\vec{p}} + e\vec{A}$ in the Dirac Hamiltonian would only yield the "paramagnetic" part and therefore give incorrect result for the linear current. Thus the Dirac Hamiltonian is insufficient when using a vector potential and one has to start with the original tight-binding Hamiltonian. The issue with using a vector potential with the Dirac Hamiltonian has been known before, as was pointed out in the works studying optical sum rules [186, 187].

This work considers the nonlinear current in response to the EM fields described by $\vec{A}(\vec{r}, t) = (1/2)\sum_{m=1,2}\left[A_m \hat{x}\, e^{\mathrm{i}(q_m x - \omega_m t)} + \text{c.c.}\right]$, at difference frequency $\omega_3 = \omega_1 - \omega_2$ and wavevector $q_3 = q_1 - q_2$. Similar to Equation 5.35 the nonlinear current can be calculated using the density matrix as

$$\langle \hat{j}_x(\vec{q}_3) \rangle = \mathrm{Tr}\left(\hat{\rho}\,\hat{j}_x(\vec{q}_3)\right) \approx \sum_{n,m} \rho^{(0)}_{nm}\, j^{(2)}_x(\vec{q}_3)_{mn} + \rho^{(1)}_{nm}\, j^{(1)}_x(\vec{q}_3)_{mn} + \rho^{(2)}_{nm}\, j^{(0)}_x(\vec{q}_3)_{mn}, \tag{5.41}$$

Using Equations 5.32 and 5.34, one finds the first term in Equation 5.41 vanishes due to the angular integral. For the second term in the summation, one notes using Equations 5.32, 5.34 and 5.36 that $j^{(1)}_x(\vec{q}_3)_{mn}$ flips sign at $\vec{K}$ and $-\vec{K}$ whilst $\rho^{(1)}_{nm}$ stays the same, thus the two contributions at $\vec{K}$ and $-\vec{K}$ cancel. There are two distinctive contributions to the matrix element $\rho^{(2)}_{nm}$ in the third term: there is one contribution coming from the nonlinear vector potential interaction Equation 5.30, which when acting upon the equilibrium density matrix $\hat{\rho}^{(0)}$ (see Equation 5.2) produces density

matrix $\hat{\rho}^{(2)}$ oscillating at the difference frequency:

$$\rho^{(2)}_{nm}(t) = -\frac{e^2A^2t}{32\hbar^2}A_1A_2^*\frac{f_m - f_n}{\omega - \omega_{nm} + \mathrm{i}\gamma}\langle n|\,\hat{\sigma}_x e^{\mathrm{i}qx}\,|m\rangle\, e^{-\mathrm{i}\omega_3 t}. \tag{5.42}$$

This term flips sign at $\vec{K}$ and $-\vec{K}$, while $j_x^{(0)}(\vec{q}_3)_{mn}$ does not. Thus the two contributions at $\vec{K}$ and $-\vec{K}$ cancel. There is a further contribution coming from the frequency 1(2) component in the linear interaction Equation 5.29 acting upon $\hat{\rho}^{(0)}$ through Equation 5.2 to generate a first order perturbation $\hat{\rho}^{(1)}$, and then the frequency 2(1) component in $\hat{H}_I^{(1)}$ acting upon $\hat{\rho}^{(1)}$, and generating a nonlinear perturbation $\hat{\rho}^{(2)}$ at the difference frequency. Using Equations 5.29, 5.2, and 5.36 one gets

$$\begin{aligned}\rho^{(2)}_{nm}(t) = \frac{e^2v_F^2A_1A_2^*}{4\hbar^2}e^{-\mathrm{i}\omega_3 t}\frac{1}{\omega_3 - \omega_{nm} + \mathrm{i}\gamma} \\ \times\sum_l\left(\frac{f_m - f_l}{-\omega_2 - \omega_{lm} + \mathrm{i}\gamma} - \frac{f_l - f_n}{\omega_1 - \omega_{nl} + \mathrm{i}\gamma}\right) \\ \times\langle n|\,\hat{\sigma}_x e^{\mathrm{i}q_1x}\,|l\rangle\,\langle l|\,\hat{\sigma}_x e^{-\mathrm{i}q_2x}\,|m\rangle\,,\end{aligned} \tag{5.43}$$

and the reverse whe $q_1 \leftrightarrow -q_2, \omega_1 \leftrightarrow -\omega_2$. One can then carry out the summation in Equation 5.41. All band combinations need to be considered $(s_n, s_m, s_l = \pm 1)$. The summation can be transformed to an integral, which in general needs to be evaluated numerically. However one can also expand the kernel in terms of q_3, and extract the leading order contributions. Under the experimental conditions of both [181] and [35]: (i.e. $\omega_3 < \omega_F \ll \omega_1 \approx \omega_2$), one obtains

$$\langle\hat{j}_x^{(2)}(\vec{q})\rangle = -\frac{e^3v_F^2A_1A_2^*}{2\pi\hbar^2}\left(\frac{q_3}{\omega_3}\right)\frac{\omega_F^4}{\left(\omega_3^2 - 4\omega_F^2\right)\omega_2^2} \quad ; \tag{5.44}$$

where the current contribution at $-\vec{K}$ is the same. Thus, changing the potentials to electric fields, using the definition $\langle\hat{j}_x^{(2)}(\vec{q}_3)\rangle = \sigma^{(2)}E_1E_2^*$, and introducing the spin and valley degeneracy factor of 4, one finally reaches

$$\sigma^{(2)}(\omega_3, q_3) \approx -\frac{2e^3v_f^2}{\pi\hbar^2}\left(\frac{q_3}{\omega_3}\right)\frac{\omega_F^4}{(\omega_3^2 - 4\omega_f^2)}\omega_2^4, \tag{5.45}$$

wherein $(\omega, v)_F$ are the Fermi angular frequency and velocity.

5.6 Comparison to field

5.6.1 Other theoretical works

Yao[14] was the first to derive the nonlinear conductivity in graphene relevant to DFG. In Figure 5.3, this derived second order nonlinear response (Equation(5) of Yao [14] converted to $\sigma^{(2)}$) is plotted along with experimental results from Constant [35], recent perturbative calculations [184] and this work's Equation 5.45. It is important to note first that the results of Wang [184] and Cheng [185] strongly agree with this work's own, suggesting this is the correct prediction from perturbation theory (in addition Tokman [15] and Rostami [189] achieve the same result except a factor of 2 which may be due to definitions not clearly identified). However, there is a rather large discrepancy between Equation 5.45 and the model derived by Yao [14], which were derived for identical conditions using perturbation theory. Moreover, the conductivity derived by Yao [14] has a non-physical divergence for $q_3 \to 0$ as discussed in Section 5.5.3. While the origin has not been clearly identified (beyond its root in the transition dipole moment), in a centrosymmetric material such as graphene this behavior is paradoxical. Meanwhile, the conductivity from Equation 5.45 tends to zero as $q_3 \to 0$, as it must in graphene due to symmetry arguments. Depending on the value of q_3 in Figure 5.3, the magnitude of $\sigma^{(2)}$ predicted by Equation 5.45 is at least 4 orders lower than that found by Yao [14].

Only Rostami [189] predicted a response similar to that of Constant[35], however Rostami showed that this agreement was only possible when invoking an extremely low decay rate (noted as "formally divergent"). This low decay rate is itself non-phsyical and also results in extraordinarily narrow resonances as can be seen in Figure 8 of [189].

5.6.2 Experimental work

The first experimental signatures attributed to DFG of plasmons were found by Constant[35]. In this experiment, by illuminating the graphene with two tunable, femtosecond laser pulses ("pump" and "probe") with well-defined angles of incidence but different frequencies, Constant[35] was able to phase-match to the plasmon. The geometry of the experiment is the same as that chosen for our theoretical

calculation defined in Figure 5.1. The graphene supports tightly guided plasmons with a dispersion relation $\omega_{pl}(k)$. The differential reflectance of the probe pulse ΔR was seen to change significantly whenever the difference frequency and wavevector were aligned to the plasmon dispersion relation, $\omega_{pl}(\vec{k}_1 - \vec{k}_2) = \omega_1 - \omega_2$, suggesting efficient plasmon excitation via DFG. In practice, a range of difference frequencies and wavevectors were scanned by continuously varying the pump wavelength, and by choosing different discrete incident beam angles.

TABLE 5.1: Differential reflectivity, normalized to pump fluence Φ, and experimentally determined $\sigma^{(2)}$ extracted using the model of [35] for three geometries (a), (b) and (c). For all geometries $\lambda_{probe} =$ 615.73nm.

Geometry	θ_{pump}	θ_{probe}	λ_{pump} nm	$\frac{\omega_3}{2\pi}$ THz	$\frac{\Delta R}{R\Phi}$ ($mJ^{-1}cm^2$)	$\sigma^{(2)}$ ($fAmV^{-2}$)
(a)	45^o	55^o	607	7.0	-0.0097	24
(b)	50^o	70^o	597	15.3	-0.025	75
(c)	125^o	15^o	587	23.8	0.062	180

Constant investigated three experimental geometries (noted in Table 5.1) with different angles of incidence, θ. One of the resonant conditions is examined for each of the three experimental geometries, as defined in Table 5.1. Assuming the differential reflection signals arise from DFG, one can use the model introduced in the Supplementary Information of Constant[35] to estimate a value for $\sigma^{(2)}$ for each measurement. The results of this analysis, i.e. values of $\sigma^{(2)}$ which describe the experimental signals, are also shown in Table 5.1.

Figure 5.3 compares the experimental values of $\sigma^{(2)}$ from Constant[35] and theoretical predictions from Equation(5.45), Wang[184] and X. Yao[14]. Firstly, the q_3 dependence of Yao[14] clearly differs greatly from that of both the experiment and the near-linear predictions of other theoretical derivations. The experimental magnitudes of $\sigma^{(2)}$ are also significantly lower than the prediction of X. Yao[14], and several orders higher than those from recent perturbative works[15, 185, 184].

To date, Rostami[189] is the only other theoretical work (excluding Yao[14]) to predict a similar response for graphene, and only by invoking an unphysically low decay rate for the plasmon (resulting in extraordinarily narrow resonances with a FWHM $\ll 1nm$). More recently, a similar experiment has been carried out by

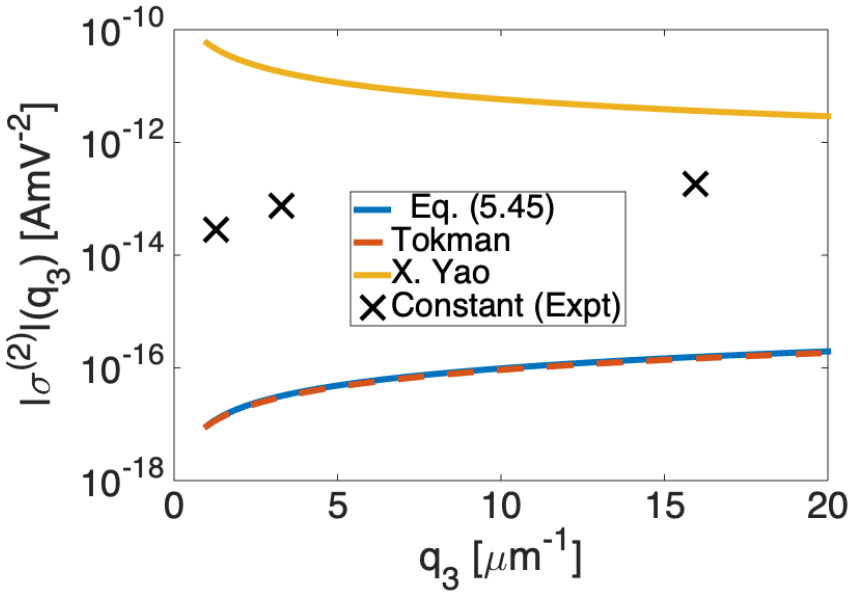

FIGURE 5.3: Comparison of the nonlinear conductivity $\sigma^{(2)}(\omega_3, q_3)$ derived here from Equation(5.45) with other results derived using perturbation theory: Equation(5) from X. Yao[14]. All theoretical curves are plotted for a Fermi energy of 500meV and difference frequency of 15.3THz. [Experimental estimates from Constant[35], for the different experimental geometries (a), (b), (c) (Table. 5.1) are indicated by black crosses.]

B. Yao[181] in a waveguiding geometry, and the theory from X. Yao[14] was used to model the experimental signals. While the geometries of B. Yao[181] and Constant[35] are significantly different, similar signals were observed in each experiment. Therefore, ignoring the nonphysical results in X. Yao[14], the large discrepancy between both experiments and the theoretical consensus points to a second order response that is not purely perturbative, as originally interpreted. Therefore other possible contributions which might account for the discrepancy between perturbation theory and the experiments of B. Yao[181] and Constant[35] have to be considered.

5.7 Alternative explanations

5.7.1 Substrate response

The first consideration to solving this discrepancy is to consider how the experimental system differs, if at all, from the theoretical model. Clearly the presence of a substrate is one such difference of note, and could contribute to the second order

response. This work therefore first sought to model response that could come from the substrate. This derivation was made and presented by Prof. Darrick Chang and is placed here for completeness of the investigative process.

This section considers the contribution of the second order nonlinearity of the quartz substrate used in experiment[35]. The analysis significantly simplifies if the nonlinear polarization is generated far from a phase-matching condition of the bulk, and depletion (the reduction of beam intensity due to the investigated processes) can be ignored, as should be the situation for Constant[35]. In this case, the pump and probe fields generate a polarization in quartz, given by

$$P_3(\vec{r},t) = \epsilon_0 \chi^{(2)} e^{i\left[(\vec{k}_{T1}-\vec{k}_{T2})\cdot\vec{r}-(\omega_1-\omega_2)t\right]} t_1 t_2^* E_{I1} E_{I2}^*, \tag{5.46}$$

where $\chi^{(2)}$ is the second order susceptibility of the substrate, $\vec{k}_{Ti}$, t_i, and E_{Ii} denote the wavevector on the transmitted (substrate) side, transmission coefficient, and the incident field amplitude of the pump ($i = 1$) and the probe ($i = 2$) fields respectively. The transmission coefficients t_i are given in Appendix A. The subscript $i = 3$ indicates quantities corresponding to the difference frequency signal at $\omega_3 = \omega_1 - \omega_2$. As charge density waves in graphene are driven by an electric field, one must relate the nonlinear polarization to the field generated in the quartz, which satisfies the wave equation

$$-\nabla^2 E_{3s} + \frac{\epsilon_3}{c^2}\frac{\partial^2 E_{3s}}{\partial t^2} = -\mu_0 \frac{\partial^2 P_3}{\partial t^2}. \tag{5.47}$$

Here, the subscript "s" denotes that this is an effective source field that will later drive a response in the graphene (distinct from the resulting plasmon field). Also, $\epsilon_3 = n(\omega_3)^2$ indicates the permittivity of quartz evaluated at the difference frequency, with the model of the frequency dependent $n(\omega)$ given in the Appendix A. Due to the plane-wave nature of P_3, E_{3s} takes on the same spatial and frequency dependence. In our regime of interest, the spatial derivative of the field, $|\nabla^2 E_{3s}| = |\vec{k}_{T1} - \vec{k}_{T2}|^2 E_{3s}$, is significantly larger than the time derivative. This is because the pump and probe fields are chosen to phase-match with surface plasmons in graphene (thus the associated wavevectors are much larger than free-space fields at the difference frequency). Thus the field amplitude created by the nonlinear polarization is

well approximated by

$$E_{3s} \approx \frac{(\omega_1 - \omega_2)^2}{c^2 |\vec{k}_{T1} - \vec{k}_{T2}|^2} \chi^{(2)} t_1 t_2^* E_{I1} E_{I2}^* . \tag{5.48}$$

In particular, it should be noted that a large wavevector mismatch results in strong suppression of the field. To simplify the discussion, one considers the scenario which produces the highest field, i.e. in which E_{3s} is completely polarized along $\hat{x}$ (parallel to the graphene sheet) so that it maximally drives a charge density wave in graphene. As shown below, even in this best case scenario, the generated field is rather small.

Since the nonlinear response is considered here to be completely within the substrate, which provides an effective source field E_{3s}, the remaining part of the calculation is completely linear in its nature. Using the conventions in Figure 5.1, one takes "reflected" and "transmitted" field components of unknown amplitude, which correspond to the plasmon field on the vacuum and substrate sides. The wavevector along $\hat{x}$ for these fields is equal to $q_3 = q_{T1} - q_{T2}$, where q_{T1} and q_{T2} are the in-plane components of $\vec{k}_{T1}$ and $\vec{k}_{T2}$, while the perpendicular components must satisfy the respective dispersion relations for each side of the interface, *e.g.*, $k_{T3z}^2 = \epsilon_3 (\omega_3/c)^2 - q_3^2$. Similar to the procedures to solve the pump (probe) field laid out in the methods, the two unknown field amplitudes can be readily solved by taking E_{3s} to be the incident field on the substrate side, and enforcing electromagnetic boundary conditions at the vacuum-graphene-quartz interface, which yields the following parallel-field component on the substrate side, evaluated at the graphene layer ($z = 0$),

$$E_{pl} = -E_{3s} \frac{(c\epsilon_0 + \sigma^{(1)}(\omega_3) \sin\theta_3) \sin\phi_3}{c\epsilon_0 \sin\phi_3 + \sin\theta_3 (c\epsilon_0 n_3 + \sigma^{(1)}(\omega_3) \sin\phi_3)} . \tag{5.49}$$

Here, $\sigma^{(1)}(\omega_3)$ is the linear conductivity of graphene evaluated at frequency ω_3.

Specifically one can numerically evaluate E_{pl} for geometry (b) in [35]. Taking a value of $\chi^{(2)} = 0.3\,\mathrm{pmV}^{-1}$ for quartz [190], one finds that $E_{pl} \approx 15\,\mathrm{Vm}^{-1}$. The modelling in [35] predicts a considerably larger value for the inferred plasmon field in experiment of $\approx 8 \times 10^4\,\mathrm{Vm}^{-1}$. Therefore it is concluded that the substrate nonlinearity contributes significantly to the signals observed in [35]. However, one notes that this substrate model does not consider any surface enhanced nonlinearity. Its

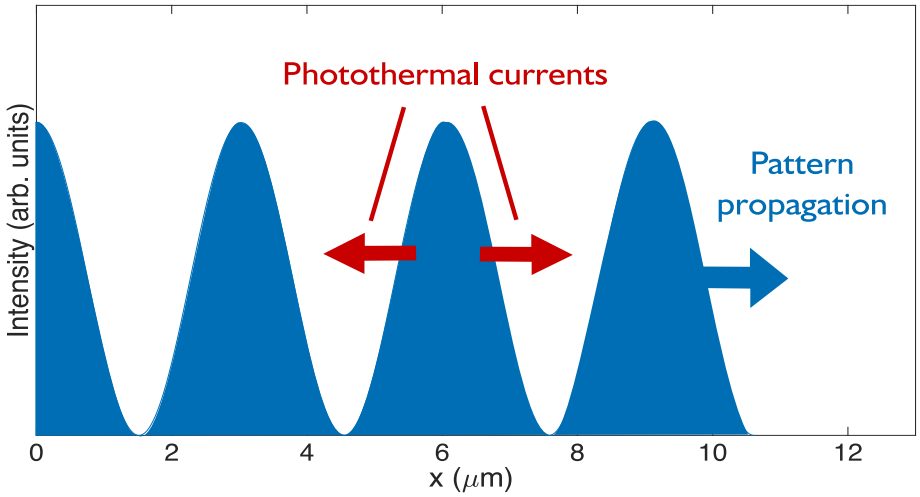

FIGURE 5.4: Intensity pattern generated from the interference of two beams in geometry (b) ($\theta_{pump} = 70^o$, $\theta_{probe} = 50^o$, $\lambda_{pump} = 587$nm, $\lambda_{probe} = 617.53$nm). The temperature gradient in the sample follows this pattern and generates photothermal currents when thermalising. The pattern propagates, phase-matched to the difference frequency field, with wavevector $q_3 = q_1 - q_2$. This intensity pattern exhibits the same distribution as the AC temperature component of Equation 5.53.

theoretical modelling would require experimental measurements of surface nonlinear coefficients relevant to our system, which is not readily available in the literature.

5.7.2 Photothermal effects

It is known that excitation of graphene carriers by intense femtosecond pulses ($\Phi \approx 0.1\text{mJcm}^{-2}$ with pulse width $\sim$ 100fs in [35]) is not perturbative in nature. The electron temperature is raised by several thousand kelvin under such excitation[191] and is not in equilibrium with the phonon temperature. Furthermore, under geometries similar to those used in B. Yao[181] and Constant[35], heating due to optical illumination is not homogeneous. When two or more light sources of similar frequency are incident on an interface at oblique angles, the result will be a near stationary interference pattern such as that shown in Figure 5.4. When the frequencies are slightly different, the pattern will propagate in the plane with a velocity equal to ω_3/q_3.

The pattern shown in Figure 5.4 represents a spatial distribution of electron temperatures, which must necessarily thermalise, upon thermalising this pattern will

give rise to real currents by at least two possible mechanisms which are the photo-Dember effect and the Seebeck effect. When developing this theory the Seebeck effect was a better quantified effect in graphene among the literature so this effect was modelled. Therefore the expected response of a current generated via the Seebeck effect is derived.

5.7.3 Modelling the Seebeck effect

The Seebeck model was initially conceptualised by Prof. Euan Hendry and expanded through discussions with Justus Bohn and the author. It was further extended to the final derivation by Dr. David Li.

The intensity pattern imprinted on the graphene sheet can be expressed as

$$\begin{aligned} I(x,t) =& \frac{c\epsilon_0}{2}\left|E_{1x}\, e^{\mathrm{i}(q_1 x-\omega_1 t)} + E_{2x}\, e^{\mathrm{i}(q_2 x-\omega_2 t)}\right|^2 \\ \approx& \frac{c\epsilon_0 |E_{1x}|^2}{2}\left[1+2\left|\frac{E_{2x}}{E_{1x}}\right|\cos(q_3 x-\omega_3 t)\right] + \mathcal{O}\left(E_{2x}^2\right). \end{aligned} \tag{5.50}$$

Here E_{1x} and E_{2x} are the in-plane components of the pump and probe fields respectively, and the probe field is assumed to be much weaker than the pump field. The ratio of the in-plane components can be calculated as

$$|E_{2x}/E_{1x}| = (t_2^{(L)}\sin\phi_2)/(t_1^{(L)}\sin\phi_1)\sqrt{I_2/I_1}, \tag{5.51}$$

with I_1 and I_2 being the incident intensities of the pump and probe beams respectively, and the linear transmission coefficient $t_i^{(L)}(i=1,2)$ is given in Appendix A considering only the linear optical conductivity of graphene. Using the parameters in the experiment of Constant[35], one obtains $|E_{2x}/E_{1x}| \approx 0.1$.

The intensity pattern acts as a heat source for the temperature distribution which, in linear response theory, satisfies a diffusion equation:

$$\frac{\partial T}{\partial t} - \alpha\frac{\partial^2 T}{\partial x^2} = \beta I(x,t) - y(T-T_0), \tag{5.52}$$

where α is the diffusivity, β is the heating rate due to the intensity pattern, and y is the relaxation rate back to the equilibrium temperature T_0. Due to the linearity of

the equation, it can be readily solved in the Fourier domain, in which when taking into account Equation 5.50 the solution takes the form

$$T(x,t) = T_0 + T_{dc} + T_{ac}\cos(q_3 x - \omega_3 t - \Psi). \tag{5.53}$$

Here, T_{dc} is the (large) position- and time-independent temperature increase arising from the incident lasers, while T_{ac} represents a position- and time-varying temperature oscillation that must necessarily be generated in the presence of moving intensity interference pattern. Ψ denotes a phase offset between the intensity and temperature modulations, whose specific form is not relevant here. Substituting $T(x,t)$ into Equation 5.52, in the regime of interest $y \ll \omega_3$, one obtains $|T_{ac}|/T_{dc} \approx 0.2\,y/\omega_3$. As expected, the temperature modulation T_{ac} is reduced significantly as the oscillation frequency ω_3 increases with respect to the damping rate. It is known that intense, femtosecond pulses similar to those in [35] lead to T_{dc} of approximately 2000 K[191]. The relaxation rate y is due to electron-phonon scattering, and a value of $y \approx 1/(100\,\text{fs})$[191] is taken. At $\omega_3 = 2\pi \times 10$ THz these parameters give a temperature modulation $T_{ac} = 60$ K.

The Seebeck effect enables the generation of a source current in the presence of a temperature gradient, and this can be described by $j_s(\omega_3, q_3) = \sigma^{(1)}(\omega_3) q_3 S\,|T_{ac}|$, where S is called the Seebeck coefficient. In principle, the Seebeck coefficient could be frequency and wavevector dependent. However, this dependence has not been measured carefully in literature, nor is it straightforward to calculate from first principles. There have been several measurements of the Seebeck effect in graphene, both in DC experiments ($S \approx 5 \times 10^{-5}$ V/K [192], $S \approx 8 \times 10^{-5}$ V/K [193]) and under illumination from 100 fs pulses (S $\approx 10^{-4}$ V/K [194]). Whilst it is hard to predict how the Seebeck effect behaves on 10 fs timescales relevant here (corresponding to peak to peak propagation time of the intensity pattern in Figure 5.4), it is likely that photothermal effects will be higher on ballistic timescales, as with other materials[195]. Here a conservative value of $S \approx 10^{-4}$V/K reported by Tielrooij [194] is used.

Now using the standard EM boundary conditions at the graphene layer (see Figure 5.1), with the aid of the charge continuity equation, one can find the relation between the electric fields and the surface current density at the difference frequency ω_3. Note now the Seebeck effect contribution needs to be added to the surface current density:

$$j_x(\omega_3, q_3) = \sigma^{(1)}(\omega_3) E_{3x} + j_s(\omega_3, q_3). \tag{5.54}$$

Then solving the equations of the boundary conditions (see Appendix A for more details), one obtains for the electric field at the difference frequency:

$$E_{3x} = -\frac{t_3^{(L)}}{2c\epsilon_0} \sigma^{(1)}(\omega_3) q_3 S \, |T_{ac}| \sin\phi_3, \tag{5.55}$$

where $t_3^{(L)}$ is the linear transmission coefficient at frequency and wavevector ω_3, q_3. For geometry (b) of Constant[35] one finds a magnitude of E_{3x}, when on plasmon resonances, of $E_{pl} \approx 2.3 \times 10^3$ V/m.

Just as the pump and probe fields can generate a plasmon field through the Seebeck effect, a back-action effect (involving Seebeck mixing of the plasmon and pump fields) results in a change of the probe differential reflectance. In principle, this could be rigorously calculated in a manner similar to above, but this would require knowledge of the Seebeck coefficient at *optical* frequencies, which has never been measured or calculated. However, one can nonetheless obtain an approximate value for the differential reflection, by exploiting conservation of energy. In particular, in steady state, the number of plasmons dissipated per unit time must equal the rate of photons removed from (added to) the pump (probe) beam. There are two contributions to the energy dissipation at the difference frequency: both the graphene layer and the substrate will exhibit absorption. For graphene, the power loss per unit area from absorption can be found by $P_g = (1/2)\,\mathrm{Re}\,\sigma^{(1)}(\omega_3)|E_{3x}|^2$[196]. In the experiment, the substrate itself (quartz) can provide a non-negligible loss, through coupling with phonons. The corresponding power loss per unit area can be calculated as $P_s = (\epsilon_0/2)\int_{-\infty}^{0} \mathrm{d}z\, \omega_3\, \mathrm{Im}\left[n^2(\omega_3)\right]\, |E_3|^2$, where this work's model for the frequency-dependent refractive index $n(\omega)$ is provided in the Methods. Then, the number of photons, at the difference frequency, absorbed per unit time and area

is $\Gamma_d = (P_g + P_s)/\hbar\omega_3$. At the individual photon level of a DFG process, an incoming pump photon breaks down to an outgoing probe photon and a plasmon, and therefore the number of plasmons created is also equal to the number of newly generated probe photons that enter either the reflected or transmitted beam. The number of photons per unit time and area in the incident probe beam is simply $\Gamma_{in} = I_2 \sin\theta_2/\hbar\omega_2$. Thus the order of magnitude of the differential reflectance of the probe beam can be estimated as $\Delta R/R \sim \Gamma_d/\Gamma_{in}$. For configuration (b) in Table 5.1, the peak differential reflectance, after normalizing to the fluence (0.1 mJ cm^{-2}) is estimated to be $\sim 7 \times 10^{-7}$ mJ^{-1}cm^2. Although the Seebeck effect and the electronic nonlinearity $\sigma^{(2)}$ are completely independent effects, nonetheless to facilitate a better comparison, one can ask what hypothetical value of nonlinear conductivity $\sigma_S^{(2)}$ would be required, in order to produce the same current as predicted from the Seebeck effect, i.e. $j_s = \sigma_S^{(2)} E_{1x} E_{2x}^*$. One finds a value of $\sigma_S^{(2)} \approx 3.1 \times 10^{-15}$AmV^{-2}.

5.8 Conclusions

The second order response of graphene has been a contentious issue for many years due to its forbidden nature. Until the work of Constant [35], there was little experimental work on graphene's second order response as many predicted it to be low. The almost simultaneous development of Yao's theory in 2014 [14], with the experimental work of Constant in 2015 [35], pushed the idea that this effect is stronger than first suspected. However, as more groups looked to verify the theoretical work of Yao it has become increasingly clear that Yao's prediction is too high [184, 15, 197]. Thus presenting a large discrepancy between the experimental results of Constant ($\sigma^{(2)} \approx 10^{-14} - 10^{-13}$AmV^{-2}) and physical theoretical models ($\sigma^{(2)} \approx 10^{-17}$AmV^{-2}).

This work was the first to address this problematic discrepancy and upon investigating it, lead to the first photothermal model of nonlinear effects in graphene. Whilst the model relies on many parameters that are either entirely unquantified, or difficult to measure and sample specific as discussed earlier, it provides a predicted response that is both physical and significantly higher than perturbative models by around two orders of magnitude ($\sigma^{(2)} \approx 3 \times 10^{-15}$AmV^{-2}).

This model provides a crucial step in understanding the unusually high second order response of graphene. Should one wish to harness graphene as a nonlinear material it is vital that the fundamental mechanism well understood, in order to optimise and investigate this effect appropriately. As such it is also crucial that what is not or very unlikely to be the fundamental cause is ruled out and this has seemingly been overlooked in this case until the work generated through this investigation. Photothermal effects are predicted to be strong in comparison to second order effects in graphene in part due to the inherent weakness of second order effects. However sample photo-excitation is affecting other nonlinear responses such as the measured $\chi^{(3)}$ in graphene [18].

The future of this model and other photothermal models depends on firmly establishing the fast cooling dynamics of graphene which is not well known. Once this is well characterised along with a samples second order response a more exact theory can be developed and put to test which may account for a more significant proportion of the graphene's nonlinear response than first predicted.

Chapter 6

Four-wave mixing in graphene

6.1 Impact

The work presented in this chapter discusses a possible cascaded response of graphene wherein one observes a four-wave mixing process that has an intermediate stage which is phasematched to the surface plasmon polariton in graphene. The work presented here shows conclusively that this cascaded effect is smaller than the four-wave mixing signal generated by the graphene sheet independent of phase matching. As such this no outputs were generated from this work beyond the work contained in this thesis. However, an estimation of the magnitude of $\chi^{(3)}$ is obtained to add to the body of work in the literature.

6.2 Motivation

The natural extension to Chapter 5 was to investigate the third order response of graphene. Additionally, the second order response of a centrosymmetric material such as graphene is forbidden within the dipole approximation [198], meaning any second order interaction is expected to be very weak. In contrast, the third order interaction is allowed in a centrosymmetric material, therefore it is possible that third order effects in graphene could be of similar size or even greater than second order.

The third order response of graphene is of great interest due to the possibility of cascaded effects. A cascaded effect is one which comprises two separate interactions, in this case a third order interaction can consist of two individual second order steps. In certain geometries cascaded third order interactions have been shown to be very

Supplementary Table

Third-order nonlinear optical processes	References	$\lvert\chi^{(3)}\rvert$ (m^2/V^2)
FWM	PRL 105, 097401 (2010)[18]	10^{-15}
	Nano Lett. 15, 4968 (2015)[19]	10^{-14}
THG	PRB 87, 121406 (2013)[17]	10^{-16}
	PRX 3, 021014 (2013)[20]	10^{-19}
	ACS Nano 7, 8441 (2013)[21]	10^{-15}
	2D Materials 4, 011006 (2016)[22]	10^{-19}
Optical Kerr effect, two-photon absorption and self-phase modulation	Nat. Photon. 6, 554 (2012)[23]	10^{-17}
	Nano Lett. 11, 2622 (2011)[24]	10^{-15}
	Opt. Lett. 37, 1856 (2012)[25]	10^{-13}
	Nano Lett. 11, 5159 (2011)[26]	10^{-15}
	Phys. Rev. Appl. 6, 044006 (2016)[27]	10^{-15}
	Opt. Lett. 41, 3281 (2016)[28]	10^{-15}

FIGURE 6.1: A table of measured values for graphene's $\chi^{(3)}$ in different systems. Table credit: Jiang [199]. The references here correspond to the original manuscript [199], in this work they are [200, 201, 202, 203, 204, 205, 206, 207, 208, 209, 153, 210] in descending order.

strong. When optimised, Smirnova [57] showed that the overall third order response could be enhanced by a factor of 5 through cascaded interactions.

This work set out with the goal of observing and quantifying resonant behaviour based on plasmon coupling within a four-wave mixing signal. This potential enhancement is investigated in the Fourier image of the four-wave mixing (FWM) light and its spatial pattern distribution in that plane. The literature shows great variation for the third order nonlinearity of graphene (see figure 6.1[199]), and seemingly very dependent on measurement setup. Therefore, it is also productive to quantify the third order response in this setup on and off resonance with the plasmon.

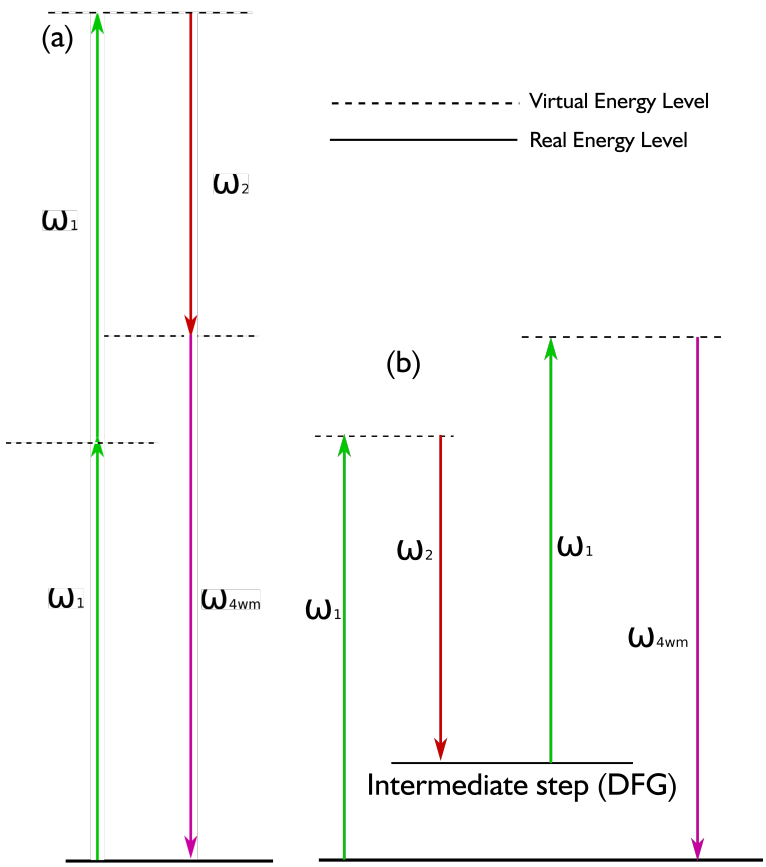

FIGURE 6.2: Energy level diagrams of two possible four-wave mixing combinations. Panel **a** represents a standard FWM process that takes place in a single interaction. Here the energy levels of intermediate states are virtual and the process is represented by a single $\chi^{(3)}$. Panel **b** represents the cascaded process that is formed of two independent interactions. Each interaction is represented by its own $\chi^{(2)}$, one for a difference frequency process and one for a sum frequency.

6.2.1 Cascaded third order effects

A cascaded effect is one in which the resultant signal is generated through multiple processes, in this case a four-wave mixing signal of frequency $2\omega_1 - \omega_2$ which is generated through a two step process. Firstly a difference frequency interaction generates a field at frequency $\omega_1 - \omega_2$, this is followed by a sum frequency process that results in a field at $2\omega_1 - \omega_2$. This process is illustrated in Figure 6.2.

Figure 6.2 demonstrates two processes resulting in the same FWM signal. In this case, Panel **a** shows the traditional FWM response through a single $\chi^{(3)}$ interaction, whilst Panel **b** represents a cascaded process of two second order interactions. This process is a real physical effect, however in an isolated system this contribution would be much smaller than the third order process, since it requires two separate

$\chi^{(2)}$ interactions. However, it is possible this interaction couples to a real energy level corresponding to the surface plasmon in graphene. Due to the plasmon coupling, the field generated at this intermediate level is enhanced, leading to an enhanced overall cascaded effect.

With any non-linear wave-mixing, the overlap of the pulses in time is crucial, and will have a large effect on the signal observed. When introducing an intermediate state one must take a similar consideration for the 'up-conversion' interaction. However, instead of the temporal overlap of the pulses, one must consider the lifetime of the intermediate state and the pulse length of the up-converting photon. For this experiment the pulse length is considered to be sufficiently short at $8ps$, as the lifetime of graphene plasmons is expected to be tens of picoseconds or more [211].

Cascaded effects have already been observed in graphene, with significant effective third order nonlinearities observed in wave-guide geometries [57]. As such, observing the FWM response of graphene, in particular one that is enhanced by a resonant plasmon mode, is a high priority for graphene nonlinear optics.

6.2.2 Fourier imaging of four-wave mixing

To illustrate the enhancement from a resonant process, ideally one should simultaneously image the resonant and non-resonant FWM signals. This is achieved by isolating the FWM signal from any incident beams (unlike many nonlinear experiments which measure the reflected probe beam e.g. [35]). In order to analyse phase-matching enhancement in the nonlinear signal, the signal is imaged in the Fourier plane. Fourier plane imaging is standard in optics, therefore only the concepts directly related to this experiment will be covered here. The entire experimental setup is described in Chapter 4.

Figure 6.3 shows a simple example of an imaging setup specifically relating the Fourier plane and the image plane. In essence, a lens, when considered at its focal lengths, will perform a Fourier transform on the beam. This means that while the image plane represents information about the spatial position of light sources from the image plane, the Fourier plane will represent the wavevectors of those light sources.

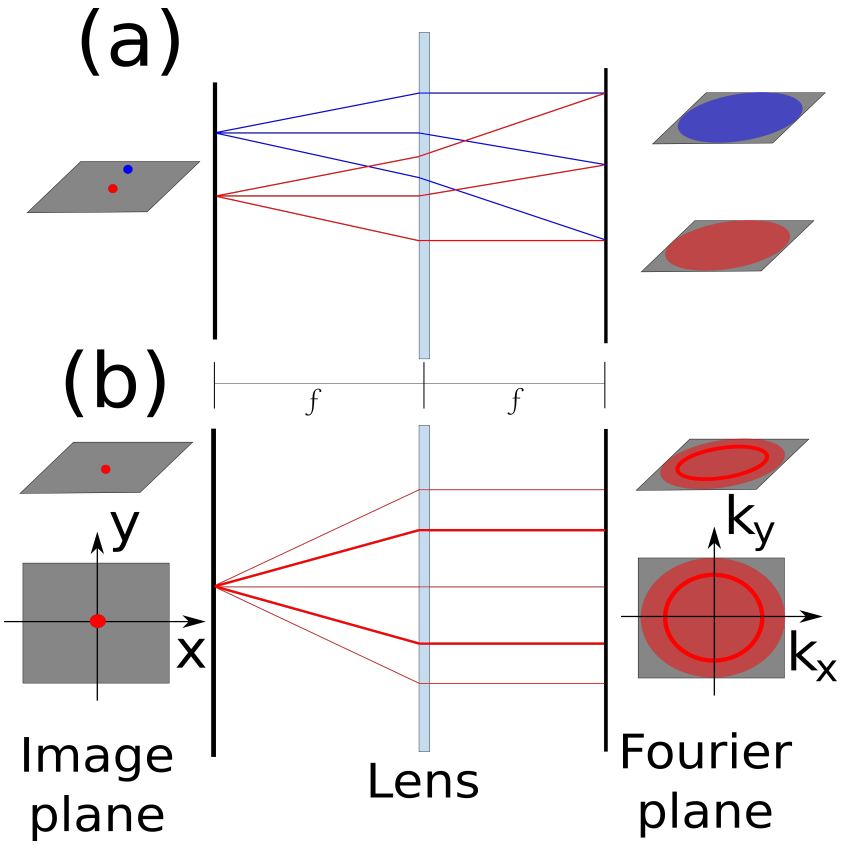

FIGURE 6.3: Representation of the Fourier transform applied through a lens. Panel **a** represents the two point sources located at different points in the image plane. Both points sources here are considered to emit uniformly in all directions. As shown in the Fourier plane, both point sources have identical spatial profiles in the Fourier plane, that is uniform distribution across all possible wavevectors. Panel **b** represents a single point source with an enhancement at a specified magnitude of wavevector, although independent of direction of that wavevector. In this case one observes a uniform distribution in the background with an enhanced ring at the specific wavevector.

As this process is symmetric, it can be exploited by patterning the beam at an objective lens to narrow the range of wavevectors in the illumination. This is discussed in Chapter 4.

6.2.3 Modelled expectations of a resonant process

The goal of this work is to measure the Fourier plane of a FWM signal, in particular one that is enhanced by a resonant second order state. Using three input signals to generate an output signal drastically increases the complexity of that signal's Fourier plane, as a result of wavevector combinations available. The Fourier plane contains a huge amount of information regarding the FWM signal, and thus it is crucial to simplify the measurement. The best way to do this is to limit the range of input wavevectors with the use of a mask. The mask creates a pattern on the back aperture of the microscope that defines the input wavevectors of the high frequency beam (ω_1), while the low frequency beam (ω_2) completely illuminates the back aperture creating a wide range of input wavevectors. This is represented in Figure 6.4 on the dispersion diagram for the investigated FWM process. Chapter 4 shows the full setup of the FWM experiment, including the mask used for the input beam.

Figure 6.4 shows two opposite wavevectors for the incident high frequency beam which is crucial for two reasons. Firstly, it allows the resultant FWM signal to lie within the light cone. If the mixing process were to use two photons of the same wavevector from the ω_1 source the resultant FWM field would not be able to propagate as it would have far too high a wavevector for the resultant frequency (illustrated by the translucent green arrow in Figure 6.4). Secondly, the only FWM signal that can be observed in the far field will be one where the wavevectors of the two ω_1 photons approximately cancel out in any enhanced FWM signal. This also simplifies the analysis as the resultant wavevector of the enhanced signal is equivalent to the wavevector of the ω_2 photon which coupled.

One can perform a FWM process as the convolution of the three input beams. The calculation is mathematically simplified if one uses the convolution theorem. The convolution theorem states that the convolution of two beams can be calculated

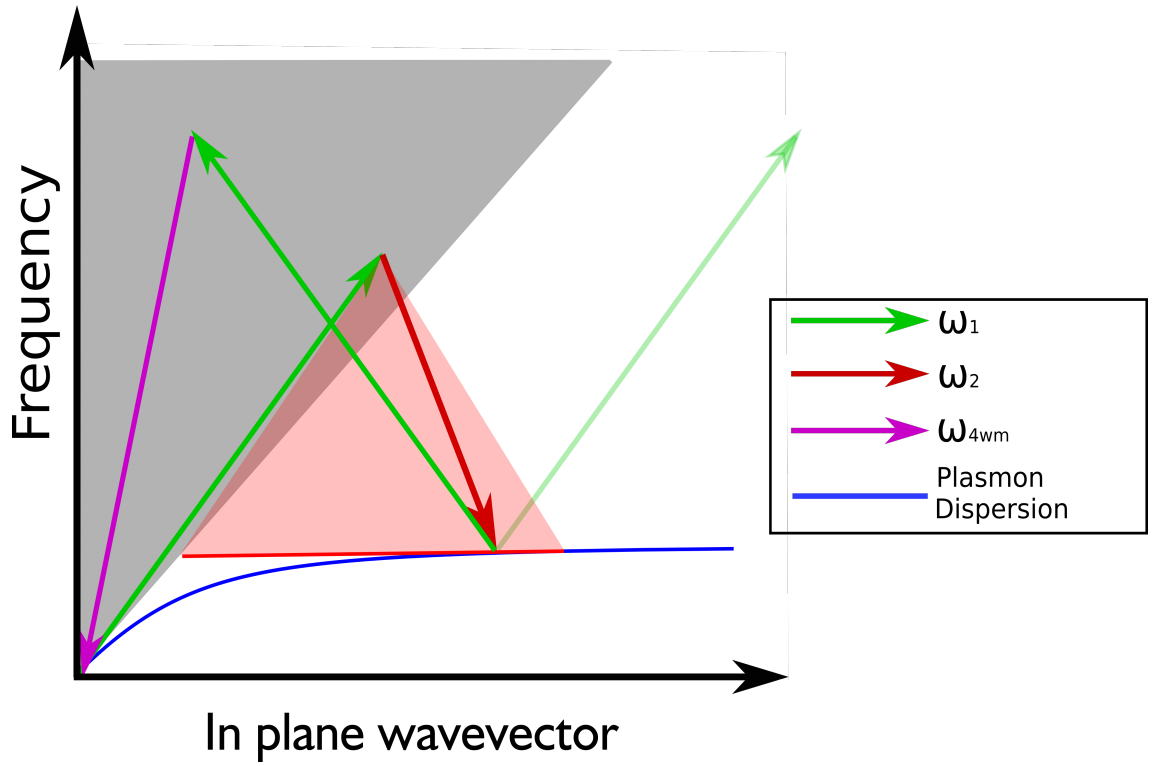

FIGURE 6.4: Dispersion diagram representing the experimental setup. The grey shaded region represents the light cone, that is combinations of frequency and wavevector that can propagate in free space and are not bound to a surface. The arrows represent the photons used in the experiment, as noted in the legend. The red triangle represents the range of photons available from the low frequency beam, with the solid red base representing the full range of coupled wavevectors. The solid red arrow shows and enhanced FWM signal when coupling to the surface plasmon dispersion. The translucent green arrow represents the final transition of a plasmon enhanced FWM process that is not allowed to propagate in the far field due to a high in-plane wavevector.

by the inverse Fourier transform of the pointwise product of their Fourier transforms. Mathematically for two arbitrary functions f and g one can state

$$f \circledast g = \mathcal{F}^{-1}\Big\{\mathcal{F}\{f\}.\mathcal{F}\{g\}\Big\},$$

where $\circledast$ represents the convolution and $\mathcal{F}$ represents the Fourier transform. This process can, in principle, be performed in frequency space or momentum space, here the momentum space calculation provides more information. This is because, as noted in Figure 6.4, we can couple to a range of wavevectors but only one frequency. In this form a FWM process is indistinguishable from a cascaded second order process as the pointwise multiplication is order invariant. In order to estimate an enhancement at the DFG step one can perform the convolution of two signals, then multiply by an enhancement matrix representing the plasmon, before once again convolving the signal with the third input, this is described in the following way

$$\begin{aligned} DFG &= \mathcal{F}^{-1}\Big\{\mathcal{F}\{S\}.\mathcal{F}\{I\}\Big\} \\ DFG_{en} &= \mathbf{P}.\mathcal{F}^{-1}\Big\{\mathcal{F}\{S\}.\mathcal{F}\{I\}\Big\} \\ FWM &= \mathcal{F}^{-1}\Big\{\mathcal{F}\{DFG_{en}\}.\mathcal{F}\{S\}\Big\} \\ &= \mathcal{F}^{-1}\left\{\mathcal{F}\left\{\mathbf{P}.\mathcal{F}^{-1}\Big\{\mathcal{F}\{S\}.\mathcal{F}\{I\}\Big\}\right\}.\mathcal{F}\{S\}\right\}, \end{aligned}$$

where DFG_{en} is the plasmon enhanced DFG field arising from the coupling to the surface plasmon represented by $\mathbf{P}$. The functional inputs are now labelled S and I to represent the signal and the idler beams.

One assumes the input signals to comprise a Gaussian beam backfilling the aperture, representing the idler beam, and two area of approximately uniform intensity, representing the masked signal beam. The matrices used for the calculations are displayed in Figure 6.5. One can now calculate the DFG response, and the enhanced response when coupling to the plasmon. Figure 6.6 shows the DFG field along with the plasmon enhancement matrix and the enhanced DFG field. The enhancement matrix is modeled with a maximal enhancement factor (EF) of 10, this corresponds to a rough estimation of the quality factor (Q-factor) of the plasmon in graphene, as

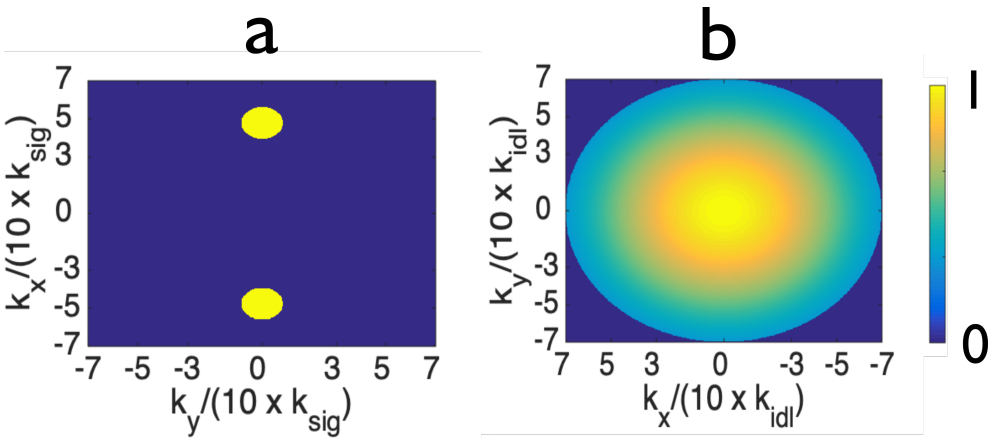

FIGURE 6.5: Input matrices used for the signal and idler beam considered at the back aperture of the microscope. The hard circular edge defines the back aperture of the microscope objective.

noted in Section 5.7.3. This enhancement then takes the form

$$EF = 1 + 9\cos\theta_{DFG} e^{-\frac{\sqrt{k_{DFG,x}^2 + k_{DFG,y}^2} - k_{plas}}{2\sigma}}, \tag{6.1}$$

where k_{plas} is the plasmon wavevector calculated from Equation 3.2, σ defines the linewidth, giving a FWHM of $\approx 0.4\mu m^{-1}$[1], and θ_{DFG} is the angle the wavevector to the vertical. The trigonometric term $\cos\theta_{DFG}$ accounts for the polarisation of the light, taking the TM projection of the incident intensity which can excite the plasmon.

The expectation of the FWM signal in the Fourier plane is displayed in Figure 6.7. In this representation one observes a background signal across the whole Fourier plane corresponding to a non-resonant FWM process. However at a specific wavevector (when coupling to the plasmon) there will be an enhancement in the FWM signal. The position of the enhanced signal in the Fourier plane can be predicted through knowledge of the plasmon dispersion in graphene and the incident beams (see Equation 3.2 in Chapter3). However, the result presented here is a figurative one to visually represent the expectation of FWM, and serves as a comparison for experimentally obtained Fourier images.

[1]This is a slightly larger value than Constant gives for the linewidth ($0.1\mu m^{-1}$)[35] for illustrative purposes

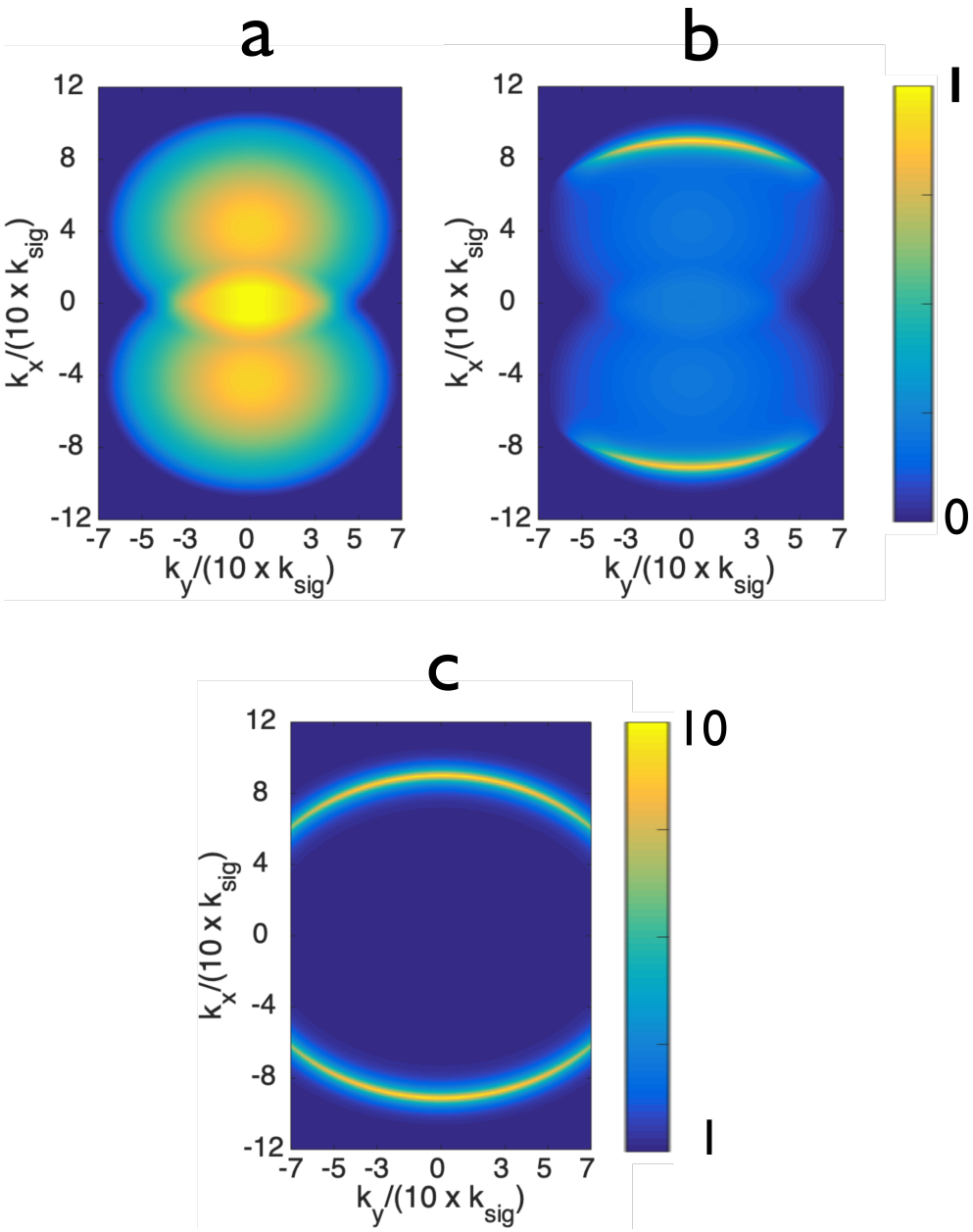

FIGURE 6.6: Images showing the plasmon enhancement of the DFG signal. Panel **a** shows the Fourier space distribution of DFG signal without enhancement. Panel **b** shows the signal when enhanced by the plasmon enhancement factor. Panel **a** and **b** are normalised to 1 as there has been no calculation of the absolute second order response, instead only the Fourier space profile is considered. Panel **c** shows the plasmon enhancement factor given by Equation 6.1, accounting for polarisation within the light.

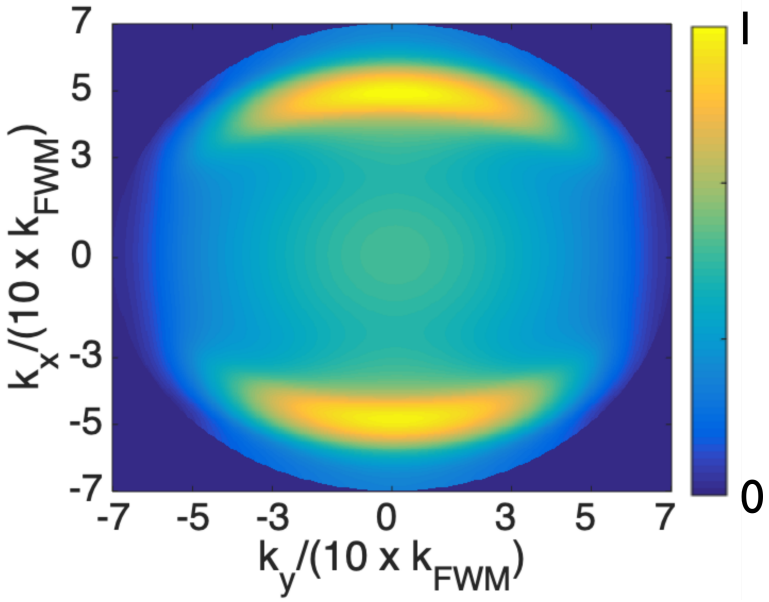

FIGURE 6.7: Four-wave mixing and input signals modelled in the Fourier plane. The colour axis represents normalised intensity in arbitrary units. This depiction represents the convolution on the enhanced DFG signal shown in Figure 6.6, with the original signal beam.

6.3 Results and discussion

6.3.1 FWM images

Figure 6.8 shows the Fourier image of the experiment at time overlap. The difference in the image comes from adjusting the scale to account for 'hot pixels' on the camera. 'Hot pixels' are artificially high signals from individual pixels on the camera's CCD array. As predicted in the modelling, there is an overall signal as well as an enhanced signal at specific wavevectors. However, when one attempts to account for background and isolate the FWM signal, it becomes apparent that a significant proportion of the signal in the Fourier plane is not FWM. This is illustrated in the Figure 6.9.

6.4 Nonlinear signal identification

6.4.1 Incident beam leaking

Figure 6.9 shows the nonlinear signal observed in the Fourier plane from the incident beams individually. Clearly there is signal generated during the experiment that is

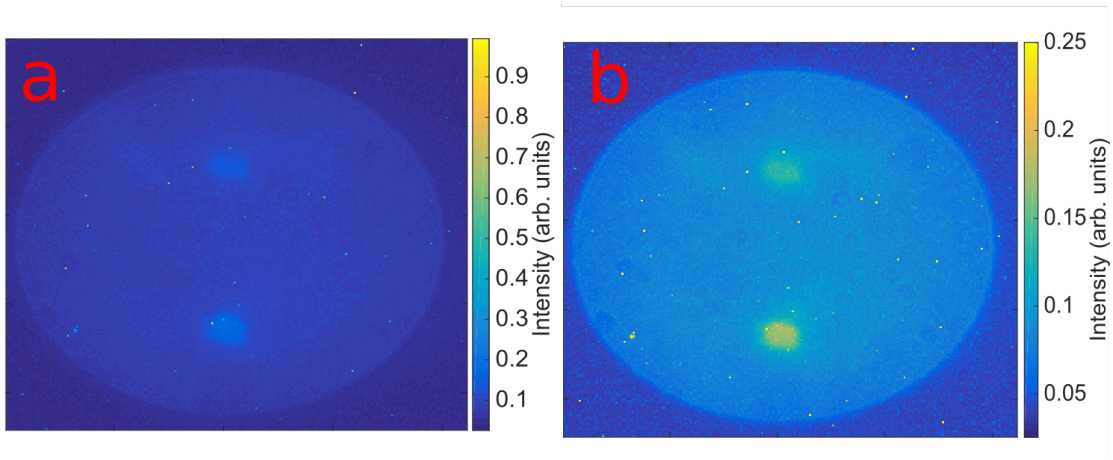

FIGURE 6.8: Camera image of FWM from exfoliated graphene. Panel **a** shows the captured FWM image from the camera, Panel **b** is the same image capped at an intensity of 0.25 (arbitrary units from camera response) to lessen the effect of 'hot pixels'. $\lambda_1 = 784nm$, $\lambda_2 = 828nm$, $\lambda_{FWM} = 744.1nm$.

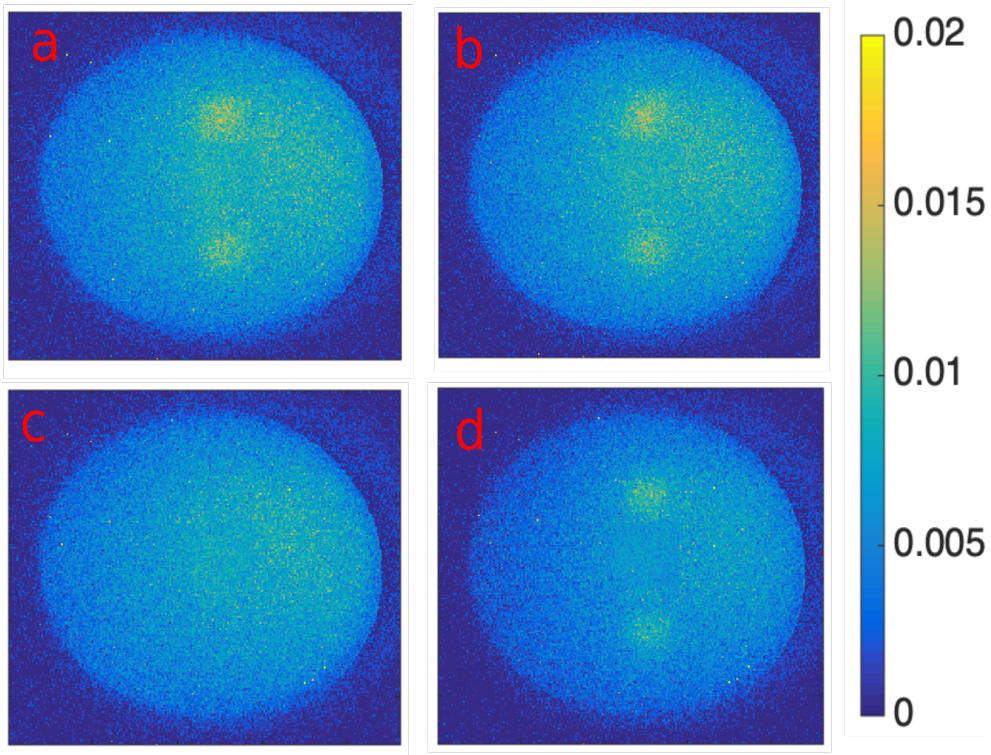

FIGURE 6.9: Images showing the breakdown of the nonlinear signal. Panel **a** shows the signal taken when the beams are overlapped in time, whereas Panel **b** is when the beams are not at time overlap. Panel **c** shows the nonlinear signal produced solely through the low frequency beam, Panel **d** is the signal produced from the high frequency beam.

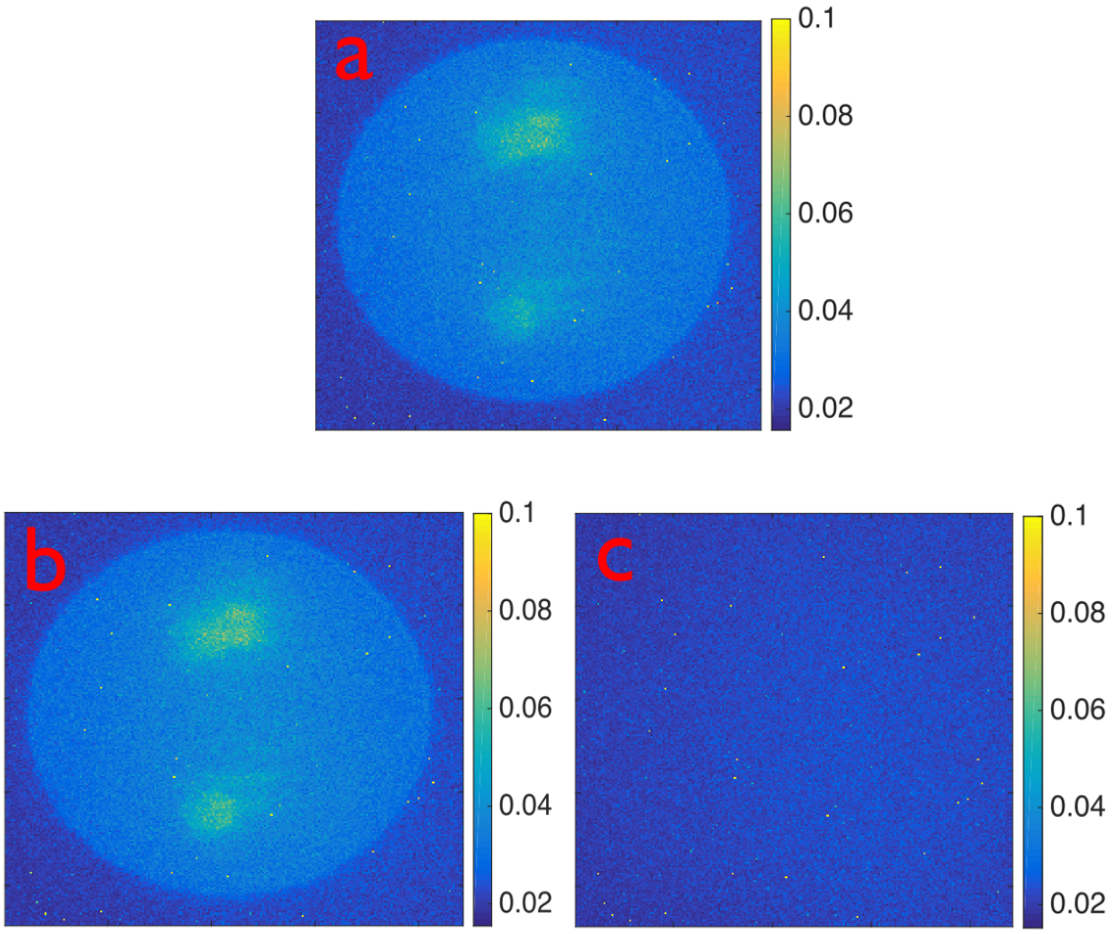

FIGURE 6.10: Images representing the testing of the nonlinear signal origins. Panel **a** shows the nonlinear signal under the standard experimental design (see Chapter 4). Panel **b** represents the same signal with one fewer short pass filter before the camera. Panel **c** is the same experimental setup as a except one shortpass filter has been move before the microscope.

not FWM as it is independent of time overlap and presence of both beams. It was crucial to first rule out that the signal observed was the incident beam itself. This was tested through the placement of the 750nm short pass filters, generally positioned before the camera. If the signal observed is the incident beam then it should be independent of the position of the filter within the beam path.

Figure 6.10 shows the images taken to rule out signal coming from the incident beams. Because signal is generated on the camera by the beams individually, the incident beams themselves must be ruled out. If the signal on the camera were of a higher wavelength than 750nm (the cut off of the short pass filter) leaking through

the filters, the removal of one of the filters significantly increase this signal [2]. Panel **b** rules out the possibility of leaking signal and/or idler through the filters. Additionally, the signal could be a wavelength below the short pass cut-off that is being transmitted through the filters. Panel **c** shows the camera response when a short pass cut-off filter is moved before the microscope. If a signal were to be present on the camera independently of the sample in the microscope, the position of a short pass filter within the optical path would have no effect. Panel **c** confirms that the signal observed on the camera is a response of the sample within the microscope as it is generated after the first short pass filter (in this specific case just before the microscope).

6.4.2 Spectral properties

One of the most defining characteristics of any nonlinear signal is the wavelength. Ideally determining the wavelength of a signal would be done utilising a spectrometer but due to experimental setup and low intensity signal no appropriate spectrometer was available.

In the absence of such a spectrometer, the nonlinear signal was imaged with a variety of band-pass filters placed immediately before the camera CCD. Table 6.4.2 shows the band-pass filters and their effective pass ranges as stated by the manufacturer.

Filter label	Filter type	Pass range (nm)	Thorlabs part number
A	Short pass	$\leq$ 550nm	FES550
B	Long pass	$\geq$ 600nm	FEL600
C	Band pass	680-720nm	FB700-40
D	Band Pass	730-770nm	FB750-40
E	Band pass	745-755nm	FB750-10

Figure 6.11 shows the Fourier image of the nonlinear signal with the inclusion of band pass filters. As a reminder, the experiment includes as standard a 775nm

[2] For reference, the 750nm short pass filter has an optical density of $\approx$ 6 above 750nm

dichroic in the microscope as well as two 750nm short pass filters prior to the camera. The FWM signal is predicted 744.1nm. It is expected that the filter D would transmit the entire FWM signal but Figure 6.11 shows a significant reduction in intensity when this filter is applied. Therefore one concludes that a significant portion of the nonlinear signal is not generated through the FWM process.

From Figure 6.11, one observes that the nonlinear signal (excluding the FWM) is broadband, however not across the whole visible spectrum. It is exclusively above the 600nm pass filter. As the incident beams must be filtered out, it is impossible to tell how far the signal extends beyond the 750nm cut off applied by the short pass filter. This signal represents a form of white light generation (WLG), which is a broadband emission from a sample due to an intense incident field known to occur in graphene [212]. When the excitation is wavelength selective, the white light generation centres around the incident wavelengths, and thus the experimental setup will transmit the higher frequency tail to this spectrum efficiently.

6.4.3 Four-wave mixing isolation

The procedures described show that there is a significant nonlinear broadband signal, however it is mixed with a spectrally narrow signal expected to be FWM. In order to make any conclusions about the FWM signal from the graphene, we must isolate this element of the signal and confirm it is the FWM. The FWM signal occurs only at time overlap, whereas the majority of the alternate nonlinear signal is independent of time overlap, as shown by the presence on individual beam tests of Figure 6.9. One can image the signal on and off time overlap, allowing the FWM signal to be isolated[3].

Experimentally, the input beams are excluded from the final image through two 750nm short pass filters. The filter edge normally cuts on a few nanometres above the expected FWM wavelength, however with a change to the input wavelengths it is possible to sweep the FWM wavelength up to this filter edge such that the FWM would be transmitted initially but gradually be excluded as the wavelength increases. Figure 6.12 shows this wavelength sweep and as expected the FWM signal reduces as it approaches the filter edge. This is also represented in Figure 6.13,

[3]This assumes a small contribution created through increased intensity of overlapping the beams

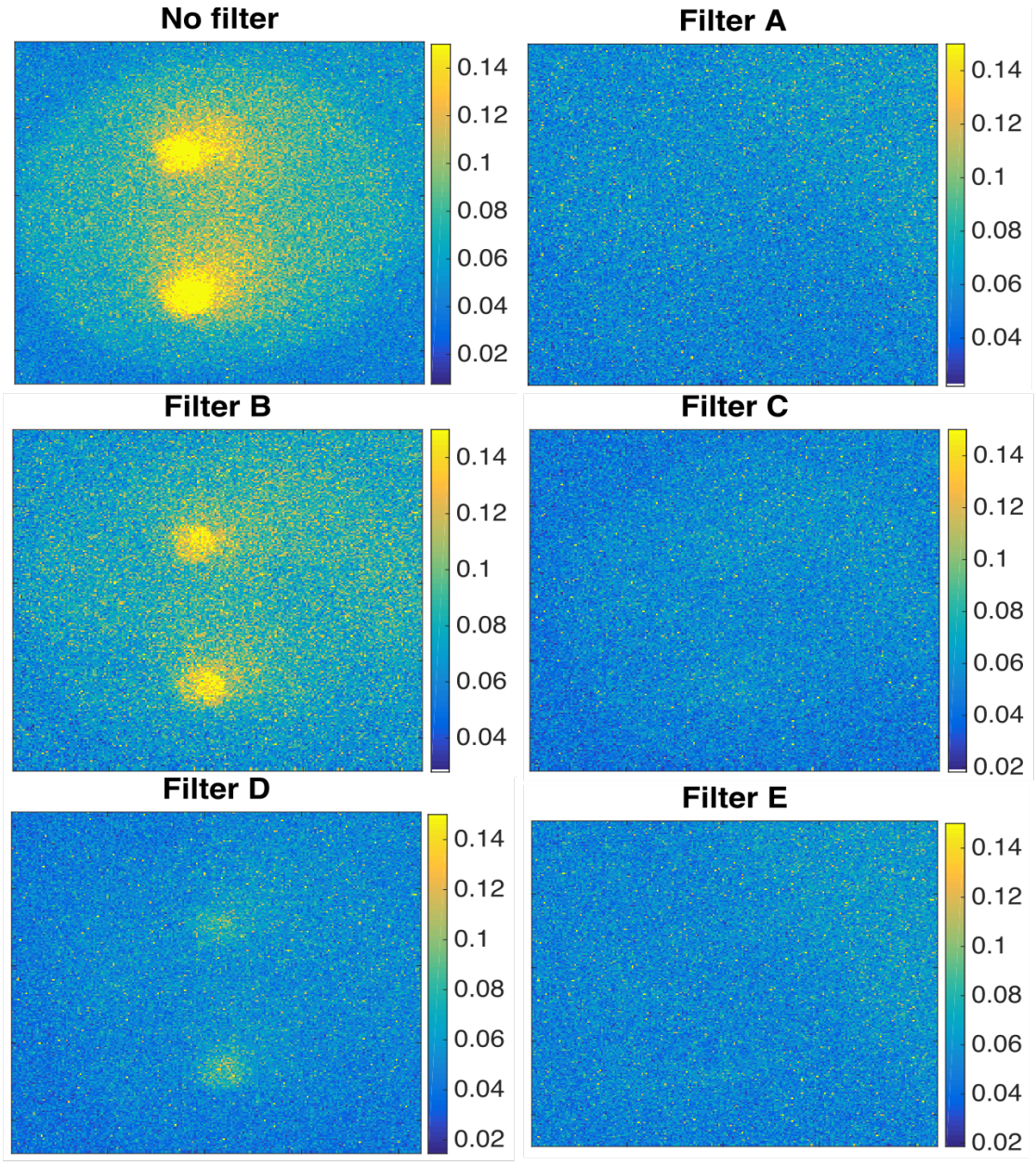

FIGURE 6.11: Filter testing images of the nonlinear signal. Table 6.4.2 shows the filters used and pass ranges for each of the filters.

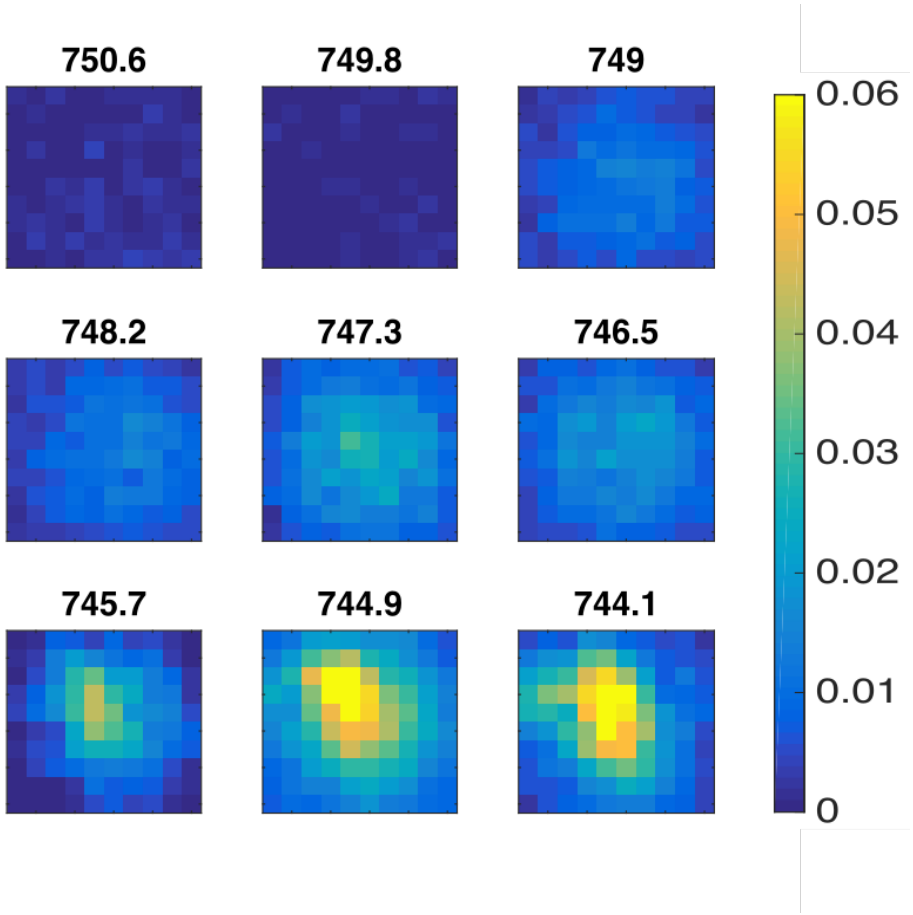

FIGURE 6.12: Images showing the wavelength sweep of FWM across the edge of a 750nm short pass filter. The signal shown in each image is the difference of a signal taken at time overlap and off time overlap. This signal is imaged in the image plane, absent of spatial patterning required for Fourier plane imaging (this choice is discussed in Section 6.6.1). The predicted FWM wavelengths from the input beams are listed above the images. Labels are expected FWM wavelengths in nm.

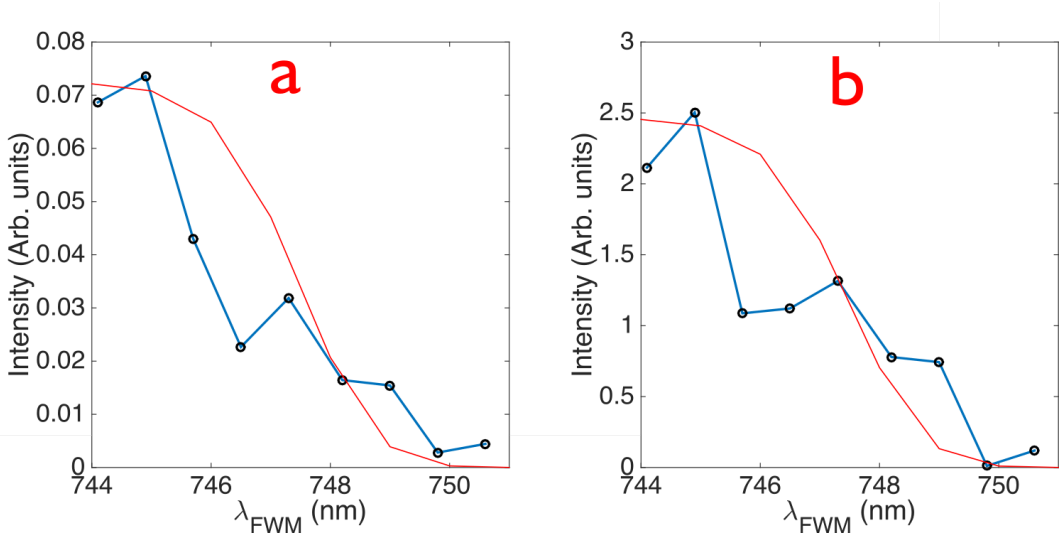

FIGURE 6.13: Intensity of isolated four-wave mixing response as a function of FWM wavelength. The blue lines represent taken data; the red plot is the quoted transmission of the filter normalised to the maximum intensity observed. Panel **a** shows the difference in the maximum pixel between images at time overlap and off time overlap. Panel **b** shows the difference between the summation of the intensity in the entire image displayed in Figure 6.12.

which shows the differential measurement of both the highest pixel in the image on and off time overlap as well as the summation of all pixels within the image. Power instability in the laser makes a power dependence measurement both challenging and unreliable, however the wavelength dependence displays a spectrally narrow signal at the FWM wavelength.

6.4.4 Four-wave mixing in the Fourier plane

Figure 6.9 shows that a large proportion of the non-linear signal generated by the graphene sheet is not FWM in origin. However, in order to investigate possible wavevector dependence in the FWM signal, one can take the differential of the images at and away from time overlap.

Figure 6.14 shows the nonlinear signal taken at, and away from, time overlap along with the difference between the two; Panel **c** shows this difference image. It is clear from Panel **c** that there is no significant wavevector based enhancement to the FWM signal that has been isolated. From this, one can deduce that no significant plasmon excitation occurred during this FWM process.

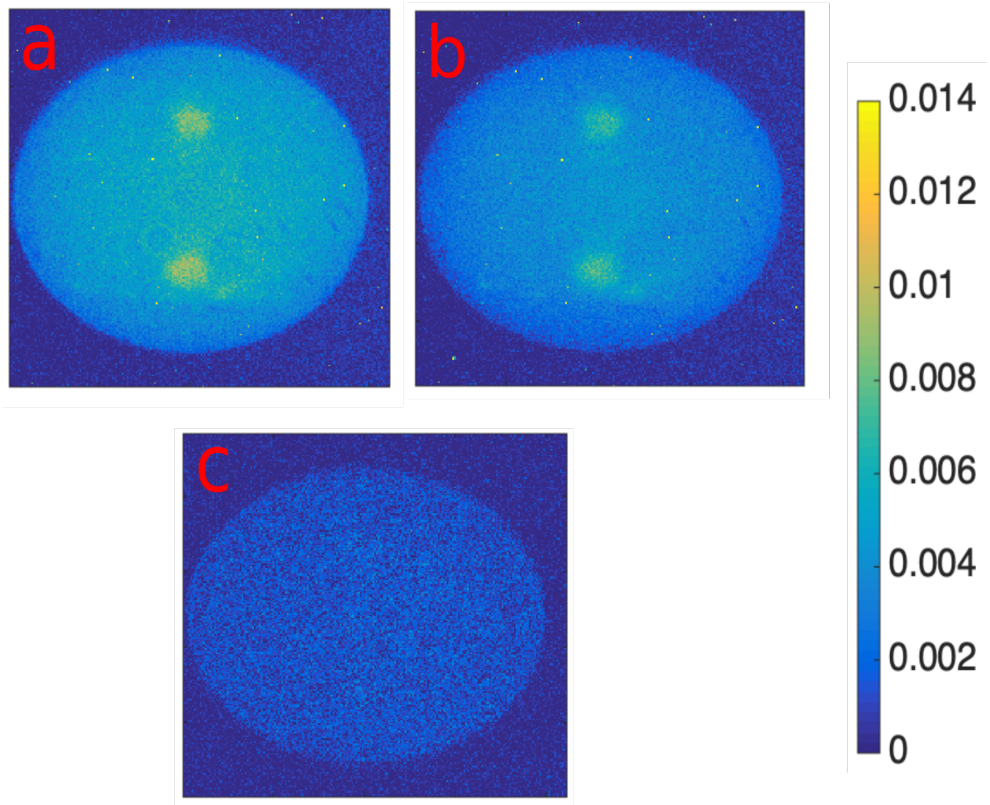

FIGURE 6.14: Figures showing the non-linear signal from the graphene sheet. Panel **a** shows the signal when the incident beams are overlapped in time. Panel **b** is the signal when the beams are not overlapped in time. Panel **c** is the difference between the two images, isolating the FWM signal from the WLG generation discussed in Section 6.4.2

6.5 Summary of nonlinear signal

The nonlinear signal generated at the graphene sheet consists of two components: a nonlinear signal independent of time overlap which shows many characteristics of white light generation (WLG); and a FWM signal. The WLG signal shows a broadband response and is generated from either beam independently. This signal is not of interest to the experiment, so further clarification is unnecessary.

The FWM signal shows no significant enhancement when the difference frequency generation (DFG) would couple to a plasmon mode, this effect would be observed in the difference image (Panel **c**) of Figure 6.14. Hence a cascaded third order effect does not contribute significantly to the overall FWM signal.

6.6 Third order conductivity of Graphene

Much work has been done on quantifying the third order nonlinearity in graphene, both theoretical and experimental, however, depending on setup and geometry, the values have been quite varied (see Figure 6.1). As a simple extension to this experiment already completed, the third order responses of the graphene samples were quantified.

6.6.1 Estimation of susceptibility

In Section 6.4.3 it was shown that the FWM signal could be effectively extracted from the data through use of time overlap. This opens up the possibility of using the samples to estimate the third order response of graphene in the experimental setup. Appendix B details the derivation to extract a third order susceptibility from an estimated power. The measurements used to calculate the $\chi^{(3)}$ response of graphene are taken in the image plane to increase signal to noise on the measurement. Additionally the spatial patterning, used in the Fourier plane imaging section of this investigation, is absent. This enables a more accurate calculation of the focal spot size as the back aperture is now filled for both input beams.

The experimental setup limits the range of FWM that can be selected due to the filtering required through the experiment. As such it is not possible to sweep a large

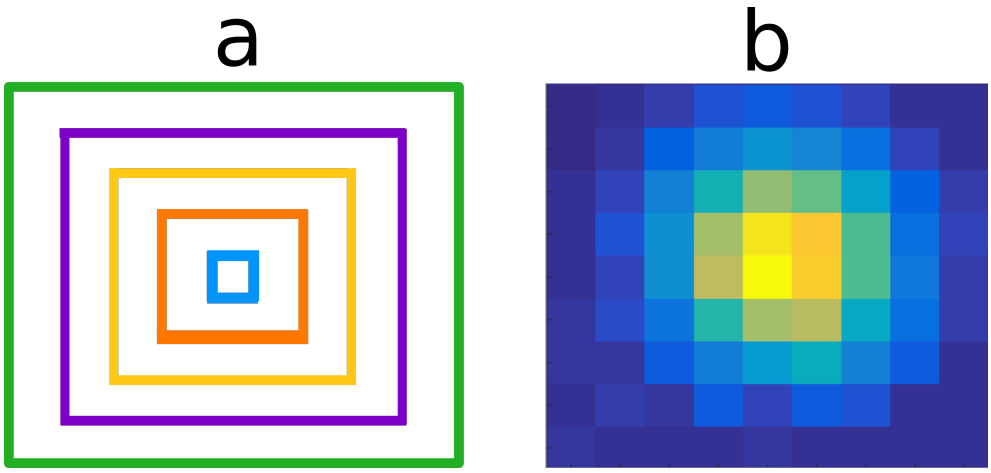

FIGURE 6.15: Image showing an example signal and mask used to estimate the value of $\chi^{(3)}$. Panel **a** shows the area averaged to obtain estimates for Figure 6.16. Panel **b** is an exemplar of the data used for this process. Specifically, Panel **b** is for a pump power of 200 μW on Flake 1.

range of input and output wavelengths[4]. The results presented here are taken for input wavelengths $\lambda_1 = 784nm$ and $\lambda_2 = 828nm$ with $\lambda_{FWM} = 744.1nm$.

Susceptibility measurements were performed on three samples: two graphene flakes, and graphene produced through chemical vapor deposition (CVD). Both flakes are mechanically exfoliated monolayer graphene on hexagonal boron nitride (HbN). The CVD graphene is commercially available (see Chapter 3 for details). For each of these samples a power dependence was measured to provide an indication of the error associated with the value of $\chi^{(3)}$.

Figure 6.16 shows the estimations of $\chi^{(3)}$ from the data obtained. Exemplar data and the mask used for calculations are shown in Figure 6.15. As expected, the non-linear response of CVD graphene is slightly weaker than that of exfoliated graphene. This is based on the quality of CVD graphene generally below lower than that of exfoliated flakes with regards to defects and impurities [135, 136, 137, 138], so one would expect a weaker coherent response of collective oscillations within a sample. Crucially, the separate measurements of both exfoliated graphene flakes show similar orders of magnitude for $\chi^{(3)} \approx 10^{-17} \frac{\mathrm{m}^2}{\mathrm{V}^2}$. This result is around two orders of magnitude less than Hendry found in 2010 [200], however, there are possible corrections necessary as noted by Cheng[157]. Additionally samples, and indeed experimental setups, have shown a wide variety of values, as shown in Figure 6.1.

[4]The experiment is limited to a $\approx 720nm - -750nm$ range in FWM output

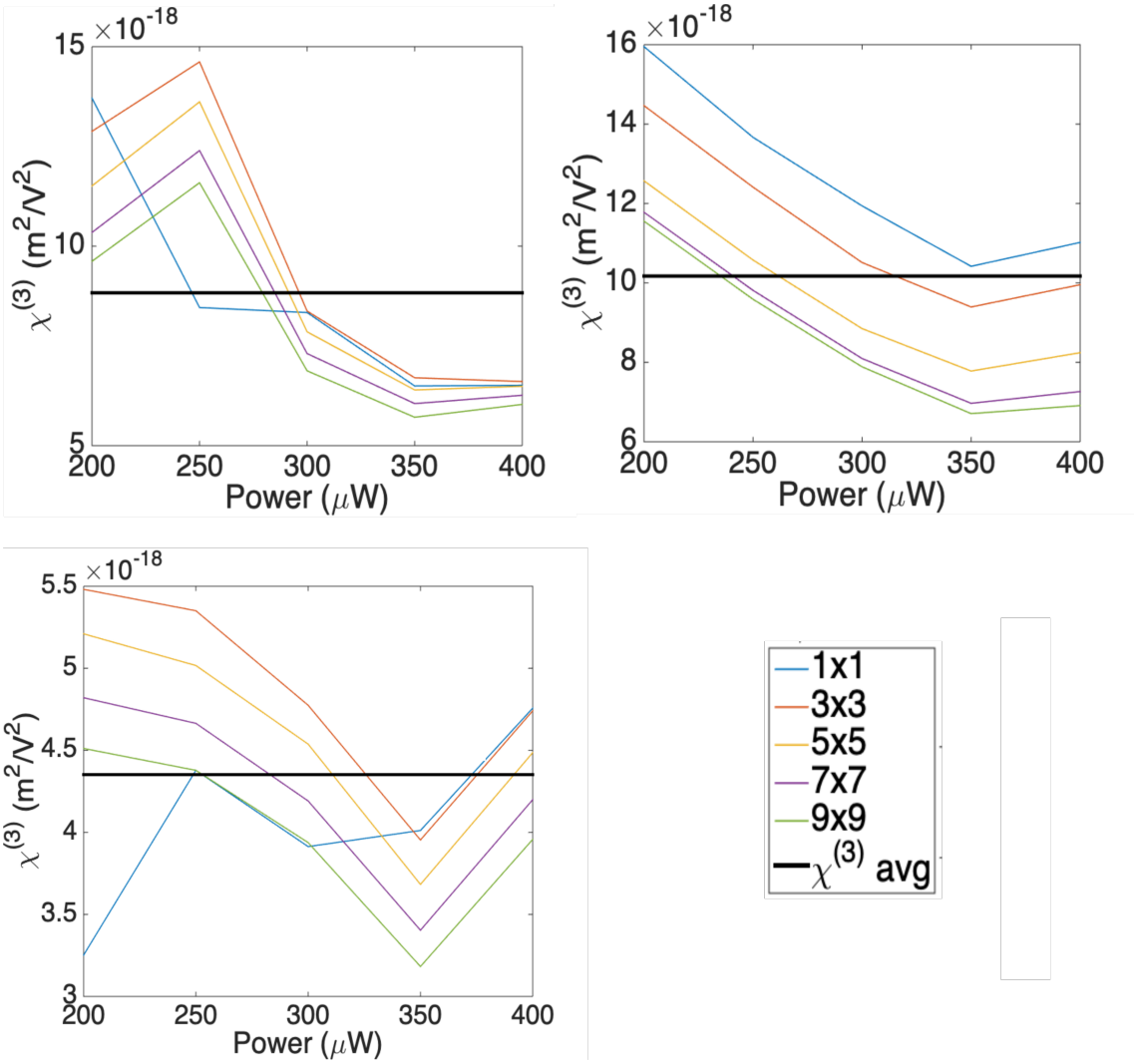

FIGURE 6.16: $\chi^{(3)}$ estimations from the graphene samples. The legend represents the area of the image taken for the calculation in pixels. All areas, shown in Figure 6.15, are centred around the maximal pixel of the image. Panel **a** and **b** are exfoliated flakes (**GF1** and **GF2** respectively). Panel **c** is CVD graphene.

6.7 Conclusion

It is clear from this investigation that there is a nonlinear signal observed, and included in this is a FWM signal. However, the signal does not appear to be enhanced for any specific wavevector, which would be indicative of a cascaded second order process. Whilst mathematically this effect is present, the conclusion therefore is that this process is not of a comparable size to the straight third order nonlinear signal or the white light generation from the graphene sample. An estimation of the third order susceptibility of graphene suggests a similar value to that already published confirming the presence of the FWM signal in the analysis. Whilst the third order nonlinear response of graphene may still be of interest to the community, it is clear that the looked-for phase-matched enhancement is not present.

Chapter 7

Differential Reflectivity of Indium Tin Oxide

In this chapter, all measurements and modelling are conducted with transverse magnetic (TM) light.

7.1 Impact

The work presented in this chapter regards intensity dependent differential reflectivity of indium tin oxide (ITO). The results presented show differential reflections of both larger absolute magnitudes and larger changes than those previously shown in the literature [67]. Additionally this work furthers the investigation into the origins of this change in reflection through a two temperature model and temperature dependent Drude parameters. It is shown that such intensity dependent reflection is only achievable on very fast timescales ($\approx 100fs$). This restriction is caused by a combination of the strong coupling between the electron and phonon temperatures and large difference between the specific heat capacity of the electrons and phonons. A manuscript is in preparation containing and expanding on the results presented here.

7.2 Motivation

Epsilon near zero (ENZ) materials have created excitement within the community, particularly in the last decade [213, 214, 215, 216]. In the ENZ region, a small change in the permittivity can lead to large changes in the refractive index. This is shown

by

$$\Delta n = \frac{\Delta \epsilon}{\sqrt{\epsilon}}, \tag{7.1}$$

where n represents the refractive index and ϵ is the permittivity. This could lead to the exciting possibility of generating an optical circuit component that can regulate its reflection solely on small changes to the intensity of the incident light, a holy grail for all-optical computing. In indium tin oxide (ITO), this effect was first modelled by Alam [67], who showed a differential transmission of up to 300% for an intensity of $250 GW/cm^2$. This change in reflection is very large, but the experimental setup of Alam was limited in excitation angle and wavelength. As such there is great value in considering whether there are stronger effects to be observed in other areas of the dispersion. The work presented in this thesis models and investigates the critical angle of a glass-ITO interface.

7.3 Modelling the ITO response

7.3.1 Material parameter changes

The work of Alam [67] observed a significant change in the reflection of an incident source beam through changes in intensity. This effect was attributed to a red shift in the plasma frequency of the ITO. Panel **a** of Figure 7.1, taken from [67], shows the transmission, reflection and absorption coefficients for an incident angle of 30^o, and Panel **b** shows the measured refractive index and extinction as a function of intensity. If one assumes that ITO behaves as a Drude metal within the experimental region, such that the permittivity and refractive index are governed by the plasma frequency (ω_p) and the scattering rate (γ), one can estimate the red shift in the plasma frequency observed. If one assumes a linear dependence of

$$\omega_p = \omega_{p_0}(1 + A \times I), \tag{7.2}$$

where ω_{p_0} is the unperturbed plasma frequency, I is the intensity and A is a coefficient to be estimated. Figure 7.1 suggests a saturation point around $80 GW/cm^2$, therefore the refractive index is modelled to this value of intensity. However, these

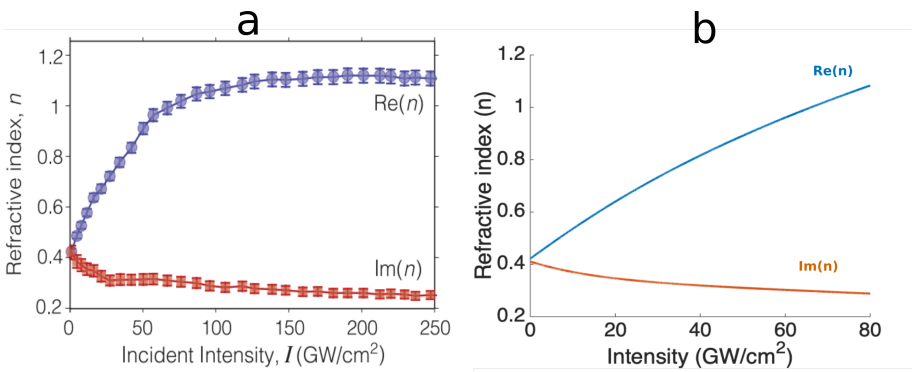

FIGURE 7.1: Response of ITO to irradiation at $1240nm$. Panel **A** represents the complex refractive index measured in [67] with a saturation point around $80GW/cm^2$. Figure obtained from [67]. Panel **b** shows the complex refractive index when modeled through the linear equations 7.4 and 7.5.

results cannot be explained through only a change in the plasma frequency, and one must also include a change to the scattering rate of the same form

$$\gamma = \gamma_0(1 + B \times I), \tag{7.3}$$

where γ_0 is the unperturbed scattering rate and B is the coefficient of scaling to I. From this simple linearised model, and the results of Alam [67], one estimates the following set of coefficients of

$$A = -1.7 \times 10^{-3} \frac{cm^2}{GW} \qquad B = 1.9 \times 10^{-2} \frac{cm^2}{GW},$$

and thus the linear equations are given by,

$$\omega_p = \omega_{p_0}(1 - 1.7 \times 10^{-3} \left\{ \frac{cm^2}{GW} \right\} I) \tag{7.4}$$

$$\gamma = \gamma_0(1 + 1.9 \times 10^{-2} \left\{ \frac{cm^2}{GW} \right\} I). \tag{7.5}$$

Using these values, one can recreate the measured refractive index and extinction observed by Alam [67]. This is shown in Figure 7.1.

An increased scattering rate at higher temperatures is an intuitive result that has a multitude of explanations. For example the increased average thermal velocity of conduction electrons will lead to an increased scattering rate for a consistent mean free path. Also increased phonon occupation will lead to a higher scattering rate as

the pump energy is transferred to the phonon temperature.

The red shift of the plasma frequency is stated to be caused by the increase in the free electron temperature of the ITO sample [67]. As the ITO is well described by a Drude model in the region of interest, one observes that the plasma frequency is given by

$$\omega_p = \sqrt{\frac{ne^2}{\epsilon_\infty \epsilon_0 m^*}}, \tag{7.6}$$

where n is the electron density, ϵ_∞ is the high frequency permittivity limit and m^* is the effective mass of the electrons. In such a system, there is no change in the electron density [217], and therefore a red shift in the plasma frequency is expected to manifest in the effective mass, as is the case in cadmium oxide, which also exhibits a red shift of its ENZ point with increasing temperature [173].

7.3.2 Temperature dependence of plasma frequency

In order to better model the changes in permittivty observed, one needs to identify the method through which a temperature increase can decrease the plasma frequency. From Equation 7.6 one can see that if the density of electrons remains constant, the effective mass must change with temperature. The effective mass of electrons in a ITO can be defined as

$$\frac{1}{m*} = \frac{1}{\hbar^2}\frac{d^2E(k)}{dk^2}, \tag{7.7}$$

where $E(k)$ is the band structure of the material. For materials with a parabolic band structure, where $E \propto k^2$, this value is constant throughout the distribution of electron wavevectors. In ITO, as well as cadmium oxide (CDO), a similar conductive metal oxide with an ENZ point in the mid infrared [173], the band structure deviates from from a parabolic distribution through a nonparabolicity correction CE^2. This correction factor can be implemented into the band structure through [218]

$$\frac{\hbar^2 k^2}{2m_0^*} = E + CE^2, \tag{7.8}$$

where C is the nonparabolicity constant [219] and m_0^* is the effective mass at the conduction band minimum. One can solve Equation 7.8 for E, taking the positive

root of the quadratic equation one arrives at

$$E(k) = \frac{-1 + \sqrt{1 + \frac{2\hbar^2 C k^2}{m_0^*}}}{2C}. \tag{7.9}$$

Equation 7.9 strongly resembles Equation (S5) of [173], which originates from the Kane model of $k - p$ perturbation [220, 221], and therefore one observes that the nonparabolicity constant C is equal to $\frac{1}{E_g}$, where E_g is the bang gap energy. Equation 7.9 can now be substituted into Equation 7.7 to solve for $m^*(k)$, with one extra consideration. For thermal distributions, and in particular highly photo-excited thermal distributions, it is crucial one takes into account the range of effective masses within the electron energy levels. Thus, more completely, one finds that the average electron mass from

$$\frac{1}{m^*} = \frac{1}{\hbar^2} \frac{\int_0^\infty f(k, \mu, T) \left(\frac{d^2 E(k)}{dk^2} \right) dk}{\int_0^\infty f(k, \mu, T_e) dk}, \tag{7.10}$$

where $f(k, \mu, T_e)$ is the Fermi distribution, T_e is the electron temperature and μ is the chemical potential. In Equation 7.10, one notes that the effective mass, m^*, is now a function of the electron temperature T. As a simple picture, one can visualise that, when an electron is photo-excited, it moves further up in the band structure to a new state. If the second order derivative of the band structure is not constant and remains a function of k, this new state will have a different effective mass. Therefore an increase in T_e can be directly translated into a change in the effective mass of the electrons and further to a change in the plasma frequency.

Panel **a** of Figure 7.2 shows the calculated $m^*(T)$ for ITO, along with CDO as an established reference material [173]. One observes that, in comparison to CDO, ITO shows a lower change in effective mass as a function of temperature, due to the difference in Fermi energies of the two systems. Normally, ITO has a Fermi energy of $1eV$ ($0.4eV$ for CDO), as the Fermi distribution is predominantly modified in a region around k_f, the excited electrons have very similar effective masses compared to their original state. Therefore, for similar changes to the Fermi distribution (similar changes in T_e), the change in effective mass decreases with increasing Fermi energy. Panel **b** shows the effect this change in effective mass has on the plasma frequency. Using Equation 7.6, one can relate the plasma frequency at $0K$ to the plasma

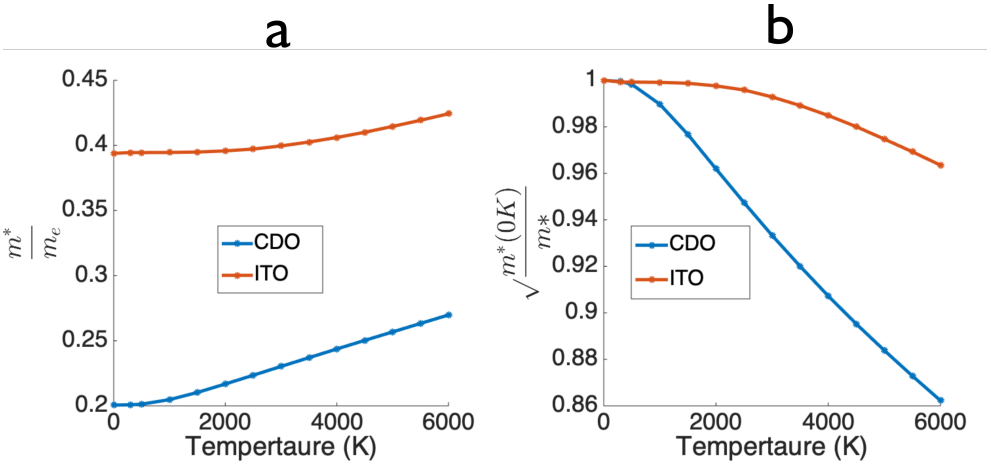

FIGURE 7.2: Temperature dependent effective mass of electrons for ITO and CDO. Panel **a** shows the effective mass relative to the electron mass m_e. Panel **b** shows the predicted effect on the plasma frequency base on Equation 7.11.

frequency under thermal excitation through

$$\frac{\omega_p(T_1)}{\omega_p(T_2)} = \sqrt{\frac{m^*(T_2)}{m^*(T_1)}}. \tag{7.11}$$

The change in ω_p predicted at $5000K$, the maximum electron temperature predicted by Alam [67], through band non-parabolicity is $\approx 3\%$. This change is significantly smaller than that obtained from the parametrisation of ω_p and γ calculated via the measured refractive index.

7.3.3 Temeprature dependence of scattering rate

In transparent conductive metal oxides (TCOs) such as ITO, the two dominant mechanisms of scattering are grain boundary scattering and ionisation impurity scattering [222]. In general, at low electron concentrations, $n_e < 9 \times 10^{26} m^{-3}$, grain boundary scattering is expected to dominate. Above this level, ionised impurity scattering becomes the dominant mechanism [222]. The samples used in this work are highly doped ITO samples ($n_e > 10^{27} m^{-3}$), meaning that their scattering should be dominated by ionised impurity scattering. However, it has been noted by many works that, in TCOs such as ITO, the ionised impurity scattering is independent of temperature [223, 224, 225]. Therefore even though the electron concentration is higher than

the regime change noted in [222], it is not so high as to negate temperature dependent effects under intense femtosecond illumination arising from other scattering mechanisms.

One can separate the scattering rate γ into a linear superposition of individual scattering rates such that

$$\gamma = \gamma_\alpha + \gamma_\beta + ..., \tag{7.12}$$

where α and β represent different scattering sources. One assume that these terms now comprise a temperature dependent grain boundary scattering term γ_{GB} and a term describing all other temperature independent scattering $\gamma_{\mathcal{O}}$, which is expected to be dominated by ionisation impurity scattering. The grain boundary temperature dependent mobility μ_{GB} can be given by [223, 226]

$$\mu_{GB} = \frac{A}{\sqrt{T}e^{\frac{eV_B}{k_bT}}}, \tag{7.13}$$

where V_B is the potential barrier between the grain boundaries and A is a constant related to the sample. This constant is given by

$$\frac{el}{\sqrt{2\pi m^* k_b}},$$

where l is the average grain boundary separation, which is taken to be approximately $5m$ in ITO [227]. In practice, for TCO films V_b is very small of the order of $\frac{eV}{100}$ [228, 229], meaning the exponential term provides a very small correction, which is negligible here and can be discarded. One can relate the attributed mobility to the scattering rate through

$$\gamma_{GB} = \frac{1}{\tau_{GB}} = \frac{e}{m^* \mu_{GB}}. \tag{7.14}$$

In order to calculate the scattering contributions from other sources, $\gamma_{\mathcal{O}}$, one can calculate $\gamma_{GB}(300K)$ and compare to the measured scattering rate without photoexcitation. The difference between this two will give the term $\gamma_{\mathcal{O}}$, which remains constant under heating.

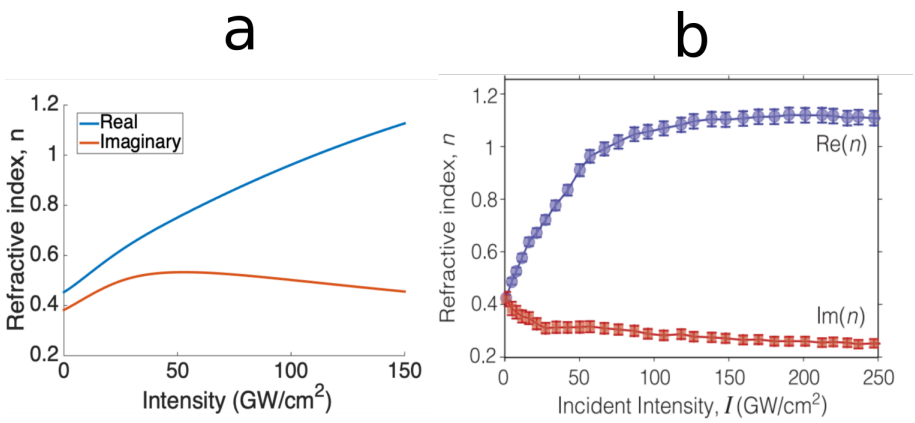

FIGURE 7.3: Predicted and measured refractive index as a function of temperature. Panel **a** shows the predicted response due to a temperature induced change in the effective mass and grain boundary scattering through Equations 7.11,7.12 and 7.14. Panel **b** shows the measured response of ITO from [67].

7.3.4 Comparison to experimental values

Figure 7.3 shows the calculated permittivty and refractive index of an ITO sample at $\lambda = 1240nm$ with the parameters of Alam [67]. One observes that there is good agreement between the real part of the refractive index predicted here and the measure values of [67]. However, the imaginary part of refractive index does not show the same level of agreement and the physical origin of this discrepancy is currently unclear.

The model presented here is likely the correct approach, however due to the highly nonlinear nature of the relationship between increased temperature and Drude parameters, small variations is input parameters can have a large effect. In particular, as can be seen in Figure 7.2, the position of the Fermi energy within the band structure leads to remarkably different effects. The Fermi energy has not been accurately measured for each sample individually, and instead an estimate from the literature is used (see Section 7.3.2).

Additionally, the model applied suffers from some simplistic approximations that are not intuitive to remove. Firstly, change in refractive index measured experimentally shows a saturation point around $80GW/cm^2$ which is not reflected in the modelling. This is likely due the absorption of the sample reducing at higher intensities as the sample becomes saturated and/or damaged as these intensities are very near the damage threshold (see section 7.6.2). Secondly, the change in plasma

frequency and scattering rate are only linked by the shared variable T_e representing the electron temperature and have no explicit relation to each other. A more complete model would require inclusion of feedback dynamics related to the absorption of pulse energy as the sample becomes photoexcited, which would account for such a saturation. Lastly, the grain boundary scattering consideration has sample dependent variables (such as barrier energy V_B and boundary separation l) that could also, in principle, be spatially varying across a sample. These values have not been individually measured for the sample modelled and could have a pronounced effect on the results.

Additionally, whilst grain boundary and ionised impurity scattering are the dominant mechanisms in ITO, there are other scattering mechanism such as lattice vibration scattering which may contribute, in particular due to a stronger temperature dependence of the associated mobility $\mu_{LV} \propto T^{-\frac{3}{2}}$. As the change in refractive index is extremely nonlinear with change in temperature and plasma frequency or scattering rate, it is not intuitive to isolate where the model deviates from the experiment.

Therefore, it is unclear if the observed red shift in the ITO plasma frequency and estimated scattering change can be entirely explained through the conduction band nonparabolicity and grain boundary effects. Until the underlying physical mechanisms can be verified, one must model future experiments using empirical data, as have been established in Equations 7.4 and 7.5.

7.4 Modelling the differential reflectivity

The observed red shift in the plasma frequency, combined with the increase in the scattering rate will change the reflectivity of ITO sample across a variety of wavelengths, some very pronounced. In particular, the ENZ point of the ITO sample will be moved, drastically changing the absorption properties and permittivities across a small region of the dispersion around this value.

Chapter 4 shows the experimental setup used for ITO differential measurements, discussing in particular the use of glass as an entrance medium allows access to high wavevector excitation of the sample. This is crucial to investigate regions of high response to the optical pumping, and the critical angle of glass-ITO-air interface.

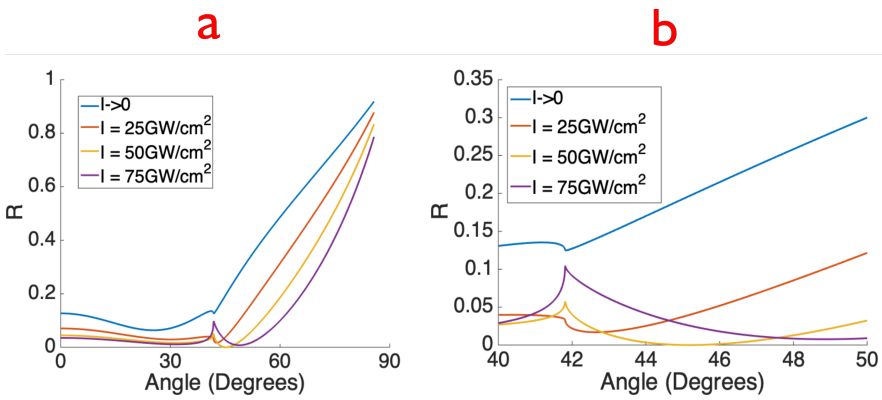

FIGURE 7.4: Modelled reflectivity of the ITO sample, R, as a function of the incident angle for a wavelength of $1240nm$. Panel **a** show the full angle range, Panel **b** shows a region of high response around the critical angle. ITO parameters for this model are taken from [67].

One can, using the transfer matrix method, model the response of an ITO sample when photoexcited in the configuration shown in Chapter 4. The photoexcitation is modelled using the empirical model described and given by Equations 7.4 and 7.5. Figure 7.4 shows the modelled differential reflection of an ITO sample, with the parameters given in [67], as a function of angle at a wavelength of $1240nm$ (selected for comparison to the work of Alam[67]).

One observes that the sample shows remarkable changes in the differential reflection beyond the critical angle of glass. The origin of this change in differential reflection is a shift in the frequency of the ENZ resonance. In order to better understand the nature of this change in the resonance, it is important to model the differential reflection across a variety of wavelengths. This representation is shown in Figure 7.5, which shows the absolute and differential reflection for an intensity of $50GW/cm^2$.

As a resonance shifts, the regions either side of this resonance within a dispersion will experience significant increases and decreases in their reflection. These specific changes are shown in Panel **c** of Figure 7.5 where the change in reflection, ΔR, relative to non-photoexcited response of the ITO is plotted. This allows for regions that exhibit both positive and negative differential reflections depending on their position relative to the ENZ mode.

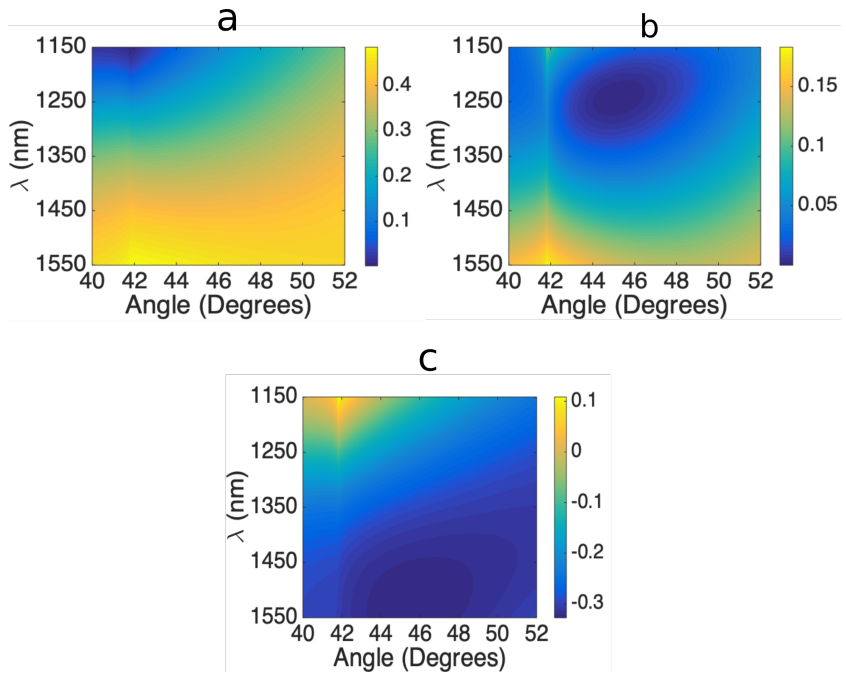

FIGURE 7.5: Modelled reflectivity changes in ITO as a function of wavelength and angle. Panel **a** shows the absolute reflection without photoexcitation, Panel **b** shows the absolute reflection under irradiation from a source of $50GW/cm^2$ and Panel **c** shows the difference between the two. All ITO parameters for this model are taken from [67] and the change in the Drude parameters is modelled through the parametrisation given in Equations 7.4 and 7.5.

7.5 Experimental results

This work first attempted to further the results of Alam [67] by obtaining a similar ITO sample (**ITO1**) and investigating the response of the ITO under similar excitation (i.e. femtosecond excitation) but beyond the glass-ITO critical angle. Figure 7.5 shows the predicted response of the ITO, Figure 7.6 shows the measured response of **ITO1** under an excitation of $50GW/cm^2$.

Figure 7.6 shows a weak interaction with the ENZ mode creating a small difference in reflection around $\lambda = 1250nm$. This weakness, when considered with previous experimental results and modelling, has two main causes. Firstly, this ITO sample is of lower quality than that used by Alam [67], this is apparent through the different scattering rates ($\gamma = 1.39 \times 10^{14}s^{-1}$ for [67] $\gamma = 2.56 \times 10^{14}s^{-1}$ for **ITO1**). Lastly, the mode is located at a higher frequency than we can access with the experimental setup[1], such that one only observes the tail of the resonance's effect in the scan. As confirmation, one notes that **ITO1** does not show an appreciable increase in

[1]The TOPAS® outputs require a manual filter change when sweeping across $1150nm$

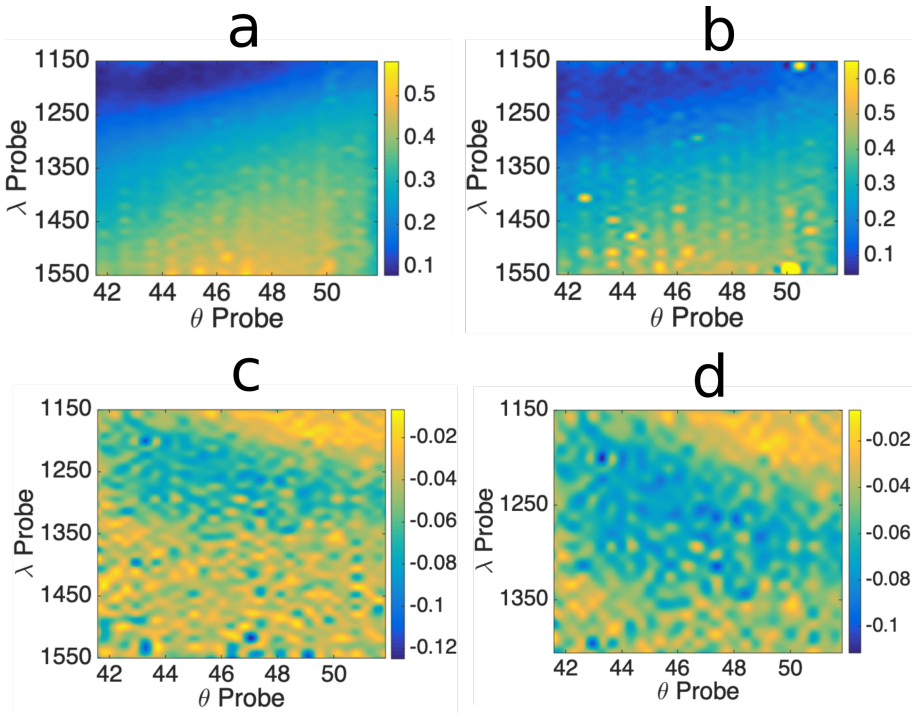

FIGURE 7.6: Measured reflectivity of **ITO1** as a function of θ_{probe} and λ_{probe}. Panel **a** is the measured reflection when the sample is not photoexcited, whereas Panel **b** represents excitation with a source of $50GW/cm^2$. Panels **c** and **d** show the minima of the difference in reflection (ΔR) and relative differential reflectivity ($\frac{\Delta R}{R}$) respectively. For this sample there was no significant increase in reflection observed. The differential reflection is of the order 10% in the region of interest.

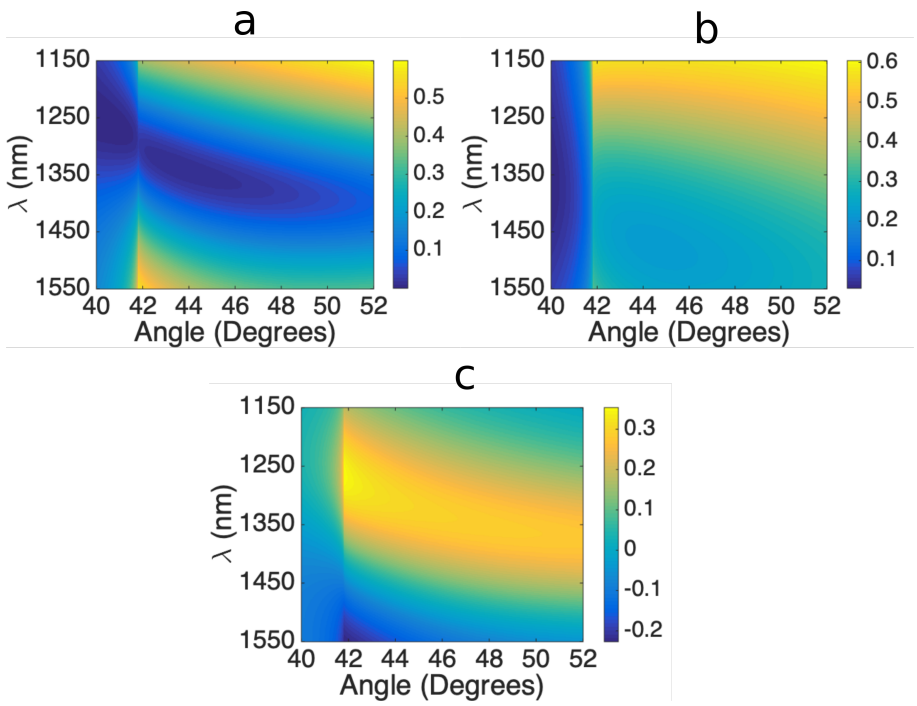

FIGURE 7.7: Modelled reflectivity using the material parameters of **ITO2** under a range of photoexcitations. Panels **a** and **b**, represent the absolute reflection without photoexcitation and irradiated at an intensity of $50GW/cm^2$ respectively. Panel **c** shows the differential reflection between Panels **a** and **b**.

reflection around the mode during the measurement, as would be expected if one investigated a region above the ENZ mode, suggesting the resonance starts at a higher frequency (lower wavelength).

However, an incredibly useful property of this resonance is that one can move its position in frequency space by changing the thickness of the sample. Not only is this useful for practical experimental purposes, but also the ability to tune the wavelength of interest is extremely valuable for any practical applications, in particular moving any switching effects towards the telecoms range ($\approx 1500nm$). Figures 7.7 and 7.8 show the absolute and differential reflection predictions of **ITO2** ($55.1nm$ thick) and **ITO3** ($109.1nm$ thick). In both cases one can observe both positive and negative changes in the differential reflection as the resonance is initially located more centrally in the TOPAS® bandwidth.

Figures 7.9 and 7.11 show good agreement with the modelling of Figures 7.7 and 7.8. The red shift in resonance is observed as predicted and the changes in reflectivity are also in very good agreement with predictions. The resonances of **ITO2** and **ITO3** are more pronounced than **ITO1**, this is likely due to a combination of the sample

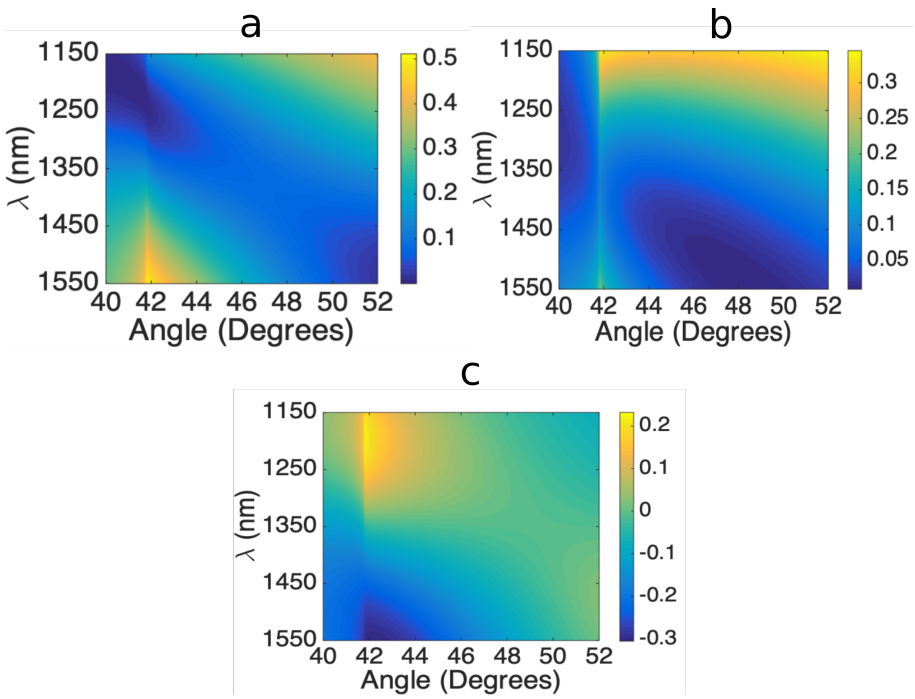

FIGURE 7.8: Modelled differential reflectivity of **ITO3**. Panels **a** and **b** represent the absolute reflection of **ITO1** with a non-perturbatively small intensity and one of $50GW/cm^2$ respectively. Panel **c** shows the differential change predicted.

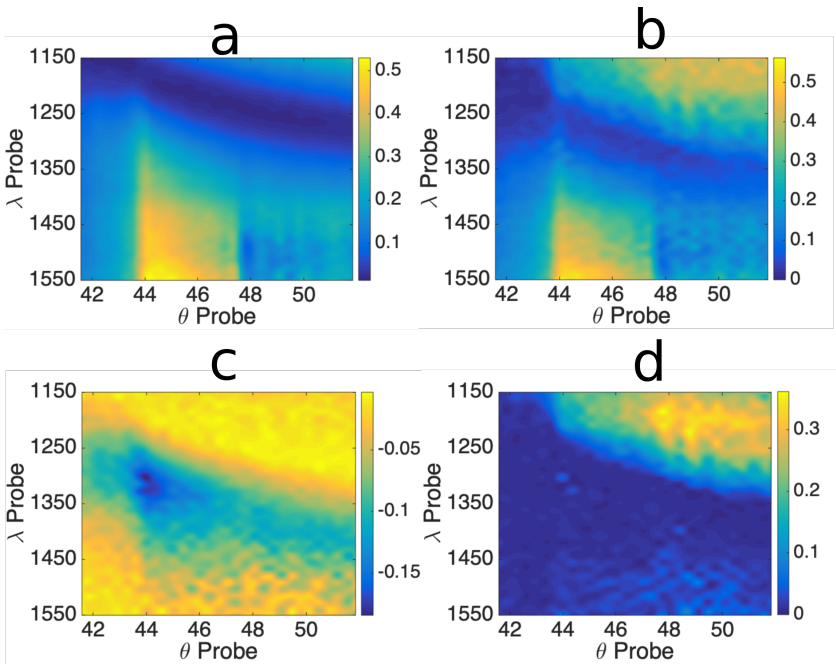

FIGURE 7.9: Measured probe reflection of **ITO2** as a function of λ_{probe} and θ_{probe}. Panel **a** and **b** show the reflection at 0 and $50GW/cm^2$ respectively. Panels **c** and **d** show the minimum and maximum change in reflectivity respectively. The pump wavelength is degenerate with the probe. Values of interest for changes of reflection are record in Table 7.5.

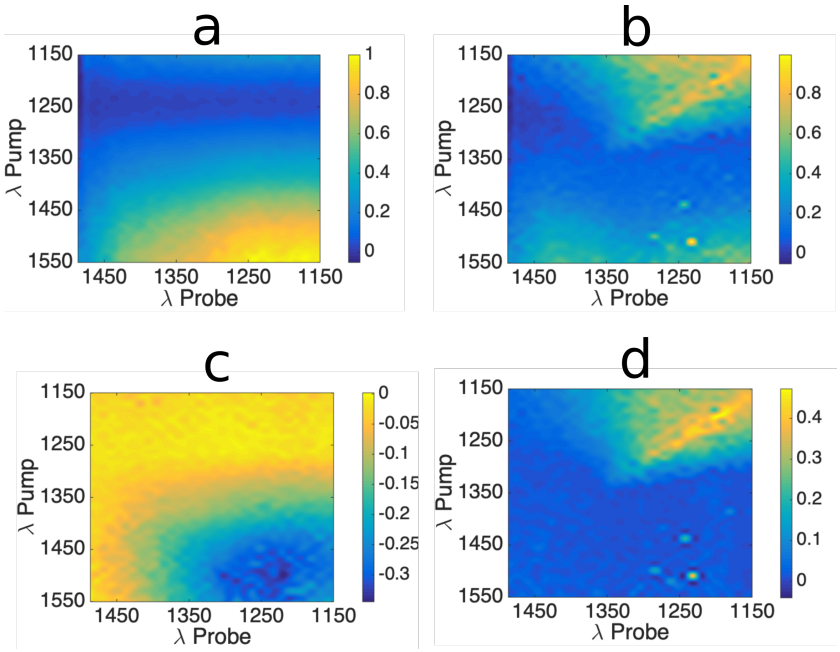

FIGURE 7.10: Measured probe reflection of **ITO2** as a function of λ_{pump} and λ_{probe} with $\theta_{probe} = 49^o$. Panel **a** and **b** show the reflection at 0 and $50GW/cm^2$ respectively. Panels **c** and **d** show the minimum and maximum change in reflectivity respectively. Values of interest for changes of reflection are record in Table 7.5.

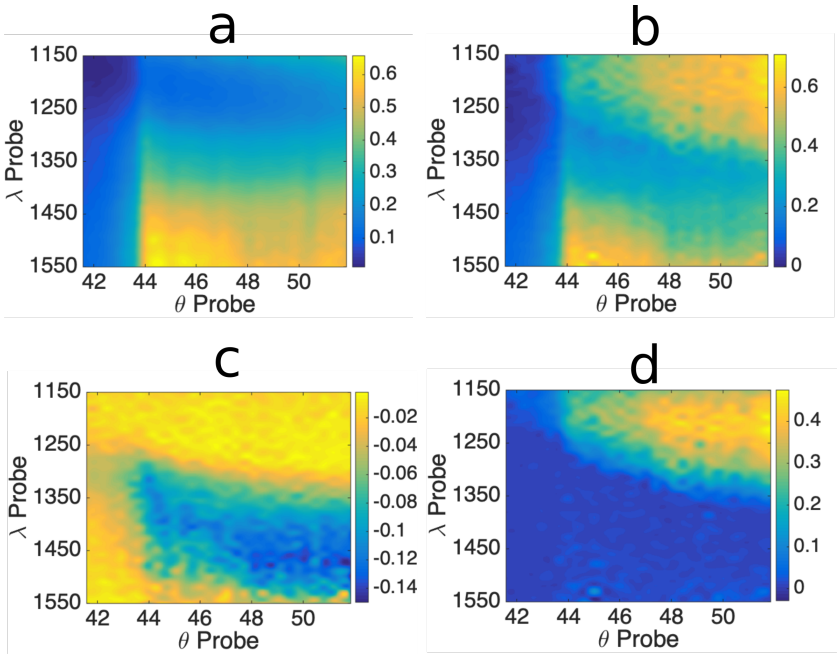

FIGURE 7.11: Measured probe reflection of **ITO3** as a function ofλ_{probe} and θ_{probe}. Panel **a** shows the non-photoexcited reflection. Panel **b** is the reflection when the sample is irradiated at an intensity of $50GW/cm^2$ at the same wavelength. Panels **c** and **d** show the minimum and maximum change in reflectivity respectively.The pump wavelength is degenerate with the probe. Values of interest for changes of reflection are record in Table 7.5.

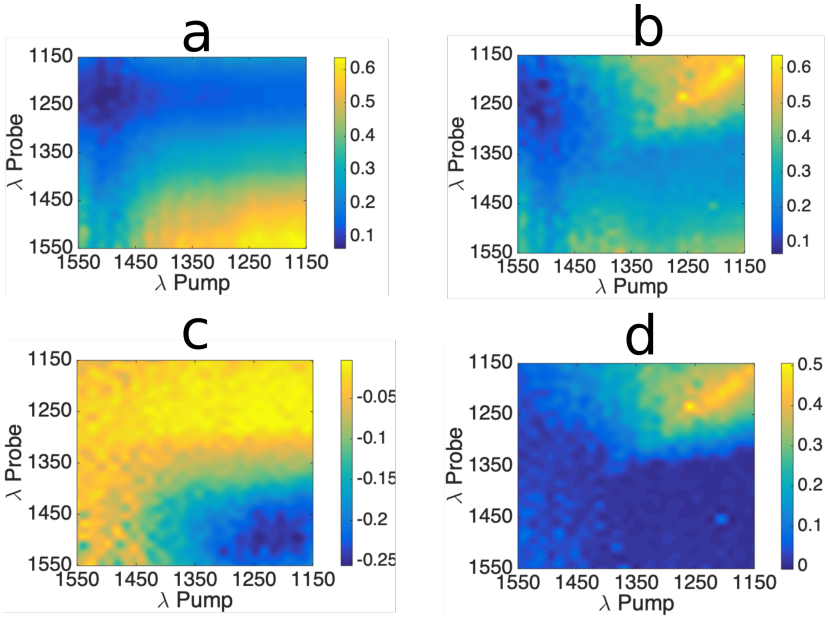

FIGURE 7.12: Measured probe reflection of **ITO2** as a function of λ_{pump} and λ_{probe} with $\theta_{probe} = 49^o$. Panel **a** shows the non-photoexcited reflection. Panel **b** is the reflection when the sample is irradiated at a pump intensity of $50GW/cm^2$. Panels **c** and **d** show the minimum and maximum change in reflectivity respectively. Values of interest for changes of reflection are record in Table 7.5.

quality, sample thickness and resonance position, as noted earlier in this Section (see also Chapter 3 for more details). The differences between sample **ITO2** and **ITO3** are less pronounced. These differences are also due to minor changes in the position of the resonance, as well as stronger resonances associated with thinner samples, similar to surface plasmons.

Sample	Scan type	min/max	ΔR	$\frac{\Delta R}{R}$	$\lambda_{probe}(nm)$	$\lambda_{pump}(nm)$	θ
ITO2	θ	max	0.36	3.67	1185	1185	47.8
ITO2	θ	min	-0.18	-1.7	1303	1303	44.0
ITO2	λ	max	0.47	11.9	1192	1201	49
ITO2	λ	min	-0.35	-1.7	1220	1499	49
ITO3	θ	max	0.47	1.22	1224	1224	51.8
ITO3	θ	min	-0.15	-1.29	1472	1472	51.67
ITO3	λ	max	0.51	2.56	1258	1234	49
ITO3	λ	min	-0.26	-1.4	1496	1177	49

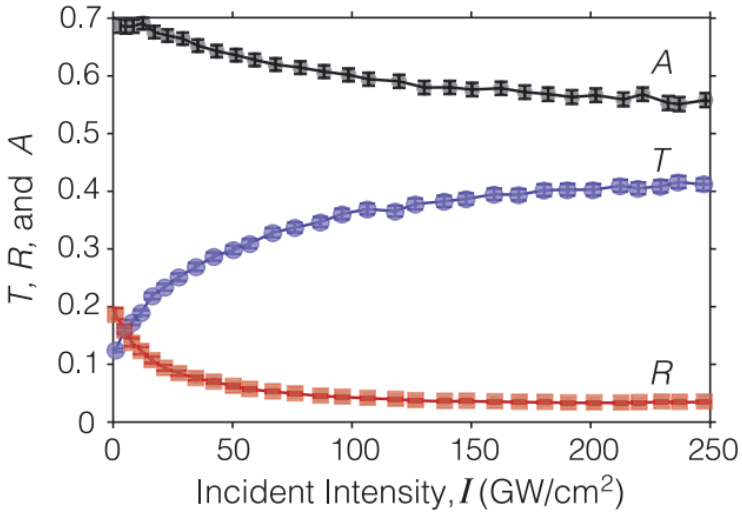

FIGURE 7.13: Measured change in absorption, reflection and transmission for ITO at a 30^o angle of incidence and $\lambda = 1240nm$. Figure obtained from [67]

The results presented here show the potential of ITO to be very useful nonlinear material, with the geometry established through this work exploiting the nonlinear nature of ITO more efficiently than previous works. The work of Alam [67] into the nonlinearity of ITO showed a maximal change in reflection of ≈ 0.16 from a value of 0.2 to 0.04, with an intensity of $250GW/cm^2$, this corresponds to $\frac{\Delta R}{R}$ that is equal to -0.8. For transmission, the maximum measured increase was 0.3 from a value of 0.1 to 0.4, once again for $250GW/cm^2$, corresponding to a $\frac{\Delta R}{R}$ that is equal to 3. This is seen if Figure 7.13 taken from [67].

As can be seen in Table 7.5, several points of interest exhibit larger absolute changes,for both positive and negative ΔR, and in the case of **ITO2** significantly larger $\frac{\Delta R}{R}$ values. And these changes are observed for a much smaller intensity of $50GW/cm^2$. Whilst there is a difference in the pulse lengths between the two measurements setups, modelling of the electron temperature predicts a lower electron temperature in the presented setup of the order $\approx 3000K$, compared with $\approx 4700K$ estimated by Alam [67], this comparison is shown in Figure 7.14. This implies that the changes in reflectivity observed beyond the critical angle in the glass-air-ITO interface are achieved with a smaller change to the material parameters than for [67].

Whilst the figure of merit quoted for the nonlinearity of a sample can vary greatly in the literature, practical applications require both a significant change in the absolute reflectivity, ΔR, and relative change in intensity, $\frac{\Delta R}{R}$. Through both these figures

of merit, one can state the the geometry presented here is more efficient at producing these changes, even for lower intensities. Of the two samples, **ITO2**, which has a thickness of 55.1nm, exhibits larger changes in absolute and differential reflectivity, this is likely due to the plasmonic nature of the ENZ mode, which creates a thickness dependence [230]. However, with a desire to push optical switching to the telecoms wavelengths, it is noteworthy that the sample **ITO3**, which has a measured thickness of 109.1nm exhibits its largest changes with a probe wavelength close to 1500nm. Such flexibility, coupled with the strength of the nonlinear signal observed, clearly push ITO to the forefront as a potential non-linear material for switching applications.

However, the measurement procedure described in Section 4.3.1 of Chapter 4, is time consuming, requiring 12-18 hours depending on sensitivity. A large portion of this is due to the angle rotation of the stage, something that additionally complicates alignment throughout the procedure. As such this work simultaneously sought to investigate the ITO response in the Fourier plane. However, even with comparable fluences, there was no discernible differential signal observed. The most significant difference between the two experimental designs is the pulse length of the laser. In using a longer pulse the same amount of energy was deposited into the system but on a much slower timescale. This could, depending on the thermal relaxation dynamics in ITO, have a significant effect on the expected response. To fully understand the potential applications of ITO, the electron behaviour under intense heating must be examined.

7.6 Two temperature model

In a two temperature model, one considers two separate temperatures within a material, representing the conduction electrons (T_e), and the lattice or phonon temperature (T_p) [231, 232]. These two temperatures will, eventually, be in thermal equilibrium with each other and the room. However, the timescale and manner with which these temperatures converge is governed by their coupling with each other (g_{ep}), scattering rates (τ_e for electrons and τ_p for phonons) and specific heat capacities (C_e and C_p for electrons and phonons respectively). Two temperature models have been successfully applied to metals irradiated by both femtosecond [233, 234] and picosecond pulses [235, 236], as in the setups considered here.

In a two temperature model, the temperature dynamics of the electrons and phonons follow

$$C_e \frac{\partial T_e}{\partial t} = g_{ep}(T_p - T_e) + \frac{N}{2\tau_e}, \tag{7.15}$$

$$C_p \frac{\partial T_p}{\partial t} = g_{ep}(T_e - T_p) + \frac{N}{2\tau_p}, \tag{7.16}$$

$$\frac{\partial N}{\partial t} = S - \frac{N}{2\tau_e} - \frac{N}{2\tau_p}, \tag{7.17}$$

where N represents the energy stored in excited electrons and S is a source term representing the absorbed energy from the laser excitation. The absorbed power density from laser excitation is given by

$$S(t) = (1 - R - T) I_0 \alpha e^{-2(\frac{t}{t_p})^2},$$

where R, T and α are wavelength dependent reflection transmission and absorption coefficients and t_p is the laser pulse duration. T and R are calculated through the transfer matrix method (see Section 4.3 of Chapter 4), and α is calculated through knowledge of the complex refractive index at the given wavelength ($\alpha = \frac{2\omega}{c}\mathrm{Im}(n)$.

One can calculate the temperature dynamics to a good approximation with an iterative solution to the dynamic temperature equations as follows

$$\Delta T_e = \left(g_{ep}(T_p - T_e) + \frac{N}{2\tau_e} \right) \frac{\Delta t}{C_e}, \tag{7.18}$$

$$\Delta T_p = \left(g_{ep}(T_e - T_p) + \frac{N}{2\tau_p} \right) \frac{\Delta t}{C_p}, \tag{7.19}$$

$$\Delta N = \left(S - \frac{N}{2\tau_e} - \frac{N}{2\tau_p} \right) \Delta t, \tag{7.20}$$

where Δt is a time parameter which must be sufficiently small to encompass the temperature dynamics ($\Delta T \ll t_p$).

7.6.1 Parameters for the two temperature model

Alam [67], is the most relevant work on applying the two temperature model to the photoexcitation of ITO. This work gives the electron phonon coupling parameter (g_{ep}) and scattering parameters (τ_e for electrons and τ_p for phonons) as

$$g_{ep} = 0.562 n_e \frac{k_b^2 \Theta_D^2 v_f}{L_f T_p E_f}, \tag{7.21}$$

$$\tau_e = C \left\{ \frac{\omega^2}{4\pi^2 \omega_p} \left\{ 1 + \left(\frac{2\pi k_b T_e}{\hbar \omega} \right)^2 \right\} \right\}, \tag{7.22}$$

$$\tau_p = 2 \frac{C_e}{g_{ep}}, \tag{7.23}$$

in which k_b is Boltzmann's constant, L_f is the electron mean free path, Θ_D is the Debye temperature, ω is the angular frequency of the laser beam, n_e is the free electron density and v_f and E_f are the Fermi velocity and energy respectively. C is a fit parameter to ensure that the Drude scattering parameter γ is equal to $\frac{1}{\tau_e} + \frac{1}{\tau_p}$ at $300K$.

For lattice temperatures lower than the the Debye temperature Θ_D (reported to be $\approx$ $1000K$ in ITO[237]), the lattice heat capacity is approximately constant at a value of $2.6 \times 10^{-6} Jm^{-3}K^{-1}$ [67, 238]. The specific heat capacity for electrons is stated by Alam[67] to be $4.53 Jm^{-3}K^{-1}$, however this is incorrect. Not only is this value much lower than discussed in the text[2], the electron density (n_e) at $300K$ associated with this value for C_e given by,

$$C_e = \frac{3\pi^2 n_e k_b T_e}{\sqrt{36 T_f^2 + 4\pi^4 T_e^2}}, \tag{7.24}$$

[2] This value is stated be over an order of magnitude less than that of gold, whereas it is in fact almost 4 orders of magnitude less than gold, $C_e = 2.1 \times 10^4 Jm^{-3}K^{-1}$ [239]

is extremely low ($n_e \approx 2.6 \times 10^{24} m^{-3}$) and leads to a much lower plasma frequency than measured. The plasma frequency in metals well described by the Drude model can be expressed as

$$\omega_p = \sqrt{\frac{n_e e^2}{m^* \epsilon_\infty \epsilon_0}}, \tag{7.25}$$

where ϵ_∞ is the high frequency permittivity limit. With the plasma frequency quoted as $\omega_p^{ALAM} = 2.97 \times 10^{15}$[67] and an effective mass of $m^* = 0.4 m_e$, one obtains an electron density $n_e = 4.4 \times 10^{27} m^{-3}$, which is far closer to other measured values for ITO ($\approx 10^{26} - 10^{27}$ [240, 241]). The expression for C_e itself is confirmed by other works in the area [231, 242, 243] who used a simplified version under the approximation $T_e < T_f$ such that

$$C_e = \frac{\pi^2 n_e}{2} k_b \frac{T_e}{T_f}.$$

Therefore, in the modelling presented here, the electron density is calculated through the experimentally measured plasma frequency and the given value for C_e discarded.

7.6.2 Predicted electron temperatures

One can now, with the model and parameters described, predict the temperature response of the electrons and phonons in ITO for both systems considered. Figures 7.14 and 7.15 show the predicted temperatures for a variety of systems under consideration.

Those systems are the experimental work of Alam [67], the experimental prism setup (Section 4.3.1 of Chapter 4), and an experimental setup using a picosecond excitation. This setup is modelled with both a single beam excitation and a separate pump excitation as was experimentally investigated to no result.

Figure 7.14 shows the electron temperatures for ITO excitation in the femtosecond geometry. One observes that in both setups the electron temperatures are raised on the order of $\approx 10^3 K$, along with a lattice temperature of $500 - 600K$. Thermal equilibrium is achieved approximately at the peak lattice temperature due to the far lower specific heat capacity of electrons, for comparison $\frac{C_e}{C_p} \approx 3 \times 10^{-3}$ in ITO whereas the same ratio is approximately $10^{-2} - 10^{-1}$ for gold [232], depending on

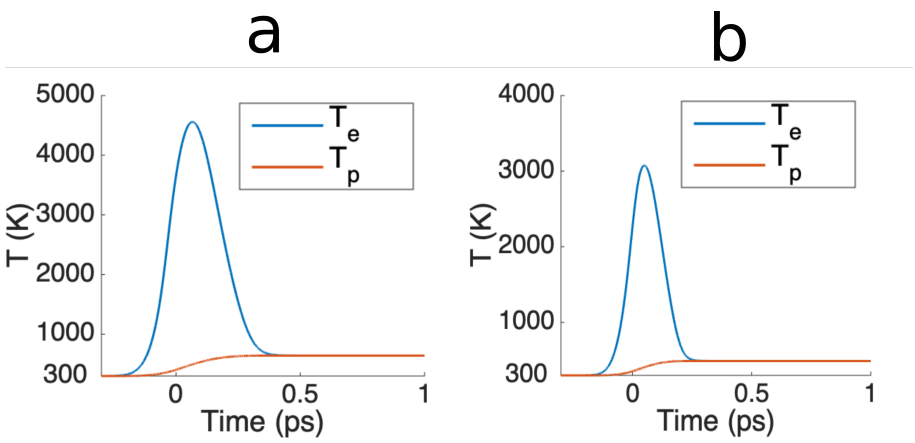

FIGURE 7.14: Electron and lattice temperature as a function of time for two femtosecond pulse. Panel **a** predicts the electron temperature in the experimental setup of Alam [67], with a pulse length of $150fs$ and a peak intensity of $66GW/cm^2$. Panel **b** predicts the temperatures for the prism setup as described in Chapter 4, with a pulse length of $110fs$ and an intensity of $50GW/cm^2$.

temperature. Due to this phenomena, energy loss from the electron bath to the lattice temperature has very little effect on the lattice temperature. The fast timescale on which this equilibrium occurs is governed by the the electron-phonon coupling parameter g_{ep}, where $g_{ep}(300K) \approx 10^{18} Wm^{-3}K^{-1}$.

Figure 7.15 highlights the constraints of using ITO as a potential switching material. For optical wavelengths, as represented in Panel **b**, the low absorption coefficient $\alpha_{532} = 5.25 \times 10^4 m^{-1}$[244] prevents efficient transfer of energy from the source to the electron temperature. Therefore, even for fluences approaching ablation ($\phi_{ab} = 3000J/m^2$ [245]) one does not achieve a large increase in T_e. At pulse lengths of the order of $> 1ps$, the rate of heating is comparable to the rate at which the electron bath couples to the lattice temperature, suppressing electron temperature response to the pumping. This behaviour causes the phonon temperature to follow the electron temperature very closely, except under extremely high fluence noted in Panel **c** ($\phi \approx 10^3 Jm^{-2}$).

The strong coupling rate, with respect to the heating of a picosecond pulse, explains the close alignment of electron and phonon temperatures, but not the relative size compared to the femtosecond models in Figure 7.14. This reduced temperature is due to the large difference in specific heat capacities, which for ITO calculated at 300K are $C_e = 7.7 \times 10^3$ and $C_p = 2.6 \times 10^6 Jm^{-3}K^{-1}$ causing a much lower temperature at thermal equilibrium.

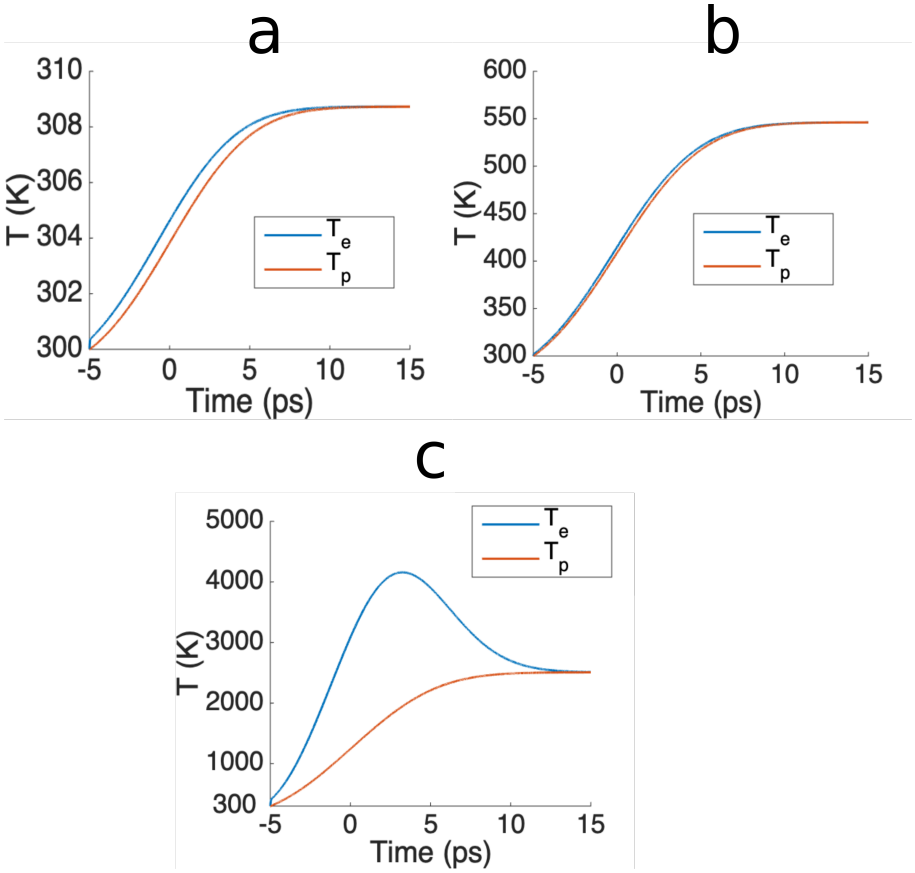

FIGURE 7.15: Electron and lattice temperatures as a function of time for picosecond excitation of ITO. All Panels are modelled for a pulse length of $8ps$. Panel **a** considers a fluence of $10J/m^2$ at $1240nm$, as is the maximum available when investigating single beam excitation in the microscope. Panel **b** represents a pumped excitation with an optical $532nm$ beam of fluence of $5 \times 10^3 J/m^2$. Panel **c** shows excitation with with $1240nm$ and a fluence of $\approx 10^3 J/m^2$, this is modelled to realise a similar temperature change as occurs in femtosecond excitation.

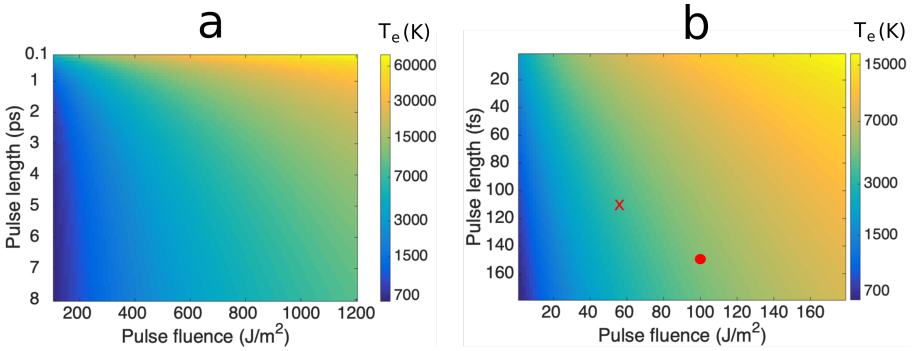

FIGURE 7.16: Predicted maximum electron temperature as a function of pulse length and pulse fluence. Panel **a** shows pulses with sufficient fluence to excite electron temperatures of $\approx 3 - 5000K$. Panel **b** shows lower fluence, shorter pulses comparable to discussed experiments. The red cross represents the experimental setup presented here, the red dot represents that of [67]. One notes that predicted temperatures larger than $15000K$, as observed in the most extreme regions, are likely to be outwith the validity of the model. In particular the specific heat of the lattice is modelled as a constant, which is only true for lattice temperatures below the Debye temperature $\Theta_D = 1000K$

In order to overcome the strong coupling and high specific heat capacity of ITO which causes the aforementioned effects, one must significantly increase the pulse fluence. This increased fluence is modelled in Panel **c** of Figure 7.15 for a pulse of $8ps$. Figure 7.16 expands on this conclusion to show the predicted electron temperature as a function of pulse length and fluence for much longer and shorter pulse lengths. The experimental region this work and Alam [67] are marked on Panel **b**. Such short pulse lengths allow for significant raised electron temperatures with relatively modest fluences of $\approx 100J/m^2$. However, in order to reduce the fluence of this experiment by a factor of two, one would require pulses of the order 30-40fs, owing to the nonlinear relationship between electron temperature and pulse length (or pulse fluence). Therefore, it is debatable whether moving to shorter fluences is advantageous for practical applications, due to increased complication associated with generating and overlapping significantly shorter pulses.

It is important to note that one of the constraints of this two temperature model is that the lattice heat capacity, C_p, is independent of temperature when the lattice temperature does not exceed the Debye temperature, $\Theta_D = 1000K$, which is not the case in such a high fluence picosecond model. In addition, the fluence of such an excitation, that achieves a comparable electron temperature to that of the femtosecond

systems (see Figure 7.14), is modelled as $\approx 10^3 Jm^{-2}$. Such a fluence is very close to the ablation level of $3 \times 10^3 Jm^{-2}$[245]. Operating at such fluences is not feasible in such samples experimentally, and even less so for practical applications.

7.7 Conclusions

Indium tin oxide remains a highly promising material with a host of routes for further exploitation (see Chapter 8). The work presented here confirms results presented in [67], that ITO is an excellent material for intensity based differential reflection applications such as ultrafast switching. The wavelength range where such changes occur can be quite broad depending on the ENZ resonance and thickness.

Further to this confirmation, the specific geometry exploited in this thesis shows an incredible flexibility to the ITO's nonlinearity, as large changes are observed at probe wavelengths of $\approx$ 1500nm, or 1200nm depending on the sample thickness. In both cases these changes are of a similar order or higher than nonlinear results presented previously [67], and with much smaller intensities.

However, the ultrafast switching highlighted as a strength of the material, is also a constraint. The two temperature model presented in this work extends previous considerations of the behaviour of ITO under intense illumination and clarifies conditions that must be met to achieve such large changes in differential reflection. The combination of strong electron phonon coupling, combined with a large difference in the specific heat capacities causes the energy in the electron bath to be transferred to the lattice temperature quickly, whilst not significantly raising the lattice temperature.

This modelling shows that, for longer pulse lengths, the increase in fluence required to achieve the same temperature change is extremely high, in the case of an 8ps excitation pulse one requires an order of magnitude increase in the fluence. This would place the excitation around the damage threshold of ITO and even approaching clean ablation [245], in addition to not being feasible for practical applications, or even most experimental investigations.

It is therefore crucial, that any potential applications of ITO are not limited by the ultrafast electron phonon coupling in ITO and can operate on the $\approx 100 - 200 fs$

scale, a consideration hitherto unmentioned.

Chapter 8

Conclusions and further work

This thesis covered three distinct areas of investigation. Those areas are the second order conductivity of graphene, plasmon enhanced four-wave mixing (FWM) in graphene and intensity base differential reflectivity in indium tin oxide (ITO). This chapter will summarise the knowledge gained in each of these and how to further each investigation.

8.1 Second order conductivity of graphene

The second order conductivity of graphene remains a highly contentious subject due to its forbidden nature. Theoretical treatments of the second order conductivity can differ significantly [14, 15, 207, 17], in approach and even predicted magnitude. As such it is clear the field is in need of more rigorous investigation, especially as some much cited works contains demonstrably non-physical predictions that have not been addressed [14]. Recently, several treatments of the second order conductivity based on perturbation theory (a common method for calculating non-linear responses [246, 16]) have produced consistent results [15, 173, 17], but significantly lower than experiments suggest [35, 181].

In view of the consistent results of theory and the discrepancy with experiments, this work set out to explore other origins of the non-linear response observed in experiments. Firstly, the substrate response is firmly ruled out as an origin of enhanced signals, before considering photothermal effects, in particular the Seebeck effect.

The Seebeck effect allows for generation of real currents when there is a spatial intensity profile to the electron temperature. These currents have a firm physical

origin and must be present in the systems described. When modeling the strength of this signal, this thesis finds a response significantly higher than predicted through perturbation theory. The Seebeck effect is a known effect in graphene, but this thesis presents the first investigation into the effect on the nonlinear signal. Advancing this model lies in more accurately measuring the ultrafast heating dynamics in graphene, which are not firmly established on the $\approx 10fs$ timescales relevant.

8.2 Plasmon enhanced four-wave mixing in graphene

Graphene is a highly promising material in the fields of both plasmonics and nonlinear optics, being able to combine these phenomena is extremely advantageous. Cascaded effects contributing to the nonlinearity of graphene have already been demonstrated, with Smirnova showing and enhancement of 5 through cascaded effects using waveguide modes [57]. The work presented here investigates the possibility of a cascaded interaction in graphene enhanced by an intermediate stage which couples to the surface plasmon polariton.

The results presented in this thesis conclusively show that there is no significant enhancement to the third order nonlinear signal in graphene when the difference frequency mode is phasematched to the surface plasmon. This result implies that the field enhancement of the surface plasmon is not sufficient to overcome the inherent weakness of second order modes, in a process that requires two separate second order interactions.

8.3 Differential reflectivity of indium tin oxide

Indium tin oxide (ITO) has recently received much attention for its nonlinear properties in the epsilon near zero region, with Alam observing a 300% change in transmission [67] for fluences of $250GW/cm^2$. In this thesis a new geometry is modelled and investigated that probes the reflectivity of a glass-ITO-air interface near the critical angle of glass.

For this geometry both modelling predictions and the measured response of the ITO show changes larger than have been previously observed. Whilst figures of

merit can vary depending on setup, in the proposed geometry one observes changes of $300 - 400\%$ in reflection at much lower intensities of $\approx 50 GW/cm^2$. The work presented here extends a highly promising area of physics with many possible extensions. One such extension is to study the dependence of the nonlinearity on the thickness of the ITO. In the work presented, one observes that a sample of $\approx 50nm$ produces a stronger nonlinearity than a sample of $\approx 100nm$, but it is unclear what thickness is optimal for this change in reflection. Additionally, one notes that the sample of $\approx 100nm$ exhibits a peak in its nonlinearity at a longer wavelength ($\approx 1500nm$ for $100nm$ and $\approx 1200nm$ for $50nm$). This opens the exciting possibility of tuning the nonlinearity to a desired wavelength with film thickness. In particular, there is a high desire for samples exhibiting such nonlinearity in the telecoms band around $1500nm$, as is the case for $100nm$ of ITO.

However, there is a strong restriction placed on the use of this differential reflection. These changes are only observable on ultrafast timescales of the order $100fs$. As the pulse length increases, the strong coupling between the electron and phonon temperatures, combined with the large specific heat capacity of phonons, prevents the electron temperature raising beyond $\approx 500K$. Potential applications of this differential reflection can only be realised on such fast timescales, a strongly limiting consideration.

As a further extension, modelling of ITO of similar parameters to that of [67] around the surface plasmon polariton resonance show significant changes in differential reflection. Figure 8.1 shows these changes for the same experimental setup as investigated in this thesis, the ITO parameters match that of [67].

The plasmon resonance exhibits very different characteristics to the ENZ mode at the air glass critical angle. Panel **c** of Figure 8.1 shows that for this geometry and resonance one predominantly observes a negative differential reflection, as opposed to the positive changes observed in Chapter 7. This is cause by the resonance broadening, as opposed to shifting with the same approximate width in frequency space. The negative differential reflections observed here are of similar order to those measured in Chapter 7, but correspond to a lower percentage change due to the higher reflection before photoexcitation. Whilst this resonance does not explicitly show more nonlinearity, the value of being able observe a similar effect to that observed

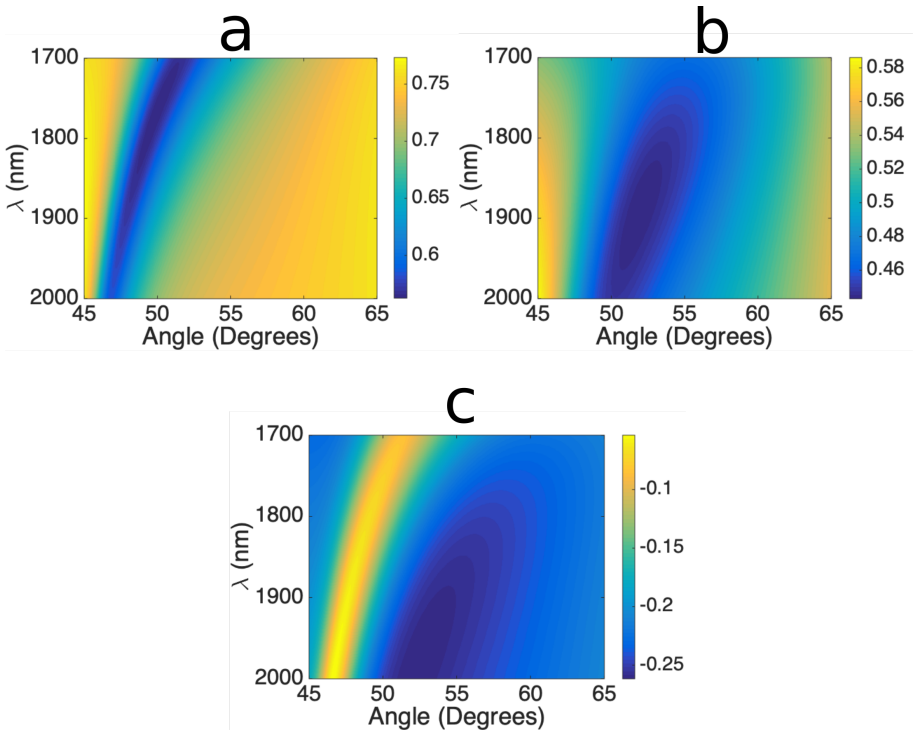

FIGURE 8.1: Modelled reflectivity changes in ITO as a function of wavelength and angle. Panel **a** shows the absolute reflection without photoexcitation, Panel **b** shows the absolute reflection under irradiation from a source of $50GW/cm^2$ and Panel **c** shows the difference between the two. All ITO parameters for this model are taken from [67] and the change in the Drude parameters is modelled through the parametrisation given in Equations 7.4 and 7.5.

in previous measurements around 1800nm could prove useful and warrants investigation.

Appendix A

Transmission coefficients

This work is taken from Constant et. al. [35], in particular Prof. Darrick Chang who developed the model and wrote this section for the manuscript "Origins of All-Optical Generation of Plasmons in Graphene"[17].

This model assumes a frequency independent susceptibility. However, this assumption has been tested and does not significantly modify the result, since the differential reflection signal in the model is predominantly determined by absorption of the difference frequency field, and hence by the magnitude of the susceptibility at the difference frequency. Throughout this derivation one follow Constant[35] and take a plasmon linewidth of order ~ 10 THz.

The convention to define the field polarizations and beam angles is illustrated in Fig. 1. In general, the transmission coefficients can be found by imposing boundary conditions at the graphene interface (continuity of the normal electric displacement and tangential electric field). For the transmission coefficient of field i ($i = 1, 2$),

$$t_i = \frac{2\sin\theta_i}{n_i\sin\theta_i + \sin\phi_i} - \left(\frac{\rho_{is}}{\epsilon_0 E_{Ii}}\right)\frac{\sin\theta_i}{n_i\cos\phi_i\left(n_i\sin\theta_i + \sin\phi_i\right)}, \tag{A.1}$$

where E_{Ii} are the incident field amplitudes, $n_i = n(\omega_i)$ denotes the index of refraction of the substrate at the field frequency, and $\rho_{is} = \rho(\omega_i, q_i)$ is the graphene surface charge density at frequency ω_i and in-plane wavevector $q_i = (\omega_i/c)\cos\theta_i$. The reflection coefficients r_i can be obtained via the relation $r_i + (\sin\phi_i/\sin\theta_i)t_i = 1$. As in Constant[35], the substrate model given by Luxmoore[247] is taken:

$$n^2(\omega) = \epsilon_\infty + \sum_{j=1}^{3}\frac{f_j\,\omega_{TO,j}^2}{\omega_{TO,j}^2 - \omega^2 - i\omega\gamma_{TO,j}}. \tag{A.2}$$

The high-frequency dielectric constant $\epsilon_\infty = 2.4$, and $\omega_{TO} = 2\pi \times (13.44, 23.75, 33.84)$ THz, $\gamma_{TO} = 2\pi \times (0.80, 1.27, 1.27)$ THz, and $f = (0.7514, 0.1503, 0.6011)$ are the frequencies, damping rates, and oscillator weights of the three transverse optical phonon modes respectively. In practice, Eq. (A.2) is only relevant at low difference frequency of $\omega_3 = \omega_1 - \omega_2$, whereas for the high pump and probe frequencies $\omega_{1,2}$ the index of refraction is nearly a constant: $n \approx \sqrt{\epsilon_\infty}$. ρ_{is} can be related to the current density j in the graphene layer via the continuity equation, in the Fourier space yielding: $\rho_{is}(\omega_i, q_i) = (q_i/\omega_i) j_x(\omega_i, q_i)$. When depletion can be ignored, as is the case in Constant[35], the current densities at these frequencies can be approximated by their linear response results:

$$j_x(\omega_i, q_i) = \sigma^{(1)}(\omega_i) E_x(\omega_i, q_i). \tag{A.3}$$

Here, $E_x(\omega_i, q_i) = t_i E_{Ii} \sin\phi_i$ are the total parallel fields in the graphene layer.

The field generated at the difference frequency $\omega_3 = \omega_1 - \omega_2$ can be found similarly by using the boundary conditions at the graphene interface. In particular, a source term j_s is included in the current density depending on the origin of DFG, this term describes the generated field independent from the graphene's linear response to the field at the frequency:

$$j_x(\omega_3, q_3) = \sigma^{(1)}(\omega_3) E_{3x} + j_s(\omega_3, q_3). \tag{A.4}$$

j_s can arise from different nonlinear processes, e.g. in Constant[35] this is taken as a result of graphene nonlinearity, however this can originate from the Seebeck effect, and can then induce a plasmon field.

Appendix B

Estimation of $\chi^{(3)}$

B.1 Polarisation of an infinite 2-D sheet

This derivation was original completed by Dr. Simon Horsley and Dr. Thomas Constant to aid with preliminary experiments into four wave mixing.

One begins with Ampere's law as follows

$$\nabla \times \vec{B} = \mu_0 \vec{J} h + \frac{1}{c^2} \frac{\partial \vec{E}}{\partial t}, \tag{B.1}$$

where $\vec{B}$ is the magnetic flux density, μ_0 is the permeability of free space, h is the thickness of graphene, $\vec{J}$ is the current density. Then, one can consider the current only in $\hat{x}$ and localised to the surface ($z = 0$).

$$\nabla \times \vec{B} = \mu_0 \delta(z) J(t) \hat{x} + \frac{1}{c^2} \frac{\partial \vec{E}}{\partial t}, \tag{B.2}$$

differentiating both side with respect to t one arrives at

$$\nabla \times \frac{d\vec{B}}{dt} = \mu_0 \delta(z) h \hat{x} \frac{d}{dt} J(t) + \frac{1}{c^2} \frac{\partial \vec{E}}{\partial t}. \tag{B.3}$$

Then replace $\nabla \times \vec{E} = -\frac{d\vec{B}}{dt}$ leading to

$$\nabla \times \nabla \times \vec{E} = -\mu_0 \delta(z) h \hat{x} \frac{d}{dt} J - \frac{1}{c^2} \frac{\partial \vec{E}}{\partial t}. \tag{B.4}$$

We know that $\vec{E} = E_x \hat{x}$, and this field does not vary in $\hat{x}$ or $\hat{y}$. Therefore the above equation reduces to

$$\frac{d^2}{dz^2} E_x + \frac{\omega^2}{c^2} E_x = -i\omega \mu_0 \delta(z) J h. \tag{B.5}$$

This equation now has a the form of Green's theorem

$$LU(z) = f(z), \tag{B.6}$$

where L is an operator, $U(z)$ is a function to be solved and $f(z)$ is a known function. In this specific case they have the following forms

$$L = \frac{d^2}{dz^2} + k_0^2$$

$$U(z) = E_x(z)$$

$$f(x) = -i\omega\mu_o\delta(z)Jh.$$

The general solution to Green's theorem is

$$U(z) = \int G(z-s)f(s)ds \tag{B.7}$$

where G is a Greens function designed such that $LG(z-s) = \delta(x-s)$. The Greens function as the chosen solution to this is

$$G = \frac{e^i k_0|z-z'|}{2ik_0}, \tag{B.8}$$

therefore we can solve for E_x using equation B.7.

$$E_x = \int G(z-z')f(z')dz' \tag{B.9}$$

$$E_x = \int \frac{e^{ik_0|z-z'|}}{2ik_0}(-i\omega\mu_0\delta(z)Jh)dz' \tag{B.10}$$

$$E_x = -\frac{\omega\mu_0 Jh}{2k_0}e^{ik_0|z|}\int e^{-ik|z'|\delta(z')dz'}. \tag{B.11}$$

With the right hand integral equal to 1 we arrive at

$$E_x = -\frac{1}{2}\sqrt{\frac{\mu_0}{\epsilon_0}}Jhe^{ik_0|z|}. \tag{B.12}$$

B.2 Field produced by non-linear polarisation

Now we need to represent the current density ($\vec{J} = \frac{d\vec{P}}{dt}$) with the nonlinear coefficient and third order susceptibility as follows

$$|E_{NL}|^2 = \frac{1}{4}\frac{\mu_0}{\epsilon_0}h^2|\frac{d}{dt}P_{NL}|^2. \tag{B.13}$$

This allows us to represent the nonlinear polarisation as a function of the susceptibility and input fields.

$$\vec{P}(2\omega_1 - \omega_2) = 3\epsilon_0\boldsymbol{\chi^{(3)}} : \vec{E}^2\vec{E}^*, \tag{B.14}$$

here we have taken the convention of Boyd [198] with regards to the prefactor form of $\boldsymbol{\chi^{(3)}}$. Additionally this equation represents the tensor nature of $\boldsymbol{\chi^{(3)}}$, however we reduce this going forward to a magnitude representing the response in the $\hat{x}$ direction to incident fields in the x direction and consider a magnitude. Replacing Eq. B.14 into Eq. B.13, with the fields have the form $\vec{E}_\alpha = |E_\alpha|e^{-i\omega_\alpha t}$ gives

$$|E_{NL}|^2 = \frac{9}{4}\mu_0\epsilon_0h^2|\chi^{(3)}|^2|\omega_2 - 2\omega_1|^2|\vec{E}_1|^2|\vec{E}_2|. \tag{B.15}$$

Rearranging for $|\chi^{(3)}|$ gives

$$|\chi^{(3)}| = \frac{2}{3}\frac{c}{h}\frac{|\vec{E}_{NL|}}{|2\omega_1 - \omega_2||\vec{E}_1|^2|\vec{E}_1|} \tag{B.16}$$

B.3 Relationship between Electric field intensity and power

The average instantaneous power during illumination by a pulse (ρ_{inst}) is given by

$$\rho_{inst} = f_s\frac{\rho}{\tau t}, \tag{B.17}$$

where ρ is the time averaged power, τ is the repetition rate of the laser system and t is the pulse length. f_s is a pulse shape factor, which for a gaussian pulse is ≈ 0.94.

We relate the intesnity to power through the time averaged Poynting vector,

$$I = \frac{\rho_{inst}}{A} = \frac{1}{2}\epsilon_0 c|E|^2, \tag{B.18}$$

where A is the beam spot area. Combining this representation with equation B.16 we find

$$|\chi^{(3)}| = \frac{A\sqrt{\rho_{NL}\epsilon_0 c^2 \tau t}}{9 f_s \rho_1 \sqrt{\rho_2}|\omega_2 - 2\omega_1|h}. \tag{B.19}$$

Bibliography

[1] T. H. Maiman. “Stimulated Optical Radiation in Ruby”. In: *Nature* 4736 (1960), p. 493.

[2] R. J. Collins et al. “Coherence, narrowing, directionality, and relaxation oscillations in the light emission from ruby”. In: *Physical Review Letters* 5.7 (1960), pp. 303–305.

[3] P. A. Franken et al. “Generation of optical harmonics”. In: *Physical Review Letters* 7.4 (1961), pp. 118–119.

[4] R.W. Terhune, P.D. Maker, and C.M. Savage. “Observation of saturation effects in optical harmonic generation”. In: *Applied Physics Letters* 2.3 (1963), pp. 54–55.

[5] C.C. Wang and E.L. Baardsen. “Optical Third Harmonic Generation Using Mode-Locked and Nonmode-Locked Lasers”. In: *Applied Physics Letters* 15.12 (1969), pp. 396–397.

[6] C.C. Wang and E.L. Baardsen. “Study of Optical Third-Harmonic Generation in Reflection”. In: *Physical Review* 185.3 (1969), pp. 1079–1082.

[7] R.C. Eckardt and C.H. Lee. “Optical Third Harmonic Measurements of Subpicosecond Light Pulses”. In: *Applied Physics Letters* 15.12 (1969), pp. 425–427.

[8] G.H.C. New and J.F. Ward. “Optical Third-Harmonic Generation in Gases”. In: *Physical Review Letters* 19.10 (1967), pp. 556–559.

[9] W.G. Rado. “The nonlinear third order dielectric susceptibility coefficients of gases and optical third harmonic generation”. In: *Applied Physics Letters* 11.4 (1967), pp. 123–125.

[10] J.F. Ward and G. H. C. New. “Optical Third Harmonic Generation in Gases by a Focused Laser Beam”. In: *Physical Review* 185.1 (1969), pp. 57–72.

[11] J.A. Armstrong et al. “Interactions Between Light Waves In a Nonlinear Dielectric”. In: *Physical Review* 19 ().

[12] N. Bloembergen and P.S. Pershan. “Light waves at the boundary of nonlinear media”. In: *Physical Review* 128.2 (1962), pp. 606–622.

[13] P. Sitz and R. Yaris. “Frequency Dependence of the Higher Susceptibilities”. In: *Journal of Chemical Physics* 49.8 (1968), pp. 3546–3557.

[14] X. Yao, M. Tokman, and A. Belyanin. “Efficient nonlinear generation of THz plasmons in graphene and topological insulators”. In: *Physical Review Letters* 112.5 (2014), pp. 1–5.

[15] M. Tokman et al. “Laser-driven parametric instability and generation of entangled photon-plasmon states in graphene and topological insulators”. In: *Physical Review B* 93.28 (2016), p. 235422.

[16] J. D. Cox and F. J. García de Abajo. “Electrically tunable nonlinear plasmonics in graphene nanoislands.” In: *Nature Communications* 5 (2014), p. 5725.

[17] C. J. Tollerton et al. “Origins of All-Optical Generation of Plasmons in Graphene”. In: *Scientific Reports* 9.1 (2019), pp. 1–12.

[18] N. Vermeulen et al. “Graphene’s nonlinear-optical physics revealed through exponentially growing self-phase modulation”. In: *Nature Communications* 9 (2018).

[19] J.A. Giordmaine and R.C. Miller. “Tunable Coherent Parametric Oscillation in LiNbO_3 at Optical Frequencies”. In: *Physical Review Letters* 14.24 (1965), pp. 973–976.

[20] S.A. Akhmanov and Klyshko D. N. “Three-photon Molecular Scattering of Light”. In: 2 (4 1965).

[21] Y Fainman, J Ma, and S.H. Lee. “Non-linear optical materials and applications”. In: *Materials Science Reports* 9.2-3 (1993), pp. 53–139.

[22] A. Rice et al. “Terahertz optical rectification from 110 zinc-blende crystals”. In: *Applied Physics Letters* 64.11 (1994), pp. 1324–1326.

[23] E. Garmire. “Nonlinear optics in daily life”. In: *Optics Express* 21.25 (2013), p. 30532.

[24] O. Schubert et al. "Sub-cycle control of terahertz high-harmonic generation by dynamical Bloch oscillations". In: *Nat. Photonics* 8.2 (2014), pp. 119–123.

[25] T.T. Luu et al. "Extreme ultraviolet high-harmonic spectroscopy of solids". In: *Nature* 521.7553 (2015), pp. 498–502.

[26] G. Vampa et al. "Linking high harmonics from gases and solids". In: *Nature* 522.7557 (2015), pp. 462–464.

[27] M. Hohenleutner et al. "Real-time observation of interfering crystal electrons in high-harmonic generation". In: *Nature* 523.7562 (2015), pp. 572–575.

[28] H. Liu et al. "High-harmonic generation from an atomically thin semiconductor". In: *Nature Physics* 13.3 (2017), pp. 262–265.

[29] S. Ghimire et al. "Observation of high-order harmonic generation in a bulk crystal". In: *Nature Physics* 7.2 (2011), pp. 138–141.

[30] J.R. Fontana and R.H. Pantell. "Theoretical Considerations on Millimeter Wave Generation by Optical Frequency Mixing". In: *IEEE Xplore: Proceedings of IRE* 50.8 (1962), pp. 1796–1800.

[31] K.E. Niebuhr. "Generation of laser axial mode difference frequencies in a nonlinear dielectric". In: *Applied Physics Letters* 2.7 (1963), pp. 136–137.

[32] F. Zernike and P.R. Berman. "Generation of far infrared as a difference frequency". In: *Physical Review Letters* 15.26 (1965), pp. 999–1001.

[33] J. Renger et al. "Free-Space Excitation of Propagating Surface Plasmon Polaritons by Nonlinear Four-Wave Mixing". In: *Physical Review Letters* 103.26 (2009), p. 266802.

[34] J. Renger et al. "Surface-Enhanced Nonlinear Four-Wave Mixing". In: *Physical Review Letters* 104.4 (2010), p. 046803.

[35] T.J. Constant et al. "All-optical generation of surface plasmons in graphene". In: *Nature Physics* 12.2 (2016), pp. 124–127.

[36] "Terahertz-wave surface-emitted difference frequency generation in slant-stripe-type periodically poled LiNbO3 crystal". In: *Applied Physics Letters* 81.18 (2002), pp. 3323–3325.

[37] C. Erny et al. "Mid-infrared difference-frequency generation of ultrashort pulses tunable between 32 and 48 μm from a compact fiber source". In: *Optics Letters* 32.9 (2007), p. 1138.

[38] O. Levi et al. "Difference frequency generation of 8-m radiation in orientation-patterned GaAs". In: *Optics Letters* 27.23 (2002), p. 2091.

[39] M.A. Belkin et al. "Terahertz quantum-cascade-laser source based on intracavity difference-frequency generation". In: *Nature Photonics* 1.5 (2007), pp. 288–292.

[40] D.M. Pepper et al. "Spatial convolution and correlation of optical fields via degenerate four-wave mixing". In: *Optics Letters* 3.1 (1978), p. 7.

[41] R.W. Hellwarth. "Generation of time-reversed wave fronts by nonlinear refraction". In: *Journal of the Optical Society of America* 68.8 (1976), p. 1155.

[42] J.H. Marburger and J.F. Lam. "Nonlinear theory of degenerate four-wave mixing". In: *Applied Physics Letters* 34.6 (1979), pp. 389–391.

[43] W.W. Rigrod, R.A. Fisher, and B.J. Feldman. "Transient analysis of nearly degenerate four-wave mixing". In: *Optics Letters* 5.3 (1980), pp. 105–107.

[44] D.A.B. Miller. "Time reversal of optical pulses by four-wave mixing". In: *Optics Letters* 5.7 (1980), p. 300.

[45] A. Yariv and D.M. Pepper. "Amplified reflection, phase conjugation, and oscillation in degenerate four-wave mixing". In: *Optics Letters* 1.1 (1977), p. 16.

[46] D.M. Bloom and G.C. Bjorklund. "Conjugate wave-front generation and image reconstruction by four-wave mixing". In: *Applied Physics Letters* 31.9 (1977), pp. 592–594.

[47] D.M. Bloom, P.F. Liao, and N.P. Economou. "Observation of amplified reflection by degenerate four-wave mixing in atomic sodium vapor". In: *Optics Letters* 2.3 (1978), p. 58.

[48] P.F. Liao, D.M. Bloom, and N.P. Economou. "Cw optical wave-front conjugation by saturated absorption in atomic sodium vapor". In: *Applied Physics Letters* 32.12 (1978), pp. 813–815.

[49] P.F. Liao and D.M. Bloom. "Continuous-wave backward-wave generation by degenerate four-wave mixing in ruby". In: *Optics Letters* 3.1 (1978), p. 4.

[50] N. V. Kukhtarev and S. G. Odoulov. "Wavefront Conjugation Via Degenerate Four-Wave Mixing In Electro-Optic Crystals". In: *Optics Photonics Applied to Communications Processes.* 0213 (1980), pp. 2–9.

[51] J-L. Oudar and Y.R. Shen. "Nonlinear spectroscopy by multiresonant four-wave mixing". In: *Physcial Review A* 22 (1980), pp. 1141–1158.

[52] R.K. Raj et al. "High-frequency optically heterodyned saturation spectroscopy via resonant degenerate four-wave mixing". In: *Physical Review Letters* 44 (1980), pp. 1251–1254.

[53] N. Bloembergen. *Recent Progress in Four-Wave Mixing Spectroscopy*. Springer, 1977.

[54] M. Baumgartl et al. "Alignment-free, all-spliced fiber laser source for CARS microscopy based on four-wave-mixing." In: *Optics Express* 20.19 (2012), pp. 21010–8.

[55] L. Lavoute et al. "High power red and near-IR generation using four wave mixing in all integrated fibre laser systems". In: *Optics Express* 18.15 (2010), p. 16193.

[56] S. Palomba and L. Novotny. "Nonlinear Excitation of Surface Plasmon Polaritons by Four-Wave Mixing". In: *Physical Review Letters* 101.5 (2008), p. 056802.

[57] D.A. Smirnova and A.S. Solntsev. "Cascaded third-harmonic generation in hybrid graphene-semiconductor waveguides". In: *Physical Review B - Condensed Matter and Materials Physics* 92.15 (2015), pp. 1–5.

[58] N. An et al. "Cherenkov high-order harmonic generation by multistep cascading in $\chi^{(2)}$ nonlinear photonic crystal". In: *Applied Physics Letters* 100.221103 (2012).

[59] H. Zheng et al. "Parametric amplification and cascaded-nonlinearity processes in common atomic system". In: *Scientific Reports* 3 (2013).

[60] M. Belotti et al. "All-optical switching in 2D silicon photonic crystals with low loss waveguides and optical cavities". In: *Optics Express* 16.15 (2008), pp. 11624–11636.

[61] T.A. Ibrahim et al. "All-optical switching in a laterally coupled microring resonator by carrier injection". In: *IEEE Photonics Technologies Letters* 15.1 (2003), pp. 36–38.

[62] M.J. Damzen and M.H.R. Hutchinson. "Laser Pulse Compression by Stimulated Brillouin Scattering". In: *Quantum Electronics and Electro-Optics* (1983), p. 401.

[63] C. Min et al. "All-optical switching in subwavelength metallic grating structure containing nonlinear optical materials". In: *Optics Letters* 33.8 (2008), p. 869.

[64] H.G. Park, C.C. Pohalski, and B.Y. Kim. "Optical Kerr switch using elliptical-core two-mode fiber". In: *Optics Letters* 13.9 (1988), p. 776.

[65] Y. Liu et al. "Ultrafast optical switching in Kerr nonlinear photonic crystals". In: *Frontier Physics China* 5.3 (2010), pp. 220–244.

[66] Q.F. Zhang et al. "Ultrafast optical Kerr effect of Ag-BaO composite thin films". In: *Applied Physics Letters* 82.6 (2003), pp. 958–960.

[67] M.Z. Alam, I. De Leon, and R.W. Boyd. "Large optical nonlinearity of indium tin oxide in its epsilon-near-zero region". In: *Science* 532.6287 (2016), pp. 795–797.

[68] V. Van et al. "All-optical nonlinear switching in GaAs-AlGaAs microring resonators". In: *IEEE Photonics Technologies Letters* 14.1 (2002), pp. 74–76.

[69] T. Volz et al. "Ultrafast all-optical switching by single photons". In: *Nature Photonics* 6.9 (2012), pp. 605–609.

[70] X. Hu et al. "Picosecond and low-power all-optical switching based on an organic photonic-bandgap microcavity". In: *Nature Photonics* 2.3 (2008), pp. 185–189.

[71] K. A. Stankov. "A mirror with an intensity-dependent reflection coefficient". In: *Applied Physics B Photophysics Laser Chemistry* 45.3 (1988), pp. 191–195.

[72] P. Drude. "Zur Elektronentheorie der Metalle". In: *Annalen der Physik* 306 (1900).

[73] P. Drude. "Zur Elektronentheorie der Metalle II: Teil. galvanomagnetische und thermomagnetische Effecte". In: *Annalen der Physik* 308(3) (1900).

[74] H.A. Lorentz. *Ergebnisse und Probleme der Elektronentheorie*. Springer, 1905.

[75] C. Kittel. *Introduction to Solid State Physics*. 8th Edition. Wiley, 2004.

[76] R.H. Ritchie. "Plasma Losses by Fast Electrons in Thin Films". In: *Physical Review* 106.5 (1957), pp. 874–881.

[77] R.E. Camley and D.L. Mills. "Collective excitations of semi-infinite superlattice structures: Surface plasmons, bulk plasmons, and the electron-energy loss spectrum". In: *Physical Review B* 29.4 (1984), pp. 1695–1706.

[78] H. Raether. *Excitation of Plasmons and Interband Transitions by Electrons*. Springer, 2006.

[79] J. Hägglund and F. Sellberg. "Reflection, Absorption, and Emission of Light by Opaque Optical Gratings". In: *Journal of the Optical Scoiety of America* 56.8 (1966), p. 1031.

[80] R. H. Ritchie et al. "Surface-plasmon resonance effect in grating diffraction". In: *Physical Review Letters* 21.22 (1968), pp. 1530–1533.

[81] R.W. Wood. "On a Remarkable Case of Uneven Distribution of Light in a Diffraction Grating Spectrum". In: *Proceedings of Physical Society of London* 18.1 (1902), pp. 269–275.

[82] Lord Rayleigh. "On the Dynamical Theory of Gratings Source". In: *Proceedings of the Royal Society of London* 79.532 (1907), pp. 399–416.

[83] J. Strong. "Effect of Evaporated Films on Energy Distribution in Grating Spectra". In: *Physical Review* 49 (1936), pp. 291–296.

[84] U. Fano. "The Theory of Anomalous Diffraction Gratings and of Quasi-Stationary Waves on Metallic Surfaces (Sommerfeld's Waves)". In: *Journal of the Optical Society of America* 31.3 (1941), pp. 213–222.

[85] D. Pines and D. Bohm. "A collective description of electron interactions: II. Collective vs individual particle aspects of the interactions". In: *Physical Review* 85.2 (1952), pp. 338–353.

[86] H. Watanabe. "Experimental Evidence for the Collective Nature of the Characteristic Energy Loss of Electrons in Solids - Studies on the Dispersion Relation of Plasma frequency". In: *Journal of the Physical Society of Japan* 11.2 (1956).

[87] L. B. Leder, H. Mendlowitz, and L. Marton. "Comparison of the Characteristic Energy Losses of Electrons with the Fine Structure of the X-Ray Absorption Spectra". In: *Physical Review* 101.5 (1956), pp. 1460–1467.

[88] W.L Barnes, A. Dereux, and T.W. Ebbesen. "Surface plasmon subwavelength optics." In: *Nature* 424.6950 (2003), pp. 824–830.

[89] T. Turbadar. "Complete absorption of light by thin metal films". In: *Proceedings of Physical Society* 73.1 (1959), pp. 40–44.

[90] T. Turbadar. "Complete Absorption of Plane Polarized Light by Thin Metallic Films". In: *Optica Acta: International Journal of Optics* 11.3 (1964), pp. 207–210.

[91] A. Otto. "Excitation of Nonradiative Surface Plasma Waves in Silver by the Method of Frustrated Total Reflection". In: *Zeitschrift fur Physica* 216 (1968), pp. 398–410.

[92] E. Kretschmann and H. Raether. "Radiative decay of non-radiative surface plasmons excited by light". In: *Zeitschrift für Naturforschung A* 23 (1968), pp. 2135–2136.

[93] I. Pockrand et al. "Surface plasmon spectroscopy of organic monolayer assemblies". In: *Surface Science* 74.1 (1978), pp. 237–244.

[94] J.G. Gordon and S. Ernst. "Surface plasmons as a probe of the electrochemical interface". In: *Surface Science* 101.1-3 (1980), pp. 499–506.

[95] B. Liedberg, C. Nylander, and I. Lunström. "Surface plasmon resonance for gas detection and biosensing". In: *Sensors and Actuators* 4 (1983), pp. 299–304.

[96] C. Nylander, B. Liedberg, and T. Lind. "Gas Detection by Means of Surface Plasmon Resonance Enhanced Ellipsometry". In: *Sensors and Actuators* 3 (1982), pp. 79–88.

[97] J. Homola, S.S. Yee, and G. Gauglitz. "Surface plasmon resonance sensors: review". In: *Sensors Actuators, B: Chemistry* 54.1 (1999), pp. 3–15.

[98] T.W. Ebbesen, C. Genet, and S.I. Bozhevolnyi. "Surface-plasmon circuitry". In: *Physics Today* 61.5 (2008), pp. 44–50.

[99] "Xiao, S. and Zhu, X. and Li, B.H. and Mortensen, N.A." In: *Frontiers of Physics* 11.2 (2016), pp. 1–13.

[100] A. N. Grigorenko, M. Polini, and K. S. Novoselov. "Graphene plasmonics". In: *Nature Photonics* 6.11 (2012), pp. 749–758.

[101] M.D. Losego et al. "Conductive oxide thin films: Model systems for understanding and controlling surface plasmon resonance". In: *Journal of Applied Physics* 106.024903 (2009).

[102] M.A. Ordal et al. "Optical properties of the metals Al, Co, Cu, Au, Fe, Pb, Ni, Pd, Pt, Ag, Ti, and W in the infrared and far infrared". In: *Applied Optics* 22.7 (1983), pp. 1099–1119.

[103] Y. Bludov et al. "A Primer on Surface Plasmon-Polaritons in Graphene". In: *International Journal of Modern Physics B* 27.1341001 (2013).

[104] S.A. Maier. *Plasmonics: Fundamentals and Applications*. Springer, 2007.

[105] W.L. Barnes. "Surface plasmon-polariton length scales: A route to sub-wavelength optics". In: *Journal of Optics A: Pure and Applied Optics* 8.4 (2006), pp. 87–93.

[106] G. Si et al. "Liquid-crystal-enabled active plasmonics: A review". In: *Materials (Basel).* 7.2 (2014), pp. 1296–1317.

[107] Y. Fang and M. Sun. "Nanoplasmonic waveguides: Towards applications in integrated nanophotonic circuits". In: *Light Science Applications* 4 (2015), pp. 1–11.

[108] C. Haffner et al. "All-plasmonic Mach-Zehnder modulator enabling optical high-speed communication at the microscale". In: *Nature Photonics* 9.8 (2015), pp. 525–528.

[109] A.G. Brolo et al. "Surface plasmon sensor based on the enhanced light transmission through arrays of nanoholes in gold films". In: *Langmuir* 20.12 (2004), pp. 4813–4815.

[110] K.S. Novoselov et al. “Electric field effect in atomically thin carbon films”. In: *Science* 306 (2004), pp. 666–668.

[111] F. Rana. “Graphene terahertz plasmon laser: A laser in a circuit”. In: *Conference Proceedings - Lasers Electro-Optics Society Annual Meeting* 7.1 (2007), pp. 862–863.

[112] R.A. Watts, Trevor W. Preist, and J.R. Sambles. “Sharp surface-plasmon resonances on deep diffraction gratings”. In: *Physical Review Letters* 79.20 (1997), pp. 3978–3981.

[113] D.C. Cullen, R.G.W. Brown, and C.R. Lowe. “Detection of immuno-complex formation via surface plasmon resonance on gold-coated diffraction gratings”. In: *Biosensors* 3.4 (1987), pp. 211–225.

[114] Z. Fei et al. “Gate-tuning of graphene plasmons revealed by infrared nano-imaging”. In: *Nature* 487.7405 (2012), pp. 82–85.

[115] J. Chen et al. “Optical nano-imaging of gate-tunable graphene plasmons”. In: *Nature* 487.7405 (2012), pp. 77–81.

[116] J. Renger, R. Quidant, and L. Novotny. “Enhanced nonlinear response from metal surfaces”. In: *Optics Express* 19.3 (2011), p. 1777.

[117] W. T. Rhodes. “History and Evolution of the Teaching of Fourier Optics”. In: *Proceedings of SPIE* 3572.July 1999 (2003), pp. 50–56.

[118] J. W. Goodman. *Introduction to Fourier Optics*. Roberts, 2005.

[119] P.R. Wallace. “The Band Theory of Graphite”. In: *Physical Review* 71.9 (1947), pp. 62–634.

[120] L.D. Landau. “Zur Theorie der phasenumwandlungen II”. In: *Physikalische Zeitschrift der Sowjetunion* (1937).

[121] R. Peierls. “Quelques propriétés typiques des corps solides”. In: *Annales de l’institut Henri Poincaré* 5.3 (1935), pp. 177–222.

[122] J. Stangl, V. Holý, and G. Bauer. “Structural properties of self-organized semiconductor nanostructures”. In: *Reviews Modern Physics* 76 (3 2004), pp. 725–783.

[123] J.C. Meyer et al. "The structure of suspended graphene sheets". In: *Nature* (76 2007).

[124] K. S. Novoselov et al. "Two-dimensional atomic crystals". In: *Proceedings of the National Academy of Sciences* 102.30 (2005), pp. 10451–10453.

[125] X. Li et al. "Large-area graphene single crystals grown by low-pressure chemical vapor deposition of methane on copper". In: *Journal of the American Chemical Society* 133.9 (2011), pp. 2816–2819.

[126] J.K. Wassei et al. "Chemical vapor deposition of graphene on copper from methane, ethane and propane: Evidence for bilayer selectivity". In: *Small* 8.9 (2012), pp. 1415–1422.

[127] Z. Liu et al. "Synthesis of three-dimensional graphene from petroleum asphalt by chemical vapor deposition". In: *Materials Letters* 122 (2014), pp. 285–288.

[128] H.J. Park et al. "Growth and properties of few-layer graphene prepared by chemical vapor deposition". In: *Carbon* 48.4 (2010), pp. 1088–1094.

[129] C. Mattevi, H. Kim, and M. Chhowalla. "A review of chemical vapour deposition of graphene on copper". In: *Journal of Materials Chemistry* 21 (2011).

[130] L. Gomez De Arco et al. "Synthesis, transfer, and devices of single- and few-layer graphene by chemical vapor deposition". In: *IEEE Transactions on Nanotechnology* 8.2 (2009), pp. 135–138.

[131] A. Reina et al. "Large area, few-layer graphene films on arbitrary substrates by chemical vapor deposition". In: *Nano Letters* 9 (2009), pp. 30–35.

[132] K.S. Kim et al. "Large-scale pattern growth of graphene films for stretchable transparent electrodes". In: *Nature* 457.7230 (2009), pp. 706–710.

[133] X. Li et al. "Large-Area Synthesis of High-Quality and Uniform Graphene Films on Copper Foils". In: *Science* 324 (2009), pp. 1312–1314.

[134] A.N. Obraztsov. "Making graphene on a large scale". In: *Nature Nanotechnology* 4 (2009), pp. 212–213.

[135] P.Y. Huang et al. "Grains and grain boundaries in single-layer graphene atomic patchwork quilts". In: *Nature* 469.7330 (2011), pp. 389–392.

[136] S. Bae et al. “Roll-to-roll production of 30-inch graphene films for transparent electrodes”. In: *Nature Nanotechnology* 5.8 (2010), pp. 574–578.

[137] X. Li et al. “Large-area graphene single crystals grown by low-pressure chemical vapor deposition of methane on copper”. In: *Journal of the American Chemical Society* 133.9 (2011), pp. 2816–2819.

[138] A. Venugopal et al. “Effective mobility of single-layer graphene transistors as a function of channel dimensions”. In: *Journal Applied Physics* 109.10 (2011), pp. 1–5.

[139] N. Petrone et al. “Chemical vapor deposition-derived graphene with electrical performance of exfoliated graphene”. In: *Nano Letters* 12.6 (2012), pp. 2751–2756.

[140] B.J. Park et al. “Defect-Free Graphene Synthesized Directly at 150 c via Chemical Vapor Deposition with No Transfer”. In: *ACS Nano* 12.2 (2018), pp. 2008–2016.

[141] P. Avouris and F. Xia. “Graphene applications in electronics and photonics”. In: *MRS Bulletin* 37.12 (2012), pp. 1225–1234.

[142] X. Huang et al. “Graphene-based materials: Synthesis, characterization, properties, and applications”. In: *Small* 7.14 (2011), pp. 1876–1902.

[143] A.H. Castro Neto et al. “The electronic properties of graphene”. In: *Reviews of Modern Physics* 81.1 (2009), pp. 109–162.

[144] K.S. Novoselov et al. “Two-dimensional gas of massless Dirac fermions in graphene”. In: *Nature* 438.7065 (2005), pp. 197–200.

[145] H. Wang et al. “Graphene Based Surface Plasmon Polariton Modulator Controlled by Ferroelectric Domains in Lithium Niobate”. In: *Scientific Reports* 5 (2015).

[146] M.I. Katsnelson, K.S. Novoselov, and A.K. Geim. “Chiral tunnelling and the Klein paradox in graphene”. In: *Nature Physics* 2 (2006), pp. 620–625.

[147] F. Schwierz. “Graphene transistors”. In: *Nature Nanotechnology* 7 (2012), pp. 51–91.

[148] F. Bonaccorso et al. "Graphene photonics and optoelectronics". In: *Nature Photonics* 4.9 (2010), pp. 611–622.

[149] D.A.C. Brownson, D.K. Kampouris, and C.E. Banks. "An overview of graphene in energy production and storage applications". In: *Journal Power Sources* 196.11 (2011), pp. 4873–4885.

[150] M. Pumera. "Graphene in biosensing". In: *Materials Today* 14.7 (2011), pp. 308–315.

[151] P.E. Gaskell et al. "Counting graphene layers on glass via optical reflection microscopy". In: *Applied Physics Letters* 94.14 (2009), pp. 2007–2010.

[152] S.A. Mikhailov. "Non-linear electromagnetic response of graphene". In: *Europhysics Letters* 79.2 (2007), p. 27002.

[153] N. Vermeulen et al. "Negative Kerr Nonlinearity of Graphene as seen via Chirped-Pulse-Pumped Self-Phase Modulation". In: *Physical Review Applied* 6.4 (2016), pp. 1–7.

[154] S.A. Mikhailov. "Theory of the nonlinear optical frequency mixing effect in graphene". In: *Physica E Low-Dimensional Systems and Nanostructures* 44.6 (2012), pp. 924–927.

[155] S.A. Mikhailov. "Theory of the giant plasmon-enhanced second-harmonic generation in graphene and semiconductor two-dimensional electron systems". In: *Physical Review B* 84.4 (2011), p. 045432.

[156] S.A. Mikhailov. "Non-linear electromagnetic response of graphene". In: *Europhysics Letters* 79.2 (2008), p. 27002.

[157] J.L. Cheng, N. Vermeulen, and J.E. Sipe. "Third order optical nonlinearity of graphene". In: *New Journal of Physics* 16 (2014). ISSN: 13672630.

[158] M. Jablan, H. Buljan, and M. Soljačić. "Plasmonics in graphene at infrared frequencies". In: *Physical Review B* 80.24 (2009), p. 245435.

[159] George W. Hanson. "Dyadic Green's functions and guided surface waves for a surface conductivity model of graphene". In: *Journal Applied Physics* 103.064302 (2008).

[160] L. Ju et al. “Graphene plasmonics for tunable terahertz metamaterials.” In: *Nature Nanotechnology* 10 (2011), pp. 630–4.

[161] F.H.L. Koppens, D.E. Chang, and F.J. García de Abajo. “Graphene plasmonics: A platform for strong light-matter interactions”. In: *Nano Letters* 11.8 (2011), pp. 3370–3377.

[162] W. Zhou et al. “Atomically localized plasmon enhancement in monolayer graphene”. In: *Nature Nanotechnology* 7.3 (2012), pp. 161–165.

[163] I. Crassee et al. “Intrinsic terahertz plasmons and magnetoplasmons in large scale monolayer graphene”. In: *Nano Letters* 12.5 (2012), pp. 2470–2474.

[164] A.C. Ferrari et al. “Raman spectrum of graphene and graphene layers”. In: *Physical Review Letters* 97.18 (2006).

[165] S.K. Son et al. “Graphene hot-electron light bulb: Incandescence from hBN-encapsulated graphene in air”. In: *2D Materials* 5.1 (2018).

[166] A. Alù et al. “Epsilon-near-zero metamaterials and electromagnetic sources: Tailoring the radiation phase pattern”. In: *Physical Review B - Condensed Matter Materials Physics* 75.15 (2007), pp. 1–13.

[167] J. Brown. “Artificial Dielectrics having Refractive Indices Less than Unity”. In: *Proceedings IEE - Part IV Institution Monographs* 100.5 (1953).

[168] N. Engheta et al. “DNG, SNG, ENZ, and MNZ metamaterials and their potential applications”. In: *Proceedings of Mediterranean Electrotechnical Conference - MELECON* (2006), pp. 258–261.

[169] J. Kim et al. “Role of epsilon-near-zero substrates in the optical response of plasmonic antennas”. In: *Optica* 3.3 (2016), p. 339.

[170] T.S. Luk et al. “Enhanced third harmonic generation from the epsilon-near-zero modes of ultrathin films”. In: *Applied Physics Letters* 106.15 (2015).

[171] L. Caspani et al. In: *Physical Review Letters* ().

[172] A. Capretti et al. “Enhanced third-harmonic generation in Si-compatible epsilon-near-zero indium tin oxide nanolayers”. In: *Optics Letters* 40.7 (2015), p. 1500.

[173] Y. Yang et al. "Femtosecond optical polarization switching using a cadmium oxide-based perfect absorber". In: *Nature Photonics* 11.6 (2017), pp. 390–395.

[174] O. Reshef et al. "Beyond the perturbative description of the nonlinear optical response of low-index materials". In: *Optics Letter* 42.16 (2017), pp. 3–6.

[175] M. Silveirinha and N. Engheta. "Tunneling of electromagnetic energy through subwavelength channels and bends using ϵ-near-zero materials". In: *Physical Review Letters* 97.15 (2006), pp. 1–4.

[176] U. Betz et al. "Thin films engineering of indium tin oxide: Large area flat panel displays application". In: *Surface and Coatings Technology* 200.20-21 (2006), pp. 5751–5759.

[177] H.G. Tompkins and E.A. Irene. *Handbook of Ellipsometry*. William Andrew Publishing, 2005.

[178] M. Born and E. Wolf. *Principles of optics:electromagnetic theory of propagation, interference and diffraction of light*. Oxford, Pergamon Press, 1962.

[179] Y. Wang et al. "Tunability of indium tin oxide materials for mid-infrared plasmonics applications". In: *Optics Materials Express* 7.8 (2017), p. 2727.

[180] T.J. Constant et al. "Intensity dependences of the nonlinear optical excitation of plasmons in graphene". In: *Philosophical Transactions of Royal Society A* 375.2090 (2017), p. 20160066.

[181] B. Yao et al. "Broadband gate-tunable THz plasmons in graphene heterostructures". In: *Nature Photonics* 11 (2017), pp. 272–278.

[182] M. Graf and P. Vogl. "Electromagnetic fields and dielectric response in empirical tight-binding theory". In: *Physical Review B* 51.8 (1995), p. 4940.

[183] L.D. Landau and E.M Lifshitz. *Quantum Electrodynamics: Volume 4*. 2nd. Butterworth-Heinemann, 1982.

[184] Y. Wang, M. Tokman, and A. Belyanin. "Second-order nonlinear optical response of graphene". In: *Physical Review B* 94.19 (2016), p. 195442.

[185] J. L. Cheng, N. Vermeulen, and J. E. Sipe. "Second order optical nonlinearity of graphene due to electric quadrupole and magnetic dipole effects". In: *Scientific Reports* 7 (2017), p. 43843.

[186] V.P. Gusynin, S.G. Sharapov, and J.P. Carbotte. "AC conductivity of graphene: from tight-binding model to 2 + 1-dimensional quantum electrodynamics". In: *International Journal of Modern Physics B* 21.27 (2007), pp. 4611–4658.

[187] V.P. Gusynin et al. "Edge states in quantum Hall effect in graphene (Review Article)". In: *Low Temperature Physics* 34.10 (2008), pp. 778–789.

[188] K. Ziegler, A. Hill, and A. Sinner. *Graphene Optoelectronics: Synthesis, Characterization, Properties, and Applications*. 2014.

[189] H. Rostami, M.I. Katsnelson, and M. Polini. "Theory of plasmonic effects in nonlinear optics: The case of graphene". In: *Physical Review B* 95.3 (2017), p. 035416.

[190] I. Shoji, T. Kondo, and R. Ito. "Second-order nonlinear susceptibilities of various dielectric and semiconductor materials". In: *Optics and Quantum Electron.* 34.8 (2002), pp. 797–833.

[191] P.J. Hale et al. "Hot phonon decay in supported and suspended exfoliated graphene". In: *Physical Review B* 83.12 (2011), p. 121404.

[192] P. Wei et al. "Anomalous thermoelectric transport of dirac particles in graphene". In: *Physical Review Letters* 102.16 (2009).

[193] Y.M. Zuev, W. Chang, and P. Kim. "Thermoelectric and magnetothermoelectric transport measurements of graphene". In: *Physical Review Letters* 102.9 (2009), pp. 1–4.

[194] K.J. Tielrooij et al. "Generation of photovoltage in graphene on a femtosecond timescale through efficient carrier heating." In: *Nature Nanotechnology* 10.5 (2015), pp. 437–43.

[195] K. Zhao et al. "Laser-induced ultrafast photovoltaic effect in La0.67Ca 0.33MnO3 films at room temperature". In: *Physica B: Condensed Matter* 373.1 (2006), pp. 72–75.

[196] J.D. Jackson. *Classical Electrodynamics*. 3rd. John Wiley & Sons, 1998.

[197] H. Rostami and M. Polini. "Theory of third-harmonic generation in graphene: A diagrammatic approach". In: *Physical Review B* 93.16 (2016), pp. 1–6.

[198] R. W. Boyd. *Nonlinear Optics*. Third. Elselvier, 2008.

[199] T. Jiang et al. "Gate-tunable third-order nonlinear optical response of massless Dirac fermions in graphene". In: *Nature Photonics* 12.7 (2018), pp. 430–436.

[200] E. Hendry et al. "Coherent nonlinear optical response of graphene". In: *Physical Review Letters* 105.9 (2010), pp. 1–4.

[201] R. Ciesielski et al. "Graphene Near-Degenerate Four-Wave Mixing for Phase Characterization of Broadband Pulses in Ultrafast Microscopy". In: *Nano Letters* 15.8 (2015).

[202] N. Kumar et al. "Third harmonic generation in graphene and few-layer graphite films". In: *Physics Review B - Condensed Matter Material Physics* 87.12 (2013), pp. 1–5.

[203] S.-Y. Hong et al. "Optical third-harmonic generation in graphene". In: *Physical Review X* 3.3 (2013), pp. 556–559.

[204] A. Säynätjoki et al. "Rapid large-area multiphoton microscopy for characterization of graphene". In: *ACS Nano* 7.10 (2013), pp. 8441–8446.

[205] R.I. Woodward et al. In: *2D Materials* 1 ().

[206] T. Gu et al. "Regenerative oscillation and four-wave mixing in graphene optoelectronics". In: *Nature Photonics* 6.8 (2012), pp. 554–559.

[207] H. Yang et al. "Giant two-photon absorption in bilayer graphene". In: *Nano Letters* 11.7 (2011), pp. 2622–2627.

[208] H. Zhang et al. "Z-scan measurement of the nonlinear refractive index of graphene". In: *Optics Letters* 37.11 (2012), p. 1856.

[209] "Purely coherent nonlinear optical response in solution dispersions of graphene sheets". In: *Nano Letters* 11.12 (2011), pp. 5159–5164.

[210] E. Dremetsika et al. In: *Optics Letters* 14 ().

[211] A. Principi et al. "Intrinsic lifetime of Dirac plasmons in graphene". In: *Physical Review B* 88 (19 2013).

[212] E. Alexeev. "Hot-carrier luminescence In graphene". PhD thesis. 2015.

[213] S. Molesky, C.J. Dewalt, and Z. Jacob. "High temperature epsilon-near-zero and epsilon-near-pole metamaterial emitters for thermophotovoltaics". In: *Optics Express* 21.S1 (2013), A96–A110.

[214] S. Feng and K. Halterman. "Coherent perfect absorption in epsilon-near-zero metamaterials". In: *Physical Review B* 86 (16 2012), p. 165103.

[215] S. Vassant et al. "Berreman mode and epsilon near zero mode". In: *Optics Express* 20.21 (2012), pp. 23971–23977.

[216] R. Maas et al. "Experimental realization of an epsilon-near-zero metamaterial at visible wavelengths". In: *Nature Photonics* 7 (2013), pp. 907–912.

[217] Ashcroft, N.W. and Mermin, N.D. *Solid State Physics*. Cengage Learning, 2011.

[218] X. Liu et al. "Quantification and impact of nonparabolicity of the conduction band of indium tin oxide on its plasmonic properties". In: *Applied Physics Letters* 105.18 (2014).

[219] T. Pisarkiewicz and A. Kolodziej. "Nonparabolicity of the Conduction Band Structure in Degenerate Tin Dioxide". In: *Physica Status Solidi* (1990).

[220] E.O. Kane. "Zener Tunneling in Semiconductors". In: *Journal of Physics and Chemistry of Solids* 12.2 (1959), pp. 181–188.

[221] L.C. Lew Yan Voon and M. Willatzen. *The k p method*. Springer, 2009.

[222] H.C. Lee. "Electron scattering mechanisms in indium-tin-oxide thin films prepared at the various process conditions". In: *Applied Surface Sciences* 252.10 (2006), pp. 3428–3435.

[223] D.H. Zhang and H.L. Ma. "Scattering mechanisms of charge carriers in transparent conducting oxide films". In: *Applied Physics A: Materials Science and Processing* 62.5 (1996), pp. 487–492.

[224] J. Elich, E.C. Boslooper, and H. Haitjema. "Electrical properties of sprayed tin oxide layers". In: *Thin Solid Films* 177.1-2 (1989), pp. 17–33.

[225] E. Shanthi et al. "Electrical and optical properties of tin oxide and antimony doped tin oxide films". In: *Journal of Applied Physics* 53 (1982), p. 1615.

[226] R.L. Petritz. "Theory of photoconductivity in semiconductor films". In: *Physics Review* 104.6 (1956), pp. 1508–1516.

[227] J.H. Lee et al. "Grain-size effect on the electrical properties of nanocrystalline indium tin oxide thin films". In: *Materials Science and Engineering B Solid-State Materials for Advanced Technology* 199 (2015), pp. 37–41.

[228] E. Shanthi et al. "Annealing characteristics of tin oxide films prepared by spray pyrolysis". In: *Thin Solid Films* 71.2 (1980), pp. 237–244.

[229] D. Belanger et al. "Thickness Dependence of Transport Properties of Doped Polycrystalline Tin Oxide Films". In: *Journal of the Electrochemical Society* 132.6 (1985), pp. 1398–1405.

[230] C. Rhodes et al. "Dependence of plasmon polaritons on the thickness of indium tin oxide thin films". In: *Journal of Applied Physics* 103.9 (2008), p. 093108.

[231] L. Jiang and H.L. Tsai. "Improved two-temperature model and its application in ultrashort laser heating of metal films". In: *Journal of Heat Transfer* 127.10 (2005), pp. 1167–1173.

[232] J.K. Chen, D.Y. Tzou, and J.E. Beraun. "A semiclassical two-temperature model for ultrafast laser heating". In: *International Journal of Heat and Mass Transfer* 49.1-2 (2006), pp. 307–316.

[233] C.K.; Sun et al. "Femtosecond investigation of electron thermalization in gold". In: *Physical Review B* 48.16 (1993), pp. 365–368.

[234] B. Rethfeld et al. "Timescales in the response of materials to femtosecond laser excitation". In: *Applied Physics A Materials Science and Processing* 79.4-6 (2004), pp. 767–769.

[235] K.S. Il'in et al. "Picosecond hot-electron energy relaxation in NbN superconducting photodetectors". In: *Applied Physics Letters* 76.19 (2000), pp. 2752–2754.

[236] G. Tas and Humphrey J. Maris. "Electron diffusion in metals studied by picosecond ultrasonics". In: *Physical Review B* 49.21 (1994), pp. 15046–15054.

[237] J.J. Lin and Z.Q. Li. "Electronic conduction properties of indium tin oxide: Single-particle and many-body transport". In: *Journal of Physics: Condensed Matter* 26 (2014).

[238] T. Ashida et al. "Thermal transport properties of polycrystalline tin-doped indium oxide films". In: *Journal Applied Physics* 105.7 (2009).

[239] W.S. Fann et al. "Direct measurement of nonequilibrium electron-energy distributions in sub-picosecond laser-heated gold films". In: *Physical Review Letters* 68.18 (1993).

[240] M. Kanehara et al. "Indium tin oxide nanoparticles with compositionally tunable surface plasmon resonance frequencies in the near-IR region". In: *Journal of the American Chemical Society* 131.49 (2009), pp. 17736–17737.

[241] H. Kim et al. "Electrical, optical, and structural properties of indium-tin-oxide thin films for organic light-emitting devices". In: *Journal Applied Physics* 86.11 (1999), pp. 6451–6461.

[242] T Q Qiu and C L Tien. "Short-pulse laser heating on metals". In: *International Journal of Heat and Mass Transfer* 35.3 (1992), pp. 719–726.

[243] D.Y. Tzou, J.K. Chen, and J.E. Beraun. "Hot-electron blast induced by ultrashort-pulsed lasers in layered media". In: *International Journal of Heat and Mass Transfer* 45.16 (2002), pp. 3369–3382.

[244] R.J. Moerland and J.P. Hoogenboom. "Subnanometer-accuracy optical distance ruler based on fluorescence quenching by transparent conductors". In: *Optica* 3.2 (2016), p. 112.

[245] Q. Bian et al. "Femtosecond laser ablation of indium tin-oxide narrow grooves for thin film solar cells". In: *Optics Laser Technology* 45.1 (2013), pp. 395–401.

[246] J.F. Ward. "Calculation of nonlinear optical susceptibilities using diagrammatic perturbation theory". In: *Reviews of Modern Physics* 37.1 (1965), pp. 1–18.

[247] I.J. Luxmoore et al. "Strong Coupling in the Far-Infrared between Graphene Plasmons and the Surface Optical Phonons of Silicon Dioxide". In: *ACS Photonics* 1.11 (2014), pp. 1151–1155.